

**BOND BEHAVIOUR OF STEEL REINFORCING BARS
EMBEDDED IN ULTRA-HIGH-PERFORMANCE STEEL FIBER
REINFORCED CONCRETE**

Rita Saikali

A Thesis Submitted to the Faculty of Graduate Studies
in Partial Fulfillment of the Requirements
for the Degree of Master of Applied Science

Graduate Program in Civil Engineering
York University
Toronto, Ontario

February 2019

© Rita Saikali, 2019

Abstract

Ultra-High-Performance Steel Fiber Reinforced Concrete (UHP-SFRC) is an emerging concrete considered as an optimal, durable material that can substitute conventional concrete owing to its distinct fresh and hard properties. Thus, it is essential to understand the mechanism of stress transfer between this concrete and conventional reinforcement that permits the composite action of both materials. A four-point bending test program (FPBT) was arranged and conducted on 19 beams designed for the bond development to occur in the constant moment region along a short embedment length in order to achieve a uniform distribution of bond stresses, enabling measurement of bond strength through reverse engineering of beam strength and deformation. Additional material testing was conducted on prisms under 4-point loading in order to extract the mechanical properties for all material mixes considered. The bond-specimens failed either by pullout or by cone formation with minimal deterioration of the concrete cover, illustrating the high confinement provided by the novel concrete surrounding the bar in tension. The bond strength was determined to be directly proportional to the tensile strength capacity of the design mix, where for the strongest material the bond strength was approximately 30 MPa. Moreover, the test results indicated a very ductile flexural beam response accompanied by significant mid-span deflection reaching 27 mm and substantial bar-slip values attaining 19 mm. Different UHP-SFRC mixes, concrete covers, and embedment lengths were considered. A numerical model was developed to simulate the FPBT using a nonlinear finite element analysis platform, VecTor2, with the ability to model this novel concrete. The high bond strength provided by the concrete cover enables a significant reduction in the design development length as compared to what is used today for conventional concrete.

Acknowledgments

These two years of Masters were the most challenging years in my life. I have learned so much from each person I met starting from both of my supervisors: Dr. Pantazopoulou and Dr. Palermo that both guided me along the way using each one their own touch and making me discover a potential I never knew I had. Their positive and motivational words always encouraged me to accomplish more and this thesis is one of my biggest achievements so far. It was an honor and a privilege to work with both of them together.

Gratitude also goes to my friends and colleagues who were always there to share our good and bad moments, laugh and cry together; Ranim Dahli, Sebnem Boduroglu, Amanda Maia, Marina Maciel, Tintu Tomy, Najmeh Eshghi and Zoi Ralli. I would like to thank those who helped in the experimental program along with the lab technician Riad Rajab who always managed to help and make the lab work more pleasant, Mena Morcos, Adrien Sparling and Kostas Tsiotsias.

An exceptional thanks goes to my boyfriend Michael Soto who I met in the beginning of this journey and who has supported me until the end. I am very thankful for all the effort he put in this research, the lab work and the belief that this project will work. Hope I will get to support you in your research as well!

The last but not least people are my family that are far by distance, starting with my mother and father that always pushed me to achieve the best I can do and supported me in all my decisions. A very special thanks goes to my two twin best friends Tracy and Mary who helped me hand by hand in this journey and to whom I owe most of my achievements. I would like to thank them as well for their patience and for always being there for me in the hardest times. I would like to thank my family that is present near me, my brothers Peter and John for their guidance and their constant support, and lastly my aunt and cousin Caroline who were there for me in Canada and never failed to make me feel like Canada is my second home.

Table of Contents

Abstract	ii
Acknowledgments	iii
Table of Contents	iv
List of Tables	xi
List of Figures	xv
List of Abbreviation	xxv
List of Symbols	xxvi
Chapter 1. Introduction	1
1.1 Background	1
1.2 Introduction of UHPFRC	2
1.3 Introduction of steel-concrete bond	6
1.3.1 The spread of the conical and transversal cracks	8
1.3.2 Rupture of the reinforcing bar	8
1.3.3 The spread of longitudinal cracks and splitting failure mode	9
1.3.4 The spread of cylindrical bond cracks and pullout failure mode	9
1.4 Thesis objectives	12
1.5 Thesis outline	13
1.5.1 Chapter 2 – Literature review	13
1.5.2 Chapter 3 – Plan of the experimental program	14
1.5.3 Chapter 4 – Execution of the experimental program	14
1.5.4 Chapter 5 – Experimental results	14
1.5.5 Chapter 6 – Numerical study	14
1.5.6 Chapter 7 – Conclusions	15

1.6 Scope and objective of the thesis	15
Chapter 2. Literature Review	17
2.1 UHP-SFRC	17
2.1.1 Development of UHP-SFRC.....	17
2.1.2 Composition of UHP-SFRC	19
2.1.3 Effect of steel fibers on UHP-SFRC properties.....	23
2.1.3.1 Effect on the tensile properties and workability	23
2.1.3.2 Effect on the compressive strength and Young's modulus.....	27
2.1.4 Mechanical properties of UHP-SFRC	28
2.1.5 UHP-SFRC under fire.....	30
2.1.6 UHP-SFRC design mixes considered as trials.....	33
2.2 Bond strength	37
2.2.1 Bond force-slip law for deformed bars embedded in conventional concrete	37
2.2.2 Different types of bond tests	41
2.2.3 Previous experimental and parametric research on UHP-SFRC	43
2.2.3.1 Modes of failure.....	43
2.2.3.2 Bond tests and results.....	44
Chapter 3. Plan of the Experimental Program	51
3.1 Choice of the experimental setup and type of specimen to be tested	51
3.1.1 Bond test type	51
3.1.2 Parametric evaluation.....	53
3.1.3 Specimen detailing.....	53
3.1.4 Design verification of the beams	55
3.1.4.1 Concrete cover	55
3.1.4.2 Shear span to effective depth ratio.....	56
3.1.4.3 Selection of longitudinal steel reinforcement ratio.....	57
3.1.4.4 Design detailing	59
3.1.4.4.1 Embedment length of $l_b = 5db$	59

3.1.4.4.2 Embedment length of $l_b = 10db$ and $l_b = 15db$	60
3.1.4.4.3 Cross-section detailing along the length of the beam.....	62
3.1.4.4.4 Additional specimens for testing.....	64
3.1.5 Detailing of the notch and the wood block.....	65
3.1.6 Test setup and procedure.....	69
3.1.7 Measuring equipment and tools.....	71
3.1.7.1 Deflection of the mid-span of the beam.....	71
3.1.7.2 Slip of the main reinforcing bar.....	73
3.1.7.3 Digital image correlation (DIC).....	74
3.1.8 Displacement rate.....	75
3.1.9 Extraction of the bond strength.....	75
3.2 Choice of the mixes considered: Preliminary and Commercial.....	76
3.2.1 In-house trials and final matrix characteristics.....	76
3.2.1.1 Equipment and tools used.....	76
3.2.1.2 Material used.....	77
3.2.1.3 Trials.....	79
3.2.1.3.1 The trial of the design mixture (Yu et al., 2014).....	79
3.2.1.3.2 The trial of the design mixture (Shao, 2016).....	84
3.2.1.3.2.1 Trial phase 1.....	84
3.2.2 Commercial.....	88
3.3 Material characterization tests.....	89
3.3.1 Compression strength.....	89
3.3.2 Flexural strength.....	89
3.3.2.1 Shear span effect.....	90
3.3.2.2 Method of casting.....	90
3.3.3 Splitting strength.....	92
3.3.4 Fiber Distribution.....	94
3.3.5 Reinforcement properties.....	95
Chapter 4. Execution of the experimental program.....	96
4.1 Preparation of the wood formwork for the beams.....	96

4.2 Preparation of the specimens	100
4.3 Batching, casting and curing of the different mixes	106
4.3.1 Commercial K.....	107
4.3.1.1 Material, design mix proportions and batching	107
4.3.1.2 Mixing procedure.....	108
4.3.1.3 Casting and curing	109
4.3.2 Commercial F.....	111
4.3.2.1 Material, design mix proportions and batching	111
4.3.2.2 Mixing procedure.....	112
4.3.3 In-house mix	115
4.3.3.1 Material, design mix proportions and batching	115
4.3.3.2 Mixing procedure.....	116
4.3.3.3 Error during casting	120
4.4 Adjustments of the specimens for testing.....	121
4.5 Experimental testing	127
4.5.1 Test setup	127
4.5.2 Modification of the test setup	129
Chapter 5. Experimental Results.....	131
5.1 Cylinder compression strength	131
5.1.1 The gain in strength values with maturity.....	131
5.1.2 Compressive strength values.....	132
5.1.3 Pre-peak compressive stress-strain behavior and Young's modulus.....	132
5.1.4 Failure crack pattern	133
5.2 Flexural strength	134
5.2.1 Load-deformation response from the four-point loading test.....	134
5.2.2 Peak load and flexural strength calculations.....	137
5.2.3 Mode of failures observed	138

5.3 Splitting tensile strength	139
5.3.1 Splitting tensile strength	139
5.3.2 Failure pattern	140
5.4 Fiber distribution.....	141
5.5 Experimental observations of the beam specimens	142
5.5.1 Beams KE1C1.....	142
5.5.2 Beams KE1C2.....	145
5.5.3 Beams KE4C1.....	147
5.5.4 Beams KE4C2.....	149
5.5.5 Beams FE1C1	150
5.5.6 Beams FE1C2	152
5.5.7 Beams FE4C1	154
5.5.8 Beams IE1C1	155
5.5.9 Beams IE1C2	157
5.5.10 Beams IE2C2	160
5.5.11 Beams IE3C2	162
5.5.12 Summary of results	163
5.6 Comparison and discussion.....	166
5.6.1 Effect of the properties of UHP-SFRC	166
5.6.2 Effect of the concrete cover	169
5.6.3 Effect of the embedment length.....	172
5.7 Comparison between deflection obtained from the linear potentiometer and DIC	174
Chapter 6. Numerical Study.....	175
6.1 Introduction.....	175
6.2 Non-linear modeling tool (VecTor2).....	176
6.3 Modeling methodology.....	180
6.4 UHP-FRC concrete modeling in VecTor2.....	181

6.4.1 Concrete model	181
6.4.2 Models of the prisms in VecTor2	183
6.4.3 Mechanical properties for each design mixture:	184
6.4.3.1 In-house design mixture.....	184
6.4.3.2 Mechanical properties for Commercial K.....	186
6.4.3.3 Mechanical properties for Commercial F	188
6.5 Finite element models developed for beam specimens.....	189
6.5.1.1 Constitutive model for reinforcing steel	191
6.5.1.2 Discrete reinforcement elements.....	192
6.5.1.3 Bond link element properties	192
6.5.1.4 Support conditions	192
6.5.1.5 Loading protocol.....	192
6.6 Results.....	193
6.6.1 Beam KE1C1	193
6.6.2 Beam KE1C2	194
6.6.3 Beam KE4C1	194
6.6.4 Beam KE4C2	195
6.6.5 Beam FE1C1	196
6.6.6 Beam FE1C2.....	196
6.6.7 Beam FE4C1	197
6.6.8 Beam IE1C1.....	198
6.6.9 Beam IE1C2.....	198
6.6.10 Beam IE2C2.....	199
6.6.11 Beam IE3C2.....	200
Chapter 7. Conclusions	202
7.1 Mechanical properties of UHP-FRC.....	202
7.2 Beam bond test.....	203
7.2.1 Resistance curve.....	203

7.2.2 Bond strength	205
7.2.3 UHP-FRC numerical modeling.....	206
7.3 Discussion for further development of the research	207
References	208
Appendices.....	219
Appendix A Instrumentation drawings and detailing	219
A.1 Four-point bending jig drawings.....	219
A.2 Deflection frame drawings.....	223
A.3 Deflection horizontal bar drawing	223
A.4 Slip frame compartments drawings.....	224
Appendix B In-house design mix trials	225
B.1 Sieve analysis to obtain the maximum grain size for each sand type S1, S2, and S3.....	225
B.2 Trial mixes for (Yu <i>et al.</i> , 2014)	226
B.3 Mixing trials for (Shao, 2016).....	230
B.4 Flow test procedure for the in-house design mixture for the different casting batches	232
Appendix C Material and equipment.....	235
C.1 Material and Equipment for batching, casting, curing and testing concrete	235
C.2 Material and Equipment for building the formwork and test setup	236
Appendix D Additional data of failed specimens	241
D.1 Cylinders mode of failure	241
D.2 Flexural prisms mode of failure	244
D.3 Bond failure and mode of failure	246
D.3.1 First cracking.....	262

List of Tables

Chapter 2: Literature review

Table 2-1 Reference design mix proposed M	34
Table 2-2 Reference design mix proposed B	35
Table 2-3 Bond strength values for the pullout PO specimens for different d_b and V_f (Schoening and Hegger, 2012).....	45

Chapter 3: Plan of the experimental program

Table 3-1 Detailing of the beam for the test setup with an embedment length equal to 5 times the bar diameter for two different concrete covers	59
Table 3-2 Detailing of the beam for the test setup with an embedment length equal to 10 and 15 times the bar diameter for two different concrete covers	61
Table 3-3 Detailing of the cross-section of the beam in the specific locations (in mm)	62
Table 3-4 Detailing of the beam for the test setup with fully embedded $10d_b$ reinforcing bar for two different concrete covers.....	64
Table 3-5 Notch detailing for the experimental setup (in mm)	66
Table 3-6 Block of wood detailing for the experimental setup (in mm)	68
Table 3-7 Detailing of the frame used to attach the linear potentiometer and measure the slip of the reinforcing bar.....	74
Table 3-8 Materials used for trial and final concrete in-house mixture.....	77
Table 3-9 Design mix of the first trial, workability and the cube compressive strength	80
Table 3-10 Elongation of mixing procedure for two mixes M8/M9	82
Table 3-11 Design mix for the 6 th batch, same liquid additives but extended mixing time	87
Table 3-12 Set of prisms for the flexural test to calculate the tensile strength.....	91

Chapter 4: Execution of the experimental program

Table 4-1 Cut-parts of the plywood and dimensions per beam	97
Table 4-2 Type of timbers cut and length per beam	97
Table 4-3 Specimen annotation according to the parameters considered.....	100
Table 4-4 Marking of the center of the holes for the wood block and notch.....	101
Table 4-5 Dimensions of the steel bars and the PVC pipe (mm).....	102
Table 4-6 Volume required per specimen.....	106
Table 4-7 Design mix proportions for 200 L (company K).....	107
Table 4-8 Casting, curing, demolding and storing of the concrete specimens	110
Table 4-9 Materials used for the design mixture of company F	111
Table 4-10 Design mix proportions for 80 L (company F)	112
Table 4-11 Measured diameters of different flow test to obtain the optimal value	114
Table 4-12 Design mixture proportions for all the in-house design mixes.....	116
Table 4-13 Mixing procedure for the in-house design mixture divided into different steps ...	117
Table 4-14 Flow tests for batch C2 of the in-house design mix	119
Table 4-15 Quantity used to smoothen the surface of one beam.....	123
Table 4-16 Prepared beams for different embedment lengths for a concrete cover $2d_b$	126

Chapter 5: Experimental results

Table 5-1 Compression strength of the design mixtures	132
Table 5-2 Mechanical properties of the cylinder IE1C1.....	133
Table 5-3 Summary of the results obtained from flexural tests for the in-house mix	137
Table 5-4 Average flexural strength of the design mixes under study	139
Table 5-5 Results for the splitting tensile test.....	139
Table 5-6 Summary of salient parameters from beam tests.....	165

Chapter 6: Numerical study

Table 6-1 Constitutive models for the concrete behavior utilized in VecTor2.....	181
--	-----

Table 6-2 Compression test results	185
Table 6-3 Constitutive models for the steel reinforcement utilized in VecTor2	191

Appendix B

Table B-1 Sieve analysis for the sand used	225
Table B-2 Design mix for the 2 nd trial to compare the flowability caused by SP1 and SP2 ...	226
Table B-3 Design mix for the 3 rd trial where the LP was replaced by FA instead of C	226
Table B-4 Design mix for the fourth trial with type of sand S1(w/b = 0.2)	226
Table B-5 Design mix for the fifth trial where the volume is doubled (w/b = 0.37).....	227
Table B-6 Design mix for the 6 th trial, addition of water and superplasticizer (w/b = 0.28)...	227
Table B-7 Design mix for the 7 th trial, addition of water and superplasticizer (w/b = 0.22)...	227
Table B-8 Design mix for the 8 th and 9 th trial with 30% FA and 70% Slg1, cubes at 7 days..	227
Table B-9 Design mix for the 10 th trial with 50% FA and 50% Slg1, cube at 28 days	228
Table B-10 Design mix for the 11 th trial with 70% FA and 30% Slg1, cube at 28 days	228
Table B-11 Design mix for the trial 12 with 70% of Slg1 and 30% of SF1, cube at 28 days .	228
Table B-12 Design mix of trial 13 with the new materials; 15% FA, 25% SF2, 60%Slg2.....	229
Table B-13 Design mix for the 14 th trial identical to M13 with different mixing procedure ..	229
Table B-14 Design mixture for the first trial with S1 and S2 divided equally (Shao, 2016) ..	230
Table B-15 Design mix for the 2 nd trial with 20% S2 and 80% S1, SP2 (w/b = 0.18).....	230
Table B-16 Design mix for the third trial (w/b = 0.2)	230
Table B-17 Design mix for the fourth trial using the same reference materials (w/b = 0.2)...	231
Table B-18 Design mix for batch 6 with same liquid additives but longer mixing time.....	231
Table B-19 Design mix for the seventh batch with less superplasticizer and same extended mixing time (w/b = 0.2)	231
Table B-20 Design mix of batch 8 with same proportions as B7 to study the size effect	232
Table B-21 Design mixture for the final batch for casting (w/b = 0.2)	232
Table B-22 Flowability tests for batch C3 (in-house design mix).....	232
Table B-23 Flowability tests for batch C4 of the (in-house design mix).....	233
Table B-24 Flowability tests for batch C5 of the (in-house design mix).....	233
Table B-25 Flowability tests for batch C6 of the in-house design mix	234

Appendix C

Table C-1 Tools used to batch, mix and cast concrete	235
Table C-2 List of materials used to build the beams (Source: Home Depot)	236
Table C-3 Materials used to build the beam setup.....	237
Table C-4 Material used for the frame measuring the slip of the reinforcing bar	238
Table C-5 Tool used for the experimental execution.....	239

Appendix D

Table D-1 Failure mode of the cylinders for the in-house design mixture	241
Table D-2 The other failed faces of the prisms from Series S1, S2, S3 and S4	244
Table D-3 Cracking pattern for all faces of Beam KE1C1	246
Table D-4 Cracking pattern for all faces of Beam KE1C2.....	247
Table D-5 Cracking pattern for all faces of Beam KE4C1	249
Table D-6 Cracking pattern for all faces of Beam KE4C2.....	250
Table D-7 Cracking pattern for all faces of Beam FE1C1.....	251
Table D-8 Cracking pattern for all faces of Beam FE1C2.....	252
Table D-9 Cracking pattern for all faces of Beam FE4C1.....	253
Table D-10 Cracking pattern for all faces of Beam IE1C1	255
Table D-11 Cracking pattern for all faces of Beam IE1C2	256
Table D-12 Cracking pattern for all faces of Beam IE2C2	258
Table D-13 Cracking pattern for all faces of Beam IE3C2	260

List of Figures

Chapter 1: Introduction

Figure 1-1 Number of bridges using UHPC in Canada (Haber et al., 2018).....	1
Figure 1-2 (a) Initial damaged surface and (b) Retrofitted with UHP-SFRC (Doiron, 2017).....	2
Figure 1-3: (a) Classification of FRC composites (b) previously based on four performance levels (Naaman and Reinhardt, 2003) recent based on their tensile and bending behavior (Naaman and Reinhardt, 2006)	3
Figure 1-4 Comparison of the stress-strain response under direct tension between (a) strain softening and (b) strain-softening behavior (Naaman and Reinhardt, 2003).....	4
Figure 1-5 Definition of UHPFRC (HABEL, 2004)	5
Figure 1-6: (a) Bridge pier prior (b) and after retrofitting (Doiron, 2017)	6
Figure 1-7: (a) Chillon Viaducts UHPC reinforced bridge deck design (b) and application (Sritharan et al., 2018)	6
Figure 1-8: Force transfer mechanisms (ACI Committee 408, 2003)	7
Figure 1-9 : Development of stresses along the interface steel-concrete (Phan, 2012).....	8
Figure 1-10 (a) Extraction of the concrete cone (b) Steel bar rupture (Ramirez, 2005).....	9
Figure 1-11: (a) Radial stresses applied to the concrete element (Tastani et al., 2016) (b) splitting failure (Ramirez, 2005).....	9
Figure 1-12: (a) Shear stresses on the concrete element causing tensile stresses (b) cylindrical cracks (Ramirez, 2005)	10
Figure 1-13 Local relationship between bond stress-slip (fib/ceb/fip 2000)	11
Figure 1-14: Enhancement of the propagation of cracks with steel fibers (Chao et al., 2009)..	11

Chapter 2: Literature review

Figure 2-1 Tensile behavior for different HSFRC (Spasojević, 2008).....	18
Figure 2-2 Transformation of the matrix-fiber interface known as “fiber energy-absorbing mechanism” (Zollo, 1997)	24

Figure 2-3 Comparison of the shear stress slip response for smooth steel fibers when embedded in HSC ($f_c' = 60$ MPa) and UHPC ($f_c' > 194$ MPa) (Wille et al., 2012).....	25
Figure 2-4 Similarities in the tensile properties for S, T and H fibers: (a) peak tensile strength (b) peak tensile strain (c) energy absorption capacity g (d) fracture energy (Wille et al., 2014)....	26
Figure 2-5 Pullout load-slip relationship for different parameters for short steel brass-coated steel fiber in UHPC (Wille and Naaman, 2013).....	27
Figure 2-6 Effect of steel fibers on the compressive strength (Shao, 2016).....	28
Figure 2-7 Pre-peak compressive stress-strain behavior of UHPC (Haber et al., 2018)	29
Figure 2-8 Mixing procedure followed to obtain the proposed design mix (Yu et al., 2014) ...	34
Figure 2-9 Mixing procedure proposed (Shao, 2016).....	35
Figure 2-10 Tensile stress-strain behavior obtained (Shao, 2016)	36
Figure 2-11 Equilibrium of forces acting on the bar with conventional concrete	37
Figure 2-12 Assumed (grey line) and measured (black line) local bond-stress slip law (Tastani and Pantazopoulou, 2010).....	39
Figure 2-13 Analytical solution for bond stress behavior with elastic behavior of the reinforcing bar and bond (a) elastic behavior of the reinforcing bar and plastic behavior of bond (c) plastic behavior of steel bar and bond (Tastani and Pantazopoulou, 2013).....	40
Figure 2-14 Frictional concept (Tastani and Pantazopoulou, 2002).....	40
Figure 2-15 (a) Forces acting on the bar in HPFRC (b) Assumed local bond-stress slip law for HPFRC (Eleftheriou, Tastani and Pantazopoulou, 2017).....	41
Figure 2-16 Bond transfer test (Cairns and Plizzari, 2003)	41
Figure 2-17 (a) Standard pullout specimen, (b) beam-end specimen, (c) DTP (Tastani and Pantazopoulou, 2002) and (d) beam anchorage specimen (Top) splice specimen (Bottom) (ACI Committee 408, 2003)	42
Figure 2-18 Concrete failure modes (Fehling et al., 2012).....	44
Figure 2-19 Relationship between different types of the failure mode (Fehling et al., 2012)...	44
Figure 2-20 Bond-stress slip response (Lagier et al., 2016)	47
Figure 2-21 Direct pullout test setup to measure bond and concrete splitting.....	47
Figure 2-22 (a)in free space cover (b)between reinforcement (Yuan and Graybeal, 2014).....	48
Figure 2-23 Load-deflection response curve for the beams (Dagenais and Massicotte, 2012) .	50

Chapter 3: Plan of the experimental program

Figure 3-1: Free body diagram of specimen under four-point loading.....	51
Figure 3-2 Free-body diagram for $0 < x < a$	52
Figure 3-3 Free-body diagram for $a < x < a + b$	52
Figure 3-4 Free-body diagram for $a + b < x < 2a + b$	52
Figure 3-5: Moment and shear diagram of the test setup.....	53
Figure 3-6 (a) Steel and (b) wood formwork	54
Figure 3-7 Specimen detailing for an embedment length of $5d_b$	55
Figure 3-8 Detailing of the formwork and beam length for embedment lengths 5 and $10d_b$	56
Figure 3-9 Detailing of the formwork and beam length for embedment lengths $15d_b$	57
Figure 3-10 3D model of the experimental test setup for all the specimens.....	69
Figure 3-11 Jig used for the four-point bending test.....	70
Figure 3-12 Test setup of the back of the beam.....	70
Figure 3-13 Test setup of the front of the beam.....	71
Figure 3-14 Detailing of the vertical frame	72
Figure 3-15 Detailing of the aluminum rod with the linear potentiometer A.....	73
Figure 3-16 Methodology to insert the T-nut inside the bar ('The Profile System,' 2003).....	74
Figure 3-17 Force diagram for the beams with a concrete cover $c = d_b$ (in mm)	75
Figure 3-18 Force diagram for the beams with a concrete cover $c = 2d_b$ (in mm).....	76
Figure 3-19 Load-actuator displacement (mm)	83
Figure 3-20 Failed prisms and cubes (a) M14 and (b) B4	85
Figure 3-21 Load-deflection behavior for mix B4, M13 and M14.....	86
Figure 3-22 Addition of the liquid material in one phase during step 2	87
Figure 3-23 Test setup for compression for the Controls Pilot testing machine	89
Figure 3-24 Prisms dimensions for third point loading test (mm).....	90
Figure 3-25 Third-point loading test setup from the front.....	91
Figure 3-26: (a) Test setup with (b) the camera and the lighting.....	92
Figure 3-27 (a) Test procedure (b) simplified force system (c) stresses on element (Wight and MacGregor, 2012).....	93
Figure 3-28 Splitting tensile test in the Controls Pilot testing machine	93

Chapter 4: Execution of the experimental program

Figure 4-1 3-D drawing of the beam formwork.....	96
Figure 4-2 Partitioning of the plywood for the three beams (hatch part is waste).....	97
Figure 4-3 Base panel of the beam by screwing base B1 on top of base B2	98
Figure 4-4 One side panel of the beam formed by the base S-1 along with the two types of 2x2 in. timber T_h and T_{v1}	98
Figure 4-5 Detailing of the stainless-steel thread rod to hold all the parts together	99
Figure 4-6 Oiling of the wood and steel formwork	99
Figure 4-7 Marking of the reinforcing bars	102
Figure 4-8 (a) Cutting of steel plate (b) T-head (50 mm x 50 mm) and (c) welded reinforcing bar and T-head plate.....	103
Figure 4-9 (a) Blockwood, notch, PVC pipe and steel bars prepared for an $l_b = 5d_b$ and $c = 1d_b$ (b) $c = 2d_b$	103
Figure 4-10 (a) Block wood, notch, PVC pipe and steel bars prepared for a fully bonded bar and $c = 1d_b$ (b) $c = 2d_b$	103
Figure 4-11 (a) Setup for the embedment length of $5d_b$ and verification (b)	104
Figure 4-12 Setup for the embedment length of $10d_b$	104
Figure 4-13 (a) Setup for the embedment length of $15d_b$ and (b) detailing of the T-head bar	105
Figure 4-14 Setup for the fully bonded beams.....	105
Figure 4-15 Setup of the mixing station	106
Figure 4-16 Addition of the wet additives on top of the pre-mixed dry materials	108
Figure 4-17 Addition of steel fibers.....	108
Figure 4-18 (a) Flow test, (b) final mixing after reaching the wanted workability and before casting (c) Covering of the concrete surface during the flowability test and casting.....	109
Figure 4-19 Emptying the concrete from the mixing pan (In-house C2 mix)	109
Figure 4-20 (a) Addition of the drymix and wet mix, (b) mixing and (c) plastic state.....	112
Figure 4-21 Preparation of (a) the table surface and (b) pouring the sample in the mold	113
Figure 4-22 Addition of two wet mix additives to increase the flowability of the mixture	113
Figure 4-23 (a) Addition of steel fibers Type 1 and Type 2 and (b) mixing	114
Figure 4-24 Bucket containing water and half of SP3 (left) half of SP3 (right).....	116

Figure 4-25 Size effect on the amount of superplasticizer used	120
Figure 4-26 Roughening of the surface of beam IE1C2	120
Figure 4-27 Poorly consolidated beam from batch C3	121
Figure 4-28 (a) Removal of the foam board and (b) extension of the auxiliary bars	121
Figure 4-29: Cutting of the auxiliary bars.....	122
Figure 4-30: Plaster powder and water used to mix the plaster.....	122
Figure 4-31(a) Addition of plaster to the water, (b) soaking and (c) final state of the plaster	123
Figure 4-32 (a) Marking the location of the rollers and the legs of the rods of the frame, (b) placing duct tape and the plaster in the concerned surface, and (c) removal of the beam and the duct tape to obtain a smooth surface.....	124
Figure 4-33 (a) Primer used as finishing, and (b) acrylic paint used to speckle the beams.....	124
Figure 4-34 (a) Examples of the speckled front face of the beams, and (b) painting of the bottom of the beam.....	125
Figure 4-35 (a) Before adjusting the end of the 15M bar, and (b) smoothening of the area ...	125
Figure 4-36 Placement of the steel beam, the supports, and the specimen.....	127
Figure 4-37 (a) Aluminum frame and linear pot B, (b) and (c) attachment of the steel frame	127
Figure 4-38 (a) Aluminum bar, (b) angle for linear pot and (c) placing bar on the steel frame	128
Figure 4-39 Test setup followed with the presence of cameras, lighting, and clocks	128
Figure 4-40 Setup to capture the face of the beam at the mid-span with the clock	129
Figure 4-41 Modification of the steel frame to accommodate beam KE4C2	129
Figure 4-42 (a) Modified test setup and (b) jig used to test beams FE1C2 and IE2C2	129
Figure 4-43 Test setup for the specimens FE4C2 and IE3C2.....	130

Chapter 5: Experimental results

Figure 5-1 Average compressive strength gain as function of days (average of 3 cylinders for each experimental point).....	131
Figure 5-2 Pre-peak stress-strain behavior for a typical cylinder IE1C1.....	132
Figure 5-3 Failure crack patterns extracted from (ASTM C39, 2015)	133
Figure 5-4 Crack pattern of two failed cylinder samples (a) IE3C2 -B- and (b) IE1C2 -B- ...	134

Figure 5-5 Load-deformation response for the 280 mm prism cast in a layered method (92 days)	135
Figure 5-6 Load-deformation response of 280 mm span prisms cast from one-side (92 days)	135
Figure 5-7 Load-deformation response of 280 mm span prisms cast in a layered manner with and without steel fibers (72 days)	136
Figure 5-8 Load-deformation response for the 500 mm prisms in a layered casting method (92 days)	137
Figure 5-9 Cracking pattern of the speckled front face for prisms (a) Set 1, (b) Set 2, (c) Set 3 and (d) Set 4	139
Figure 5-10 Cracking pattern for the splitting tensile test	140
Figure 5-11 Longitudinal cracks developed along the height of the cylinder (a) in a wet state and (b) in a dry state	140
Figure 5-12 (a) Cross section of Prism I (b) and number of fibers per section	141
Figure 5-13 (a) Cross section of Prism D and (b) number of fibers per section	141
Figure 5-14 Load versus mid-deflection – Beam KE1C1	143
Figure 5-15 Crack pattern after the failure of the beams front face	143
Figure 5-16 (a) Crack pattern after the failure of the bottom cover, (b) pull out of the bar and (c) slip of the bar	144
Figure 5-17 Average bond-stress vs. slip (loaded end)– Beam KE1C1	145
Figure 5-18 Load versus mid-deflection – Beam KE1C2	145
Figure 5-19 (a) Crack pattern of the front face, (b) cover after failure, (b) pullout of the bar and (c) slip of the bar	146
Figure 5-20 Average bond-stress vs. slip (loaded end) – Beam KE1C2	147
Figure 5-21 Load versus mid-deflection – Beam KE4C1	148
Figure 5-22 (a) Front face of the beam, (b) crack pattern of the bottom face, (c) rupture of the bar and (d) no slippage	148
Figure 5-23 Load versus mid-deflection – Beam KE4C2	149
Figure 5-24 (a-b) Crack pattern at failure at the front and bottom face and (c) no slip of the bar	149
Figure 5-25 Load versus mid-deflection – Beam FE1C1	150
Figure 5-26 Crack pattern after failure - Beam FE1C1	150

Figure 5-27 (a) Crack pattern of cover after failure, (b) pullout of the bar and (c) slip of the bar	151
Figure 5-28 Average bond-stress vs. slip (loaded end) – Beam FE1C1	152
Figure 5-29 Load versus mid-deflection – Beam FE1C2	152
Figure 5-30 Crack pattern after failure - Beam FE1C2	153
Figure 5-31 Average bond-stress vs. slip (loaded end)– Beam FE1C2	153
Figure 5-32(a) Crack pattern of cover after failure, (b) pullout of the bar and (c) slip of the bar	154
Figure 5-33 Load versus mid-deflection – Beam FE4C1	154
Figure 5-34 Crack pattern after failure - Beam FE4C1	155
Figure 5-35 Load versus mid-deflection – Beam IE1C1	155
Figure 5-36 Crack pattern after failure - Beam IE1C1	156
Figure 5-37 (a) Crack pattern of cover for IE1C1 -A-, (b) IE1C1-B- and (c) IE1C1 -C-	156
Figure 5-38 Bond-stress vs. slip – Beam IE1C1	157
Figure 5-39 Load versus mid-deflection – Beam IE1C2	158
Figure 5-40 Crack pattern after failure - Beam IE1C2	158
Figure 5-41 Local bond-stress vs. slip (loaded end)– Beam IE1C2	159
Figure 5-42(a) Crack pattern of cover after failure, (b) pullout of the bar and (c) slip of the bar	159
Figure 5-43 Load versus mid-deflection – Beam IE2C2	160
Figure 5-44 Crack pattern after failure - Beam IE2C2	160
Figure 5-45 Crack pattern of cover after failure, (b) pullout of the bar and (c) slip of the bar	161
Figure 5-46 Loaded end bar-stress vs. slip – Beam IE2C2.....	162
Figure 5-47 Load versus mid-deflection – Beam IE3C2	162
Figure 5-48 (a) Crack pattern on the front, (b) crack pattern of cover after failure, (c) pullout of the bar and (d) no slip	163
Figure 5-49 Shape of the concrete in between the ribs (Beam IE1C1 – A).....	164
Figure 5-50 Evolution of the development of the crack	164
Figure 5-51 Load vs. mid-deflection for different mixes (I, K and F) for a concrete cover equal to the bar diameter and an embedment length equal to 5 times the bar diameter (E1C1)	166

Figure 5-52 Comparison of the bond strength for different mixes with a concrete cover equal to the bar diameter.....	167
Figure 5-53 Load vs. mid-deflection for different mixes (I, K and F) for a concrete cover equal to twice the bar diameter and an embedment length equal to 5 times the bar diameter (E1C2)	168
Figure 5-54 Comparison of the bond strength for different mixes with a concrete cover equal to twice the bar diameter	168
Figure 5-55 Load vs. mid-deflection for mixes (K and F) for a concrete cover equal to the bar diameter (E4C1).....	169
Figure 5-56 Load vs. mid-deflection for the in-house mix (I) for two different concrete covers (C1 - C2) and (E1)	169
Figure 5-57 Comparison of the bond strength for the different mixes with a concrete cover equal the bar diameter.....	170
Figure 5-58 Load vs. mid-deflection for the company (K) for two different concrete covers (C1 - C2) and the same embedment length equal to 5 times the bar diameter (E1)	171
Figure 5-59 Load vs Mid-deflection for company F for two different concrete covers (C1 – C2) and the same embedment length equal to 5 times the bar diameter (E1)	171
Figure 5-60 Load vs. mid-deflection for the in-house mix (I) for the same concrete cover equal to twice the bar diameter (C2) and different embedment length (E1-E2-E3).....	173
Figure 5-61 Variation of the average bond strength in terms of the embedment length	174

Chapter 6: Numerical study

Figure 6-1 Finite element model representation of a simply supported beam subjected to a point load.....	175
Figure 6-2 Reinforced concrete membrane element (Vecchio and Collins, 1986).....	176
Figure 6-3 Transfer of stresses across cracks (Vecchio and Collins, 1986)	177
Figure 6-4 Uniaxial tension stress-strain curve representing the post-peak branch known as tension-stiffening (Vecchio and Collins, 1986)	177
Figure 6-5 Description of the link elements in VecTor2	178

Figure 6-6 The change of stress in the reinforcing bars due to the presence of a bond (Martin-Perez and Pantazopoulou, 2001).....	179
Figure 6-7 Tension stress-strain curve of concrete.....	179
Figure 6-8 (a) Strain-hardening response of HPFRC composites (b) strain-softening response of FRC composite and (c) HPFRC tensile stress-strain response (Naaman and Reinhardt, 2006).....	182
Figure 6-9 Custom input-strain based tension softening in VecTor2.....	183
Figure 6-10 FE model for the prisms (a) 280 mm and (b) 500 mm in VecTor2.....	184
Figure 6-11 (a) Material properties and (b) tension softening behavior of In-house design mixture.....	185
Figure 6-12 Experimental and analytical response curve of the 500 mm long prisms.....	186
Figure 6-13 Experimental and analytical response curve of the 280 mm long prisms.....	186
Figure 6-14 (a) Material properties and (b) tension softening behavior.....	187
Figure 6-15 Experimental and analytical response curve of the 500 mm long prisms.....	187
Figure 6-16 Experimental and analytical response curve of the 280 mm long prisms.....	188
Figure 6-17 Concrete properties and tension softening input.....	188
Figure 6-18 Experimental and analytical response curve of the 500 mm long prisms.....	189
Figure 6-19 Experimental and analytical response curve of the 280 mm long prisms.....	189
Figure 6-20 Finite element model developed for beam specimens K-F E4C1.....	190
Figure 6-21 Finite element model developed for beam specimen K-E4C2.....	190
Figure 6-22 Finite element model developed for beam specimens I-K-F E1C1.....	190
Figure 6-23 Finite element model developed for beam specimens I-F-K E1C2.....	190
Figure 6-24 Finite element model developed for beam specimens IE2C2.....	191
Figure 6-25 Finite element model developed for beam specimens IE3C2.....	191
Figure 6-26 FE model – Load vs. mid-deflection response for KE1C1 specimens.....	193
Figure 6-27 FE model – Load vs. mid-deflection response for KE1C2 specimens.....	194
Figure 6-28 FE model – Load vs mid-deflection response for KE4C1 specimens.....	195
Figure 6-29 FE model – Load vs. mid-deflection response for KE4C2 specimens.....	195
Figure 6-30 FE model – Load vs mid-deflection response for FE1C1 specimens.....	196
Figure 6-31 FE model – Load vs mid-deflection response for FE1C2 specimens.....	197
Figure 6-32 FE model – Load vs mid-deflection response for FE4C1 specimens.....	197

Figure 6-33 FE model – Load vs. mid-deflection response for in-house IE1C1 specimens	198
Figure 6-34 FE model – Load vs. mid-deflection response for in-house IE1C2 specimens	199
Figure 6-35 FE model – Load vs. mid-deflection response for in-house IE2C2 specimens ...	199
Figure 6-36 FE model - Load vs mid-deflection response for in-house IE3C2 specimens	200
Figure 6-37 Cracking pattern and the slippage of the reinforcing bar for the FE beam KE1C1	201
Figure 6-38 Experimental cracks on the front face of the beam KE1C1	201
Figure 6-39 Cracking along the notch and rupture of the reinforcing bar for beam KE4C1 ...	201

Appendix A

Figure A-1 Side and Front view of the jig	219
Figure A-2 Detailing of part A and B	220
Figure A-3 Detailing of part A.....	220
Figure A-4 Detailing of part B.....	221
Figure A-5 Detailing of part C.....	221
Figure A-6 Detailing of part D.....	222
Figure A-7 Detailing of part E	222
Figure A-8 Dimensions of the different parts of the frame	223
Figure A-9 Front and top view of the support aluminum bar	223
Figure A-10 Dimensions of the parts forming the frame.....	224

Appendix D

Figure D-1 First crack for beam KE1C1 - A -	262
Figure D-2 First crack for beam FE1C1 - A -	263
Figure D-3 First crack for beam IE1C1 - B -	263
Figure D-4 First crack for beam IE1C1 - C -	264

List of Abbreviation

DFRCC	Ductile Fiber Reinforced Cement Composited
DSP	Densified Small Particles
ECC	Engineering Cementitious Composites
FRC	Fiber-Reinforced Concrete
MDF	Macro-Defect-Free
RPC	Reactive Powder Concrete
SIFCON	Slurry Infiltrated Fiber Concrete
SIMCON	Slurry Infiltrated Mat Concrete
UHPC	Ultra-High-Performance Concrete
UHP-FRC	Ultra-High-Performance Fiber Reinforced Concrete
UHP-SFRC	Ultra-High-Performance Steel Fiber Reinforced Concrete

List of Symbols

a	shear span (mm)
a_{max}	maximum aggregate size (mm)
A_s	cross-section of the reinforcing bar (mm ²)
A_{sf}	cross-sectional area of the fiber (mm ²)
b_o	width of the beam (mm)
c	weight of the cement (kg)
c_b	concrete bottom cover (mm)
c_c	clear cover (mm)
c_s	concrete side cover (mm)
d	depth of the beam (mm)
d_b	diameter of the main reinforcing bar (mm)
d_f	diameter of the steel fibers (mm)
d_h	diameter of the hole (mm)
D	diameter of the flow table (mm)
f_{adh}	chemical adhesion (MPa)
F_b	force in the bar (kN)
f_t	tensile strength (psi)
f'_c	concrete compressive strength at 28 days (psi)
f'_{cc}	concrete cube compressive strength (MPa)
f'_{ct}	UHPC compressive strength at age t (days)
f_{c2}	stress equal to 40% of the compression peak load (MPa)
f_{ca}	bearing force from the concrete to the bar rib (Mpa)
$f_s(x)$	tensile stress of the bar at point x (Mpa)
$f_s(x + dx)$	tensile stress of the bar at point x + dx (Mpa)
g	energy absorption capacity (kJ/m ³)
h	height of the beam (mm)
h_n	height of the notch (mm)
ℓ	length (mm)
l_b	embedment length (mm)

ℓ_{bf}	embedment length of the steel fibers (mm)
ℓ_f	length of fiber (mm)
K_r	resistance factor (MPa)
K	constant factor
M	internal moment along the beam (kN.mm)
P	applied load (kN)
P_b	perimeter of the reinforcing bar (mm)
P_{max}	maximum applied load (kN)
P_u	ultimate load applied (kN)
S_p	slip at P_{max} (mm)
t	time after casting (days)
t_{PVC}	thickness PVC (mm)
T_s	bar force (kN)
y	distance of the fiber from the neutral axis (mm)
UL	ultimate load (kN)
w	weight of the water (kg)
w/b	water-binder ratio
w/c	water-cement ratio
V	shear force of the cross-section (kN)
V_f	volumetric fraction of fibers (%)
α	angle formed by the concrete bearing force and the horizontal axis of the bar (deg)
\emptyset	diameter (mm)
\emptyset_f	diameter of fiber (mm)
σ_{cc}	tensile strength corresponding to first crack in direct tension(MPa)
$\sigma_{flexure}$	bending stress (MPa)
σ_n	radial stresses (MPa)
σ_{hoop}	Hoop stresses (MPa)
σ_{pc}	peak tensile strength in direct tension (MPa)
λ	group effect parameter
τ	equivalent bond strength between fiber and matrix (Mpa)
χ_f	fiber factor

$\varepsilon_{axial,30}$	axial strain at 30% of f_c
$\varepsilon_{axial,10}$	axial strain at 10% of f_c
ε_{cc}	tensile strain corresponding to first crack in direct tension
$\varepsilon_{circ,30}$	circumferential strain at 30% of f_c
$\varepsilon_{circ,10}$	circumferential strain at 10% of f_c
ε_{ct}	matrix tensile strain
ε_{pc}	tensile strain corresponding to peak load in direct tension
ε_s	bar strain

Chapter 1. Introduction

1.1 Background

Owing to its inexpensive constituents and its mechanical strength, conventional concrete is considered as the predominant alternative building material adopted worldwide for all sorts of structures; bridges, highways, residential houses, high-rise buildings, tunnels, etc. that reflect the urban infrastructure development of a city. Unfortunately, it was seen that these infrastructures, generally built using normal concrete, tend to degrade progressively when exposed to severe climate exposures. As a matter of fact, applying de-icing salt in sub-zero weather leads to the mechanical deterioration of concrete and reveals the reinforcing bars which initiates their corrosion (Mindess et al., 2003). Even though these structures were initially designed according to the codes (CSA, 1995), with an estimated service life between 50 to 99 years, this value is experimentally proven to drop to 30 years (Kumar *et al.*, 2001). These damaged structures become not only visually unpleasant but also structurally unfit for their intended purpose. Thus, maintenance and rehabilitation interventions are required with an estimated yearly cost exceeding \$1 billion for bridges and \$20 billion for structures surpassing the average annual amount spent on building new structures (Gürkan et al., 2018). After several failed unsustainable repairing solutions, such as grout injection to fill the cracks or replacement of the entire damaged concrete, Ultra-High-Performance Steel Fiber Reinforced Concrete (UHP-SFRC) was proposed as the optimal economic and innovative sustainable material to be used. In fact, research was conducted in 2016 on the number of bridges that are using UHP-SFRC in their recent construction which has reached 87 in Canada, as presented in Figure 1-1 (Haber *et al.*, 2018).

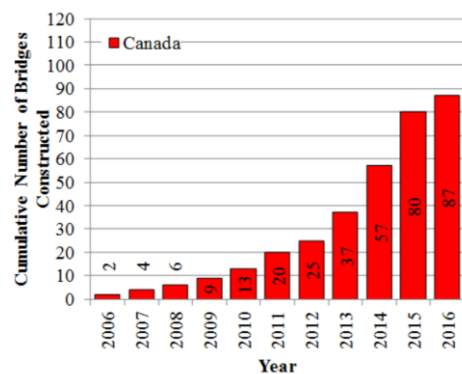


Figure 1-1 Number of bridges using UHPC in Canada (Haber et al., 2018)

Ductal® is one of the most commonly used products in North America; it was developed in 1990 based on the RPC (Reactive Powder Concrete) principle with the merged efforts of Lafarge, Bouygues and Rhodia along with the help of universities and researchers. Characterized by its high fresh and hard properties with a flexural strength of 40 MPa (Fehling, 2004), it was then commercialized in the dawn of the 21st century. As stated by Doiron (2017), this product has been recently used to retrofit several infrastructure projects opting for high durability with an incredible reduction of future maintenance cost. Figure 1-2 (a - b) below is the example of the pier jacketing of the CN Rail Bridge in Montreal. This concrete is being incorporated in new constructions as well. Due to its high cost, it is applied as a thin protective layer covering regular concrete decks. The first application in North America was in Iowa with the retrofitting of the Mud Creek Bridge (Sritharan *et al.*, 2018).



(a)



(b)

Figure 1-2 (a) Initial damaged surface and (b) Retrofitted with UHP-SFRC (Doiron, 2017)

1.2 Introduction of UHPFRC

The abbreviation of this innovative concrete can be divided into two parts; the first “UHPC” and the second “FRC.” “UHPC” denotes the concrete matrix composed of a high content of cementitious materials, cement substitutes, fine aggregates with a grain diameter limited to 600 μm , water and high-range water reducers known as superplasticizers (Bache, 1981). Following an optimized packing procedure for the dry materials, reducing the water/binder ratio (w/b) to vary between 0.18 and 0.25 and adding the adequate amount of superplasticizers, several researchers were able to obtain a very dense paste with high fresh properties and a compression strength greater than 150 MPa in ambient temperatures with conventional mixers (Wille *et al.*, 2011; Maca *et al.*, 2012; Wille *et al.*, 2012; Yu *et al.*, 2014). “FRC” indicates the presence of steel fibers that prevent the development of the micro-

cracks and eliminate the brittle failure of concrete under tension where the fiber's tensile strength, their shape and their bond-interaction with the matrix should be optimized to reach high mechanical properties while maintaining an appropriate workability (Wille and Naaman, 2010, 2012). Naaman initially classified FRC composites into four performance categories based on their behavior, directly related to the fiber volume content as described in Figure 1-3 (a). This starts by bridging through the opening of cracks with a deflection softening behavior. This type of material would be sufficient for shrinkage cracking. The second level of performance corresponds to the deflection hardening materials known as Ductile Fiber Reinforced Cement Composites (DFRCC) characterized by the development of several cracks under flexure but not in tension. These materials are adequate for structural elements controlled by flexure. The third level of materials have the strain hardening property known as High Performance Fiber Reinforced Cement Composites (HPFRCC) where in that case multiple cracks will develop under tension prior to crack localization and finally the last level is to obtain a high energy absorption "g" rating before crack localization greater than 50 kJ/m^3 (Naaman and Reinhardt, 2003). The third and final levels are qualified to be used in earthquake design for structures under cyclic or impact load. This classification was then enhanced starting by dividing the materials based on their strain hardening (HPFRCC) and strain softening behavior as depicted in Figure 1-3 (b) (Naaman and Reinhardt, 2006).

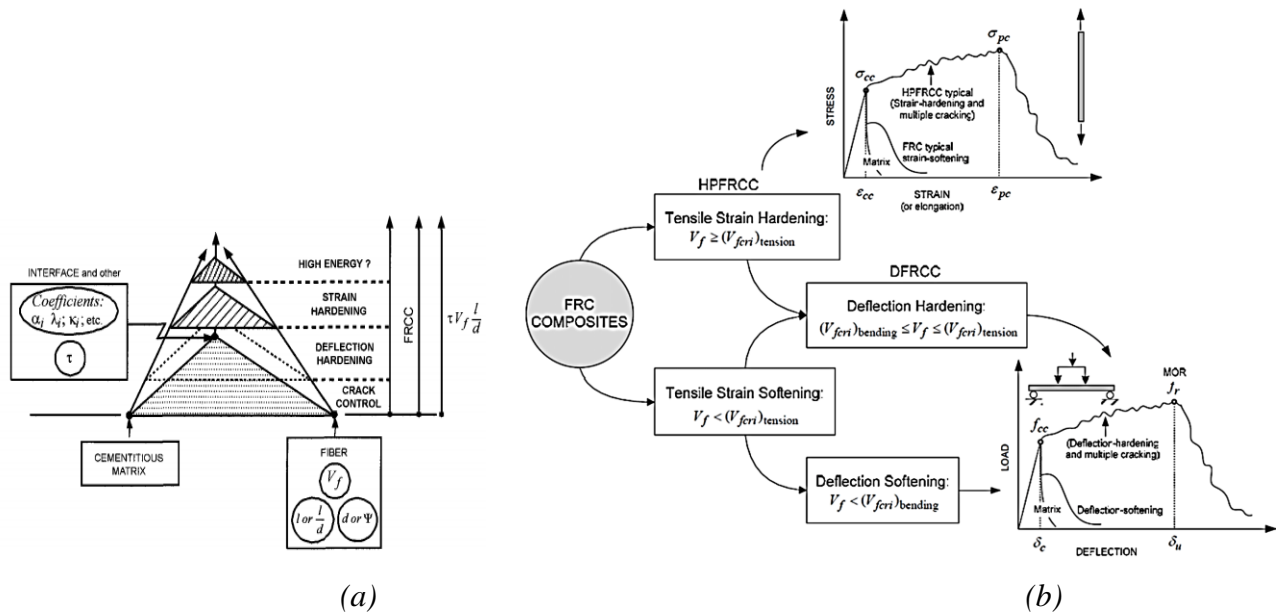


Figure 1-3: (a) Classification of FRC composites (b) previously based on four performance levels (Naaman and Reinhardt, 2003) recent based on their tensile and bending behavior (Naaman and Reinhardt, 2006)

A strain-softening material, with an adequate fiber content for bending, can become a deflection hardening material. If not, it remains a deflection-softening material. It is important to state that a strain hardening material is always deflection hardening but not vice versa. For a direct tension test, as described in Figure 1-4 (b), HPFRC materials are mainly distinguished by the presence of phase II behaviour known as the “strain-hardening” phase in direct tension defined by the capability to develop multiple cracking after the development of the first crack ($\sigma_{cc}, \epsilon_{cc}$) and prior to the initiation of crack localization once the peak load ($\sigma_{pc}, \epsilon_{pc}$) is reached (Wille et al., 2014). This property characterizes UHPFRC as a “strain hardening” material. However, the other FRC composites have Phase I and Phase II only; where Phase I corresponds to an initial ascending linear elastic phase behavior until the first crack occurs, defined by ($\sigma_{cc}, \epsilon_{cc}$) in Figure 1-4 (a) and (b). Then, Phase III directly starts with the localization of the first crack representing the stress as a function of the crack opening rather than the strain. Thus, these FRC composites follow a “strain-softening behavior” under tension.

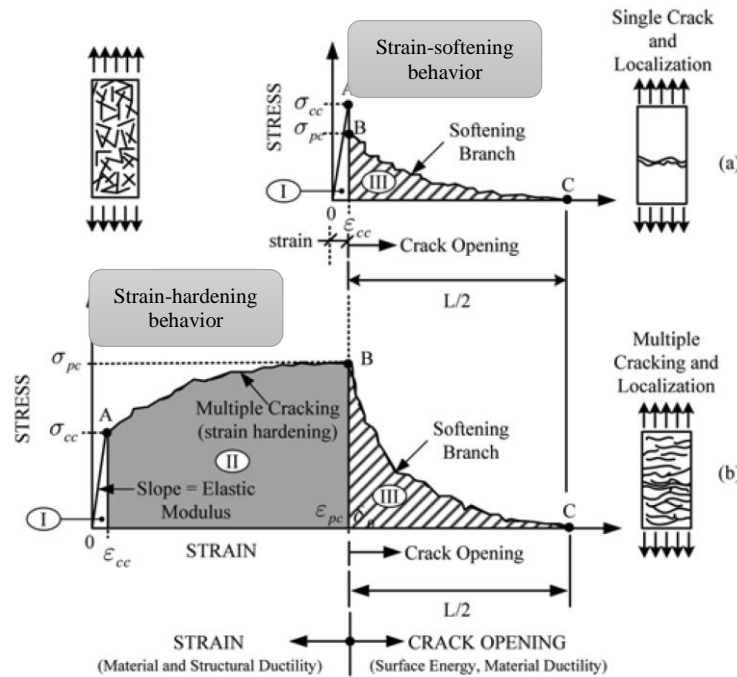


Figure 1-4 Comparison of the stress-strain response under direct tension between (a) strain softening and (b) strain-hardening behavior (Naaman and Reinhardt, 2003)

(Naaman and Reinhardt, 2006) classified HPFRC based on their first crack with a strain not exceeding 0.0002 and an elastic modulus greater than 10500 MPa. Eventually, they classified them in classes of

T- σ_{pc} ranging between T-2.5 until T-20 with a minimum peak strain of $\varepsilon_{pc} = 0.005$. Common HPFRC are mainly Engineered Cementitious Composite (ECC), Slurry Infiltrated Fibrous Concrete (SIFCON), Slurry Infiltrated Mat Concrete (SIMCON) and Ultra-high performance steel fiber reinforced concrete (UHP-SFRC) discussed previously. ECC's have mainly a mortar base matrix (sand, cement and fly ash) along with polyvinyl alcohol (PVA) fibers (Sahmaran *et al.*, 2007). Once ECC is cracked, even with a width not exceeding 0.1 mm, it is considered to have a very high permeability (2×10^{-10} m/s) particularly greater than conventional concrete (Lepech and Li, 2009). SIMCON is an enhancement of SIFCON where the manual dispersion of fibers was replaced by a pre-made well distributed and easily placed fiber mat infiltrated with the concrete matrix. They are both characterized with a high percentage of steel fibers (greater than 5%) (Krstulovic-Opara *et al.*, 1997; Breitenbucher, 1999). UHPFRC are considered the highest class of HPFRCC owing to their high strength mechanical properties and their dense matrix, as can be seen in Figure 1-5.

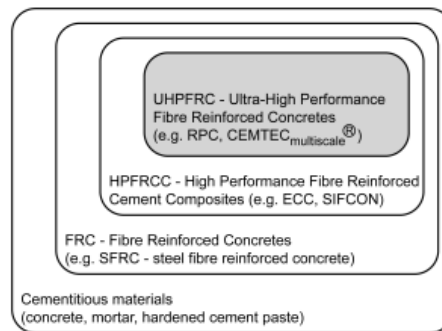


Figure 1-5 Definition of UHPFRC (HABEL, 2004)

Therefore, this new concrete with high mechanical characteristics, flexural strength and toughness, used as an impermeable solution for external attacks, can now substitute conventional concrete when designing reinforced concrete structural elements that require a higher ductility and energy absorption. Figure 1-6 (a) and (b) depicts the seismic retrofitting of the piers of the Mission Bridge located in Abbotsford, BC using UHPC Ductal® (Doiron, 2017).



Figure 1-6: (a) Bridge pier prior (b) and after retrofitting (Doiron, 2017)

Also, reinforced deck overlay for the repairing of the Chillon Viaducts in Switzerland was accomplished using UHPC to strengthen and protect the slab as can be seen in Figure 1-7 (a) and (b) (Sritharan *et al.*, 2018).



Figure 1-7: (a) Chillon Viaducts UHPC reinforced bridge deck design (b) and application (Sritharan *et al.*, 2018)

Hence, it is essential to understand the behavior of UHP-SFRC reinforced concrete structures, particularly the force transfer between conventional reinforcing bars and this innovative concrete when subject to different types of loading. This perception could extend its type of application and develop proper design codes for future structural applications.

1.3 Introduction of steel-concrete bond

In general, a concrete beam subject to an external force perpendicular to its midline, generates a bending moment, placing the lower part of the beam in tension, which is considered as a fragile property for conventional concrete. Once the developed stresses exceed the tensile strength of concrete, cracking occurs leading to a brittle mode of failure in tension (Chao *et al.*, 2009). Therefore, reinforcing bars with high tensile strength are placed in this region to receive and resist these tensile stresses instead of concrete forming together a reinforced concrete structure treated as a single system. However, this composite action is only possible due to the presence of the third factor “bond

strength”, which allows the transfer of stresses between the reinforcing bars and the surrounding concrete. If this detailing was not taken into consideration properly, a structure that is properly designed could have less durability and poor performance. However, the deformed rebar subject to a tensile force tends to slip relative to the surrounding concrete. At this stage, the response of the whole system depends on the capacity of the concrete to deform as much as the steel. Therefore, bond strength corresponds to the capacity of the concrete to deform and degrade locally. The surrounding concrete exhibits then a system of interfacial reaction forces known as the “force transfer mechanisms” presented in Figure 1-8 showing that if it exceeds the bond strength between these two materials de-bonding will occur (Kabir and Islam, 2014).

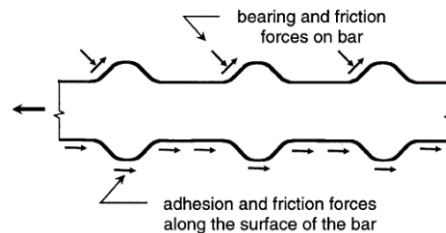


Figure 1-8: Force transfer mechanisms (ACI Committee 408, 2003)

Lutz and Gregely stated that this interfacial phenomenon is divided mainly into three mechanisms for conventional deformed reinforcing bars. The first is achieved by chemical adhesion f_{adh} between the two materials. This adhesion is directly broken due to a relative slip between the reinforcing bars and the concrete (LeRoy and Peter, 1967). The loss of this force transfer mechanism leads to the second type of force mechanism known as “frictional forces” which mainly depends on the roughness of the interface along the barrel of the bar. However, for larger slip values, these transversal frictional stresses along the smooth part of the rebar are lost. As a consequence, bearing and frictional forces along the ribs are mobilized due to the presence of the ribs along the deformed bar. It’s noteworthy that frictional forces proportionally increase with the upsurge of bearing forces. However, when slip values become greater, the frictional forces will no longer be effective. Eventually, the force transfer between the concrete and the steel is only ensured by the bearing forces (ACI Committee 408, 2003). As seen in Figure 1-9 the bearing force applied on the surface of the rib is divided into two components; the horizontal is the bond or shear force, and the vertical is the radial compression force.

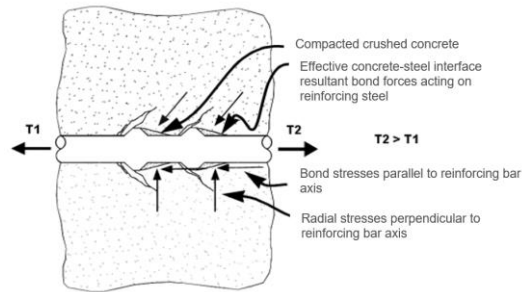


Figure 1-9 : Development of stresses along the interface steel-concrete (Phan, 2012)

Consequently, the surrounding concrete elements will be subject to a system of shear and compression stresses along their surfaces, causing tensile stresses in the concrete in both longitudinal and transverse directions of the bar (Lemnitzer and Curbach, 2012). The loss of the concrete-steel bond strength leads to the initiation of radial micro-cracks. Their growth can cause different mechanisms of rupture and in some cases can lead to the failure of the entire “steel-bond-concrete” system. Ramirez proposed four different types of failures discussed below for a deformed reinforcing bar (Ramirez, 2005). In fact, failure can occur in the concrete due to the formation of longitudinal and conical cracks or in the reinforcing bar once they enter their plastic stage or in the bond strength itself due to the formation of cylindrical cracks.

1.3.1 The spread of the conical and transversal cracks

The shear stress places the surrounding concrete in tension causing conical micro-cracks with a possibility to propagate and reach the surface of the concrete leading to the conical extraction of the concrete block as seen in Figure 1-10 (a) (Ramirez, 2005).

1.3.2 Rupture of the reinforcing bar

Figure 1-10 (b) shows a yielded reinforcing bar resulting from a high force interaction between the steel and concrete. This occurs in a highly dense and reinforced matrix that can lead, in some cases, to the rupture of the bar (Ramirez, 2005).

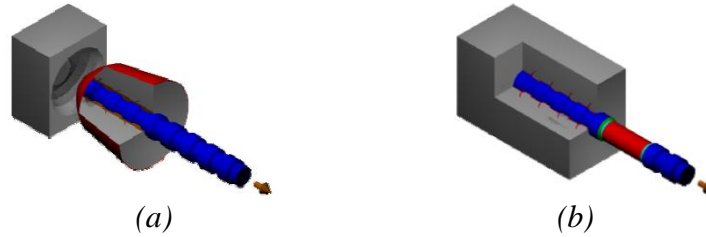


Figure 1-10 (a) Extraction of the concrete cone (b) Steel bar rupture (Ramirez, 2005)

1.3.3 The spread of longitudinal cracks and splitting failure mode

Splitting failure is the most common failure mode occurring to reinforced concrete elements. As mentioned previously, the resulting radial stresses along the perimeter of the ribs will create internal tensile hoop stresses that once they exceed the tensile strength of concrete, longitudinal cracking starts to appear resulting in a splitting failure mode of the system, as shown in Figure 1-11 (a) and (b). At this point, a minimal displacement of the reinforcing bar is caused by the shear force in the concrete leading to shearing cracks (Ramirez, 2005).



Figure 1-11: (a) Radial stresses applied to the concrete element (Tastani et al., 2016) (b) splitting failure (Ramirez, 2005)

1.3.4 The spread of cylindrical bond cracks and pullout failure mode

The emergence of longitudinal cracks depends mainly on the tensile strength of concrete, the concrete cover, the spacing between the longitudinal reinforcing bars, the stirrups, and the lateral pressure. If these parameters were applied correctly, they would contribute along with the tensile strength of concrete to encounter the tensile hoop stresses leading to the delay or even elimination of the splitting failure mode. A study revealed that sufficient confining conditions would result in higher radial stresses. The latter will increase the frictional coefficient μ and amplify the frictional resistance of the concrete along the longitudinal axis of the bar to reach the maximum bond strength. The

accumulation of the shear cracks created around the bar will cause cylindrical cracks. Once this frictional stress applied on the bar exceeds the shear capacity strength of the concrete cylinders in between the ribs, the bar will pull out (Tastani and Pantazopoulou, 2010). At this point, maximum displacements of the reinforcing bar are achieved due to complete shearing of the concrete in between the ribs (Ramirez, 2005). This mode of failure presented in Figure 1-12 (b) describes best the degradation of the concrete-steel bond strength.

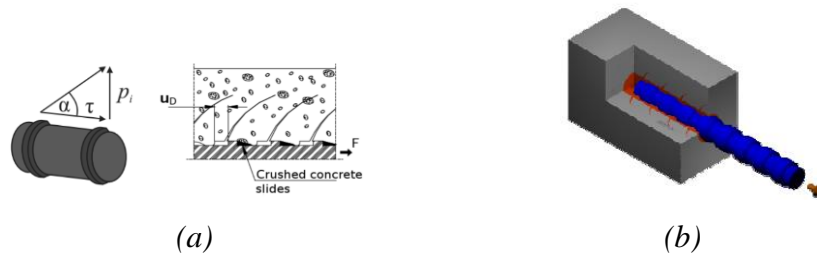


Figure 1-12: (a) Shear stresses on the concrete element causing tensile stresses (b) cylindrical cracks (Ramirez, 2005)

These “force transfer mechanisms” discussed previously are defined with the local bond stress-slip relationship, obtained by conducting pullout-test under monotonic loading for reinforcing bars anchored along a short embedment length of $5d_b$ where the bond stress is assumed uniform. Figure 1-13 shows the phases of the three previously mentioned force mechanisms when occurring with high confinement ratio: adhesion in part I, bearing in part II and III and friction in part IVa, b and c. Smooth bars cannot reach high bond strength values compared to ribbed bars due to the absence of the deformations along their surface. Thus, the bond strength is only controlled by the adhesive and frictional phase as seen in the response curve (Phase I and Phase IVa) in Figure 1-13 (a) (Will, 1997). This is why deformed bars are used instead of plain bars.

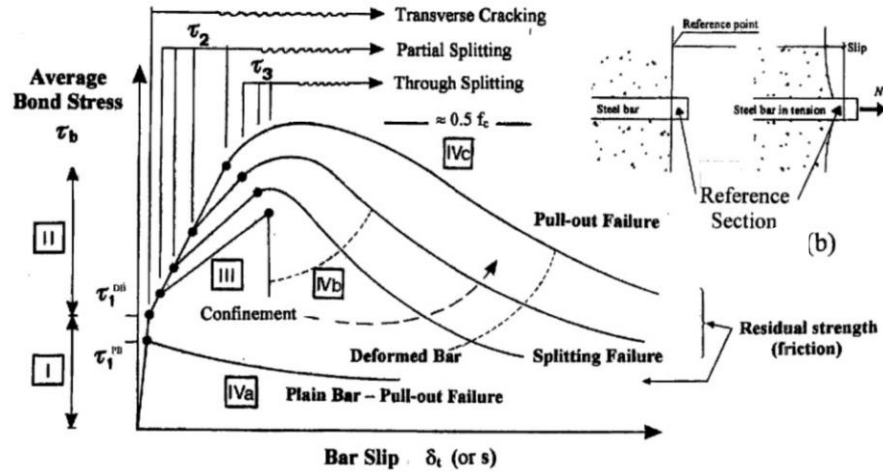


Figure 1-13 Local relationship between bond stress-slip (fib/ceb/fip 2000)

The bond-interaction between the reinforcing bars and the normal concrete defining the overall performance of the system is found to be easily deteriorated due to the cracking strains developed in the surrounding concrete. Thus, the addition of steel fibers is one of the adopted methods to enhance the concrete matrix in contact with the reinforcing bar without any external confinement. Furthermore, it was proven that adding fibers in the concrete matrix has the same effect as adding passive confinement to minimize the splitting crack and optimize the bond strength (Eleftheriou *et al.*, 2017). Therefore, fibers will bridge the opening of cracks to ensure load transfer and will mainly act as confinement to the concrete to stop it from expanding and reaching its limit of incompressibility, thus enabling the reinforcing bar to accomplish its initial role. Figure 1-14 shows the bridging effect of fibers on the splitting cracks and the change in the “force transfer mechanism” leading to a pullout failure mode.

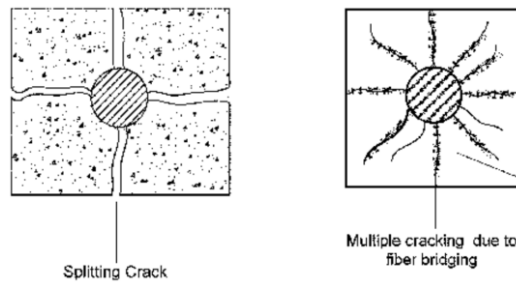


Figure 1-14: Enhancement of the propagation of cracks with steel fibers (Chao *et al.*, 2009)

1.4 Thesis objectives

The primary objective of this research project is to offer an understanding of the bond-stress slip relationship (experimental and numerical) for the system “steel-bond-UHP-SFRC” and to explore the contribution of this novel concrete on the development length of a regular reinforcing bar. The following tasks were completed to achieve this objective:

- 1- A literature review to understand the historical background of UHP-SFRC and its mechanical properties. This is followed by an understanding of bond strength, an investigation of different types of bond tests available and recent bond tests obtained on conventional reinforcing bars embedded in UHP-SFRC.
- 2- A selection of an optimal and conservative bond test setup to be conducted. The choice of the specimen detailing and the adequate measuring tools.
- 3- Various trials on the previously proposed UHP-SFRC design mixes, to compare the fresh and hard properties in order to choose the most appropriate one to cast in-house. In addition, commercial mixes currently being used in Canada were cast to study their bond performance. These three design mixes differ in their mechanical properties constituting one parameter of the study.
- 4- A selection of two additional experimental parameters: the concrete cover and the embedment length, to study their effect on bond strength when using this innovative concrete.
- 5- Material tests such as cylinder compression strength, splitting tensile strength and four-point loading on prisms in order to extract the mechanical properties for all material mixes considered.
- 6- Experimental testing to analyze the failure modes, extract the load-displacement response and the bond-stress slip relationship for different concrete covers of the three different mixes

(commercial and in-house). Three embedment lengths are also studied in the in-house mix UHP-SFRC.

- 7- Modeling of the beam bond test to compare the numerical load-deformation response with the experimental behavior based on the understanding of the constitutive models of the 2D software VecTor2.

1.5 Thesis outline

This thesis includes 7 chapters. Chapter 1 is an introduction of all the materials to be covered such as the concerned materials followed by a general presentation of bond strength in a reinforced concrete structure. Chapter 2 is a literature review of the new concrete as well as the methods to measure bond strength and the recent research conducted. Chapter 3 and Chapter 4 focus on the planning and execution of the experimental program, respectively. Chapter 5 showcases the experimental results obtained and their discussion. Chapter 6 presents the modeling of these experiments and the comparable results obtained between the experimental, and modeling test. Chapter 7 will elaborate the conclusions and recommendations following the study conducted on the bond behavior of steel reinforcing bars embedded in UHP-SFRC.

1.5.1 Chapter 2 – Literature review

The first part of this chapter provides a general description of the history behind the development of UHP-SFRC and its main components and their effect on the fresh and hard properties of this concrete (dry and liquid materials, fibers). Examples of recently developed UHP-SFRC and their design mixtures will be presented as well. The second part will discuss the different types of experimental tests to measure the bond strength, their advantages, and disadvantages, and the recently conducted bond tests on UHP-SFRC and their results.

1.5.2 Chapter 3 – Plan of the experimental program

The first part of this chapter will discuss the chosen experimental program that includes the type of bond test, the specimens detailing, and a detailed representation of the test setup. The second part will focus on the trials conducted on two different design mixes to choose the one with the best fresh and hard properties. The third part will introduce all the mechanical tests to be performed on the in-house design mixture to extract their properties.

1.5.3 Chapter 4 – Execution of the experimental program

This chapter focuses on the execution of the experimental program, particularly the preparation of the formwork and the specimens, and the casting of the commercial and in-house mixes. It will explain the adjustments implemented for the specimens followed by the actual installation of the test setup.

1.5.4 Chapter 5 – Experimental results

Chapter 5 contains the experimental results for each beam series. It will measure the mechanical properties obtained for the in-house design mixture. The results will be divided into two parts: the plotting of the load-deflection behavior, and the bond stress-slip response. The digital image correlation procedure (DIC) is also introduced to verify the experimental response obtained. Moreover, it will present the analysis of each parameter studied and its effect on the bond strength. In addition, it will describe the different modes of failure observed. In the end, a simple conclusion of the whole experimental process will be made.

1.5.5 Chapter 6 – Numerical study

The first part of this chapter will discuss the proposed modeling for the UHP-SFRC based on the actual constitutive models available in the analytical program regarding the response of the flexural prisms. The second part focuses on the development of the finite element (FE) model for the reference fully bonded beam test. The third part consists of the presentation of the final FE analysis for all the

beam series of the experimental program. The plot of both the experimental and analytical model responses will be demonstrated to verify the ability of the model to capture the performance of the UHP-SFRC.

1.5.6 Chapter 7 – Conclusions

This chapter summarizes the study conducted. It also provides recommendations to be adopted in future projects.

1.6 Scope and objective of the thesis

The understanding of UHP-SFRC has been under study for more than two decades where its high mechanical properties have been profoundly identified. However, these distinct properties are not considered in structural designing since no appropriate design codes specific to this novel concrete are available yet. An actual example can be the choice of the required development length proposed in concrete design codes to develop the strength of the reinforcing bar. Thus, the knowledge of the bond-stress slip at the interface of steel reinforcement and UHP-SFRC is needed. The purpose of the thesis is to participate in the bond database to confirm numerical or analytical models recently being developed for future enhancement of design codes, concerning the development length of reinforcing bar in this material such as embedment, anchorage, and lap-splice lengths. Taking into consideration the high tensile strength of this concrete, it can economically reduce the required embedment length to develop the yielding stress of bars and therefore will facilitate the design in buildings where limited space is available or even complicated.

Based on the author's knowledge and research, there are no beam anchored bond test performed on UHP-SFRC to study the bond strength for anchored reinforcing bars. Even though the bond test setup is based on previous work (Tastani *et al.*, 2016), the novelty in the current research relies on the experimental testing of longer beams for a different type of HPFRC with a broader scope of parameters. In addition, the development of a finite element (FE) model to represent UHP-SFRC and the bond models in a 2D finite element platform, lacking constitutive models to represent this new concrete, contributes to understanding its modeling process.

Chapter 2. Literature Review

This literature review aims at shedding light on the historical evolution of UHP-SFRC while emphasizing its composition and mechanical properties. In addition, it includes a detailed explanation about the design mixes selected to perform trials of in-house mixes to be studied consequently. This chapter will concentrate as well on the understanding of one mechanical property between reinforcement and concrete “bond” with a brief review on the recently developed numerical equations describing the bond-stress slip relationships pertaining to both conventional concrete and HPFRC that is under development. It will contain the most common experimental bond measurement test setups, while stating their main advantages and disadvantages, in addition state of the art findings and results on previously conducted bond experiments on UHP-SFRC is presented.

2.1 UHP-SFRC

2.1.1 Development of UHP-SFRC

In 1824, the construction world faced a radical change with the emergence of the inorganic Portland cement produced by Aspdin (Aspdin, 1824). This powder is substantially formed by calcium silicates (alite Ca_3SiO_5 (C_3S) and belite Ca_2SiO_4 (C_2S)), aluminate (C_3A) and aluminoferrite (C_4AF) obtained from exposing both limestone and clay to elevated temperatures up to 1600°C (Anon. 1979). The hydration of Portland cement, dominated by the reaction between calcium silicates and water, produces a distinctive binder paste characterized by its strength once it hardens (Bye, 1983). Portland cement paste was then used as an adhesive combined with coarse and fine aggregates to obtain the normal concrete with a water/cement ratio ranging around 0.4. One century later, several types of research lead to obtaining a low porous matrix by reducing the w/c ratio to 0.2 following the vacuum mixing procedure (Yudenfreund *et al.*, 1972) or heat treatment (Roy *et al.*, 1972). These procedures allowed the concrete to reach a typical compressive strength of 230 MPa and 680 MPa, respectively.

In the early 1980s, the newly discovered pozzolans and superplasticizer admixtures were added to reduce the porosity of the matrix forming mixes known as the Macro-Defect-Free (MDF) (Bache, 1981) and the Densified Small Particles matrix (DSP) (Alford *et al.*, 1982). In terms of ductility, the

poor tensile strength of the matrix imposed a brittle failure of the structure. Thus, the concretes with high-compressive strength and the conventional concrete, unfortunately, remained much the same under tension. The addition of fibers in the matrix enhances the behavior of concrete in tension found in Slurry Infiltrated Fiber Concrete (SIFCON) and Engineering Cementitious Composites (ECC) (Lankard, 1985; Li and Leung, 1992). These two products only fit the HPFRC category since SIFCON has a low tensile strength for a high content of fibers ($V_f = 20\%$), while ECC develops a compressive strength below 70 MPa. Nevertheless, other composites containing steel fibers were developed following an optimized packing procedure and are denoted as UHP-SFRC for their high mechanical properties as described in Figure 2-1 (Alford and Birchall, 1985; Bache, 1987).

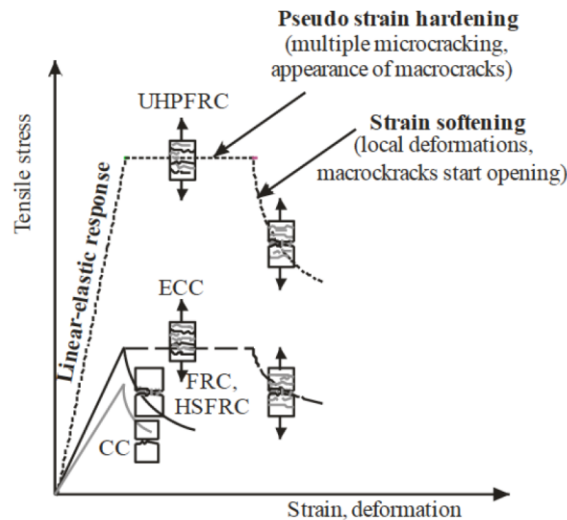


Figure 2-1 Tensile behavior for different HSFRC (Spasojević, 2008)

Based on that, DSP is transformed to the compact reinforced composite (CRC) by adding to the highly strong cementitious matrix short steel fibers ($l = 6 \text{ mm}$; $\phi = 0.15 \text{ mm}$) accounting to 5-10% of the total volume. Afterwards, two UHP-SFRC design mixes were developed in France; the first named RPC, known for using longer steel fibers than CRC ($l = 13 \text{ mm}$; $\phi = 0.16 \text{ mm}$) with a V_f below 2.5% (Richard and Cheyrezy, 1995) and a tensile strength of 8 MPa. RPC is the design mixture behind the commercial product Ductal® mentioned in Section 1.1 and known for a flexural strength reaching 35 MPa (Orange, *et al.*, 2000). The second type of UHP-SFRC was developed in the Laboratoire Central des Ponts et Chaussées (LCPC) titled as the Multiscale Cement Composite (MSCC) and characterized with the addition of a mixture of short steel fibers ($l = 5 \text{ mm}$; $\phi = 0.25 \text{ mm}$; $V_f =$

5%) with long hooked end fibers ($l = 25 \text{ mm}$; $\phi = 0.3 \text{ mm}$; $V_f = 2\%$) (Rossi, 1997). This was based on the “Multi-Scale Fiber Reinforced Concept” which had been proposed (Rossi *et al.*, 1987) so as to show that adding short steel fibers to conventional concrete plays an important role in limiting the propagation of the micro cracks, hence, increasing the material’s tensile strength.

At the same time, long steel fibers restrain the development of macrocracks and therefore increasing the load capacity and ductility of the element prior to the structure’s failure (Rossi *et al.*, 1987). Later on, MSCC was modified by adding three types of steel fibers instead of two and by increasing the volumetric fiber fraction from 7% to 11% resulting in the CEMTEC_{multiscale}. This concrete can achieve a compression strength of about 220 MPa and an average modulus of rupture of 50MPa (Rossi *et al.*, 2005). Habel proved that self-consolidating UHP-FRC could be designed (Habel *et al.*, 2008). Self-Consolidating Concrete (SCC) is known for their ability to fill the space in between the formwork and reinforcing bars due to the SCC’s self-weight without any external vibration. SCCs were initially introduced in Japan in 1986 to enhance the workability of the mixture, so as to eliminate durability issues caused by weak external compaction from the lack of expertise of laborers on site (Okamura, 1988).

2.1.2 Composition of UHP-SFRC

UHP-FRC is designed based on three principles. The first one considers a higher homogeneity because of the elimination of coarse aggregates. The second one focuses on the reduction of the porosity and the improvement of the microstructure with the use of cementitious materials (CM) and superplasticizer (SP). Finally, the third principle is based on the gain in ductility by the addition of fibers (Richard and Cheyrezy, 1995). As a result, UHP-FRC mixes are formed by fine aggregates, cement, water, admixtures (mineral and chemical) and a small percentage of fibers $V_f = 2 - 5\%$ with a water/binder ratio around 0.2. Each of the different constituents will be discussed below, along with their role in the above mentioned principles.

Aggregates: Fine aggregates are only used in the concrete matrix. The largest particle size starts with the sand, uniformly graded with a mean diameter ranging between 0.4 – 0.5 mm for regular class and 0.15 – 0.3 mm for a finer one. Silica sand, in quartz form, is characterized by a spherical, constant

and stable shape qualifying it to be the best rheological fit for UHP-FRC. Knowing that the difference in the mechanical and thermal properties between the cement paste and the coarse aggregates tends to generate cracks, the elimination of coarse aggregates reduces the development of cracks and enhances the homogeneity of the matrix.

Portland Cement: Cement is considered to have the second biggest particle size in the matrix around 15 μm . CEM 1 52.5, ASTM Type I and II are the most commonly used. It is well known that the main disadvantage of UHP-FRC is its high cement content, almost double the amount used in conventional concrete. The more significant amount of cement leads to the increase of the design mixture's cost and the CO_2 emissions while generating a strongly exothermic reaction, that in some cases causes premature shrinkage cracking in structures. Once the cement is in contact with water, the hydration of (C_3S) and (C_2S) produces the Calcium Silicate Hydrate gel (CSH_{gel}) that mainly provides the compressive strength of concrete. According to Wille et al's (2011) study, the amount of calcium silicates added to the cement should be greater than 65%. Also, the (C_3A) content must be limited to 8% since it can reduce the workability of the mixture (Cheyrezy *et al.*, 1995). In fact, (C_3A) reacts with the superplasticizers thus reducing their initial required amount to ensure adequate workability (Zdeb and Śliwiński, 2009). Besides, cement should be based on low alkali content since it tends to increase the porosity and decrease the compressive strength of concrete in the long term.

Two types of mineral additives are generally used in UHP-FRC; cementitious materials and inert fillers. Cement and the mineral additives constitute the binder of the mixture. The cementitious materials are divided between “pozzolans” such as silica fume and fly ash Type F on one hand and “hydraulic material” such as ground granulated blast furnace slag (GGBS) and fly ash Type C on the second hand. In fact, the hydration of cement produces calcium hydroxide (CH) that does not contribute to the concrete's strength. Nevertheless, it was proven that once the pozzolanic materials rich in silicic acid are added, they will react with (CH) causing a second hydration that produces more (CSH) to increase the concrete's strength with the same initial amount of cement (Massazza, 1993; Weng *et al.*, 1997). Therefore, one unit of pozzolanic material can replace a unit of cement, leading to the reduction of the initial amount of cement, to eventually obtain the same amount of CSH. It was proven that the addition of these mineral admixtures tends to improve the concrete's strength with time, which is not applicable to normal concrete (Bilodeau and Mohan Malhotra, 2000).

Regarding the hydraulic materials, they present cementitious properties and can directly react with water. Both of these cementitious additives are industrial waste, rendering the usage of UHP-FRC an eco-friendly and economical choice while preserving the same mechanical strength. However, inert materials such as limestone, rice husk ash, recycled glass cullet, palm oil fuel ash, waste ceramics, and waste bottom ash do not participate in the hydration process. Yet, their ability to fill the void reduces the porosity of the mixture, making the hardened concrete denser, stronger and less permeable

Fly Ash: Fly ash (FA) is a waste of the coal combustion process and can only be used as concrete filler. FA is classified into three types; Type F, CI, and CH differing by their content of calcium CaO (A3001, 2013). Type F is generally used as an admixture since it has the lowest content of CaO (< 8%) and therefore relies on its pozzolanic properties without any hydraulic behavior to obtain high compressive strength. FA Types CI and CH contain a high amount of calcium and have hydraulic properties which allows them to directly react with water, resulting in a normal strength concrete (Thomas, 2007). FA is characterized by a spherical shape that smoothens the contact area and enhances the workability of the design mix (Best and Lane, 1980). It is the only admixture with a particle size greater than cement (70 μm). So, it is less reactive with a low surface adsorption capacity resulting in the reduction of the required water in the mixture. In fact, 10% of the adequate fly ash can actually reduce 3% of the required amount of water (Thomas, 2007). Fly ash also contributes to an increase in the setting time, causing a delayed reactivity, which is beneficial in terms of the exothermic heat and shrinkage cracking. However, its usage is not recommended for early strength projects and in cold weather, especially for FA Types CI and CH (hydraulic properties). In fact, the replacement of cement with 20% of FA can increase the compressive strength of the mixture 90 days after its casting (Ibrahim et al., 2017).

Slag: Slag, also known as ground-granulated blast-furnace slag (GGBS), a particle size around 0.45 μm , is another admixture resulting from the steel and iron industry. Slag has the same effect as FA in terms of workability and hydration rate owing to its angular particle shape. A replacement of 30% of slag delays the hydration process but leads to high long-term compressive strength (Shao, 2016). In addition, it was shown that the presence of slag in an amount exceeding 40% of the cement's unit weight could decrease the flexural properties of the concrete (Ibrahim *et al.*, 2017).

Silica Fume: Silica fume is the finest pozzolan particle with a diameter of 0.3 μm recognized as micro-silica and condensed silica fume. This small particle with a high surface area is the most reactive pozzolan material that accelerates the hydration process and provides high strength at an early age (Yoo and Banthia, 2016). It is characterized by its capability to fill the smallest voids which optimizes the packing procedure and increases the density and the strength of concrete, making it the most common admixture used in UHP-FRC (Bache, 1981). Not only does it improve the contact interface between the binder and sand but also between the cement and steel fibers. (Habel *et al.*, 2006). (Shao, 2016) showed that 10% of silica fume would lead to greater workability and strength than using 18% of the binder weight. Moreover, the addition of micro-silica fume densifies the mixture and leads to higher compressive strength (Lee *et al.*, 2018).

Inert fillers: Fillers are usually admixtures that replace a portion of the binder without engaging in any chemical reactions while still influencing the workability and the strength of the mix. Limestone is a type of filler commonly added to the binder of UHP-FRC (Yu *et al.*, 2014). It is characterized by a fine aggregate size that tends to fill all the voids, increasing the density of UHP-FRC. This will lead to the enhancement of the mechanical properties of the mix and its impermeability.

Chemical admixtures: The addition of chemical additives is necessary to ensure low water to binder ratio with high workability (Plank *et al.*, 2009). Superplasticizer is a type of water reducer (such as polycarboxylates and polycarboxylate ethers) that is frequently used in UHP-FRC to reduce the water to binder ratio leading to low porosity. The reduced amount of water enhances the compressive strength of the concrete (Alsadey, 2013; Basheerudeen and Anandan, 2015). It is to be noted that the way of adding superplasticizers affects the workability of the mixture. It is advised to incorporate it gradually (Ma *et al.*, 2008).

Steel fibers: Two main types of fibers are generally added to UHPC: synthetic and metallic. The former can control the propagation of early age concrete cracking owing to its low modulus of elasticity that is yet greater than the fresh concrete's Young modulus (Leboeuf, 2016). As for steel fibers, they are generally used due to their high modulus of elasticity (200 GPa), their high tensile strength (up to 2000 MPa), high ductility and toughness that control cracking development in the service life of concrete (Habel, 2004). There are different types of steel fibers: straight (S), hooked

(H1), hooked (H1) combined with hook (H2), high twisted (T1) and low twisted (T2) (Wille and Naaman, 2012). For straight steel fibers, three different lengths ranges are typically used: 5mm, between 5 and 25mm and greater than 30 mm. The length of the steel fiber should be 3 to 4 times greater than the maximum aggregate size. For instance, with an aggregate presenting a maximum diameter less than 1mm, the short steel fiber can be used in UHP-FRC while taking into consideration the steel fiber's necessary development length to reach its tensile strength.

2.1.3 Effect of steel fibers on UHP-SFRC properties

2.1.3.1 Effect on the tensile properties and workability

A flexural test was conducted on UHPC with and without the presence of short steel fibers ($\ell_f = 13$ mm; $\varnothing_f = 0.2$ mm; $V_f = 0 - 3$ %). The test showed that the incorporation of steel fibers improved the post-peak response of the concrete marked by the ability to sustain a higher load (Wu *et al.*, 2016). Moreover, a direct tension experimental program reported a high dependency of the tensile strength of the matrix to the volume fraction of steel fibers (Wille *et al.*, 2014) as presented in Equation (2.1):

$$\sigma_{pc} = -0.9V_f^2 + 9V_f \quad (2.1)$$

A volumetric fraction of short steel fibers more significant than 3% increases the tensile strength of the matrix but decreases its workability. This low flowability provides the concrete with a viscous property that will entrap a significant amount of air. Once the concrete matrix hardens, the trapped air becomes void space, decreasing both the compression strength and the young modulus values. The optimal volumetric fraction of steel fiber ranges between 2-3% with a tensile strength of 10 MPa leading to a strain-hardening behavior prior to crack localization while maintaining effective workability (Maca *et al.*, 2012). Furthermore, steel fibers can be added in accordance with another parameter; the fiber factor χ_f . The factor is directly proportional to the mechanical strength of the mixture and indirectly proportional to its workability. Therefore, it was advised to limit the fiber factor to 2.5 for short steel fibers ($\ell_f = 13$ mm ; $d_f = 0.2$ mm ; $\ell_f/d_f = 65$) to prevent the formation of fiber clumps using Equation (2.2) (Markovic, 2006):

$$\chi_f = K = \frac{L_f}{d_f} \times V_f \quad (2.2)$$

The “fiber energy-absorbing mechanism” presented in Figure 2-2 allows the steel fibers to achieve their functions. Zollo, (1997) explains this mechanism as follows; the low tensile strength of the matrix generates strain cracks prior to the peak load. Thus, the fibers will de-bond and bridge through the crack to finally pull-out and/or yield, then rupture.

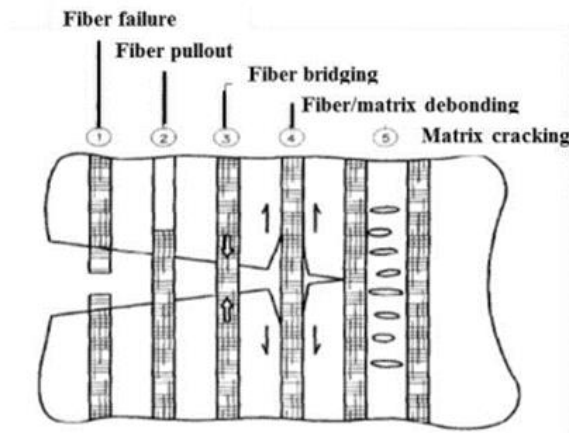


Figure 2-2 Transformation of the matrix-fiber interface known as “fiber energy-absorbing mechanism” (Zollo, 1997)

Therefore, even if the concrete matrix is vastly dense and the steel fibers have a high tensile property, the bond strength at their interface determines the tensile strength of the material and its ability to present a strain hardening behavior. If both materials are bonded properly, the fibers are able to stop the opening of the cracks and ensure a stress transfer mechanism leading to a ductile behavior of the structural element. Thus, the pullout force should be less than the fiber-breaking force as mentioned in Equation (2.3) (Spasojević, 2008):

$$\frac{L_f}{d_f} \leq \frac{\sigma_{pc}}{2 \times \tau} = 150 \quad (2.3)$$

This composite action depends on several additional parameters such as the control matrix, the properties of the fibers and their surface interaction. Bond strength was proven to be directly proportional to the density and strength of the matrix (Abu-Lebdeh *et al.*, 2011). A study showed that

adding short straight steel fibers ($\ell_f = 13 \text{ mm}$; $d_f = 0.2 \text{ mm}$) in a UHPC matrix, rather than in an HSC, transforms the composite response under tension from fragile to ductile as illustrated in the graphs in Figure 2-3 (Wille *et al.*, 2012). It was concluded that an amount of silica fume equal to almost 20-30% of the cementitious volume, enhances the bond interface between the concrete matrix and the steel fibers leading to a pullout mode of failure (Chan and Chu, 2004).

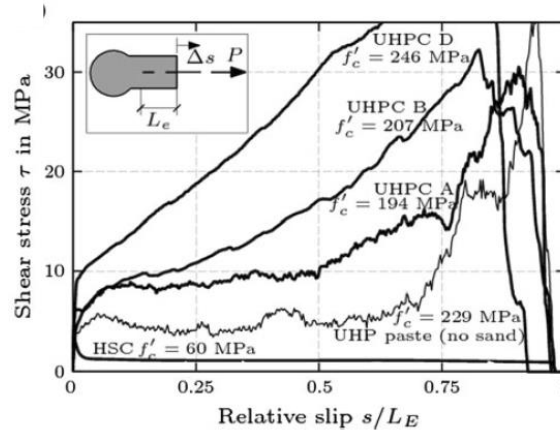


Figure 2-3 Comparison of the shear stress slip response for smooth steel fibers when embedded in HSC ($f'_c = 60 \text{ MPa}$) and UHPC ($f'_c > 194 \text{ MPa}$) (Wille *et al.*, 2012).

With regards to steel fibers, different properties affect this fiber-concrete composite action such as the tensile strength, the type, geometry, and orientation. A preliminary study indicated that using hooked end fibers (H) ($\ell_f = 30 \text{ mm}$; $d_f = 0.38 \text{ mm}$) and twisted fibers (T) ($\ell_f = 30 \text{ mm}$; $d_f = 0.3 \text{ mm}$) instead of short straight fibers (S) ($\ell_f = 13 \text{ mm}$; $d_f = 0.2 \text{ mm}$) leads to higher tensile properties due to their mechanical bond (Wille *et al.*, 2011; Wille and Naaman, 2012). However, when a recent direct tension test was conducted on UHP-SFRC dog bones, no difference in behavior between the types of fibers was noticed (Wille *et al.*, 2014). This was explained by the calculation of the group effect parameter λ through calibration of the experiment using Equation (2.4) proposed below:

$$\sigma_{pc} = \lambda \times \tau \times \frac{\ell_f}{d_f} \times V_f \quad (2.4)$$

It was observed that the group effect parameter was more important for S fibers ($\lambda = 0.95$) than for H and T steel fibers ($\lambda = 0.24$) resulting with the same tensile properties presented in Figure 2-4. Thus, the group effect parameter proves that the effect of mechanical bond of H and T steel fibers is similar

to the effect produced when using short straight, smooth fibers that enable a high bond strength with the matrix.

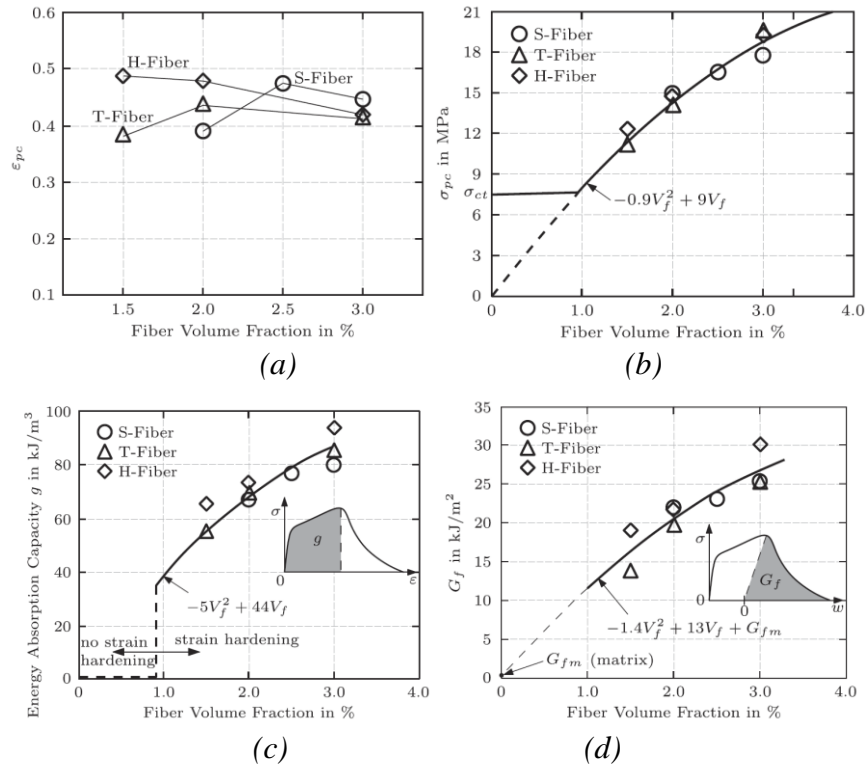


Figure 2-4 Similarities in the tensile properties for S, T and H fibers: (a) peak tensile strength (b) peak tensile strain (c) energy absorption capacity g (d) fracture energy (Wille *et al.*, 2014)

It was also proven that the surface contact of short steel fibers and their abundance surpass the effect of the hooked and twisted ends on the behavior of the material (Rossi, 2013). Moreover, long fibers tend to crumble inside the mixture creating obstacles and slowing the flow of the concrete mixture. They have limited enhancement on the first crack of the matrix (Yoo *et al.*, 2016). Several design mixes were proposed for UHP-SFRC encouraging the use of short, straight and smooth steel fibers since they have no tremendous effect on the flowability of the matrix (Maca *et al.*, 2012).

Commercial UHP-SFRC mixes started using brass-coated short steel fibers to reduce corrosion attacks. However, it was proven that brass coated steel fibers lead to a higher fiber/matrix adhesion than regular steel fibers (Chan and Li, 1997). A pullout-test was conducted on straight steel brass-coated fibers ($\ell_f=13$ mm; $d_f=0.2$ mm ; $\ell_{bf} = 6.5$ mm) in different UHPC design mixtures to analyze their behavior (Wille and Naaman, 2013). As depicted in Figure 2-5, the response curves present a

very ductile behavior with a pullout mode of failure reaching a pullout strength of $\sigma_f = 1273 \text{ MPa}$ when sand (SiO_2) is added. The pullout can be detected by the abrasion of the surface of the coated steel fibers. Moreover, due to the cutting process in the manufacturing, the short steel fibers developed small deformations on their edges contributing to the anchorage strength.

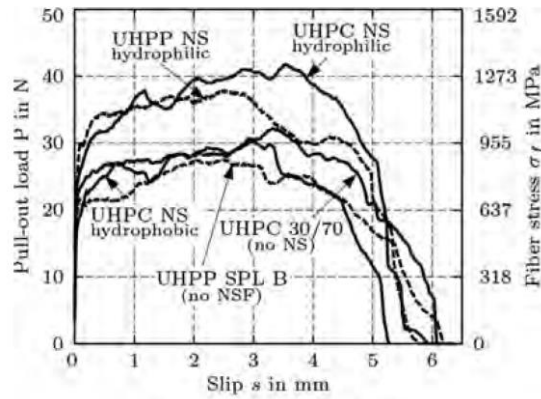


Figure 2-5 Pullout load-slip relationship for different parameters for short steel brass-coated steel fiber in UHPC (Wille and Naaman, 2013)

The method of casting and the orientation of fibers have an essential effect on its tensile properties. In fact, a replication of concrete and steel fibers were experimentally realized by using a transparent and viscous material (Carbopol) with PVA fibers to show that the casting from one side showed that fibers were mostly oriented vertically in the constant moment region causing the reduction of the number of horizontal fibers participating in the flexural behavior (Zhou and Chida, 2013). This was observed as well by Shao (2016), where the difference was more than 50%.

2.1.3.2 Effect on the compressive strength and Young's modulus

The addition of steel fiber enhances the post-peak flexural strength of the mixture, yet this has limited effect on its compressive strength and Young's modulus. Some studies claim that the addition of 2% of straight steel fibers will increase the compressive strength by 20% of the control mixture (Hassan *et al.*, 2012). Nonetheless, in other cases, adding 2.5% of steel fibers slightly increases it by 7% as can be seen in Figure 2-6 (Shao, 2016).

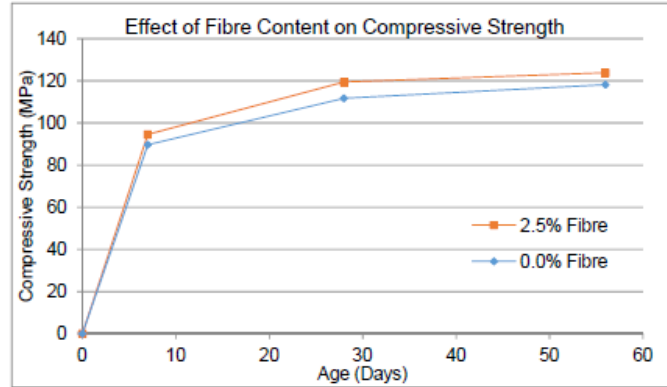


Figure 2-6 Effect of steel fibers on the compressive strength (Shao, 2016)

Steel fibers are only useful in the plastic deformation stage. Therefore, the modulus of elasticity is not affected by their presence (AL-Ameeri, 2013). In fact, the Young's modulus of UHPC without fibers is very high and ranges between 50 GPa to 70 GPa (Spasojević, 2008). However, the addition of steel fibers changes the mode of failure of the specimens in compression from brittle bursting to ductile (Wille *et al.*, 2014).

2.1.4 Mechanical properties of UHP-SFRC

The compressive strength of 50 mm x 50 mm cubes is 8% higher than the compressive strength of 75 mm x 150 mm cylinders (Graybeal and Davis, 2008). Still, there is no difference between both specimens for a compression loading rate between 0.24 and 1.7 MPa/s (Graybeal, 2006). Several design codes previously proposed a compression stress-strain response depicted by an ascending linear behavior followed by a plateau, considered to be very conservative, limiting the use of the properties of UHP-FRC. Hence, a constitutive pre-peak behavior of UHPC was proposed as described in Figure 2-7 (Haber *et al.*, 2018).

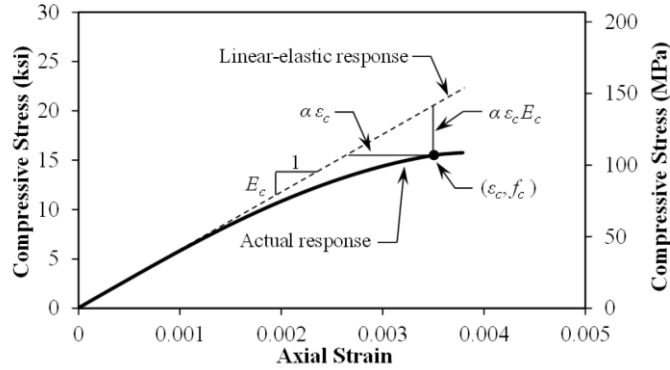


Figure 2-7 Pre-peak compressive stress-strain behavior of UHPC (Haber et al., 2018)

Initially, the response curve follows a linear-elastic response. Once it reaches half of the peak load, there is a possibility of a slight softening based on Equation (2.5) (Graybeal, 2007). The parameter α is considered as a linearity deviation factor that is calculated by data calibration:

$$f_c = \varepsilon_c E_c (1 - \alpha) \quad (2.5)$$

The compressive strength of UHP-FRC should be greater than 120 MPa (Aaleti and Sritharan, 2014). The compressive strain at peak stress ranges between 0.0035 and 0.004 for cured concrete in normal conditions (Baqersad et al., 2017). Equation (2.6) is proposed to calculate the Young's modulus E_c out of the compressive strength (Graybeal, 2007). The Elastic modulus E_c for UHP-FRC varies between 40 to 55 GPa (Haber et al., 2018):

$$E_c = 1460 \sqrt{f'_c} \text{ (ksi)} \quad (2.6)$$

Based on the standards, Equation (2.7) suggests another calculation of the Young's modulus where 0.00005 is considered the strain for the stress f_{c1} (ASTM C496/C496M):

$$E_c = \frac{(f_{c2} - f_{c1})}{(\varepsilon_{c2} - 0.00005)} \quad (2.7)$$

A direct correlation between the compressive strength at 28 days and any other day (t) is specified in Equation (2.8) (Graybeal and Baby, 2013). However, in some situations, it was documented that it did not provide accurate values and needed more investigation:

$$f'_{ct} = f'_c \left[1 - e^{\left(-\frac{t-0.9}{3}\right)^{0.6}} \right] \quad (2.8)$$

The Poisson's ratio can be calculated using Equation (2.9), where the range stands between 0.145 and 0.175 (Haber *et al.*, 2018):

$$\nu = -\frac{\varepsilon_{circ,30} - \varepsilon_{circ,10}}{\varepsilon_{axial,30} - \varepsilon_{axial,10}} \quad (2.9)$$

Direct Tension Tests (DTT) were conducted to obtain the tensile stress-strain response presented in Figure 1-4 and divided into the elastic phase (phase I), the multi-cracking phase (phase II) and the localized deformation phase (phase III). The strain of the first crack is represented by the intersection between the tension stress-strain curve and the line at an offset of 0.02% from the origin with a slope equal to the Young's modulus. Furthermore, it was shown that the splitting tensile strength gives higher values than the direct tensile test. In fact, the direct tensile strength was about 10 MPa compared to 17 MPa for the splitting tensile strength (Haber *et al.*, 2018). Equation (2.10) was proposed to determine the tensile strength of UHP-FRC from the compressive strength at 28 days depending on the type of curing applied (Graybeal and Baby, 2013) where K is equal to 6.7, 7.8 and 8.8 for the untreated, air-treated and steam-cured specimen, respectively:

$$f_t = K \sqrt{f'_c} \quad (2.10)$$

2.1.5 UHP-SFRC under fire

Fire is considered a tremendous hazard for infrastructures and bridges, that can destroy the structure, disrupt the traffic flow and jeopardize life safety in general (Garlock *et al.*, 2012). Moreover, the behavior of this innovative concrete is not fully developed once subject to fire increases this risk. For this reason, excessive research is done in this field for a safer application in future infrastructure

designs or in the retrofitting of existing damaged ones aiming for a “fire resilient environment” in both domains of application. Any reinforced structure can be designed to be “fire resilient”, bearing elevated temperatures and protecting reinforcing bars, to maintain an Operational (LOP-H) or even an Occupancy performance level (LOP-M) post-fire up to a limited extent of “Life Safe” (LOP-L) performance state where there are no risks of collapse, nonetheless the structure requires a more extended period to be repaired. The operational level state should be reached for infrastructure to avoid heavy traffic in case no alternative roads can be used. The reduced amount of pores in a high-performance concrete under heat, known for its optimized compacted mix and permeability, prevents the evaporated water from escaping thus causing elevated capillary pressures that exceed the concrete’s tensile strength and thereafter explodes (Phan and Carino, 2000). Thus, this novel matrix was exposed to heat and showed great residual strength, however, spalling occurred, which diminished its strength. Several ongoing studies on this concrete resulted in methods that prevent spalling. These studies will allow the design of resilient structures.

The initiation of spalling is interpreted in two ways; from pressure inside the pores or from the prevention of thermal expansion (Ulm *et al.*, 1999). Both mechanisms are explained below:

- The first hypothesis relies on the transfer obstruction of the pressure gradient from the dehydrated zone near the heated surface to the partially saturated area inside the concrete owing to the highly water saturated zone “moisture clough” present in between, reaching a point where this accumulated water pressure inside these pores exceeds the tensile strength of concrete and spalling occurs.
- The second hypothesis relies on the prevented thermal dilatation created by the thermal gradient, from the difference between the temperatures of the heated surface and the internal zone of concrete, causing compressive stresses parallel to the surface. At the same time, the same zone enters the plastic phase caused by the fire-damaged symptoms discussed previously leading to spalling.

The occurrence of both phenomena can be accelerated from the pore pressures where they play a second role in this case (De Morais *et al.*, 2010).

According to the Eurocode, the content value of the former should be taken around 2% (European Committee for Standardization, 2004). Nevertheless, the effect of moisture was not observed in Yermak's experiment (Yermak *et al.*, 2017). While according to (Hertz, 2003), the condensed UHPC blend spalled without the presence of any water. Whereas for NC, spalling occurs for moisture content between 3 – 4 % by weight. For the case where no water was present, spalling happened from the water formed from the dehydration of cement paste once exposed to fire.

Another method used to prevent spalling and that is currently under research is the addition of a small volume of PP fibers. Eurocode 2 advised the use of 2kg/m^3 of PPF (European Committee for Standardization, 2004). The experiment conducted by (Yermak *et al.*, 2017), with the addition of 0.75kg/m^3 to the mixture design initially containing 60kg/m^3 of steel fibers stopped the spalling from occurring, whether they were 6 mm or 12 mm long with the same diameter 0.032mm. This was as well observed by another experiment where it was noticed that for 1kg/m^3 , the most beneficial outcome was obtained for the shortest and thinnest PP fiber. The thinnest diameter used ($\emptyset = 0.032\text{mm}$; $\ell = 18\text{mm}$) presented no superficial cracks until 800°C , while for all the other values ($0.5\text{mm} < \emptyset < 1.1\text{mm}$; $40\text{mm} < \ell < 50\text{mm}$) discoloration and holes appeared around 300°C . The thin fibers as well had a better gradual decrease of the relative compressive strength in comparison to the thick fibers (Balázs *et al.*, 2017). In fact, the prevention of spalling when adding polymer fibers was explained by their decomposition around 500°C , creating channels to release the pressure gases formed from the annealing of cement around 800°C (Czoboly *et al.*, 2017). (Serrano *et al.*, 2016) stated that around 400°C , due to the high permeability caused by PP fibers, lower temperatures are reached regarding the heated specimens with a slower cooling phase that limited the number of cracks.

Serrano *et al.*, (2016) experienced that the addition of PP fibers leads to a higher compressive strength, before and after the direct fire, when thick hooked steel fibers are only added. The most beneficial response was for 1% V of PP fibers leading to higher ultimate strain and stresses. (Kodur *et al.*, 2003) observed as well that PPF improved the ductility of the columns in compression when subject to high temperatures. Another method that prevented spalling was the addition of air entrainment. In response

to that, (Akca and Zihnioğlu, 2013) demonstrated that air entrainment only prevents the explosive behavior of concrete when polypropylene fibers are present. Otherwise spalling occurs around 500°C.

There have been several standard designs of HSC and UHSC but very few regarding fire resistance and none in major codes until very recently, such as the French Standards of UHPFRC (2016) and the Swedish (2011) recommendation for preventing fire spalling in concrete structures for Civil Engineering purposes. An example of a commercialized mix design that used PP fibers as a solution to prevent spalling was Ductal® and was tested for different structural elements and different types of loading subject to the ISO fire curve (Fehling, 2004).

2.1.6 UHP-SFRC design mixes considered as trials

A simple mixture of the materials discussed in Section 2.1.2 does not lead directly to the formation of UHP-FRC. Two steps must be achieved in the process: the first step is based on optimizing the concrete matrix with reference to the compressive strength and the flow; while the second step focuses on obtaining high bond strength at the fiber-matrix interface. Previously developed UHP-FRC design mixes were characterized by a high amount of cement content greater than 1000 kg/m³ (Habel *et al.*, 2008; Maca *et al.*, 2012a). Two design mixes are exposed due to their unique usage of low amounts of cement to create an eco-friendly concrete and reduce global warming.

For this reason, research was followed to study the ability to reduce the amount of cement down to 650 kg/m³ by replacing 20% of its portion by quartz or 30% by limestone, following the modified (Andreasen and Andersen, 1930) particle packing model and the mixing procedure presented in Figure 2-8. This resulted in a slight decrease of the fresh and hard properties by a maximum value of 10% where the flexural strength reached 30 MPa for a short steel fiber volumetric fraction of 2.5% while the compressive strength attained 150 MPa at 28 days (Yu *et al.*, 2014).

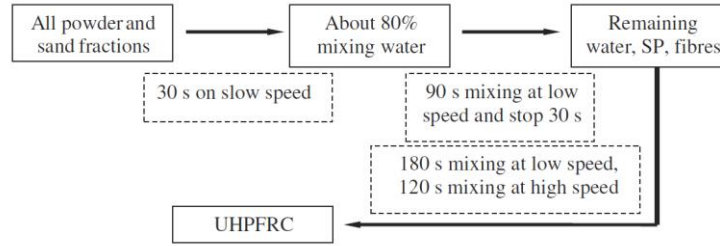


Figure 2-8 Mixing procedure followed to obtain the proposed design mix (Yu et al., 2014)

The design mixture was then enhanced by reducing the proportions of the dry materials where cement's weight was taken equal to 594.2 kg/m^3 for a 2% volumetric fraction of steel fibers. The relative slump flow was around 28.8 cm based on the codes (ASTM C1856, 2017). The compressive strength at 28 days was 140 MPa with a flexural strength of 28 MPa obtained from a four-point bending test on prisms (500 x 100 x 100 mm) causing the development of multiple cracking that depicts a ductile behavior (Yu *et al.*, 2015). The proportions of the reference design mixture considered are presented in Table 2-1. This design mixture is noted as Mix M.

Table 2-1 Reference design mix proposed M

Materials	Type	Symbol	Amount	Unit
Cement	CEM I 52.5 R	C	594.2	kg/m^3
Filler	Limestone powder	LP	265.3	kg/m^3
Fine sand	Microsand 0.3 mm	M-S	221.1	kg/m^3
Coarse sand	Sand 0-2	N-S	1061.2	kg/m^3
Pozzolanic material	Nano-silica	nS	24.8	kg/m^3
Superplasticizer	Polycarboxylate ether	SP	44.2	kg/m^3
Water	-	W	176.9	kg/m^3
Short Straight fibers	$\ell_f = 13 \text{ mm}$; $\varnothing_f = 0.2 \text{ mm}$	LSF	2	%
$w/c = 0.2$				

Another design mixture follows the same principle as the previous one where the limestone powder is industrially incorporated in the cement material rather than in the mineral additives. Integrating limestone in Portland cement is a recent method proposed, to lower the amount of clinker and reduce CO_2 emissions (Hooton *et al.*, 2007). Portland limestone cement (PLC) containing 6 – 15 % of limestone, used in Canada since 2011, is proposed in the design mixture. Table 2-2 presents the followed design mixture. The researcher varied the proportions of each material to obtain optimum

fresh and hard properties with a volumetric fraction of 2.5% of steel fibers ($\ell_f = 13$ mm; $\varnothing_f = 0.2$ mm) and a 30% and 10% substitution of cement by slag and silica fume, respectively.

Table 2-2 Reference design mix proposed B

Materials	Symbol	Amount (kg/m ³)	
Cement	C2	724.13	757.81
Fine Sand	S3	668.60	699.70
Pozzolanic material	Slg2	362.06	378.90
	SF2	120.69	126.30
Superplasticizer	SP3	17.01	25.83
Water	W	241.13	227.34
Steel fibers (2.5%)	SSF	195.75	197.75
w/b		0.2	0.18

Following the mixing procedure proposed in Figure 2-9, the diameter of the slump flow was around 570-680 mm based on ASTM C1611 and the compression strength at 56 days was 139.16 and 141.92 MPa for w/b = 0.2 and 0.18, respectively. The mixing procedure emphasizes at the beginning of mixing the dry materials from the smaller grain size to the largest to ensure a full blending of all the materials. The mixing procedure is proposed for a vintage 15 L mixer with a total mixing time around 28 minutes. What mainly changes the following mixing procedure with the one described in Figure 2-8 is the addition of the superplasticizer in two steps (Step 2 and 3) while in the previous mixture water was added in two phases and the superplasticizer was poured entirely in one phase.

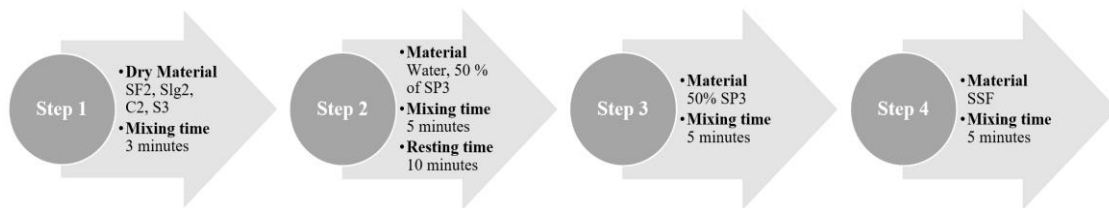


Figure 2-9 Mixing procedure proposed (Shao, 2016)

Shao (2016) cured the specimens by placing on top of them polypropylene sheets covered by wet burlap sheets. After 7 hours, once the surface of the concrete hardened, it was covered by two layers of wet burlap sheets and a layer of plastic sheet. The specimens are then demolded one day after casting and then wrapped in wet burlap and plastic sheets for 3 days. Finally, they are unwrapped and stored in room temperature until testing.

The casting methodology orients the steel fibers in a specific direction, influencing the tensile and flexural behavior of the mix. The researcher compared three different ways of pouring concrete: the flow method applied from the center, the flow method from the side and the layered method. The latter gave the highest flexural strength value of 21.3 MPa compared to 10 MPa for the two other methods (Shao, 2016). Plus, the layered method of casting resulted in a high modulus of elasticity of about 44 GPa and a stress-strain response under direct tension as depicted in Figure 2-10.

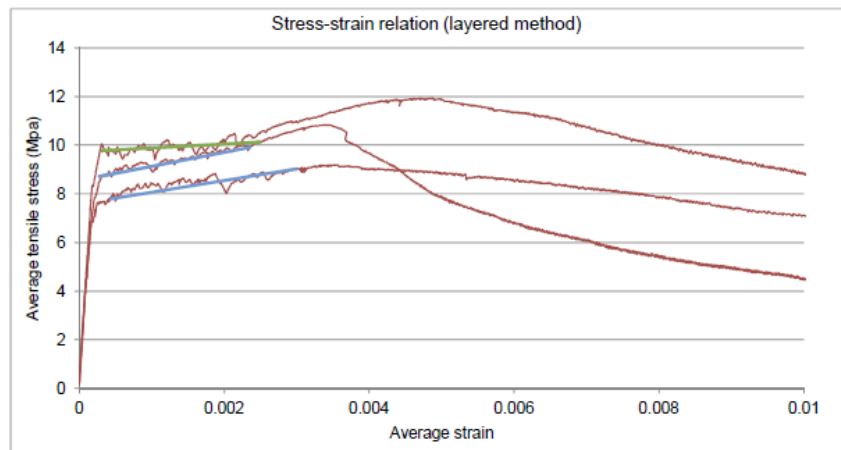


Figure 2-10 Tensile stress-strain behavior obtained (Shao, 2016)

It is acknowledged that UHP-FRC needs a high energy input, thus requiring a more significant time of mixing leading to the overheating of the mixture. However, this issue can be solved with a high energy mixer or by decreasing the temperatures of each component (Graybeal, 2013). In addition, several researchers advised the use of ice in the mixing procedure instead of water to prevent overheating mixtures (Baqersad *et al.*, 2017). The mixing procedure is essential to obtain a dense matrix. Accordingly, researchers initially proposed to mix the dry materials first and then add the wet materials gradually because it is easier to break the clusters formed by these fine aggregates in dry conditions rather than in wet conditions (Richard and Cheyrezy, 1995). The steel fibers should also be gradually added in the cementitious mixture to eliminate the possibility of mass knots formation (Maca *et al.*, 2012).

2.2 Bond strength

2.2.1 Bond force-slip law for deformed bars embedded in conventional concrete

Bond strength is defined by the bond-stress-slip relationship. Generally, it is obtained experimentally by conducting bond tests. Figure 2-11 presents the Free Body Diagram of the reinforcing bar in tension and the forces acting on it.

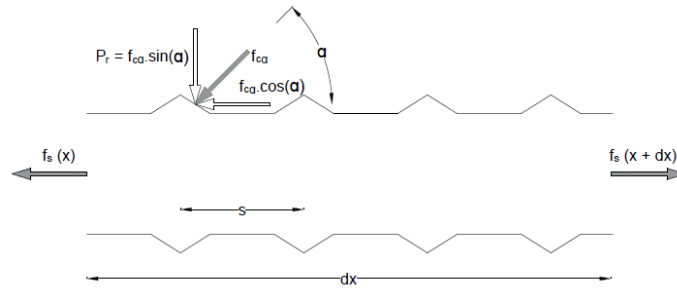


Figure 2-11 Equilibrium of forces acting on the bar with conventional concrete

The equilibrium of forces acting on the bar in tension along a short bonded length dx is written:

$$-f_s(x) \cdot A_b + f_s(x+dx) \cdot A_b - f_{ca} \cos(\alpha) \cdot \frac{dx}{s} \pi D_b = 0$$

$$\frac{f_s(x) + df_s(x) - f_s(x)}{dx} \cdot A_b \cdot dx - f_{ca} \cos(\alpha) \cdot \frac{dx}{s} \pi D_b = 0$$

$$\frac{df_s(x)}{dx} \cdot \pi \cdot \frac{D_b^2}{4} - \frac{f_{ca} \cos(\alpha)}{s} \cdot \pi D_b = 0 \quad ; \quad \text{where} \quad \frac{-f_{ca}(x) \cos \alpha}{s} = f_b$$

Thus, Equation (2.11) shows that the bond strength is directly proportional to the variation of the tensile force of the bar on a section dx :

$$\frac{df_s(x)}{dx} = \frac{-4}{D_b} f_b(x) \quad (2.11)$$

In design codes, mathematical equations are available to calculate the minimum required embedment length of a reinforcing bar to develop its yield stress in conventional concrete. These equations are based on Equation (2.12) assuming an average and uniform distribution of bond stress along the studied embedment length:

$$\int_0^{l_b} dx = \int_0^{f_y} \frac{df \times D_b}{4 \times f_b} \quad (2.12)$$

Therefore, the minimum required embedment length to yield the reinforcing bar is presented in Equation (2.13):

$$l_b = \frac{D_b \times f_y}{4 \times f_b} \quad (2.13)$$

Nevertheless, the constant average bond stress assumption is only valid when the behavior of the reinforcing bar is elastic (linear variation of the steel stress $\frac{df}{dx} = 0$) and in a short embedment length since shear stresses in the concrete cover are limited. Thus, numerical equations of the bond-stress slip law concerning reinforced steel embedded in conventional concrete were recommended to determine the variation of the bar strain, the bond stress and the bar slip starting from the loaded end of the reinforcing bar propagating along the entire considered embedment length (Tastani and Pantazopoulou, 2013). They are based on Equation (2.11) and the compatibility equation presented in Equation (2.14):

$$\frac{ds(x)}{dx} = -[\varepsilon_s(x) - \varepsilon_{ct}(x)] \quad (2.14)$$

Three main assumptions were given to solve these equations. Firstly, strains in the concrete were considered negligible compared to the strains in the reinforcing bar due to their poor tensile properties. This lead to the compatibility equation presented in Equation (2.15):

$$\frac{ds(x)}{dx} = -[\varepsilon_s(x)] \quad (2.15)$$

Secondly, the reinforcing bars were characterized by an elasto-plastic behavior. Thirdly, the local bond-stress slip law represents a splitting-pullout failure mode presented by the grey line in Figure 2-12. It was obtained by conducting a series of direct pullout tests for regular reinforcing bars embedded in conventional concrete where the local bond-stress slip relationship measured depicts the black line with a conservative average bond stress f_b^{ave} (Tastani and Pantazopoulou, 2010). However, the grey line presents the assumed local bond-stress slip law divided in an initial elastic segment up to a maximum bond stress f_b^{max} for a relative slip s_y . At the end of the elastic phase, a plateau of the maximum bond stress is formed. Once the relative slip reaches the distance between the ribs s_u , the bond force drops to reach a residual bond stress f_b^{res} defined by the local bond failure. Afterwards, the only mechanism of force transfer known as “friction” occurs between the ends of the ribs and the formed cylindrical surface of the concrete cover (Tastani and Pantazopoulou, 2010).

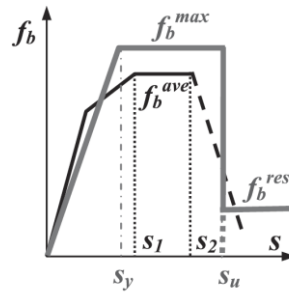


Figure 2-12 Assumed (grey line) and measured (black line) local bond-stress slip law (Tastani and Pantazopoulou, 2010)

Figure 2-13 presents the calculated solution of the state of bond stress obtained by solving the previously described differential equations, using the bond-slip law depicted by the grey line in Figure 2-12. Response is divided mainly into three stages. The first stage observed in Figure 2-13 (a) represents the linear elastic behavior of both the reinforcing bar and the bond stress. The second stage in Figure 2-13 (b) determines the bond deterioration failure mode. If sufficient confinement or embedment length were provided, the bond stress enters the plastic phase, enabling the bar to experience higher strains with slips greater than their yield slip values. Therefore, the embedment length L_b experiences from the loaded end until a certain plastic length l_p a plastic distribution of the

maximum bond stress f_b^{max} whereas it remains elastic along the rest of the embedment length of $(L_b - l_p)$. In the third phase, the reinforcing bar and the bond enter the plastic phase together throughout a yielding or de-bonding length l_r . Along this length, the bond stress decreases to reach f_b^{res} when using deformed bars (Tastani and Pantazopoulou, 2013).

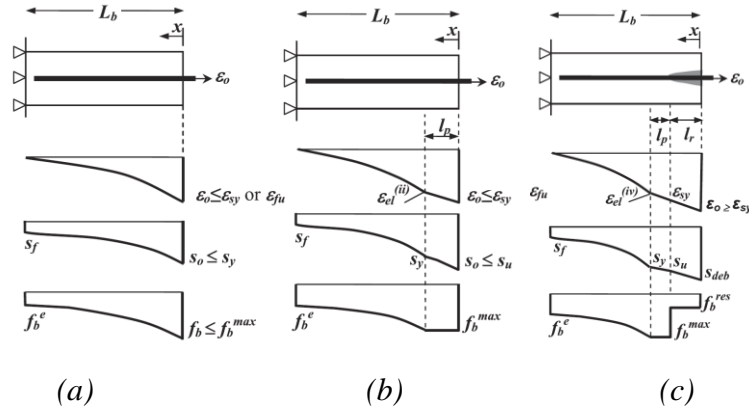


Figure 2-13 Analytical solution for bond stress behavior with elastic behavior of the reinforcing bar and bond (a) elastic behavior of the reinforcing bar and plastic behavior of bond (c) plastic behavior of steel bar and bond (Tastani and Pantazopoulou, 2013)

Tastani and Pantazopoulou (2002) studied the effect of the radial state of stress on the longitudinal component by correlating them with a frictional factor as shown in Figure 2-14 and presented in Equation (2.16):

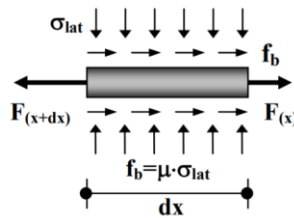


Figure 2-14 Frictional concept (Tastani and Pantazopoulou, 2002)

$$f_b^{max} = \frac{2 \mu}{\pi} \sigma_n + f_{adh} \quad (2.16)$$

Several experiments have been proposed in the past to characterize the local bond stress-slip laws concerning reinforced steel embedded in conventional concrete to facilitate the improved design of structural concrete. However, the bond model is still in development regarding UHP-SFRC. In fact, the bond-stress slip equations presented in Figure 2-13 are not valid for HPFRC since the assumption

of the compatibility deformation equation cannot be applied because the tensile strain for this novel concrete cannot be neglected. A mathematical solution for ECC was recently proposed to highlight the main differences between both numerical models (Eleftheriou *et al.*, 2017). Firstly, the compatibility deformation used is given in Equation (2.14) without any simplifications. Secondly, the equilibrium of the forces for the studied element presented in Figure 2-15 (a) includes the forces of the concrete matrix. The latter presents the tensile stress-strain behavior of HPFRC such as presented in Figure 2-1 with an initial linear elastic response of $f_t = E_c \cdot \varepsilon_{ct}$. This tensile strength remains constant until the ultimate strain. Lastly, the assumed state of bond stress is modified in the post-peak phase presented in Figure 2-15 (b) highlighting the presence of bond toughness. However, this solution is limited to the elastic behavior of steel reinforcing bars.

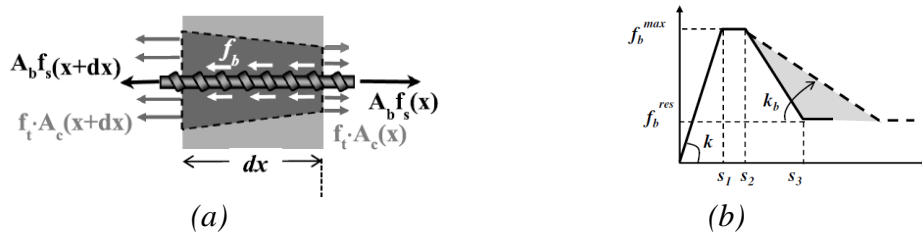


Figure 2-15 (a) Forces acting on the bar in HPFRC (b) Assumed local bond-stress slip law for HPFRC (Eleftheriou, Tastani and Pantazopoulou, 2017)

2.2.2 Different types of bond tests

Bond tests are divided into two main categories. The first is the “transfer” type shown in Figure 2-16 where the reinforcing bar is pulled by both ends, and the bond is measured indirectly by the use of strain gages placed on the reinforcing bar or on the concrete which is a complicated process (Cairns and Plizzari, 2003).

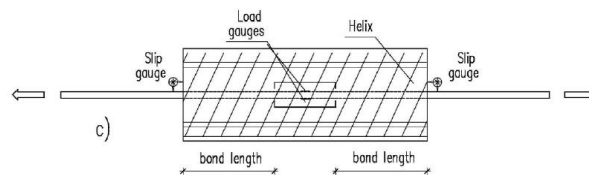


Figure 2-16 Bond transfer test (Cairns and Plizzari, 2003)

The second is the “anchorage or development type” test where one end of the reinforcing bar is embedded in the concrete, and the other end is pulled out. The bond strength is directly calculated by applying external equilibrium. Hence, most of the experimental tests conducted are based on this

principle. Initially, the standard “pullout test” (SPT) as shown in Figure 2-17 (a) was mostly used for its simple application, yet two main disadvantages were noticed. The formation of compression struts between the support and the surface of the reinforcing bar due to the support conditions, placing the surrounding concrete in compression, whereas the concrete cover is in tension in RC flexural members. Thus, the effect of transverse cracking is not taken into consideration (ACI Committee 408, 2003). The second disadvantage is an overestimation of bond strength values generated by the pullout failure since the concrete cover is greater than the minimal cover (Cairns and Plizzari, 2003). Figure 2-17 introduces the beam end test known as the “eccentric pullout” test where both the reinforcing bar and the surrounding concrete are placed in tension showing the actual stress state. This test is rarely used because of its need for adequate transversal reinforcement to avoid a premature shear failure instead of splitting. A Direct Pullout Test (DPT) presented in Figure 2-17 (c) has been used as an alternative test where the bar and the surrounding concrete are both placed in tension (Tastani and Pantazopoulou, 2002). The state of bond stress along the developed length was established based on the test results. Despite its advantages, the DPT is difficult to perform since it requires perfect alignment of the gripped ends of the specimen. Another alternative favored by laboratories is the standard “Four Point Bending Beam Test” such as the beam anchored specimen as shown in Figure 2-17 (d) (Top) and the spliced beam specimen presented in Figure 2-17 (d) (Bottom). They depict the actual situation occurring in flexural beam members, with the distribution of stresses along their cross-section. The beam anchored specimen is based on the choice of a bonded length along with the creation of one main flexural crack. This test setup, with the presence of the supports, was proven to increase the bond strength. The beam splice specimen is considered to be the most straightforward and reliable test to set up. It was commonly used to develop most design codes (Cairns and Plizzari, 2003).

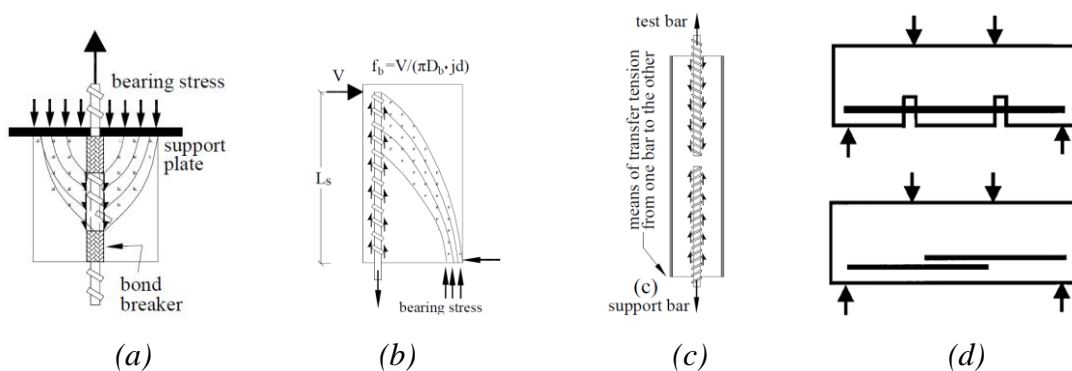


Figure 2-17 (a) Standard pullout specimen, (b) beam-end specimen, (c) DTP (Tastani and Pantazopoulou, 2002) and (d) beam anchorage specimen (Top) splice specimen (Bottom) (ACI Committee 408, 2003)

A recent modification of the anchored beam specimen was proposed where the bonded length is developed in the constant moment region. The setup enables the back-calculation of the developed force in the reinforcing bar through global equilibrium of the specimen, from which the bond along the embedment length is estimated. The author studied the bond behavior for a HPFRC, where the test specimens failed by pullout rather than splitting (Tastani *et al.*, 2016a).

2.2.3 Previous experimental and parametric research on UHP-SFRC

Bond strength depends on the concrete matrix properties (composition, workability and mechanical properties), the reinforcing bar geometry and property (diameter, rib geometry, tensile strength), the loading regime (loading regime and rate) and lastly the system parameters (concrete cover, confinement, the position of the reinforcing bars). Also, the constituents and mechanical properties of UHP-FRC have a positive impact on the bond strength between the reinforcing bars and the surrounding concrete contrary to that of conventional concrete. Since UHPC has only fine aggregates, the effect of aggregate interlock is reduced. In fact, it was denoted that the elimination of coarse aggregate could change the mode of failure from pullout to splitting for small concrete cover (Holschemacher *et al.*, 2004). However, the adhesive bond stress is more important for UHPC than it is for normal concrete due to the dense matrix that bounds tightly the steel and the surrounding concrete together. This innovative concrete is characterized by a ductile capacity after the first cracking in tension, enabling it to sustain greater hoop tensile stresses developed in the concrete cover surrounding the reinforcing bar. Thus, based on Equation (2.16), higher bond strength values are reached.

2.2.3.1 Modes of failure

According to a pullout test on 12 mm diameter reinforcing bars embedded in UHPC blocks with a volumetric fiber fraction of 1.5%, three modes of failure were observed in the concrete (Fehling *et al.*, 2012). Figure 2-18 illustrates the concrete cone type failure, the v-type splitting, and the splitting failure. It was as well reported that at the end of the bonded length, a transversal crack was developed.

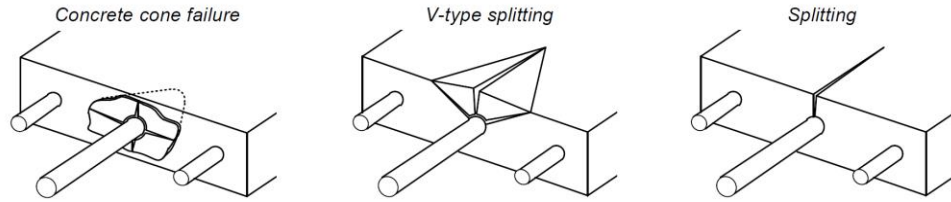


Figure 2-18 Concrete failure modes (Fehling *et al.*, 2012)

The study also included the analysis of concrete cover varying from $1d_b$ to $2.5d_b$ and the embedment length starting from $2d_b$ until $12d_b$ to define the failure modes (Fehling *et al.*, 2012). Consequently, a correlation between the different failure mode was developed and is presented in Figure 2-19. The researcher pointed out that the cone failure results in a brittle post-peak branch while the V-split and the splitting failure are more ductile (Fehling *et al.*, 2012).

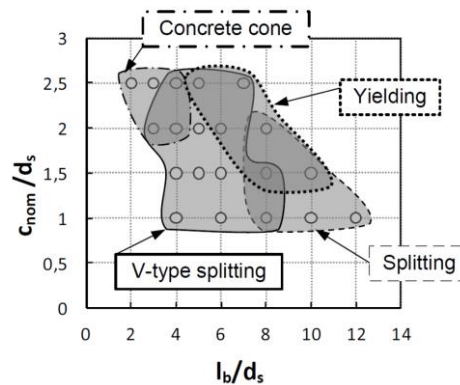


Figure 2-19 Relationship between different types of the failure mode (Fehling *et al.*, 2012)

The fourth mode of failure observed in this bond test is the yielding or the rupture of the reinforcing bar as can be seen in Figure 2-19 which occurs when large concrete covers and embedment lengths are applied.

2.2.3.2 Bond tests and results

One of the first bond tests on UHPC was performed in Germany by conducting a standard pullout-test on RILEM-specimens to study the behavior of conventional reinforcing bars (diameter 10 mm) for an embedment length of 1.5 times the bar diameter (15 mm) and a concrete cover of 4.5 cm. Different loading rates, ranging between 0.001 mm/s and 0.1 mm/s were applied for several UHPC

mixes at different age days. Firstly, the bond strength and stiffness increased with time, where the bond strength reached 60-70 MPa at 56 days. The increase of strength with time was particularly noticed when fly ash is added rather than silica fume. Moreover, low loading rates result in a steeper ascending bond-stress slip curve and a flatter post-peak descending branch. However, the loading rate and the bond stress-slip increase proportionally (Holschemacher *et al.*, 2004). In 2012, a continuity of the pullout test was conducted on the same specimens while varying the concrete cover between 4.5 and 2 cm. It was noticed that the bond-stress relationship was similar for both concrete covers for the pre-peak while it presented a steeper reduction in the post-peak for the smaller concrete cover. The peak bond stress was slightly higher for a concrete cover of 4.5 cm equal to 65 MPa compared to 58 MPa for a concrete cover of 2 cm (Weisse and Holschemacher, 2012).

The same pullout test was conducted on 14 mm and 20 mm reinforcing bars embedded in UHPC for two volumetric fractions of steel fibers ($V_f = 1\%$ and 2%) with the same bonded length of $1.5d_b$ and a concrete cover of $4.5d_b$. It is noted as well that the maximum aggregate size is about 5mm. All the specimens failed by pullout except the one with a 20 mm rebar and 1% of steel fibers. However, the latter reached the highest bond strength values of 86 MPa in comparison to 77 MPa for higher fiber content of 2% or 67 MPa for a smaller bar diameter of 14 mm as can be seen in Table 2-3. For a 14 mm reinforcing bar, the increase of the embedment length from $1.5d_b$ to $2d_b$ for the same volumetric fiber content $V_f = 1\%$ did not affect the matrix bond strength of 67 MPa (Schoening and Hegger, 2012).

Table 2-3 Bond strength values for the pullout PO specimens for different d_b and V_f (Schoening and Hegger, 2012)

Test		PO1	PO2	PO3	PO4	PO5	PO6
\emptyset	[mm]	20	14	20	14	20	14
steel fibre content	[% p.v.]	1	1	2	1	-	-
l_b	[mm]	30	21	30	28	30	21
$f_{cm,cube150}$	[MPa]	184	179	186	177	136	142
f_{cm}	[MPa]	163	139	141	123	116	116
$f_{fctm,fl}$	[MPa]	10	10	18	9	9*	9*
τ	[MPa]	86	67	77	67	64	53
$\tau/f_{cm,cube}$	[-]	0.47	0.37	0.41	0.38	0.47	0.38
τ/f_{cm}	[-]	0.53	0.48	0.55	0.54	0.55	0.46

Another standard pullout test was conducted on a block of 200 mm of UHPC (compressive strength of 154 MPa) for 12, 16 and 20 mm reinforcing bars embedded along a standard embedment length of

$5d_b$ where all the steel bars ruptured. Thus, smaller embedment lengths were proposed of 2, 3 and $4d_b$ for the 16 mm rebar. For a bonded length of $3d_b$, the bond stress was around 55 MPa where the specimen failed somewhat in bond and steel rupture (Vitek *et al.*, 2013).

To summarize, the standard pullout test was giving unrealistic high bond strength values where the minimum required embedment length to measure bond stress was $1.5d_b$ instead of the standard value $5d_b$ to prevent the rupture of the reinforcing bar. Moreover, based on the results of this type of test it was noticed that the bond strength depends on the bar diameter. However, it is slightly influenced by the concrete cover. Moreover, as mentioned previously and based on several experiments, the standard pullout test was not able to predict the effect of fibers and the contribution of the concrete properties on bond strength (Harajli *et al.*, 2002).

A direct tension lap-splice test was conducted on 25 mm and 35 mm reinforcing bars in UHP-FRC for a volumetric fiber fraction ($l_f = 10$ mm, $\phi_f = 0.2$ mm) of 1-2% (splice lengths of 5, 10 and $18d_b$) and 4% (splice lengths of 5, 8, 10, 12 and $18d_b$) while maintaining a concrete cover of $1.2d_b$ (30 mm). Most of the specimens failed by splitting failure while a few failed by yielding of the reinforcing bars when the embedment length reached $12d_b$ (for $d_b = 25$ mm) and $18d_b$ (for $d_b = 35$ mm). The splitting mode of failure presents no crushed concrete in between the ribs while the yielding of the reinforcing bar could be followed with splitting cracks or only presents a pure strain-hardening behavior of the steel. It can be seen that the average bond strength for all the different lap-splices and bar diameter values was about 10-11 MPa for $V_f = 4\%$, 8 MPa for $V_f = 2\%$ and 6 MPa for $V_f = 1\%$. However, longer embedment lengths such as $18d_b$ lead to the reduction of the bond strength (Lagier *et al.*, 2015). For a splice length of $8d_b$, the bond stress was considered locally uniform after the strains and stresses were measured along the splice length. Moreover, the increase of the steel fiber content from 1% to 4% for the embedment lengths 5, 8 and $10d_b$ regarding a 25 mm reinforcing bar, leads to the increase of the bond strength by 47% where the bar stress reached 400 MPa as can be seen in the measured bond-stress slip relationship presented in Figure 2-20 (Lagier *et al.*, 2016).

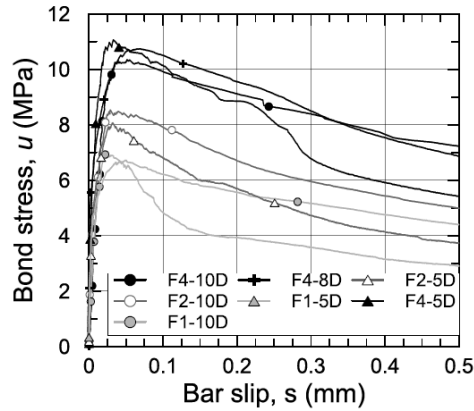


Figure 2-20 Bond-stress slip response (Lagier et al., 2016)

Figure 2-21 presents the pullout splice length test setup conducted on #5 reinforcing bar ($d_b = 15.875$ mm) embedded in two types of UHP-FRC with 2% of short steel fibers. Different splice lengths ($4d_b$, $6d_b$, $8d_b$, and $10d_b$) were considered with a clear cover $c_{so} = 2d_b$ and a clear bar spacing of $4d_b$ concerning a concrete with $f'_c = 97.4$ MPa. It was shown that the bar stress is linearly proportional to the increase of the spliced length. For this test setup, the bar yielded for an embedment length of $6d_b$. Moreover, different concrete clear covers c_{so} were chosen for a Grade 120 bar and an embedment length $l_d = 6d_b$ for two different concrete strengths ($f'_c = 134$ MPa and $f'_c = 93$ MPa). The bar stress increases when concrete cover values were higher. This increase was observed for UHP-FRC with higher compressive strength. For the UHP-FRC with $f'_c = 93$ MPa, the bar stress augmented from 600 MPa to 650 MPa when the side cover went from $2d_b$ to $3.5d_b$. However, in the case of the concrete with $f'_c = 134$ MPa, the bond stress didn't experience any change for a side cover of $2d_b$ while it reached 800 MPa for a $c_{so} = 3.5d_b$ (Yuan and Graybeal, 2014).

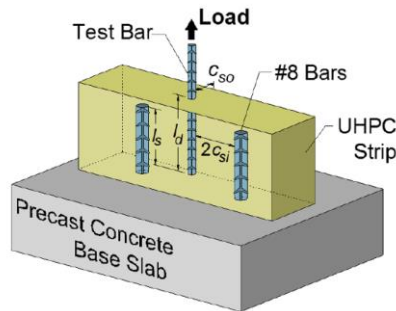


Figure 2-21 Direct pullout test setup to measure bond and concrete splitting

Moreover, the splitting crack pattern depends on the concrete side cover c_{so} and the bar spacing c_{si} . The concrete splitting can occur in the free space cover as shown in Figure 2-22 (a) or in the concrete between the reinforcing bars as depicted in Figure 2-22 (b). Moreover, it was stated that when the adjacent reinforcing bars are located far from the auxiliary bar, they no longer interfere in the bond strength that becomes dependent of the concrete's properties only (Yuan and Graybeal, 2014).

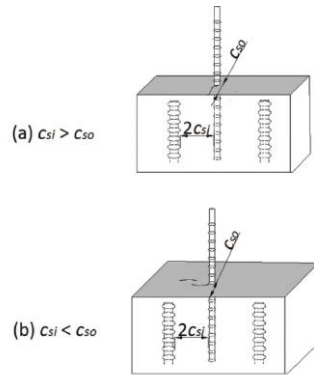


Figure 2-22 (a)in free space cover (b)between reinforcement (Yuan and Graybeal, 2014)

The modified pullout tests were conducted on UHPC with conventional reinforcing bars (13, 16 and 19 mm) for three different embedment lengths ranging between $4d_b$ and $8d_b$. Tests showed that the bond stress drops when the embedment length increases. It was noted that the bar with the smallest diameter of 13 mm surpassed yielding to reach rupture for all the embedment lengths. However, the specimen with the 16 mm reinforcing bar failed by splitting and developed bond stress about 16.7 MPa with a bonded length of $4.8d_b$ and 2% V_f . The specimen with a 19 mm reinforcing bar faced a conical mode of failure (Alkaysi and El-tawil, 2016).

Thus, a new direct splice pullout test was conducted on #4(M13) with A615 grade 60 and #7(M22) with A615 grade 80 bars embedded in UHPC for different spliced lengths ($6d_b$ to $10d_b$) and concrete side covers ($1d_b$ to $3.5d_b$). Most of the specimens failed by splitting mode of failure except for the specimens with a high concrete cover of $3.5d_b$ and a short embedment length of $6d_b$ that experienced a cone failure. It was evident that the reinforcing bar could yield in two cases: when the splice length is $8d_b$ with a high concrete cover of $3d_b$ or when the embedment length is $10d_b$ with a small concrete cover of $1.8d_b$. Moreover, the bar stress increases with the development length; a specimen with a concrete cover of $2d_b$ developed bar stress of 280 MPa for a splice length of $6d_b$ in comparison to 480 MPa for an embedment length of $10d_b$. In addition, a slight increase in bond stress with the increase

of concrete cover is observed. For an embedment length of $6d_b$, the bar stress developed at bond failure remained at 280 MPa for a concrete cover of $1.6d_b$ and $2d_b$. Thus, a slight increase of the bond strength from $1.6d_b$ (11 MPa) until $2d_b$ (12MPa) was noticed (Ronanki *et al.*, 2016).

Haber conducted the same experiment as described in Figure 2-21 for different types of commercial UHPC with a standard reinforcing bar (#5 (M16) & Gr.120) and embedment lengths varying between $8d_b$ to $10d_b$. The mode of failure was investigated depending on the steel fiber volume fraction; where it started with a large splitting crack for a $V_f = 2.5\%$, then multiple small splitting cracks for $V_f = 3.5\%$ and lastly a cone mode of failure for a $V_f = 4.5\%$ (Haber *et al.*, 2018).

Along with the direct splice length test, several beam tests were conducted to study the bond strength and modes of failure in comparison to the other tests. A third-point load test was performed on slabs presenting a lap-splice of 10 M reinforcing bars in the constant moment region with the variation of the splice length between 18 mm ($1.8d_b$) in the presence of shear reinforcement and 26 mm ($2.6d_b$) without. It is noteworthy that the concrete matrix contained 2/5 mm coarse aggregates and the concrete cover was 2 cm. It was shown that slabs with a considerable splice length of 26 mm and transverse reinforcement lead to yielding of the longitudinal bars accompanied with concrete cracking in the tensile zone. However, failure occurred due to crushing of the concrete in the compression zone with a mid-deflection reaching 23 mm. Nevertheless, the shorter lap-splice of 18 mm lacking shear reinforcement failed by the bond splitting along the lap-splice with a deflection of 18 mm (Weisse and Holschemacher, 2012).

Another beam test was conducted with splice length of about $6d_b$ under four-point bending of #6(M19) and #7(M22) A615 grade 80 bars for a concrete clear cover of 1 in and 1.5 in. Nonetheless, the beams failed by shear prior to bond failure due to the specimen detailing (Ronanki *et al.*, 2016).

Lastly, four-point bending beam tests were conducted on retrofitted beams ($V_f = 3\%$) with 25 mm and 35 mm reinforcing bar diameters that are lap-spliced along a $6d_b$, $12d_b$ and $18d_b$ lengths in the constant moment region. The beams were filled with UHPC in a small portion of the section in tension. It was shown that the splice length of $6d_b$ with a repair depth of $1d_b$ lead to the splitting mode of failure. However, it was reported that this material could delay or eliminate this splitting mode of failure for

splice lengths greater than $12d_b$. In this case, for a splice length of $12d_b$ and $18d_b$ all the reinforcing bars yielded and in some cases could not reach rupture. Figure 2-23 exhibits the response curve of the beams presenting a ductile behavior reaching a maximum applied load of 200 kN for a minimum repaired depth of $1d_b$ (Dagenais and Massicotte, 2012).

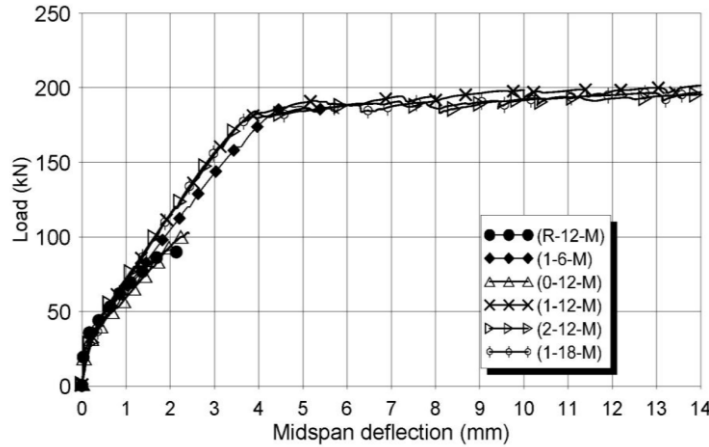


Figure 2-23 Load-deflection response curve for the beams (Dagenais and Massicotte, 2012)

As a summary of all the experiments discussed previously, three types of tests were conducted on UHP-SFRC: standard pullout, direct splice pullout, and beam splice test. For the standard pullout test, the bond strength was extremely high reaching 60 MPa as mentioned previously where the embedment length needed to be reduced to $1.5d_b$ in order to prevent the rupture of the reinforcing bars. As for the direct splice test, the bond strength was around 10-11 MPa. Moreover, both tests proved that the use of UHPC effectively reduces the splice length required to yield the reinforcing bar: in standard pullout tests the splice length could go as far down as $2.5d_b$, whereas for direct pullout tests it was around $6d_b$. This allows a tremendous enhancement for future design codes since it enables the entire development of the reinforcing bar strength. To the author's knowledge, there is no beam anchored bond test performed on UHP-FRC to study the bond strength. In this regard, the author conducted this test set-up to study the outcomes of this type of bond test and enrich the bond test database for UHP-SFRC.

Chapter 3. Plan of the Experimental Program

The experimental program is mainly divided into three parts. The first part provides a full description of the experimental bond test setup. The second part concerns the development of two in-house design mixtures to obtain the most suitable and optimized one. The third part presents all the necessary testing to determine the mechanical properties of the materials under study.

3.1 Choice of the experimental setup and type of specimen to be tested

3.1.1 Bond test type

The experiment setup was chosen based on a former successful anchored beam specimen (Tastani *et al.*, 2016). Figure 3-1 presents the directly supported beam subjected to two equal loads ($P/2$) placed symmetrically at the mid-span at a constant distance (b) creating a central region of constant moment. The shear span is equal to (a) having a linear moment diagram (constant shear).

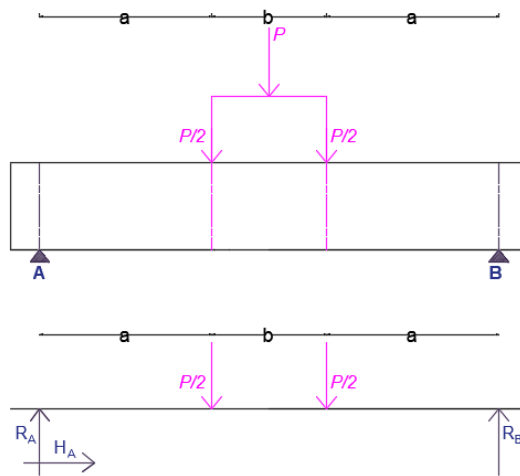


Figure 3-1: Free body diagram of specimen under four-point loading

Based on the equilibrium of the external forces, the support reactions are obtained in Equation (3.1). From equilibrium of the free body diagrams presented in Figure 3-2 to Figure 3-4, Equation (3.2) until Equation (3.7) are used to determine the moment and shear forces:

$$R_A = R_B = P/2 \quad (3.1)$$

$$\underline{0 < x < a}$$

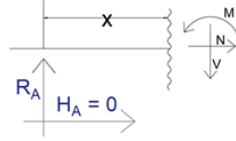


Figure 3-2 Free-body diagram for $0 < x < a$

$$M(x) = \frac{P}{2} x = \begin{cases} M(x=0) = 0 \\ M(x=a) = \frac{Pa}{2} \end{cases} \quad (3.2)$$

$$V(x) = \frac{P}{2} \quad (3.3)$$

$$\underline{a < x < a + b}$$

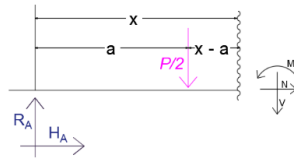


Figure 3-3 Free-body diagram for $a < x < a + b$

$$M(x) = \frac{Pa}{2} \quad (3.4)$$

$$V(x) = 0 \quad (3.5)$$

$$\underline{a + b < x < 2a + b}$$

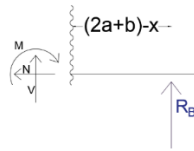


Figure 3-4 Free-body diagram for $a + b < x < 2a + b$

$$M(x) = \frac{P}{2} [(2a + b) - x] = \begin{cases} M(x = a + b) = \frac{Pa}{2} \\ M(x = 2a + b) = 0 \end{cases} \quad (3.6)$$

$$V(x) = \frac{-P}{2} \quad (3.7)$$

Thus, the moment and shear diagram of the test setup are presented in Figure 3-5.

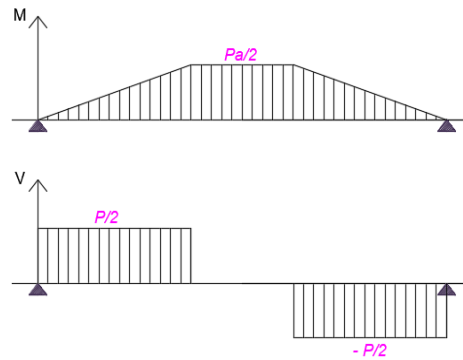


Figure 3-5: Moment and shear diagram of the test setup

3.1.2 Parametric evaluation

In the present study, the effect of three important parameters on bond of UHPC will be investigated: the design mixture, the concrete cover and the embedment length. The last two parameters are scaled to the bar diameter. Three different UHP-SFRC mixes (two commercial and one in-house) with different fresh and hard properties were selected to study a broader range of UHP-SFRC and point out the effect of the workability and the tensile strength on the bond strength since each design mixture is characterized by their proper mechanical properties. The bond strength is determined for a reinforcing bar embedded along a short length of $5d_b$ where the bond stress is assumed uniform for two different concrete covers of $1d_b$ and $2d_b$. The ratio of concrete cover c_c to bar diameter d_b studies the effect of confinement on the bond strength. For the specimen series cast using the in-house design mixture and considering a concrete cover of $2d_b$, a total of 3 different embedment lengths l_b were tested 5, 10 and $15d_b$. This parameter studies the variation of the bar stress and the bond strength for increasing the bonded length

3.1.3 Specimen detailing

Three steel beam formworks, 36 in. (914 mm) long, were available in the laboratory presenting a cross-section ($a \times b = 6 \text{ in} \times 6 \text{ in} = 152 \text{ mm} \times 152 \text{ mm}$) as can be seen in Figure 3-6 (a). In addition, wooden formwork beams were fabricated with the same dimensions since the following experiment

will cover a broad range of parameters that requires in some cases additional formwork as shown in Figure 3-6 (b). The fabrication procedure is described in Section 4.1.



Figure 3-6 (a) Steel and (b) wood formwork

The constant moment present in between the applied loads as depicted in Figure 3-5 generates pure tensile stresses at the bottom of the section. Thus, no shear reinforcement is needed in this section since there is no shear force. The embedment length will be developed in this region to study the contribution of the tensile properties of the concrete to resist the tensile hoop stresses as a confinement methodology. The desired embedment length was attained by covering the reinforcing bar with PVC pipe (polyvinyl chloride) ensuring that it remains in the constant moment region. (Tastani *et al.*, 2016) placed a notch before the studied embedment length to be able to back calculate through global equilibrium of the specimen, the bar forces that are developed through bond over the studied bonded length. This was achieved in the current setup by inserting a foam board to isolate the bar from the surrounding concrete.

The longitudinal steel reinforcement under study was chosen as 15M rebar since it is the most commonly used in the industry nowadays with a nominal bar diameter d_b equal to 16 mm. The design strength of these reinforcing bars as considered in North America are 400 MPa and 600 MPa for the nominal yield strength and ultimate strength, respectively. Additional tests were conducted to verify these main properties.

Figure 3-7 presents the beam setup for one case as an example. It is mainly based on the parameters of the study and the factors that will be measured experimentally such as the slip of the reinforcing bar.

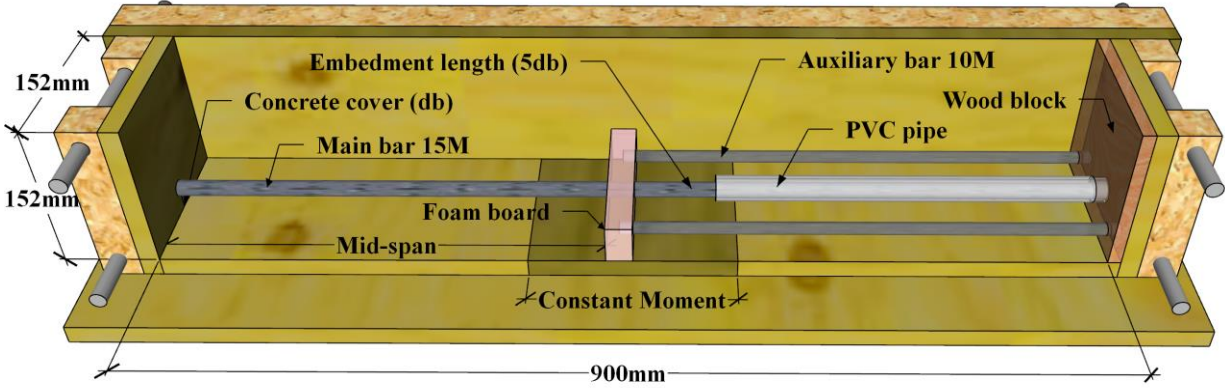


Figure 3-7 Specimen detailing for an embedment length of $5d_b$

3.1.4 Design verification of the beams

3.1.4.1 Concrete cover

Depending on the bar diameter and the adequate pouring control realized in the laboratory, the minimum concrete clear cover c_c known as the distance between the external surface of the steel bar to the closest concrete surface was calculated from Equation (3.8) (European Union, 2004) :

$$c_{nom} = c_{min} + \Delta c_{dev} = 16mm \quad (3.8)$$

$\Delta c_{dev} = 0$ since there is control in the laboratory.

$$c_{min} = \max(c_{min,b}; c_{min,dur}) = \max(16mm; 10mm) = 16mm$$

$$c_{min,b} = \max \phi = 16 mm$$

$c_{min,dur} = c_{min,dur} - 1 = 10 mm$; the resistance of the concrete is $\geq C40/50$ with a class (S4).

This experiment mainly considered the effect of the bottom concrete cover c_b on the bond strength. Two concrete covers will be followed: $c_b = d_b = 16mm$ and $c_b = 2d_b = 32 mm$. The side concrete cover for the auxiliary bars is considered $c_s = 16 mm$.

3.1.4.2 Shear span to effective depth ratio

The length of the beam is chosen about 16 mm shorter than the length of the formwork to create an extension of the primary reinforcing bar for slip measurement. This was achieved by placing a 12.7 mm thick wooden block with the same cross-sectional dimension as the beam in the considered void. As can be seen in Figure 3-8, the length of the formwork would be 36 inches (914.4 mm) including the length of the beam (900 mm) and the wood thickness 12.7 mm. For an embedment length of $5d_b$ (80 mm) and $10d_b$ (160 mm), the distance between the applied loads is taken to be equal to 200mm. Moreover, a flexural shear span requires a shear span to effective depth ratio around 2. Therefore, the shear span should have a minimum value of 300 mm for a beam cross-section of (150 x 150 mm). Also, the extended part of the beam could vary up to 50 mm outside the supports.

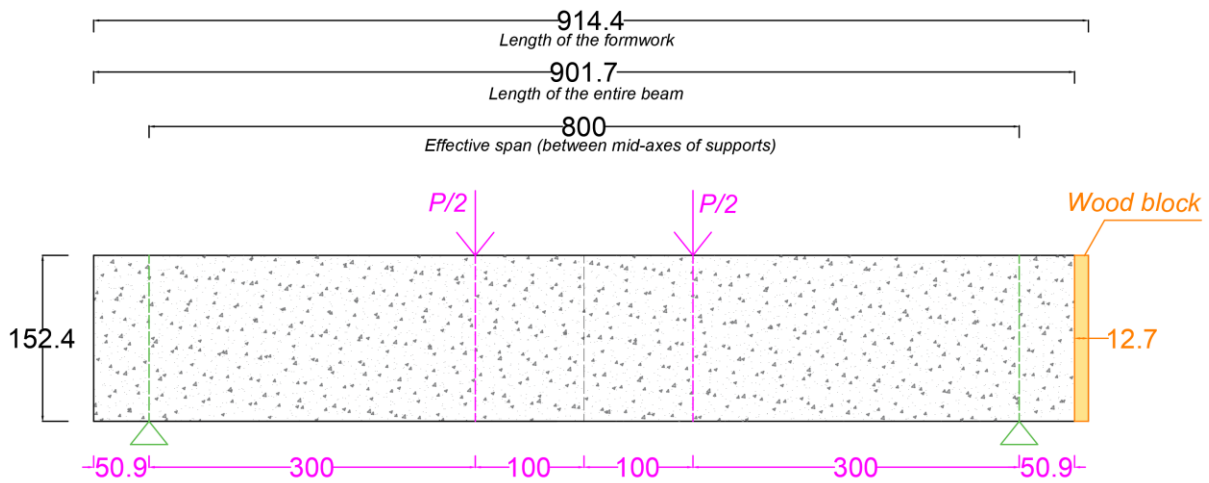


Figure 3-8 Detailing of the formwork and beam length for embedment lengths 5 and $10d_b$

However, the most extended embedment length reaches $15d_b = 240$ mm meaning the inquiry of a constant moment around 260 mm as can be seen in Figure 3-9. Verification of the shear resistance from the shear force applied was followed to eliminate premature shear failure prior to bond failure.

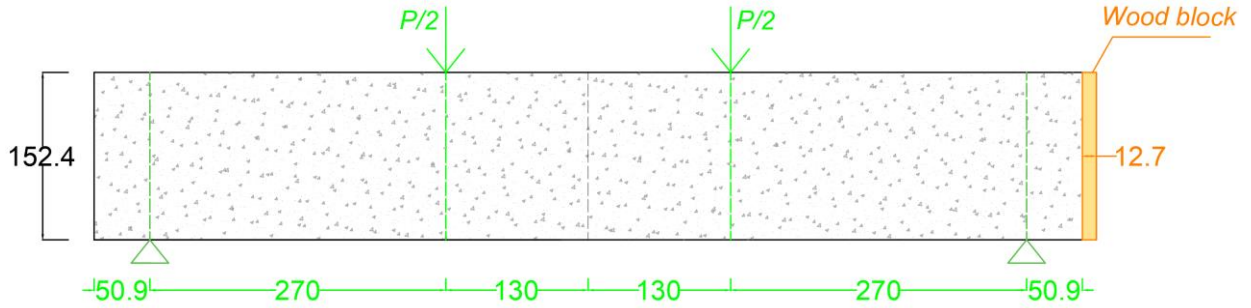


Figure 3-9 Detailing of the formwork and beam length for embedment lengths $15d_b$

3.1.4.3 Selection of longitudinal steel reinforcement ratio

A pertinent calculation as shown below which was followed in order to choose the adequate amount of longitudinal reinforcement in the studied region, thereby preventing any other modes of failures such as shear or flexural failure. Due to the novelty of this concrete, the estimated load was obtained from proposing the flexural stress of 25 MPa, obtained from four-point bending test trials on prisms to be equal to the tensile strength of the concrete and bond strength. Considering these values, the highest embedment length $l_b = 15 \times d_b$ considered can cause the yielding of the bar. With a conservative assumption of a uniform distribution of the bond equal to strength, the moment developed from the loading is defined in Equation (3.9):

$$M = T_s \times 0.9 \times d \quad (3.9)$$

Equation (3.10) calculates the effective depth for the case of the smallest concrete cover to assume the highest load:

$$d = h - (c_c + \frac{d_b}{2}) = 150 - (16 + \frac{16}{2}) = 126 \text{ mm} \quad (3.10)$$

The developed moment is calculated based on the bar force required to reach its yield capacity:

$$T_s = f_y \times A_s = 400 \times 200 = 80 \text{ kN}$$

$$M = 80000 \times 0.9 \times 126 = 9.072 \text{ kN.m}$$

From the internal moment calculated previously, the load obtained is equal to:

$$P = \frac{2xM}{a} = \frac{18}{0.3} = 60 \text{ kN}$$

The bending moment resistance factor K_r defined in Equation (3.11) is calculated:

$$K_r = \frac{M_r \times 10^6}{b_o \times d^2} = \frac{9 \times 10^6}{150 \times 126^2} = 3.78 \text{ MPa} \quad (3.11)$$

Afterward, the reinforcement ratio $\rho = 1.2\%$. Therefore, the required tension reinforcement:

$$A_s = \rho \times b_o \times d = 0.012 \times 150 \times 126 = 226.8 \text{ mm}^2$$

One 15M reinforcing bar in the tension region is not enough to prevent failure in flexure. Therefore, two auxiliary bars 10M were placed on both sides of the main bar, where the embedment length is studied, to prevent any premature failure of the specimens other than bond failure which was the study objective (Tastani *et al.*, 2016). However, for the embedment lengths $l_b = 10$ and $15d_b$, an additional criterion is taken into consideration. As longer embedment lengths are considered on the right of the notch, the development length of the part of the reinforcing bar present to the left of the notch is reduced. Thus, to prevent the slippage of the reinforcing bar along the left side, a T-head was attached to the reinforcing bar. Based on the CSA (CSA (Canadian Standards Association), 2014), it is stated that the reinforcing bar can reach its yield strength when the T-head has an area equal to 10 times the bar's cross-section noting that the compressive strength of the concrete is greater than 25 MPa and the yield strength of the 15M is less than 500 MPa — assuming a square T-head section where each side is equal to c . Based on Equation (3.12), a T-head with a cross-section of (50 mm x 50 mm) as shown in Table 3-3 (section A') is required to prevent the slippage of the reinforcing bar:

$$A_{T-head} = c^2 \geq 10 \times A_s = 10 \times \frac{(\pi d^2)}{4} = 2000 \text{ mm}^2 \quad (3.12)$$

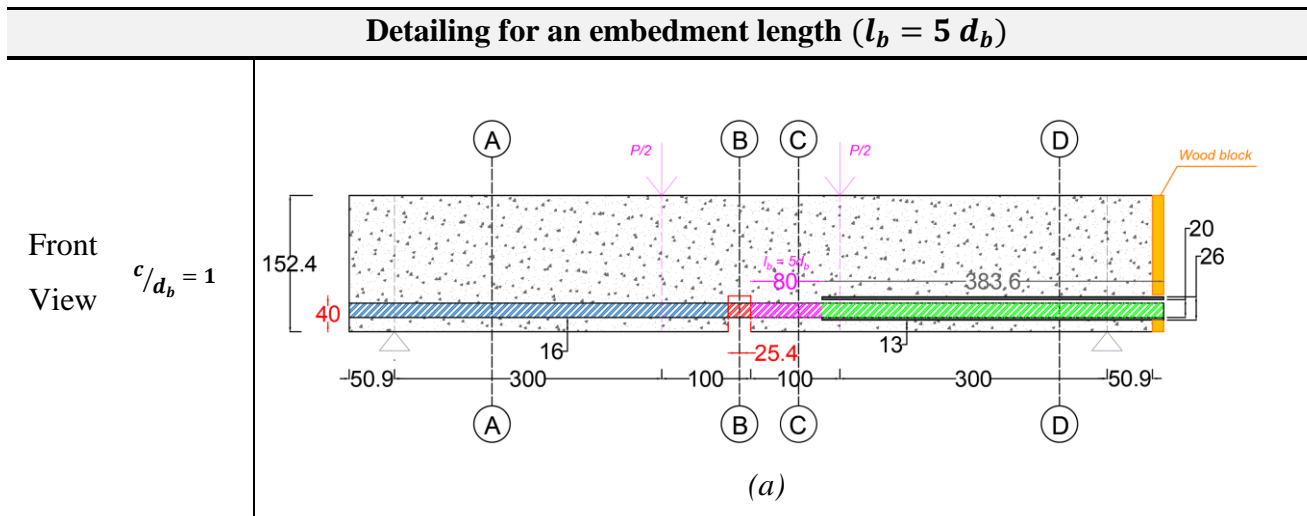
3.1.4.4 Design detailing

The detailing of all the beam specimens is described below divided in different section along its length. The cross-section of each section will be presented in detail in Section 3.1.4.4.3.

3.1.4.4.1 Embedment length of $l_b = 5d_b$

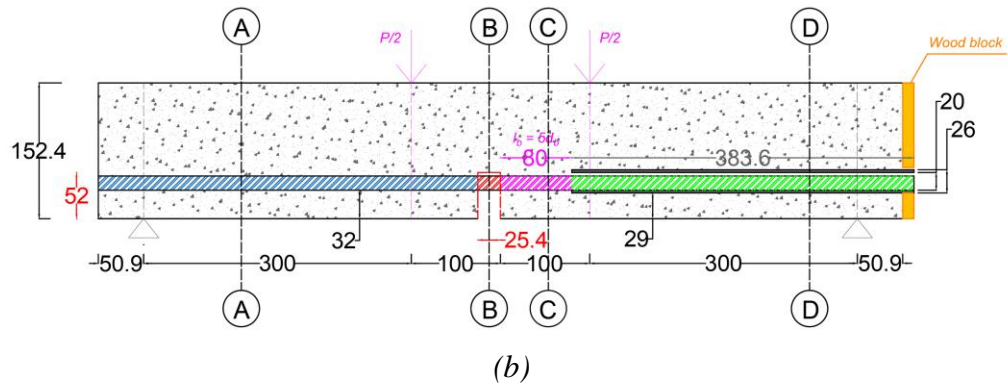
As can be seen in Table 3-1 (a) and (b), the main reinforcing bar is about 916 mm and goes through both the foam board and the wooden block. Moreover, to realize the embedment length of 80 mm in between the 200 mm constant moment region, the notch was placed to the left of the mid-span while a PVC pipe of 383.6 mm length was placed on the right side passing through the wooden block as well. Table 3-1 (c) presents the top view of the test setup pointing out the length of the auxiliary bars (476.3 mm) and their location according to the main rebar preserving a side cover c_s of 16mm. The auxiliary bars are supported by the notch and the wood block as well. In addition, Table 3-1, cases (a) and (b) differ mainly in the concrete cover to be developed which mainly affects the height of the notch, the height of the holes in the notch and the height of the holes in the wood block that will be discussed in the next paragraph. The designation of each color are presented in Table 3-3 based on each section (A), (B), (C) and (D).

Table 3-1 Detailing of the beam for the test setup with an embedment length equal to 5 times the bar diameter for two different concrete covers

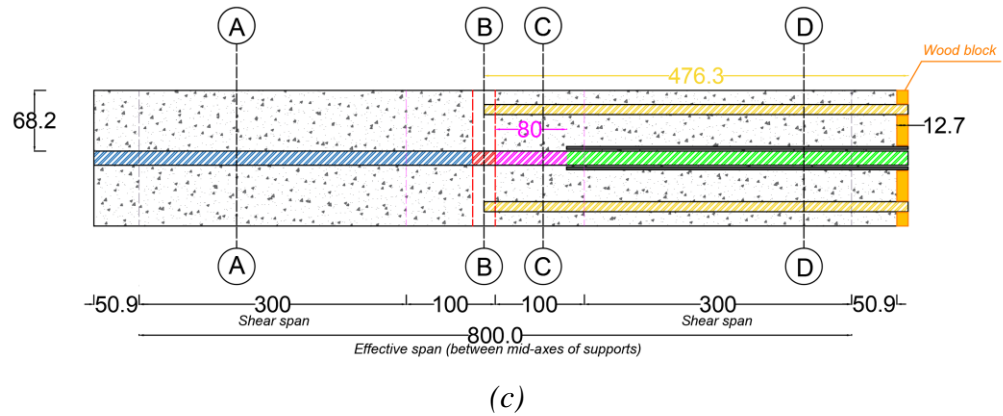


Detailing for an embedment length ($l_b = 5 d_b$)

Front View
 $c/d_b = 2$



Top View
 $c/d_b = 1 = 2$

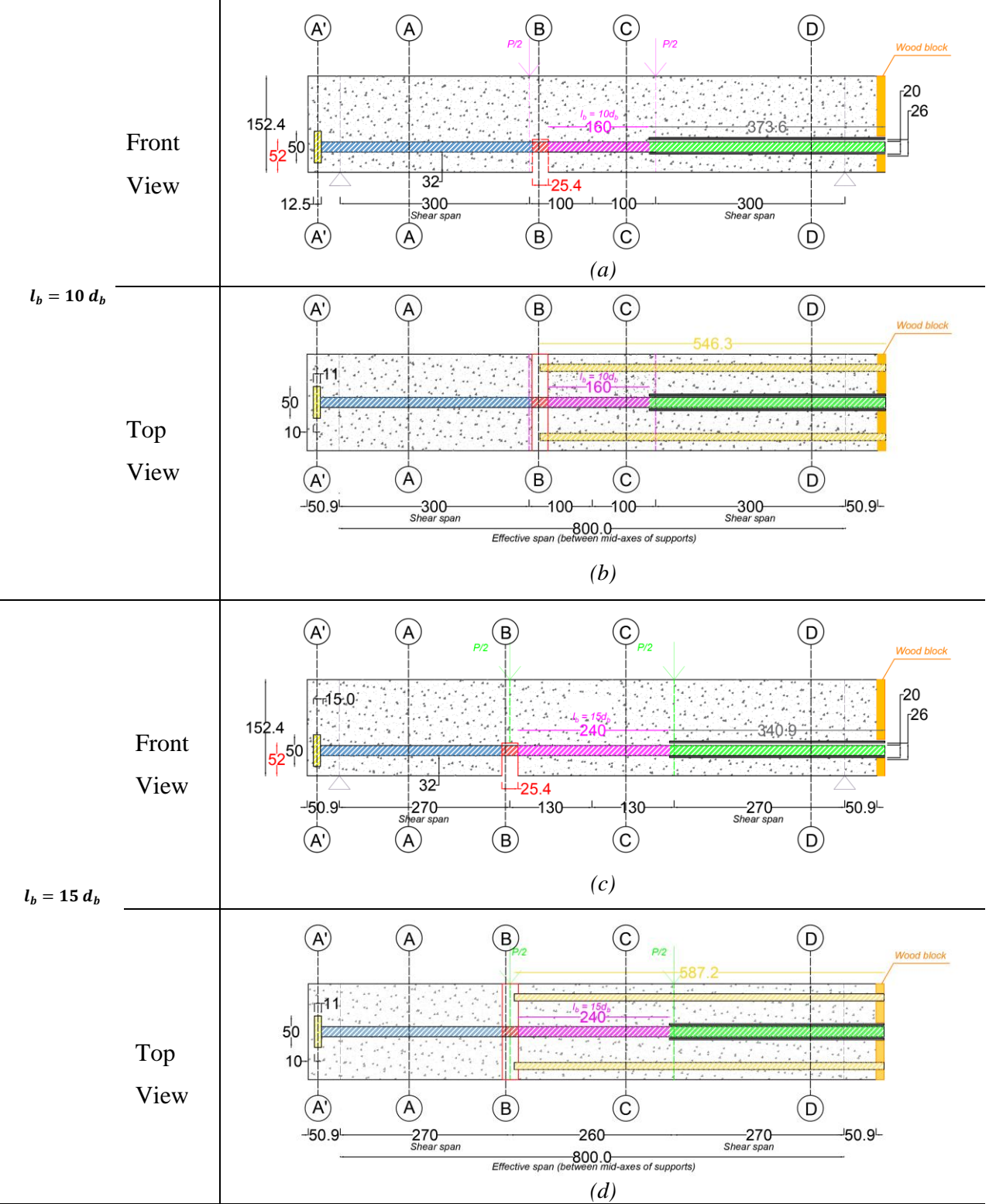


3.1.4.4.2 Embedment length of $l_b = 10d_b$ and $l_b = 15d_b$

The ratio of concrete cover c_c to bar diameter d_b equal to two is only considered for an embedment length equal to 10 and $15d_b$. For an embedment length of $10d_b$, 160 mm of the reinforcing bar should be in the constant moment region as seen Table 3-2 (a). Thus, the PVC pipe is chosen to be equal to 373.6 mm and the foam board is moved 70 mm from its original location presented in Table 3-1 (b). From Table 3-2 (b) the auxiliary bars are equal to 546.3 mm. The same is followed for the case of $15d_b$ to ensure a bonded length of 240 mm where the detailing is presented in Table 3-2 (c) and (d). The designation of each color are presented in Table 3-3 based on each section (A'), (A), (B), (C) and (D).

Table 3-2 Detailing of the beam for the test setup with an embedment length equal to 10 and 15 times the bar diameter for two different concrete covers

Detailing for an embedment length of $l_b = 10 d_b = 15 d_b$ for $c/d_b = 2$

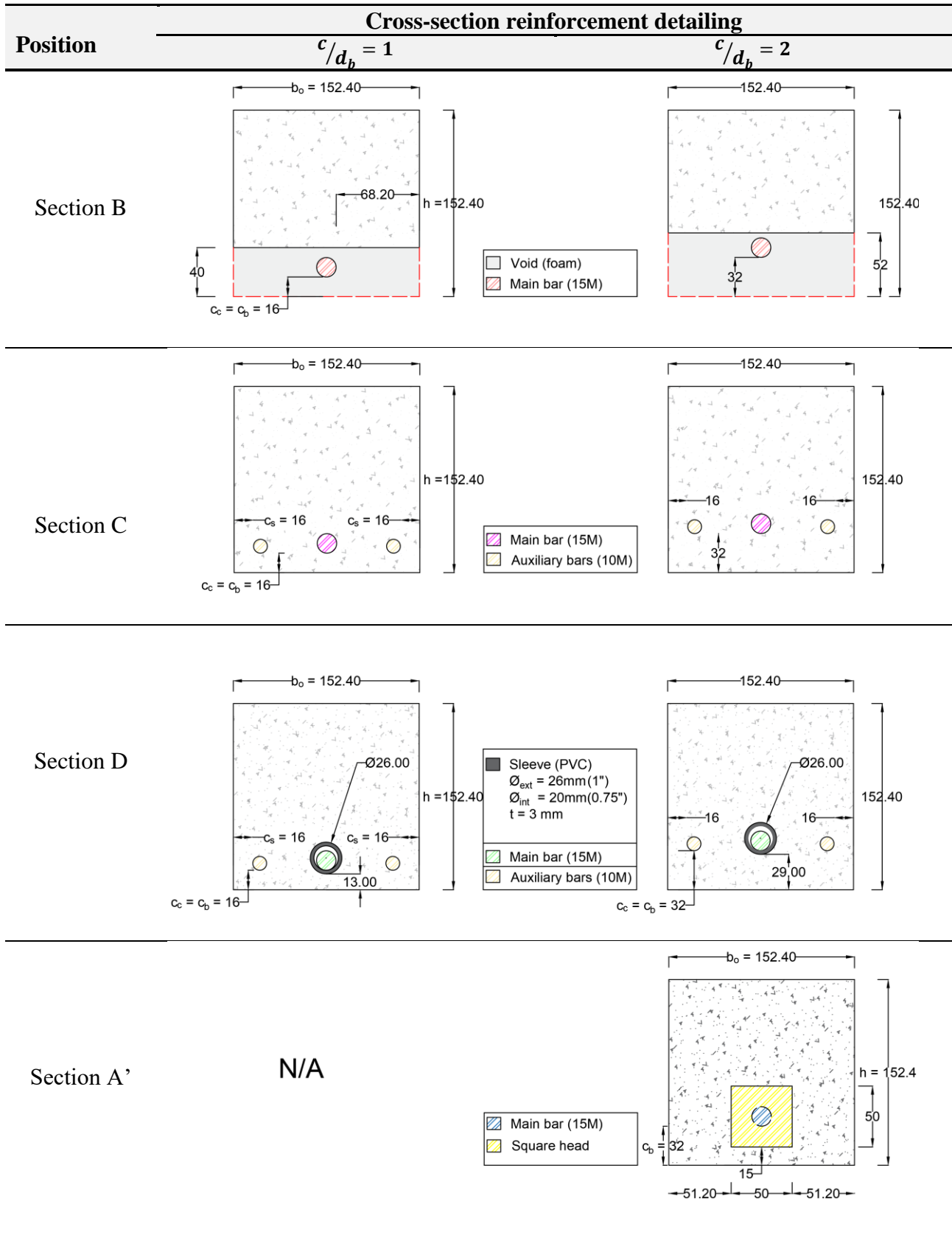


3.1.4.4.3 Cross-section detailing along the length of the beam

All the beams present similar cross-sections, but they differ in the longitudinal portion of each cross-section along their length. These cross-sections are marked in the drawings of Table 3-1 and Table 3-2. Firstly, the cross-section of the beam under study is presented in Table 3-3 Section C. The latter illustrates the reinforcement detailing of the principal and auxiliary bars for the two different concrete covers evaluated. Table 3-3 Section D presents the cross-section of the beam where the main bar is covered with the pipe while the two auxiliary bars are still considered bonded. Section B in Table 3-3 presents the cross-section of the beam at the notch where the only element resisting the moment is the 15M bar. Fourthly, since the cross-section presented in Section C Table 3-1 is the critical cross-section where failure will first occur, then the part of the beam on the left of the notch is irrelevant to the research. Since the required development length is achieved for the left part of the reinforcing bar, the auxiliary bars were not added along this section, and the main bar is embedded entirely along the length as can be seen in Section A Table 3-3. Section A' in Table 3-3 presents to T-head detailing for the embedment length of $10d_b$ and $15d_b$.

Table 3-3 Detailing of the cross-section of the beam in the specific locations (in mm)

Position	Cross-section reinforcement detailing	
	$c/d_b = 1$	$c/d_b = 2$
Section A		

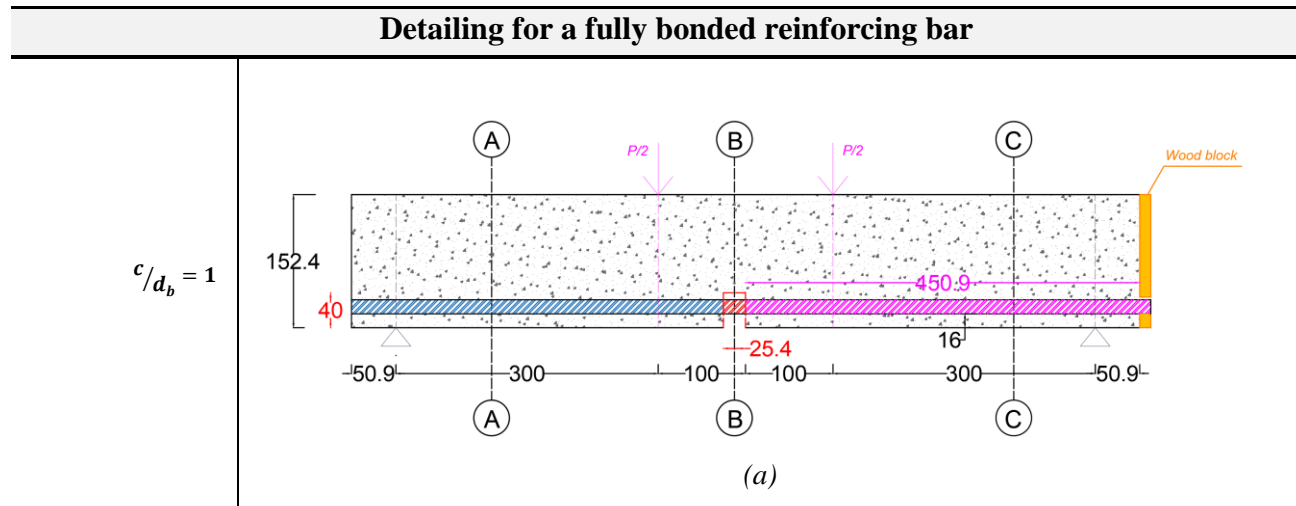


3.1.4.4.4 Additional specimens for testing

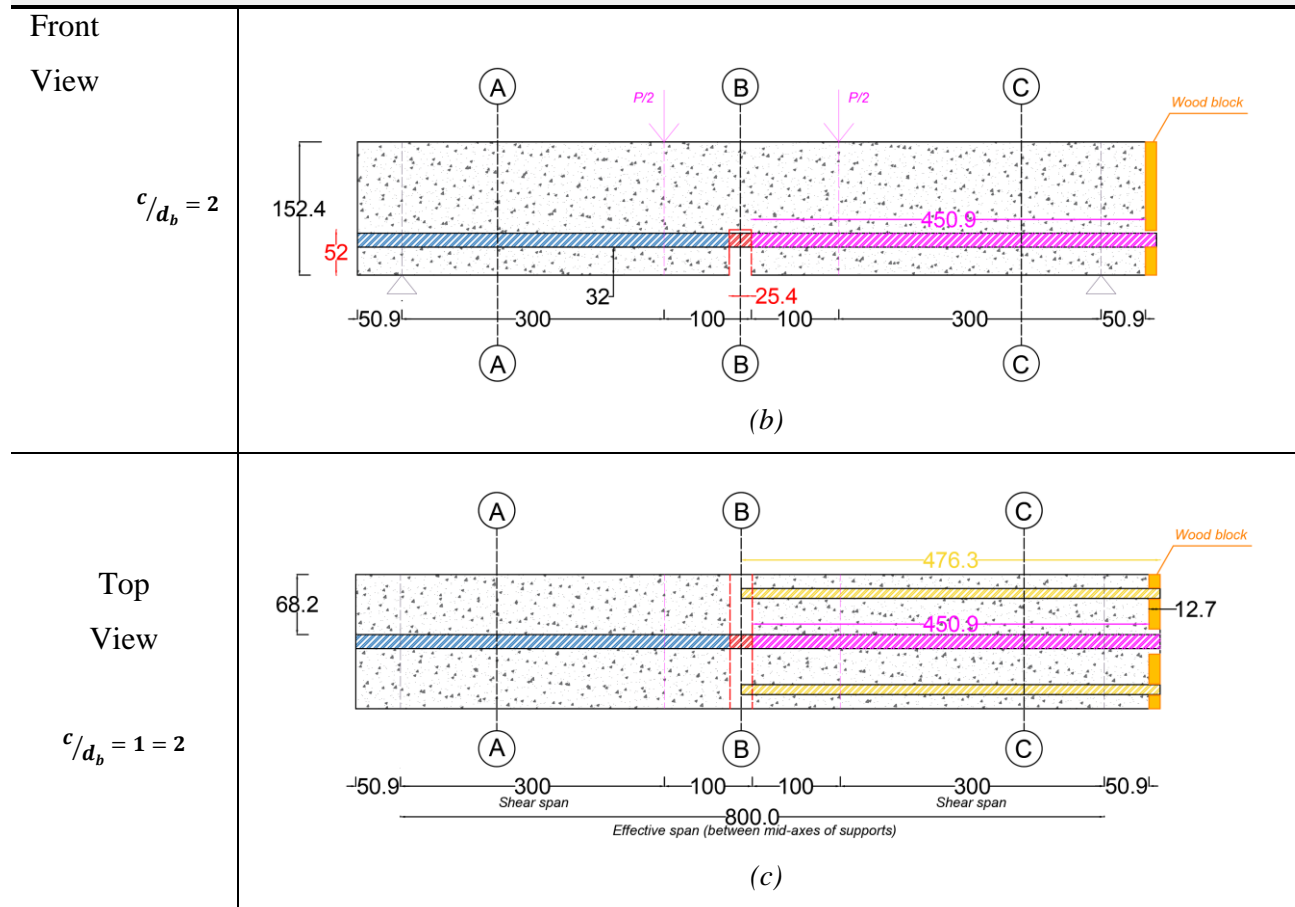
Beams presenting fully bonded 15M reinforcing bar without the presence of a PVC pipe were also prepared. This setup had mainly two purposes. The first was to study the behavior of the beam for a fully embedded reinforcing bar and obtain its ultimate capacity. The second purpose was to facilitate the modeling of the following four-point bending test setup and enrich the database eliminating one parameter which is the PVC pipe.

The test setup was identical to that presented in Table 3-1, where the only difference relies on the absence of the PVC pipe. As presented in Table 3-4, the test setup has the same notch position and length as that of the auxiliary bars.

Table 3-4 Detailing of the beam for the test setup with fully embedded 10d_b reinforcing bar for two different concrete covers



Detailing for a fully bonded reinforcing bar



3.1.5 Detailing of the notch and the wood block

In addition to the role of the notch and the wood block, holes were pierced in both elements to support and maintain a straight and stable height for both auxiliary bars. This eliminates the need for concrete cover chairs in the test setup. The notch is formed by placing a foam board in the required position. This foam board is easily removed during demolding. A third hole is perforated in the notch through which the 15M steel bar can pass. Moreover, to achieve the primary purpose of the test setup and isolate the bar from the surrounding concrete, the height of the notch should not be less than:

$$h_n > c_b + d_b$$

Thus, for a concrete cover c_b of 16 and 32 mm, the height of the notch is taken as 40 and 52 mm, respectively. The Top View detailing in Table 3-5 presents the depth of the perforated holes for the auxiliary bars. It can be seen that they penetrate halfway through the notch in order to stabilize the 10M bars. The notch detailing is shown in Table 3-5 for both values of the concrete cover. For all cases, the height of the center of the hole for both the auxiliary and main bar is the same and equal to:

$$h_n = c_b + \frac{d_b}{2} \text{ (or } d_{b,aux})$$

Table 3-5 Notch detailing for the experimental setup (in mm)

c/d_b	Notch detailing			
	Front View	Top View	Sections	h_n (mm)
1				10M
				15M $h_n = 24$
2				10M
				15M $h_n = 40$

During the test setup, the wooden block will have drilled holes allowing both the reinforcing bar and the PVC to pass through it while remaining inside the formwork. Then, during beam demolding, upon concrete hardening, the block of wood can be removed, and the reinforcing bar would be visible. The detailing and positions of the holes to be drilled for each case are presented in Table 3-6.

For the 10M bar:

A slightly greater diameter is considered for the holes compared to the diameter of the steel bars:

$$d_{spade\ bit} > d_b = 0.44'' ; \quad \text{based on the available spade bit dimensions: } d_{spade\ bit} = 0.5''$$

The height of the center of the hole in the wood block h_w :

$$h_w = c_b + \frac{d_h}{2} = c_b + \frac{12.7}{2} \quad (\text{in mm})$$

The offset of the center of the hole from the lateral sides of the wood block:

$$s_w = c_s + \frac{d_{b,aux}}{2} = 16 + \frac{11.3}{2} \quad (\text{in mm})$$

For the 15 M bar:

Since the PVC pipe will pass through the block, the diameter of the middle hole is drilled, taking into consideration the diameter of the PVC pipe while the height of the center of the hole depends on the proposed concrete cover:

$$d_{spade\ bit} > \varnothing_{ext\ PVC} = 1.05'' \quad \text{based on the available spade bit dimensions: } d_{spade\ bit} = 1^{1/8}''$$

$$h_w = c_b - t_{PVC} + \frac{d_b}{2} = c_b - 3 + \frac{28.575}{2} \quad (\text{in mm})$$

However, for the fully embedded reinforcing bars, no PVC is used, therefore:

$$d_{spade\ bit} > d_b = 0.63''$$

Based on the available spade pit dimensions: $d_{spade\ bit} = 3/4''$

$$h_w = c_b + \frac{d_h}{2} = c_b + \frac{19.05}{2} \quad (\text{in mm})$$

Table 3-6 Block of wood detailing for the experimental setup (in mm)

l_b	c/d_b	Woodblock detailing		$h_h - d_{spade\ bit}$
		Front View	Top View	
5 d_b 10 d_b 15 d_b	1			10 M bar: $h_h = 22.35\text{ mm}$ $d_{spade\ bit} = 0.5''$ 15 M bar: $h_h = 27.3\text{ mm}$ $d_{spade\ bit} = 1^{1/8}''$
	2			10 M bar: $h_h = 38.35\text{ mm}$ $d_{spade\ bit} = 0.5''$ 15 M bar: $h_h = 43.29\text{ mm}$ $d_{spade\ bit} = 1^{1/8}''$
Fully bonded	1			10 M bar: $h_h = 22.35\text{ mm}$ $d_{spade\ bit} = 0.5''$ 15 M bar: $h_h = 24.3\text{ mm}$ $d_{spade\ bit} = 3/4''$
	2			10 M bar: $h_h = 22.35\text{ mm}$ $d_{spade\ bit} = 0.5''$ 15 M bar: $h_h = 41.525\text{ mm}$ $d_{spade\ bit} = 3/4''$

3.1.6 Test setup and procedure

Figure 3-10 represents the entire test setup proposed to be conducted for all the beam tests. However, in the following drawings, the poles of the test setup are ignored for visual clarification. The static hydraulic universal test system was used to impose a displacement control on the test specimens.

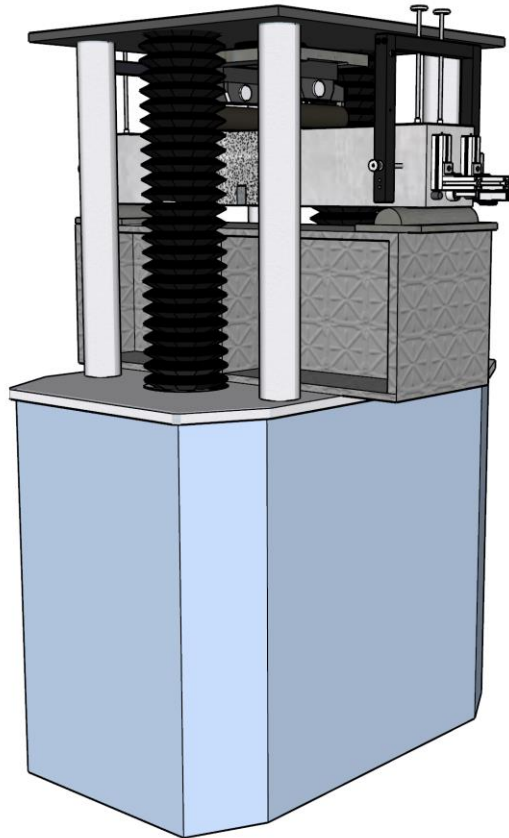


Figure 3-10 3D model of the experimental test setup for all the specimens

The span of the beam is 800 mm, while the length of the platform of the MTS universal testing machine is approximately 600 mm. This is why a steel beam was placed underneath to accommodate the needed span. The structural capacity of this beam was verified in terms of buckling and shear capacity. A two-point load jig was designed to be attached to the system to realize the four-point bending test, as can be seen in Figure 3-11. The design was taken from previous drawings where rollers were intended to transfer the load, thereby enabling the movement of both in the plane and out of plane directions. This would eliminate any type of friction that occurs between the loading system and the beam. Appendix A presents the detailed drawings of the jig.

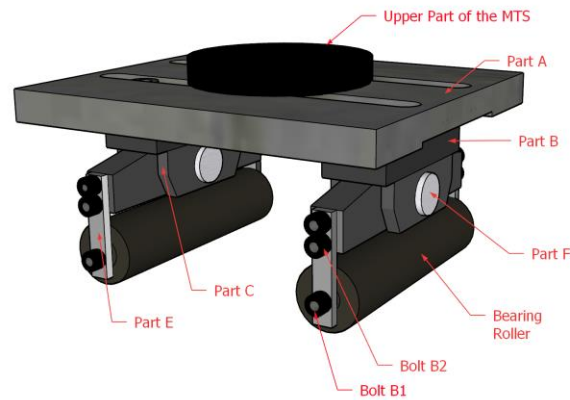


Figure 3-11 Jig used for the four-point bending test

Figure 3-12 demonstrates the back side of a test setup where the linear potentiometer A is attached to the beam by a frame cord system to measure the mid-deflection of the beam. The aluminum bar eliminates the effects of the rotations of the supports on the mid-deflection measurements. The whole arrangement will be explained in detail in Section 3.1.7.1. Moreover, the linear potentiometer B is attached to a frame which is turn attached to the side of the beam. Thus, the linear potentiometer B is directly connected to the extended part of the 15M bar for slip measurement. Specific details of the frame will be given in Section 3.1.7.2.

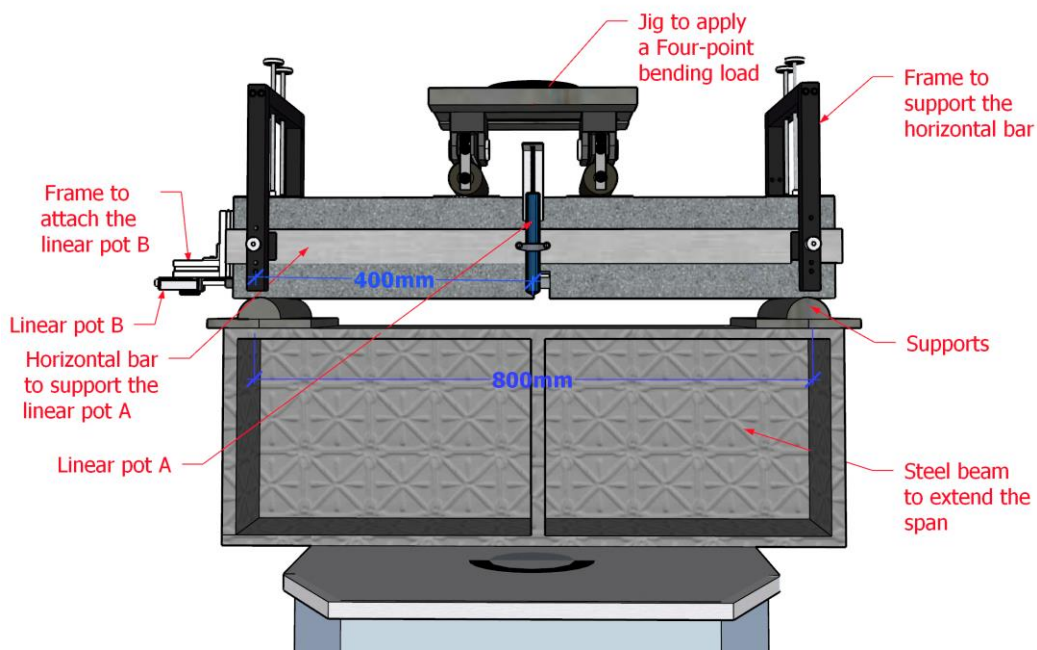


Figure 3-12 Test setup of the back of the beam

Another method was followed to measure the mid-deflection of the beam. This was realized by conducting a digital image correlation (DIC). Figure 3-13 demonstrates the front of the test setup, where the beam was speckled using white and black paint in the middle region. The primary challenge, while using the MTS universal testing machine, is the presence of the poles where for each specimen type, the steel beam was rotated in order to accommodate this intrusion in the field of the camera. Moreover, the bar inside the notch was speckled as well, in order to obtain the strain in the reinforcement by using DIC.

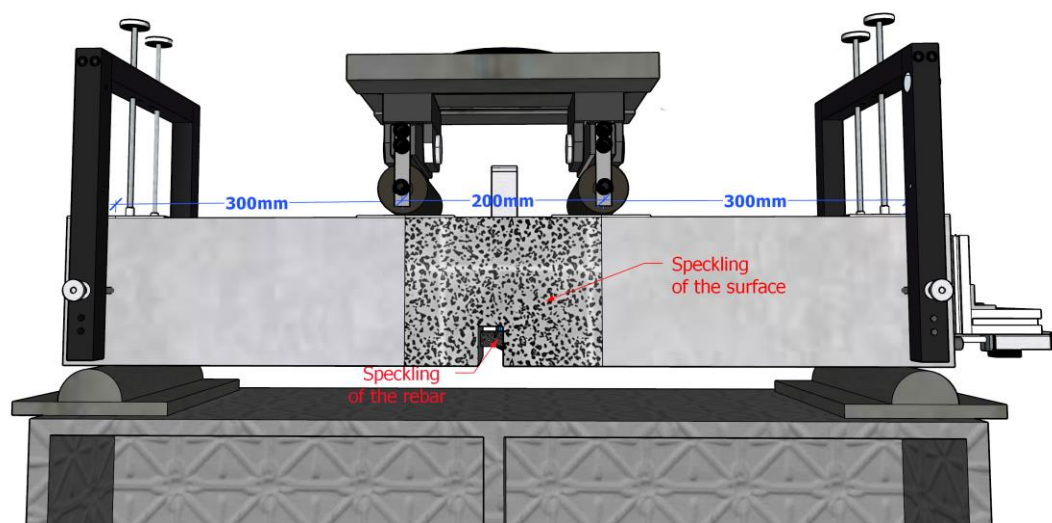


Figure 3-13 Test setup of the front of the beam

3.1.7 Measuring equipment and tools

During the experiment, several parameters were measured such as the applied load, mid-deflection, slip of the reinforcing bar under study and strain in the reinforcing bar. In addition, the cracking and mode of failure were also observed and analyzed.

3.1.7.1 Deflection of the mid-span of the beam

Two steel frames were pinned on both sides of the beam at the supports, as can be seen in Figure 3-12. From Figure 3-14, the steel frame is composed of 2 vertical steel elements (Part K) connected by a horizontal element (Part J). The drawings with the measurements of each element are presented

in Appendix A. Moreover, two vertical rods are screwed onto the Part J of the frame to reach the upper face of the beam. Small legs are attached to each of the vertical rods, allowing them to sit on the surface, and providing in-plane movement stability. Thus, the frame rotates along with the support without causing disruption. The frame also provides support for the aluminum bar holding the linear potentiometer A for the mid-span deflection measurements.

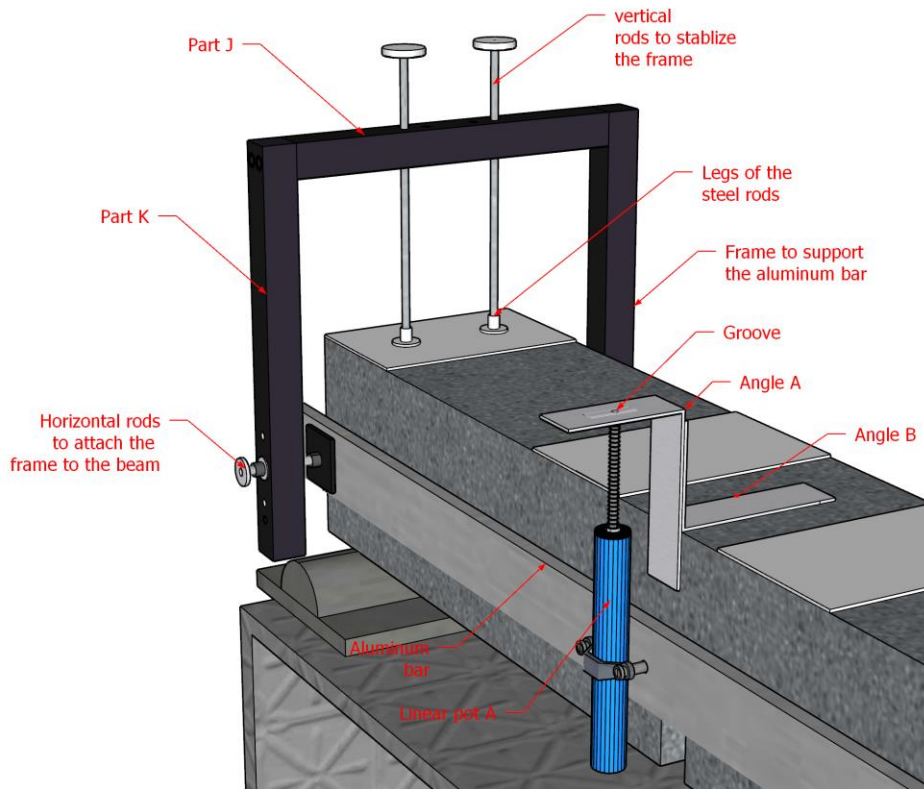


Figure 3-14 Detailing of the vertical frame

The ends of the aluminum bar are cut to form a circular notch on one end and a rectangular notch on the other as shown in Figure 3-15 (a). The distance between the center of both notches is equal to the distance between the mid-axis of both supports known as 800 mm. The diameter of the angular notch is drilled to perfectly fit the horizontal rod having a diameter of $\frac{3}{8}$ – 16 bar. This notch is used to fix the aluminum bar on the pin, accordingly restricting any horizontal and vertical movement. However, the pin supporting the rectangular slot permits the horizontal movement, yet blocks the vertical displacement of the aluminum bar. Moreover, two holes are perforated in the center of the aluminum bar to attach the linear potentiometer A at the mid-span of the beam as can be seen in Figure 3-15 (b). The detailing and the dimensions of the aluminum bar are presented in Appendix A.

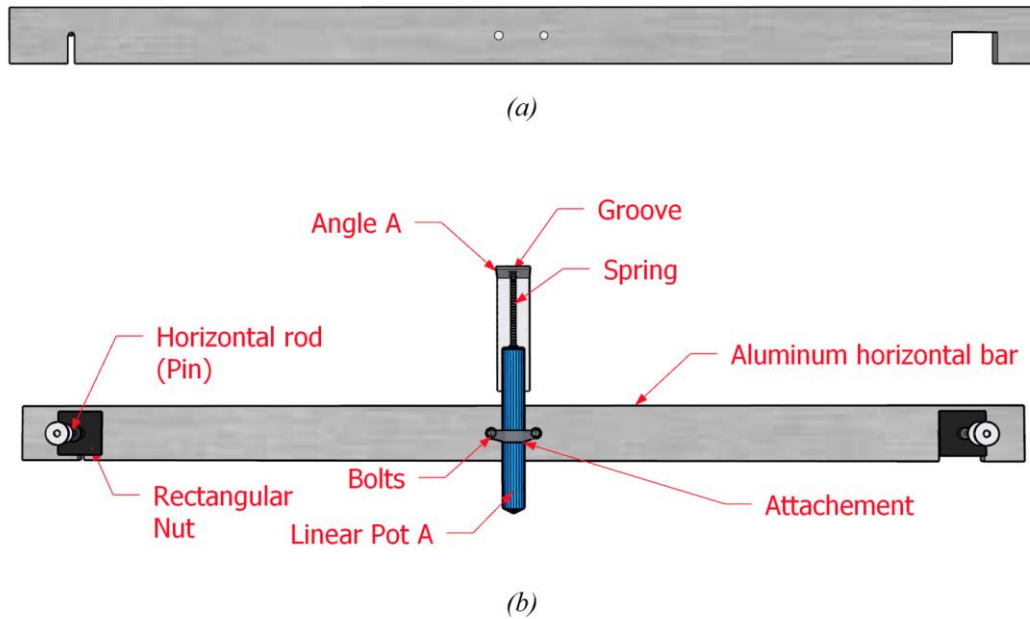


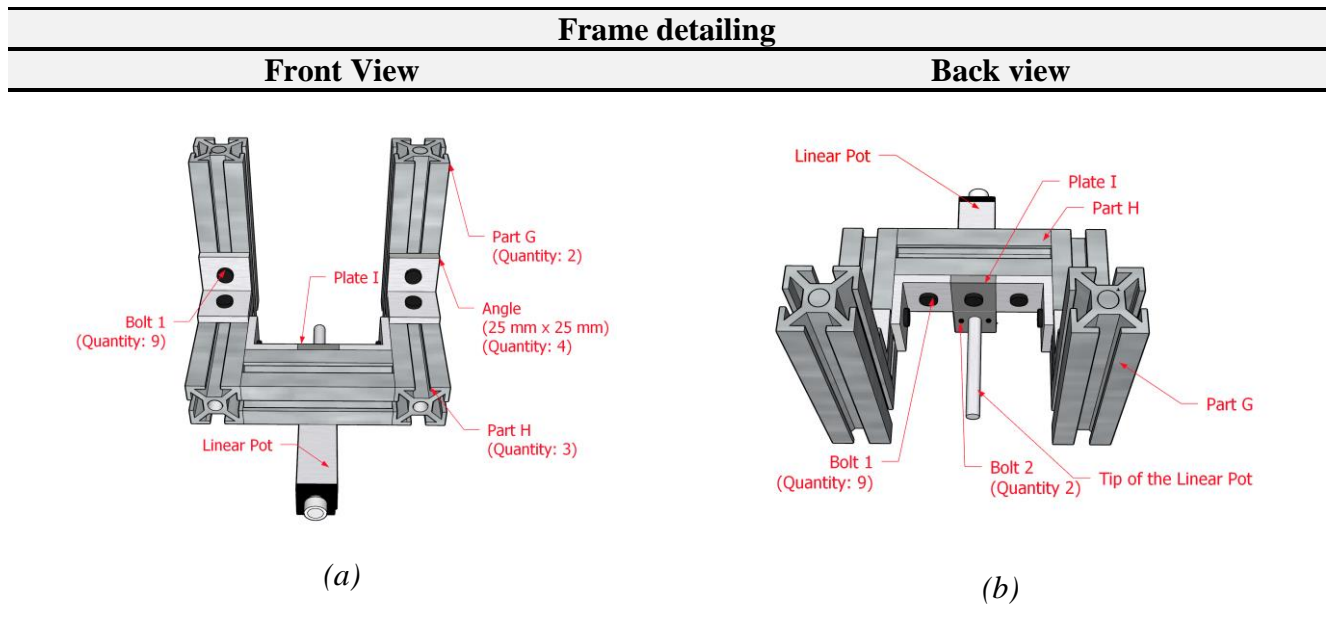
Figure 3-15 Detailing of the aluminum rod with the linear potentiometer A

The mid-deflection is measured from the top of Angle A. The latter was hot glued to the surface of the beam, given that it should follow the beam's deflection. To prevent the out-of-plane movement of Angle A, Angle B was attached to it and taken as a stiffener. In addition, a groove was hammered in order to control and limit movement of the linear potentiometer A as shown in Figure 3-14.

3.1.7.2 Slip of the main reinforcing bar

The linear potentiometer B was fixed to a small frame as shown in Table 3-7 to measure the slip of the main reinforcing bar as shown in Figure 3-12. The frame is formed by three pieces of part G and two pieces of part H. As shown in Table 3-7 (b), linear potentiometer B is attached to the frame by the intermediate of the steel plate I that is screwed onto the linear potentiometer and the part H. The two vertical parts G of the frame were hot glued to the side of the beam presenting the extension of the 15M bar. Therefore, the frame follows the movement of the beam eliminating the effect of the rotation on the slip measurement. The tip of the linear potentiometer B touches the extended surface of the 15M bar.

Table 3-7 Detailing of the frame used to attach the linear potentiometer and measure the slip of the reinforcing bar



The materials were purchased from D & D Air & Hydraulic Components Inc. The 6 m long extruded bar presented in Table C-4 (a) was cut to size. All the parts were connected to each other using angles as shown in Table 3-7. However, the angles were attached to each part by T-nuts and screws following the methodology described in Figure 3-16.



Figure 3-16 Methodology to insert the T-nut inside the bar ('The Profile System,' 2003)

3.1.7.3 Digital image correlation (DIC)

The digital image correlation (DIC) was another method adopted to calculate the deflection of the beam. The latter was also compared with the results obtained from the linear potentiometer A. For this reason, as can be seen in Figure 3-13, the middle region of the front of the beam was speckled using black and white paint. The DIC was conducted using the GeoPIV-RG software, programmed within Matlab to calculate the deflection of a beam at the desired point (White *et al.*, 2003). The

software, based on localizing the centroid of a small group of pixels, uses an initial picture captured at the beginning of the test. Then, it determines the movement of this centroid, varying according to the timing of the images placed in sequence. This image processing program has been validated in previous research (White *et al.*, 2003; Gales *et al.*, 2012).

3.1.8 Displacement rate

In order to observe a detailed behavior of the beams, the displacement rate of 0.005 mm/min was chosen for all the flexural tests. The MTS universal testing machine was connected to the two linear potentiometers A and B using a data acquisition system to extract all the necessary measurements. The data was recorded at a frequency of 1 Hz. The test was terminated once the load dropped by 80%.

3.1.9 Extraction of the bond strength

The applied moment is calculated using the Equation (3.4). Based on the force diagram in Figure 3-17 and Figure 3-18, the reinforcing bar resists the applied moment following Equation (3.13):

$$M = T_s \times (\beta d) = A_s \times f_s \times (\beta d) \quad (3.13)$$

The internal lever arm is 128.4 mm for a concrete cover of $1d_b$ (ref: Figure 3-17) and 112.4 mm for a concrete cover of $2d_b$ (ref: Figure 3-18).

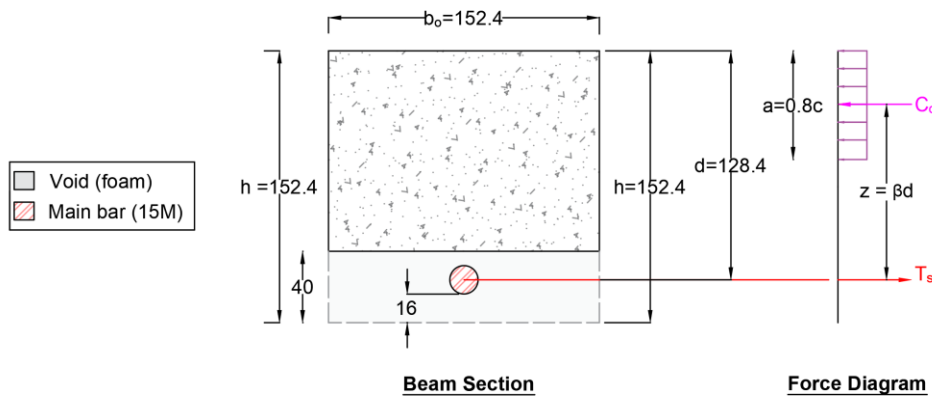


Figure 3-17 Force diagram for the beams with a concrete cover $c = d_b$ (in mm)

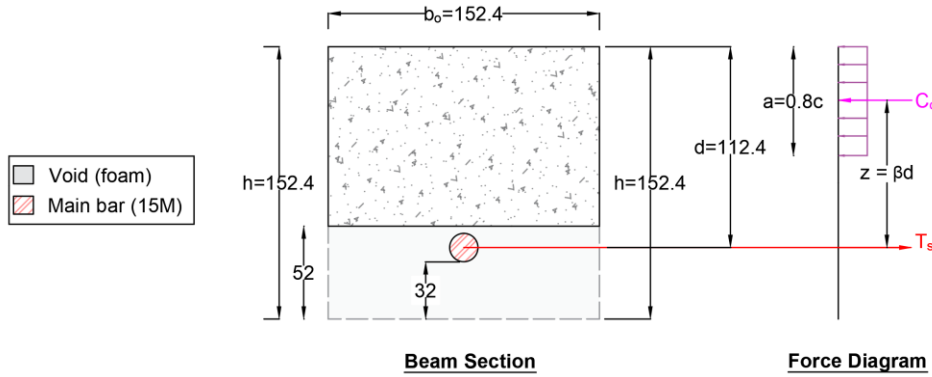


Figure 3-18 Force diagram for the beams with a concrete cover $c = 2d_b$ (in mm)

However, assuming a uniform distribution of the bond stress along the embedment length, the bond strength can be determined at the loaded end using Equation (3.14):

$$f_b = \frac{D_b \times f_s}{4 \times l_b} \quad (3.14)$$

The average bond stress is then defined in Equation (3.15):

$$f_b = \frac{D_b \times P \times a}{8 \times l_b \times A_s \times \beta d} \quad (3.15)$$

3.2 Choice of the mixes considered: Preliminary and Commercial

3.2.1 In-house trials and final matrix characteristics

3.2.1.1 Equipment and tools used

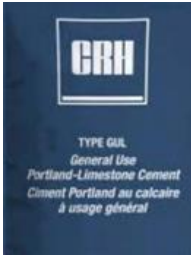
All the equipment and tools used for batching and weighing materials, mixing and pouring are presented in Table C-1 in Appendix C. Table C-1 also presents the small steel formwork for concrete cubes and prisms. However, determining the concrete's compressive strength was done using the

Controls Pilot testing machine. The beam test to extract the flexural strength of the material was conducted in the MTS universal testing machine.

3.2.1.2 Material used

As known, there are six components other than water that constitute UHP-SFRC: fine sand, cement, pozzolanic materials, inert materials, superplasticizer, and steel fibers. Table 3-8 presents all the materials with their symbol that were used in the research concerning the in-house design mixture. Sieve analysis was conducted for all the silica sand to determine the fine aggregate distribution and nominal diameter size as presented in Table B-1.

Table 3-8 Materials used for trial and final concrete in-house mixture

Material	Picture	Properties	Annotation	Supplier
Silica Sand		Max aggregate size 0.771 mm	S1	K & E
		Max aggregate size 0.370	S2	
		# 530 Max aggregate size 0.542	S3	Bell & Mackenzie Co Ltd
Cement		Type GUL General use Portland-Limestone Cement	C1	CRH

Material	Picture	Properties	Annotation	Supplier
		GUL (6 to 15% limestone powder)	C2	Lafarge Stoney Creek Valley
Slag	N/A	Ground Granulated Blast Furnace	Slg 1	St Mary Cement
	N/A	Ground Granulated Blast Furnace	Slg 2	Holcim
Silica Fume		MasterLife® SF 100 Densified Silica Fume	SF 1	BASF
		Densified Silica Fume	SF2	Norchem
Fly Ash		Type F	FA	Lafarge
Superplas ticizer	N/A	MasterGlenium® 3030	SP1	BASF
	N/A	MasterGlenium® 7700	SP2	
	N/A	MasterGlenium® 3400	SP3	

Material	Picture	Properties	Annotation	Supplier
Steel Fibers		Uncoated hybrid mix Diameter: 0.2 mm Type I length: 13 mm Type II length: 19 mm	CSF	N/A
		Coated SF Type I (Needles) Diameter = 0.2mm; Length = 13mm Tensile strength = 1900 MPa	SSF	Nycon

3.2.1.3 Trials

From the literature review discussed in Section 2.1.6, two types of design mixes were chosen (Yu *et al.*, 2015; Shao, 2016). The approach followed in the trials was to first obtain a flowable mixture with a high cube compressive strength based on the design mix proportions proposed. Secondly, to test small prisms under four-point bending in order to extract an approximation of the flexural strength, and thirdly to study the distribution of the steel fibers to observe any possibility of segregation. Therefore, several trial batches were conducted to test and compare their fresh and hard properties and finally choose the most qualified UHP-SFRC.

3.2.1.3.1 The trial of the design mixture (Yu *et al.*, 2014)

The design mixture as depicted in Table 2-1 was followed as closely as possible as not all the materials were available in Canada especially limestone powder (LP) that was difficult to find. Thus, the LP quantity was taken into consideration by using limestone cement instead of normal cement such as C1 presented in Table 3-8. Thus, the amount of cement used would be the combination of the regular cement and the amount of limestone powder considered.

$$C_{used\ for\ M1} = (C + LP)_{reference(Yu,2015)} = 594.2 + 265.3 = 859.5\ kg/m^3$$

The amount of limestone present in the binder content is reduced from 40% to 15% taking into consideration the percentage available in the cement C1. Mix M1 was considered a stiff material since it was not able to fill the molds by its own self-weight and the cube compressive strength reached 93 MPa after 7 days. Therefore, it did not meet the requirement of UHP-SFRC. Table 3-9 presents the concerned batch M1, mixed volume, date of the mixture, proportions, fresh state, and cube compressive strength. All of the other batches are presented in tabular forms in Appendix B, where the blue writing highlights the modified parameters.

Table 3-9 Design mix of the first trial, workability and the cube compressive strength

M1 (V = 1.1 L, 11/07/2017)				
Material	kg/m ³	(g)	Workability	f'_{cc} (MPa)
C1	859.5	945.45		07 days: 07/18/2017 93
LP	0	0		14 days: 07/25/2017 98
S2	221.1	243.21		28 days: 08/08/2018 100
S1	1061.2	1167.3		
SF1	24.8	27.28		
SP1	44.2	48.62		
W	176.9	194.59		
CSF	156	171.6		

Since the superplasticizer (SP) has a significant effect on the flowability of the mixture, another type SP2 defined in Table 3-8 was chosen instead of SP1 for the same design mixture presented in Table B-2. The comparison between Table 3-9 and Table B-2 demonstrates an improvement of the flowability. Therefore, SP2 was considered instead. No samples were taken to test the mechanical properties of the mixture.

For an economical and eco-friendly concrete, the limestone content in the binder paste was replaced by pozzolanic materials instead of cement, such as fly ash (FA), silica fume (SF) and slag (Slg). Fly ash was considered as the first reactive additive to be as a substitute to limestone powder instead of the cement as shown in Table B-3. After mixing all the materials, the mixture was in a powdery state. Even though FA is considered to enhance the workability of the mixture, it was noted that in some

cases, if the carbon level was high, it leads to an increase in water demand (Thomas, 2007). A proposition to reduce the amount of water needed for the aggregates was to use the sand with the higher aggregate diameter (S1) as seen in Table B-4 since it presents a lower surface area. However, this parameter did not affect the flowability of the mixture, since it remained powdery as well.

Mix M5 has the same design proportion yet; the volume was doubled in order to study the size effect as presented in Table B-5. The mixture remained powdery where 89g of water was added to make it a flowable mixture. The water binder ratio was $w/b = 0.37$ disqualifying the batch from being considered as an UHP-SFRC. Moreover, this high flowability can result in the segregation of the steel fibers. This addition of water decreased the concrete's cubic compressive strength to $f'_{cc} = 45 \text{ MPa}$ considerably less than plain concrete. Adding water is not an appropriate method to increase the flowability, therefore superplasticizers must be as well considered. Mixture M6 is identical to the two previous mixes M4 and M5, where both water and superplasticizers were added to increase the workability. The addition of 4g of SP2 and 20g of water was needed to transform the mixture from a powdery state to a more flowable texture, as presented in Table B-6. The use of one type of sand was not a good option since it reduces the flowability of the mixture and requires a greater amount of water and superplasticizers. Since C2 contains around 10% of limestone, this value must be considered in the design mixture. Thus, to maintain the same initial amount of cement as the reference design, C2 is equal to:

$$C_2 = C_{reference(Yu,2015)} + 9\%C_2 = 594.2 + 9\%C_2$$

$$C_2 = \frac{594.2}{(1 - 0.09)} = \frac{594.2}{0.91} = 653 \text{ kg/m}^3$$

Therefore, from the 653 kg/m³ of C2, 594.2 kg/m³ are ordinary cement, and the 58.8 kg/m³ are LP. Considering the amount of limestone to be 9% $C_2 = 58.77 \text{ kg/m}^3$ and assuming LS and the replacement pozzolan material have nearly the same density to maintain a unit volume of study:

$$Pozzolan = LS_{reference} - LS_{9\%C_2} = 265.3 - 58.77 = 206.53 \frac{\text{kg}}{\text{m}^3}$$

This amount of FA constitutes about 30% of the cement content, the average range typically used in UHP-SFRC mixes. The design mixture M7 was initially dry but reached the level of flowability presented in Table B-7 with the addition of 7 g of water and 8 g of SP2. The cube compressive strength reached $f'_{cc} = 80$ MPa at 14 days. The mixing procedure was doubled for the design mixture M7, yet no changes in the flow were observed.

Since adding FA by itself caused some flowability problems, other pozzolanic materials were considered to study their effect on the workability, the cube compressive strength and tensile strength of the mixture. Therefore, the residual amount of LS calculated previously (206.53 kg/m³) was divided between the two additives following different proportions: Mix M8/M9 with 30%FA - 70%Slg1 (ref Table B-8), Mix M10 with 50%FA - 50%Slg1 (ref Table B-9) and Mix M11 with 70%FA – 30%Slg1 (ref Table B-10).

For the mix M8 and M9, the duration of the mixing procedure was analyzed to study its effect on the workability as presented in Table 3-10, to verify if the initial mixing time is sufficient to complete the reaction between all these components. The mixture M8 presented in Table B-8 hardened during Step 3 in the fast rate phase to the point where it could no longer be cast. A new mixture of M9 was done with the same design mixture, yet the last phase was reduced to 2 minutes instead of 10 minutes. The workability of the mixture was enhanced without adding SP.

Table 3-10 Elongation of mixing procedure for two mixes M8/M9

Steps	Mixing rate	Initial time	Modified time (M8)	Modified time (M9)
1	Slow rate mixing	30 sec	5 min	5 min
2	Slow rate mixing	1 min 30 sec	7 min 30 sec	7 min 30 sec
	Rest	30 sec	2 min 30 sec	2 min 30 sec
3	Slow rate mixing	3 min	15 min	15 min
	Fast rate mixing	2 min	10 min	2 min
Total mixing time		7 min 30 sec	40 min	32 min

All three mixes presented the same flowability. Therefore, mechanical tests were conducted on small cubes and prisms to study the effect of these additives on the hard properties of the mixture. The graph in Figure 3-19 shows that the mix M11 containing the highest dosage of FA experienced the lowest load equal to 6kN. This can be due to the fact that FA interferes in the long term. Mixes M9

and M10 obtained the same peak load of 8kN which explains that the effect of slag Slg1 on the concrete's flexural strength stops after a determined threshold. For this reason, another mixture M12 presented in Table B-11 was proposed, where the pozzolanic additives were SF1 and Slg1 without the presence of any FA. It can be seen in Figure 3-19 that this design mixture experienced the highest peak load reaching 8.6 kN. The mix M11 experienced the highest strain-hardening behavior and cube compressive strength which concludes that having a small amount of FA is beneficial.

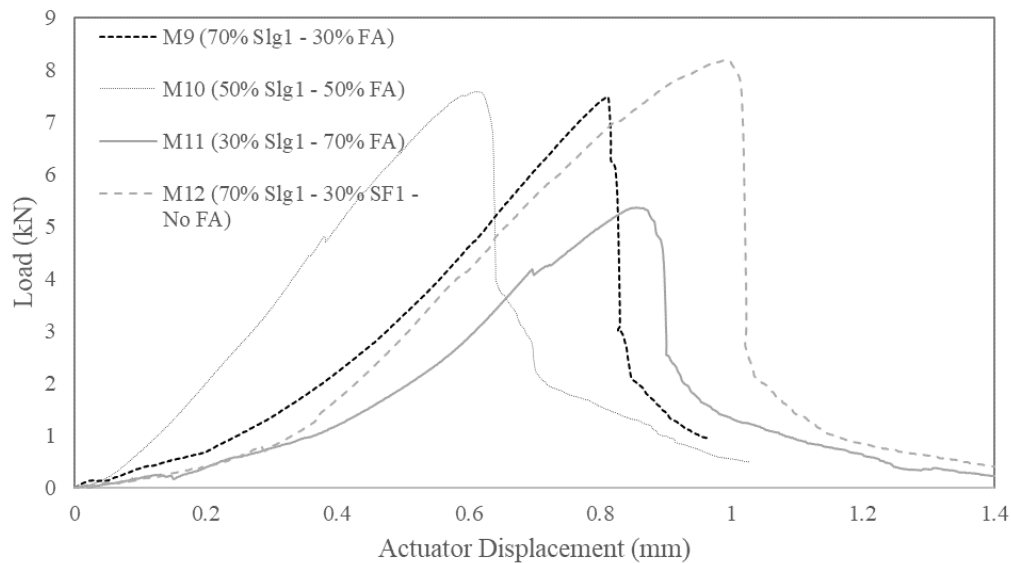


Figure 3-19 Load-actuator displacement (mm)

Based on the previous observations, the final mixture proposed contained all three additives with the following proportions: 15% FA, 60% Slag and 25% SF. However, some of the materials used were modified and replaced by C2, Slg2, S3, SF2, SP3 as introduced previously in Table 3-8. In addition, straight coated steel fibers were introduced instead of the cocktail uncoated mixed fibers to study the effect of the type of fibers on the response curve. These materials are highlighted in blue in Table B-12. The same mixing procedure was used as explained for M9. The concrete mix M13 was considered flowable as can be seen in Table B-13 and can be classified in the “stiff” category of UHP-SFRC. All prisms were poured and then hammered 25 times on each side. Another batch M14 was prepared following the same mix design as presented in Table B-14, yet using a different mixing procedure. The main difference relies on the time when the superplasticizer SP3 was added, where half the

amount was introduced in the second step and the other half in the third step. This step did not make a significant difference in the results.

3.2.1.3.2 The trial of the design mixture (Shao, 2016)

This part is divided into three different steps: trial phase 1, first casting and trial phase 2. The proportions of each trial batch are presented in Appendix B.

3.2.1.3.2.1 Trial phase 1

The design mixture corresponding to the lower water-binder ratio of 0.18 presented in Table 2-2 was chosen to obtain higher mechanical properties. Since the materials of the proper design mixture were not delivered, the materials specified in Table B-14 for the mixture B1 were used instead. At first, the total amount of sand was divided between S1 and S2 equally. The mixing resulted in a dehydrated material that required the addition of 49 grams of SP1 and 10 grams of water to reach the level of workability depicted in Table B-14.

Therefore, mix B2 was proposed where the proportions of the sand varied between 20% for S2 and 80% for S1. Moreover, the superplasticizer SP1 was replaced by SP2 based on the previous results obtained in mix M2. However, a very minimal improvement of the flowability was observed where Table B-15 presents a more or less muddy texture. There was no bond between the matrix and the steel fibers. For this reason, extra superplasticizer and water were added until a flowable mixture was obtained. To enhance the workability of the mixture, the proportions for water to binder ratio equal to 0.2, presented in Table 2-2, were used for the third batch B3. However, the mixture remained in a mud-state and needed 20 additional grams of SP2 to become flowable as shown in Table B-16. Therefore, these materials were set aside until the appropriate materials were delivered. Batch B4 represented in Table B-17 presents the actual mix proportions of the reference design mix (Shao, 2016). A flowable mixture was obtained where f'_{cc} reached approximately 140 MPa. A 2 liter batch volume was casted to form 3 cubes and 2 prisms to be tested and compared with the mechanical result of batch M13 and M14 (Yu et al., 2015) in terms of compression and flexural strength.

In terms of flowability, the mixes M13 and M14 fall under the “stiff” UHP-SFRC where they are flowable enough to be able to fill parts of a formwork, yet require additional external compaction. The mix B4 is considered a flowable design mixture, where its self-weight is sufficient to mobilize it. The failed prisms and cubes for mix M14 and B4 are presented in Figure 3-20.

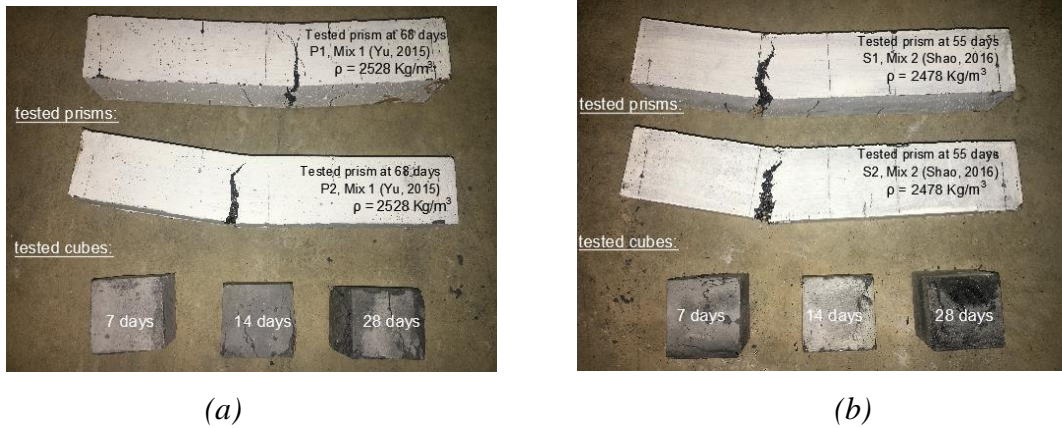


Figure 3-20 Failed prisms and cubes (a) M14 and (b) B4

On one hand, the cubic compressive strength of M13 and M14 at 28 days was approximately 116 and 120 MPa as shown in Table B-12 and Table B-13, which most likely fall in the limit of the UHP-SFRC category. On the other hand, the cube for mix B4 was able to reach 140 MPa at 28 days as depicted in Table B-17. For determining the flexural strength of both concrete mixes, all the corresponding prisms were tested under four-point bending load with a displacement control of 0.005 mm/min. The main parameters of comparison are the peak load, pre-peak behavior in terms of strain hardening and post-peak behavior. The flexural behavior is presented in Figure 3-21, where all the resistance curves present a pre-peak hardening capacity confirming an adequate bond between the steel fibers and the concrete matrix where the steel fibers were pulled out and not ruptured. In addition, the curve presents a post-peak softening behavior. Mainly both mixtures presented the same maximum peak load of around 12.5 kN and a flexural strength of 20 MPa. The mixture of batch B4 was chosen in this case, since it presented higher workability and all the materials were available in Ontario (Shao, 2016).

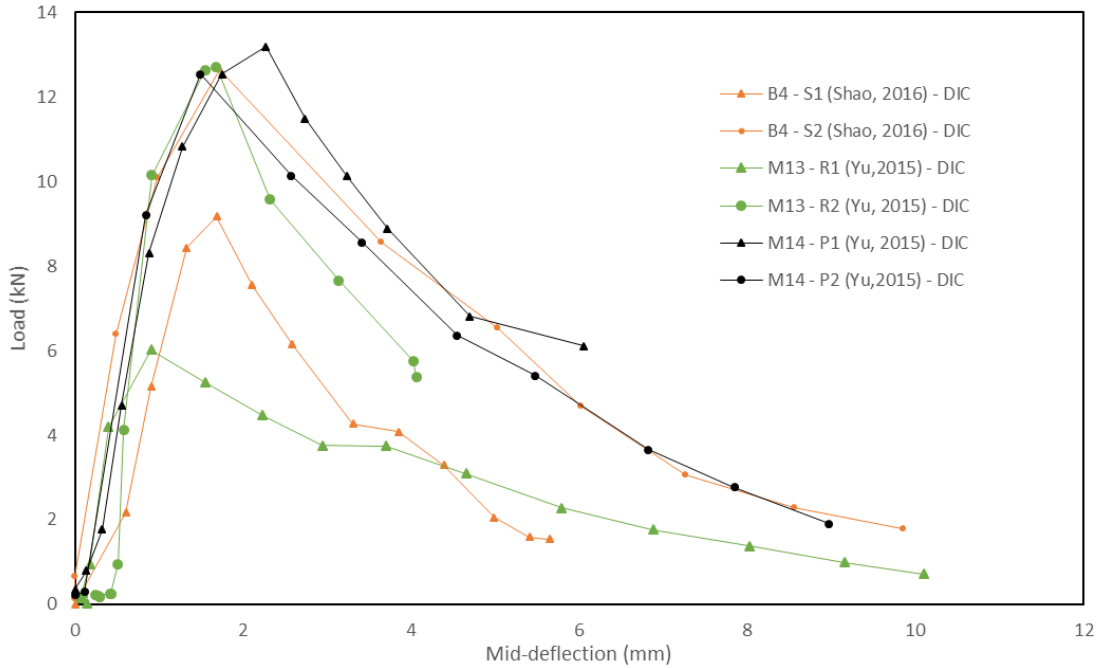


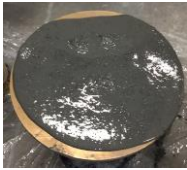
Figure 3-21 Load-deflection behavior for mix B4, M13 and M14

Moreover, it can be noticed that the behavior of the prisms in Figure 3-19 are highly stiff with a deflection of 1 mm at the end of the test in comparison with the prisms from (Yu *et al.*, 2015) in Figure 3-21 with a deflection of 10 mm. The main difference between these two mixes M9-M12 and B4 is the steel fiber used, where for the former the steel fibers were hybrid while for the latter the steel fibers were straight and covered with brass-coat. Thus, the use of brass-coated straight short steel fibers enhances the ductility of the mixture.

First casting

Even though the first casting that was conducted had the same design mixing proportions as B4, it did not meet the requirements of a UHP-SFRC. Table 3-11 presents the results of the first flow test, showing a very flowable mix to an extent it overflowed the flow table (greater than 230 mm). In addition, a segregation problem became apparent when the steel fibers concentrated in the center and became easily separated from the matrix.

Table 3-11 Design mix for the 6th batch, same liquid additives but extended mixing time

B5 In-house casting 1 (V = 115L, 25/05/2018)			Flow test	
Material	kg/m ³	(kg)		
C2	724.13	83.27 + 3.6	 D > 230 mm	 D after addition of dry material > 230 mm
Slg2	362.06	41.64 + 1.8		
S3	668.6	76.89 + 3.3		
SF2	120.69	13.88 + 0.6		
SP3	17.01	1.96		
W	241.13	27.73		
SSF	195.75	22.51		

Based on the flowability test, three main points were highlighted in step 2 and step 3 during the mixing. Firstly, both steps required an extended period of mixing to ensure that all materials were merged properly together than was followed for the trials. Secondly, as shown in Figure 3-22, the liquid materials were added all at once, instead of a gradual insertion. Thirdly, no flow test was done prior to the addition of steel fibers to control the flowability of the mixture. The first two steps are very critical given that the margin of error for larger concrete volumes is higher than when mixing small batches. During the mixing, an attempt to reduce the flowability of the mixture was made by adding 5L of dry materials as seen in blue font in the design proportions of Table 3-11. However, the mixture still surpassed the flow table.



Figure 3-22 Addition of the liquid material in one phase during step 2

Trial Phase 2

Additional trials were conducted to deeply understand the main points discussed previously and how to control the fresh properties of the mixture for future casting. Therefore, the same design mixture was repeated for a 2L of concrete with the prolongation of all the different mixing steps, in order to

observe the change in the design texture. The trial B6 is presented in Table B-18 with 15 minutes resting time and an 11.5 minutes duration for step 3. The flowability was more significant than 230 mm and did not meet the UHP-SFRC requirements. However, the matrix was considered dense with no apparent segregation. This is due to the gradual addition of superplasticizer that had an effect on the concrete's texture once compared between batch B5 and B6. Moreover, it is evident that the extension in the mixing duration can actually reduce the amount of superplasticizer needed. This time increase permits the materials to react between one another to reach a point where it becomes flowable before all the amount of superplasticizer is consumed. Therefore, the addition of all the amount of superplasticizer leads to a very flowable mix than required.

This problem can be solved by reducing the mixing time or the amount of SP added. Given that the casting of large volumes requires additional mixing time, the only variable parameter, in this case, would be the amount of superplasticizer to be added. For this reason, batch B7 was realized for a volume of 2L where the original amount of superplasticizer was reduced as seen in Table B-19. Even though B7 resulted in a good flow test after the addition of steel fibers, the same mixture was repeated as seen in Table B-20 with a higher volume to verify the size effect on the amount of superplasticizer to be added. Only 80% of the first SP3 was used to obtain a flow test of about 250 mm before the addition of steel fibers. After the addition of steel fibers, the flow test was around 210 mm, which falls in the margin of UHP-SFRC. Therefore, it was evident that with the increase of the volume, the mixer is used to its full energy where the materials are appropriately blended and require less wet additives to reach the proposed flowability. The same mixture was repeated for the same volume to verify that the amount of superplasticizer used to lead to the same results. The mixture was consistent where only 2g of SP3 was taken out to decrease the flowability. The final design mix presented in Table B-21 will be the one used for casting.

3.2.2 Commercial

The research participated with the casting of two Canadian concrete mixing companies, where each one followed their own design mix proportions, mixing procedure and fresh properties criteria. For confidential purposes, they will be named Commercial K and Commercial F.

3.3 Material characterization tests

3.3.1 Compression strength

The compressive strength was determined based on the standards by testing 150 mm long cylinders with a 75 mm diameter at a loading rate of 1.0 ± 0.05 MPa/s to reduce the time required for the testing (C1856/C1856M). The compression test setup is presented in Figure 3-23 and conducted on the Controls Pilot testing machine identified in Table C-1. Due to the limited available equipment to obtain the stress-strain behavior of the material, the DIC methodology was used to obtain the pre-peak behavior and the Young's modulus of the in-house concrete. Thus, one side of the cylinders was speckled as can be seen in Figure 3-23. Prior to testing, the ends of each cylinder were grinded to produce parallel and smooth surfaces. Moreover, three different values of the length and diameter were measured to determine the average dimensions for each specimen.



Figure 3-23 Test setup for compression for the Controls Pilot testing machine

3.3.2 Flexural strength

In general, the tensile strength of concrete can be determined directly by executing a Direct Tension Test (DTT). However, the latter presents difficulties with the grips generating additional stresses that can affect the results. Moreover, the values obtained depend on the initial gauge length considered. Therefore, indirect methods to calculate the tensile strength were proposed such as flexural prisms or splitting cylinder test.

3.3.2.1 Shear span effect

The flexural strength ($\sigma_{flexure}$) or modulus of rupture (MOR) was obtained based on the four-point bending test conducted on two different prisms presented in Figure 3-24 (ASTM C1856, 2017). Since the length of the fibers is less than 15 mm, the nominal cross-section of both prisms is 75 mm x 75 mm. The testing was realized in the MTS universal testing machine with a loading rate of 0.005 mm/min instead of 0.05 mm/min to observe a detailed behavior of the beams.

All prisms were tested on the side surface opposite to the casting surface for a smooth platform to apply the load and place the supports. Two sets of prisms were cast to interpret the effect of the shear span-to-depth ratio on the flexural strength where $a/d = 1$ for prism P1 and $a/d = 2$ for prism P2. Thus, the results of series S1 and S4 from Table 3-12 are compared.

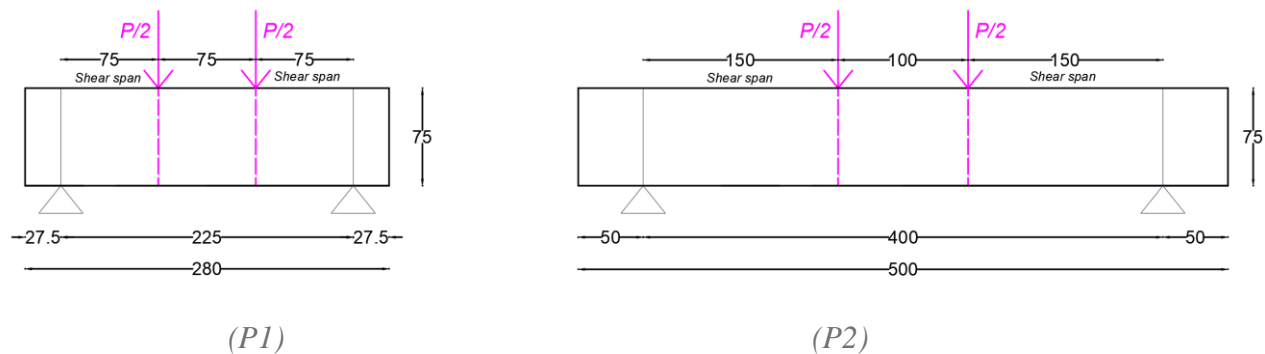


Figure 3-24 Prisms dimensions for third point loading test (mm)

3.3.2.2 Method of casting

Table 3-12 presents a detailing of the prisms divided into sets for comparison. The effect of the pouring methodology on the flexural strength was studied for a layered casting method and a flow method applied from one side of the mould. The results of series S1 and S2 are then compared. Moreover, the comparison of both prisms G and H from series S3 shows the effect of adding steel fibers on the flexural strength.

Table 3-12 Set of prisms for the flexural test to calculate the tensile strength

Set	Prism	Dimensions (mm)	Casting method	Steel fiber presence	Casting date	Testing date
S1	Prism A	75 x 75 x 280	Layered	✓	06/05/2018	06/09/2018
	Prism B					
	Prism C					
S2	Prism D	75 x 75 x 280	One-side	✓	06/06/2018	07/09/2018
	Prism E					
	Prism F					
S3	Prism G	75 x 75 x 280	Layered	✓	22/06/2018 (Batch 3)	07/09/2018
	Prism H			x		
S4	Prism I	75 x 75 x 500	Layered	✓	11/06/2018	20/09/2018
	Prism J				12/07/2018	20/09/2018
	Prism K					

The load-deflection relationship was plotted to depict the pre-peak and post-peak behavior of all the specimens. The mid-span deflection was measured using a smaller version of the frame previously described in Section 3.1.7.1. The frame, pinned to the prism, supports an extruded bar holding the linear potentiometer as can be seen in Figure 3-25. The latter is connected to a data acquisition system recording directly the mid-deflection of the prisms without taking into consideration the displacement and rotation of the supports.

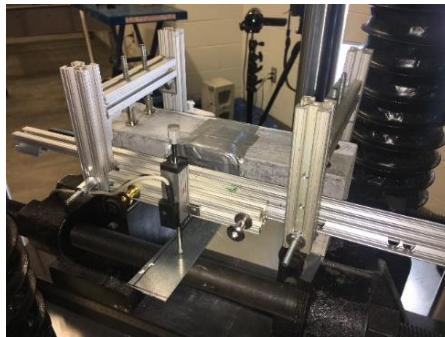


Figure 3-25 Third-point loading test setup from the front

The mid-deflection was obtained from the DIC as discussed previously in Section 3.1.7.3. The specimens were speckled from one side as seen in Figure 3-26 (a). The actual test setup along with the camera, the lighting and the clock used for the image correlation system is presented in Figure 3-26 (b).



(a)



(b)

Figure 3-26: (a) Test setup with (b) the camera and the lighting

Assuming a linear distribution of stress and strain, the flexural strength is calculated from Equation (3.16):

$$\sigma_{flexure} = \frac{M y}{I} = \frac{6 M}{b h^2} = \frac{6 M}{h^3} \quad (3.16)$$

In this equation

$\sigma_{flexure}$ = Flexural strength or MOR (MPa)

M = Moment at peak load (N.mm)

b = Width of the prism (mm)

h = Overall depth of the prism (mm)

3.3.3 Splitting strength

The procedure for the splitting test is based on (ASTM C496/C496M – 17, 2011) for concrete cylinders (100 mm x 200 mm) using the same Controls Pilot testing machine as the compression cylinders. The former were laid on their side to apply a linear load. The loading rate was modified to be 1 MPa/min to shorten the time required for the test (Dean and Graybeal, 2006). The test setup is conducted in a way to develop tensile stresses that once it reaches the concrete's tensile strength, longitudinal cracks will develop as shown in Figure 3-27.

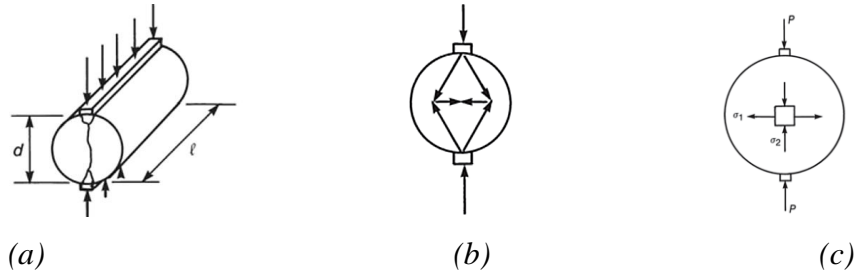


Figure 3-27 (a) Test procedure (b) simplified force system (c) stresses on element (Wight and MacGregor, 2012)

The maximum splitting tensile stress in the center of the specimen is calculated from Equation (3.17):

$$T = \frac{2 P}{\pi d l} \quad (3.17)$$

T = Splitting tensile stress (MPa)

P = Maximum applied load recorded on the Controls Pilot testing machine (N)

d = Average measured diameter of the cylinder (mm)

l = Average measured length of the cylinder (mm)

A plywood piece was cut into 3 mm thick strips, 25 mm width and 345 mm long. After the lateral surface of the cylinder was marked with two parallel lines, the specimen was placed between the two bearing strips as shown in Figure 3-28. Moreover, an additional 50 mm wide steel bearing plate was placed on top of the upper plywood since the upper bearing block of the Controls Pilot testing machine was smaller than the length of the cylinder.

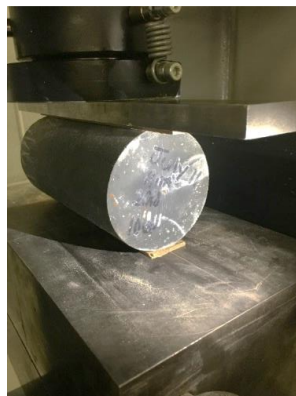


Figure 3-28 Splitting tensile test in the Controls Pilot testing machine

3.3.4 Fiber Distribution

Some of the prisms tested under flexure were cut at a section near the failure area. Thus, the smoothed cross-section was photographed to analyze the steel fibers distribution based on the “image analysis technique”. The purpose is to determine the number of fibers per unit cross-sectional area. The diameter of the steel fibers used were 0.2mm. The cross-sections were subject to a bright light to separate the steel fibers from the concrete matrix itself. On each image, the cross-section is divided into identical squares, where the number of fiber present in each section were calculated for each section. Based on that, the total number of fibers present in the concerned cross-section can be calculated.

The equation to estimate the number of fibers per unit area was given in Equation (3.18) proposed by (Georgiou and Pantazopoulou, 2016):

$$n_f = \frac{\rho_f \alpha_2}{A_f} = \frac{4 \rho_f \alpha_2}{\pi d_f^2} = \frac{4 \times 2.5\% \times 0.5}{\pi (0.2)^2} \quad (3.18)$$

In this equation:

n_f = Number of fibers per unit area

ρ_f = Volumetric ratio of fibers = 2.5% for the in-house design mixture chosen

α_2 = Fiber orientation factor = 0.5 for a random orientation of fibers

d_f = Fiber diameter = 0.2 mm

Based on the information given, the number of fibers per area of (10mm x 10mm) should be:

$$n_f = 39.78$$

Moreover, for a cross-section of 75 mm x 75 mm considered as 64 sections of the unit area, the total of steel fibers N_f present should be:

$$N_f = n_f \times 64 = 2545 \text{ fibers in } 5625 \text{ mm}^2$$

3.3.5 Reinforcement properties

Direct tension pullout tests were conducted according to the ASTM E8 Tension Testing of Metallic Materials to determine the properties of the tested reinforcing bars: 10M and 15M. Firstly, the 10M reinforcing bar presented a yielding strength of 440 MPa and a yield strain of 0.31 %. The onset of strain hardening was around 16 me with an ultimate tensile strength of 624 MPa. Secondly, the yielding strength of the 15M reinforcing was about 425 MPa and ultimate tensile strength of 584 MPa. For this reinforcing bar, the onset of strain hardening was around 12 me.

Chapter 4. Execution of the experimental program

This chapter will discuss the execution of the entire experimental program starting with the construction of the wood formwork and the preparation of the specimens. Afterwards, it will thoroughly describe the batching, mixing, casting and curing of the commercial and in-house design mixes. Moreover, a detailed explanation will be given regarding the procedure followed to prepare the beams for testing. Lastly, it will present the experimental setup to be conducted.

4.1 Preparation of the wood formwork for the beams

For more accurate results, it is advised to have three samples for each test experiment conducted. Thus, three additional wooden beams were designed to match the available steel beams. The beams were formed in a way to be easily connected or separated. Each beam is mainly composed of 5 different pieces, as shown in Figure 4-1: one base panel, two longitudinal side panels and 2 square side panels.

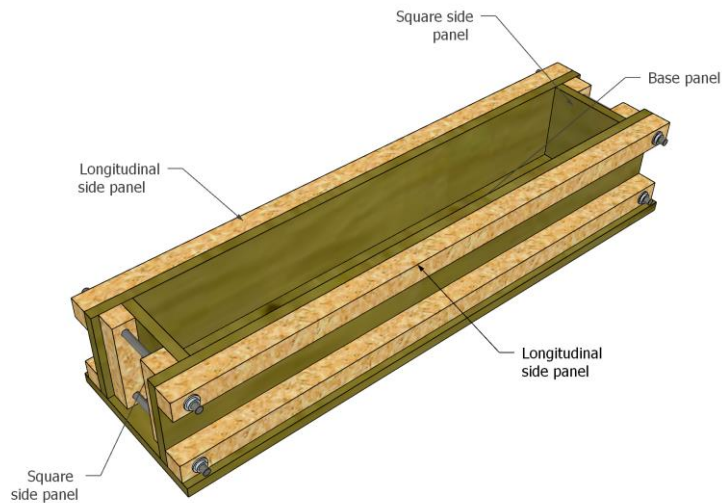


Figure 4-1 3-D drawing of the beam formwork

All the materials required to design three beams were purchased from Home Depot (Home Depot, 2018) and are presented in Table C-2 in Appendix C. The tools used to assemble them are presented in Table C-5. The plywood panel presented in Table C-2 (a) was used to form the base and the four

sides of the three beams. The former was cut into different parts as shown in Figure 4-2 with their appropriate dimensions as presented in Table 4-1.

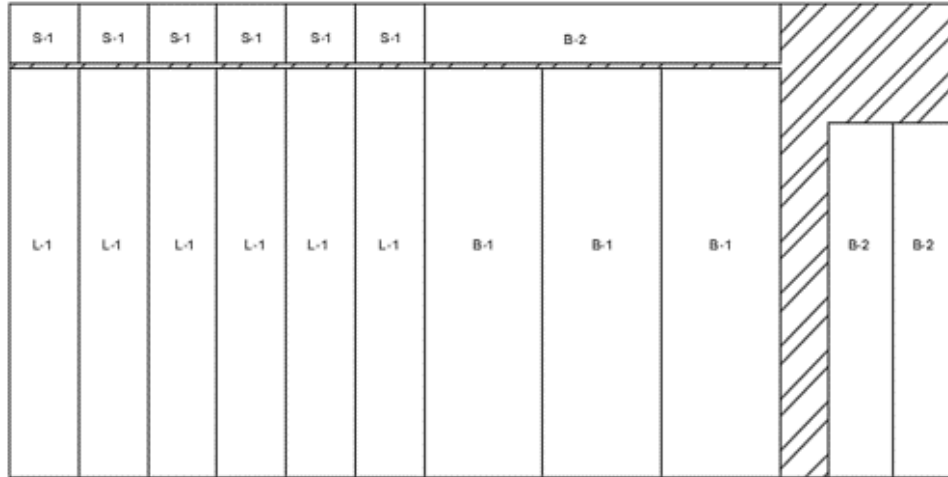


Figure 4-2 Partitioning of the plywood for the three beams (hatch part is waste)

Table 4-1 Cut-parts of the plywood and dimensions per beam

Cut-parts	Dimensions (width x length) (inches)	Number/beam
B-1 (Base 1)	11.5 x 41.5	1
B-2 (Base 2)	6 x 36	1
L-1 (Longitudinal 1)	6.75 x 41.5	2
S-1 (Side 1)	6 x 6	2

In addition, timber wood was cut according to the quantity and dimension presented in Table 4-2. The timber blocks are considered supports, preventing the opening of the lateral sides during casting due to the liquid concrete's lateral pressure.

Table 4-2 Type of timbers cut and length per beam

Timbers	Length (inches)	Number/beam
T _h	41.5	4
T _{v-1}	6.75	4

To form the base of the beams, the wood piece B-2 is centered and screwed on the base B-1 as depicted in Figure 4-3. Since the thickness of the plywood is chosen 0.75 inches, both panels were

attached together using the drilling tool presented in Table C-5 and $1^{1/4}$ in. long screws from Table C-2 (d). The wood piece B-2 constitutes the lower base of the beam.

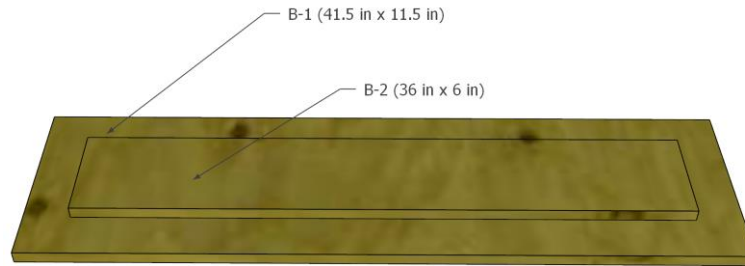


Figure 4-3 Base panel of the beam by screwing base B1 on top of base B2

Afterwards, the two identical longitudinal side panels were formed using part L-1 as their base along with four, 2x2 in. timber pieces as can be seen in Figure 4-4. The two horizontal T_h pieces were bolted to the lower and upper part of the external face of the wood board using the $8 \times 1^{1/4}$ in. bolts (ref Table C-2 (d)) to strengthen the sideboard against the pressure of the liquid concrete as mentioned previously. The other two vertical pieces T_{v-1} are attached to the internal side of the wood panel as support, for the side square panels S-1 forming the cross-section of the beam from opening. Moreover, considering the length of the beam (36''), and the thickness of the square side panels to be 0.75 inches each, the 2x2 in. pieces are screwed to the board to be internally distant by 37.5 in. In addition, for both side panels, a 3.75 in. deep hole is drilled through the upper and lower horizontal timber T_h pieces, the longitudinal wood panel (L-1) and the vertical piece T_{v-1} as depicted in Figure 4-4.

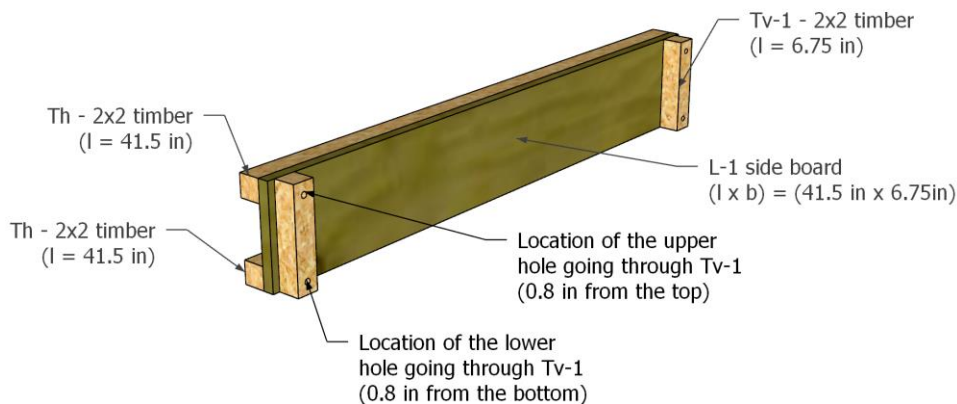


Figure 4-4 One side panel of the beam formed by the base S-1 along with the two types of 2x2 in. timber T_h and T_{v1}

As can be seen in Figure 4-5, a steel rod is then inserted in the opposite holes of each panel then tied with the washers and wing-nuts exerting confining pressure on the formwork and mainly the side square panel S-1.

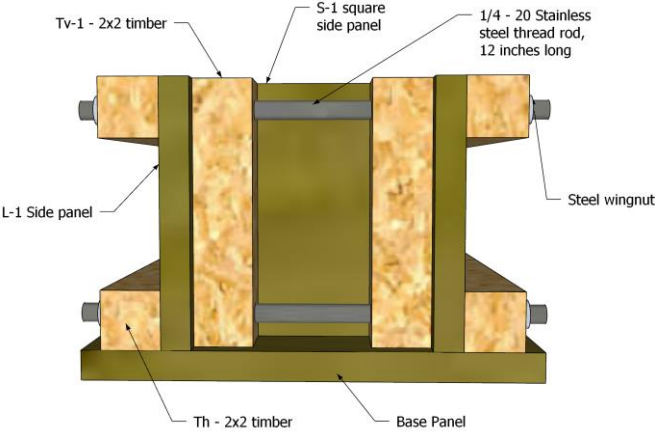


Figure 4-5 Detailing of the stainless-steel thread rod to hold all the parts together

In preparation for the casting, both the wood and the steel formwork were oiled thoroughly for easy demolding of the specimen as shown in Figure 4-6.



Figure 4-6 Oiling of the wood and steel formwork

4.2 Preparation of the specimens

Twenty specimens were prepared according to the parameters of the study proposed and cast as seen in Table 4-3. Therefore, the beams were grouped in three categories depending on the design mix used, where each one is divided into two or three beams differing by the concrete cover and the embedment length.

Specimen designation is divided into three parts. The first letter corresponds the first initial of the concrete mix used K, F and I where K is for the commercial K's specimens, F for the commercial F's specimens and I indicated the in-house design mix proposed. The second notation indicated the embedment length studied where E1, E2, E3 and E4 correspond to the embedment lengths of $5d_b$, $10d_b$, $15d_b$ and fully bonded respectively. The third notation corresponds to the proposed concrete cover C1 and C2, where C1 considers a cover of $1d_b$ and C2 considers a cover of $2d_b$. In addition, most of the specimens were replicated 2-3 times, and the similarity in the response illustrates the accuracy, and repeatability of the experimental tests.

Table 4-3 Specimen annotation according to the parameters considered

Design Mix	King	Facca	In-house
Concrete cover	2 KE1C1 - 2 KE1C2 1 KE4C1 – 1 KE4C2	2 FE1C1 & 1 FE1C2 1 FE4C1	3 IE1C1 & 3 IE1C2
Embedment length	0	0	3 IE2C2 & 3 IE3C2
Total	6	4	12

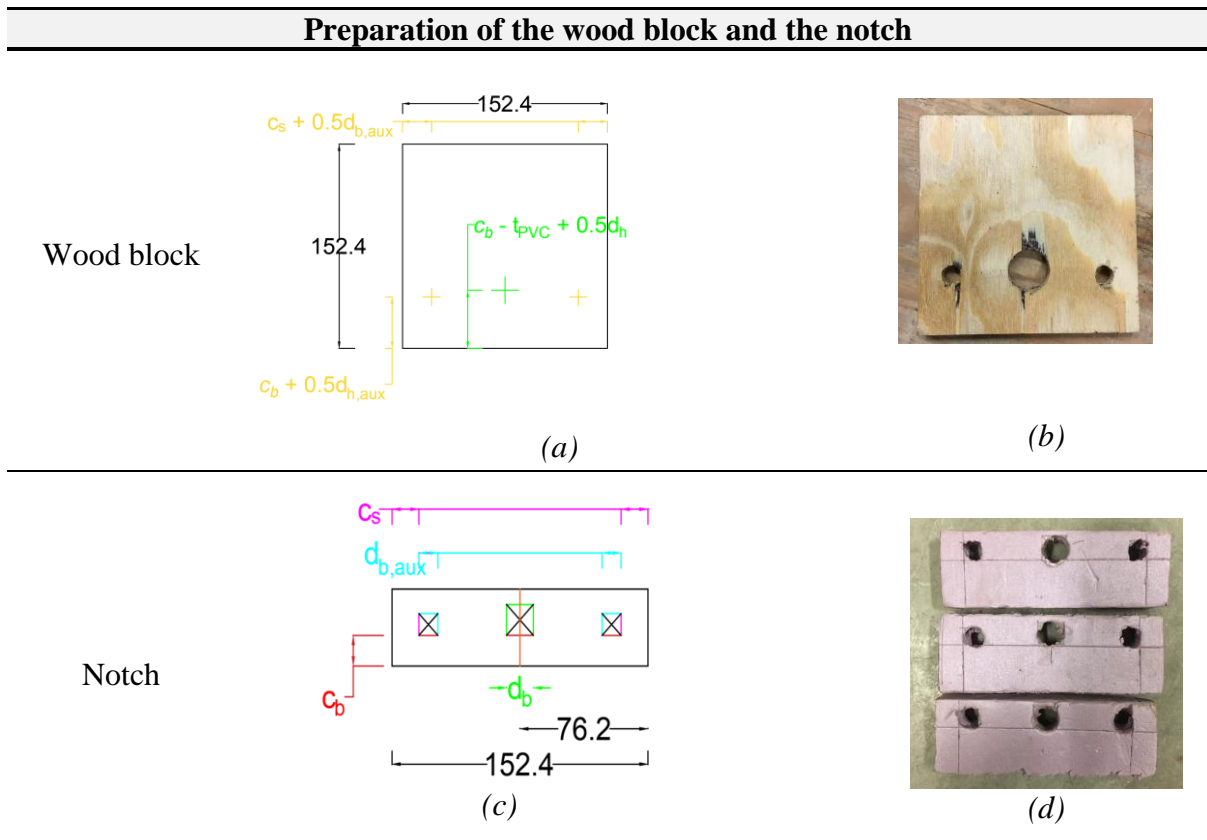
Table C-3 presents all the necessary materials used to build the specific setup (all purchased from local suppliers). All the beams were prepared using the same procedure, materials, and tools. Firstly, the wood block was cut at Home Depot with the same dimensions as the cross-section of the beam ($6'' \times 6''$) = (152 mm x 152 mm) using the plywood from Table C-2 (a). Based on the calculations obtained in Section 3.1.5 from Table 3-6, the center of the hole for the auxiliary bars and the main reinforcing bar are marked depending on the concrete cover chosen and the presence of the PVC pipe. The wood block is then fixed on the bench vise (ref Table C-5 (c)) where, using the drill (ref Table

C-5 (b)) along with the drill bit (ref Table C-5 (d)), a small hole was pierced through the wood to mark the center. Afterwards, depending on the case setup, a spade bit (Table C-5 (e), (f) and (g)) is chosen to finalize the drilling for the 15M bar with PVC and without PVC and the 10M bars, respectively.

The notch was cut in rectangle shapes with a blade knife where the center of the holes was marked based on Table 3-5. A small hole was perforated manually using the sharp edge of a compass since the foam material was fragile. Afterwards, the edge of the reinforcing bar was inserted by a torsional motion halfway through the notch for the auxiliary bars while all the way through for the main bar.

Table 4-4 (a) and (b) present an example of a wood block for the case of a concrete cover equal to twice the bar diameter $c = 2d_b$ taking into consideration the presence of PVC pipe in the wood block. Similarly, the example of the notch prepared is shown in Table 4-4 (c) and (d).

Table 4-4 Marking of the center of the holes for the wood block and notch



The different embedment lengths were dependent on the length of both the PVC pipes and auxiliary bars. Table 4-5 presents the length measurement for the 15M, 10M and PVC pipe extracted from the drawings of Section 3.1.4.4.

Table 4-5 Dimensions of the steel bars and the PVC pipe (mm)

Length (mm)	$l_b = 5 d_b$	$l_b = 10 d_b$	$l_b = 15 d_b$	Fully bonded
15 M bar	916	894	894	916
10M bar	476.3	546.3	587.2	476.3
PVC pipe	383.6	373.6	340.9	N/A

All reinforcing bars are marked according to their lengths as seen in Figure 4-7, and then cut accordingly with the cutting, and bending rebar saw mentioned in Table C-5 (a). Moreover, the ends of the reinforcing bars were smoothed to remove any sharp edges during the setup using the bench grinder in Table C-5 (h). The PVC pipes were cut as well.



Figure 4-7 Marking of the reinforcing bars

For the $10d_b$ and $15d_b$ embedment lengths, the 15M reinforcing was cut in shorter lengths of 894 mm as presented in Table 4-5 to attach a T-head steel plate. In fact, the steel plate presented in Table C-3 (e) is then cut into small squares of 50 mm x 50 mm as shown in Figure 4-8 (a) and (b). Afterwards, a T-head steel plate was welded on the reinforcing bar as seen in Figure 4-8 (c).

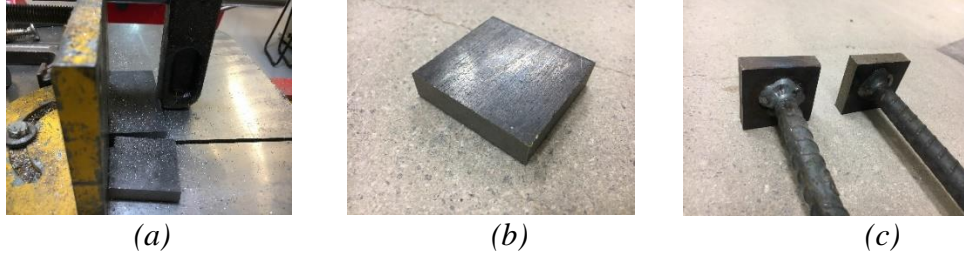


Figure 4-8 (a) Cutting of steel plate (b) T-head (50 mm x 50 mm) and (c) welded reinforcing bar and T-head plate

Figure 4-9 and Figure 4-10 present examples of the materials prepared as discussed previously to form the setups presented in Section 3.1.4.4.1 and Section 3.1.4.4.4, respectively.



Figure 4-9 (a) Blockwood, notch, PVC pipe and steel bars prepared for an $l_b = 5d_b$ and $c = 1d_b$ (b) $c = 2d_b$

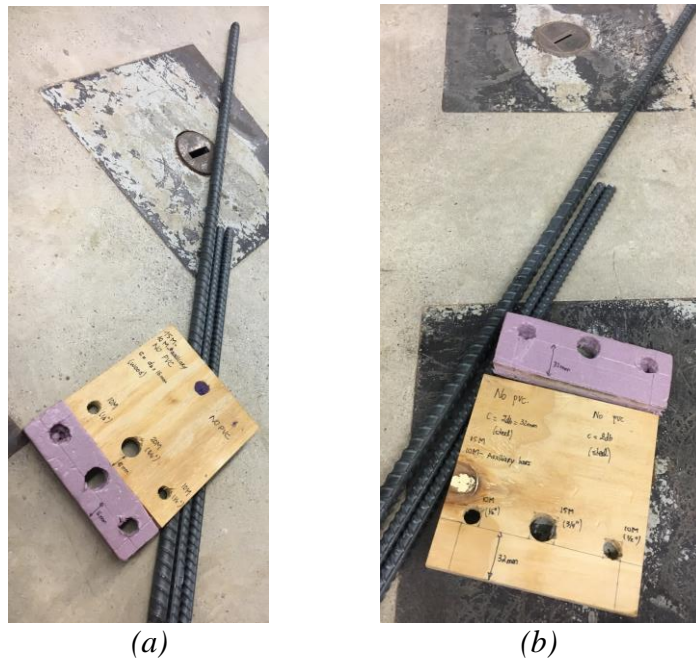


Figure 4-10 (a) Block wood, notch, PVC pipe and steel bars prepared for a fully bonded bar and $c = 1d_b$ (b) $c = 2d_b$

Moreover, Figure 4-11 (a), Figure 4-12 and Figure 4-13 (a) and Figure 4-14 present the test setup presented in Section 3.1.4.4.1, Section 3.1.4.4.2 and Section 3.1.4.4.4 for a $5d_b$, $10d_b$ and $15d_b$ embedment length and a fully bonded bar, respectively. An example of the development length was shown in Figure 4-11 (b) for a $5d_b$ bonded length of 80 mm. Moreover, Figure 4-13 (b) shows the bar with the T-head reinforcing bar.

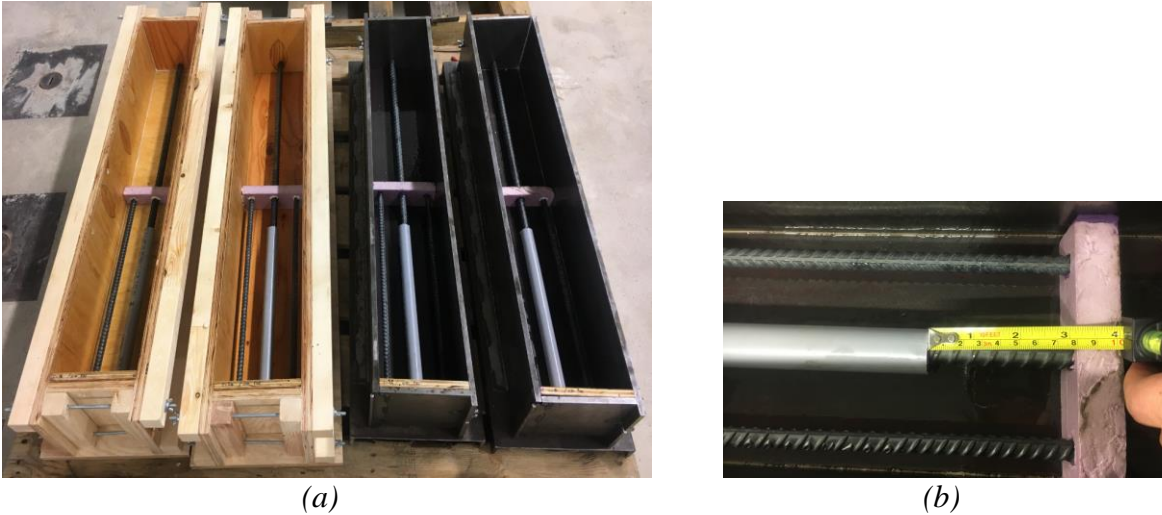


Figure 4-11 (a) Setup for the embedment length of $5d_b$ and verification (b)



Figure 4-12 Setup for the embedment length of $10d_b$



(a)



(b)

Figure 4-13 (a) Setup for the embedment length of $15d_b$ and (b) detailing of the T-head bar



Figure 4-14 Setup for the fully bonded beams

4.3 Batching, casting and curing of the different mixes

All the design mixes were conducted in the concrete room of the high-bay laboratory. The mixing was done using the Creteangle mixer (ref Table C-1) as shown in Figure 4-15.



Figure 4-15 Setup of the mixing station

It is known that the batching, casting and curing method is similar for all the design mixes. Therefore they will be explained in Section 4.3.1. Moreover, the volume required for each of the following castings depended initially on the number of beams to be cast per batch, the compression cylinders, and the flexural prisms. Table 4-6 presents the unit volume for each specimen to be considered for the batching procedure.

Table 4-6 Volume required per specimen

Specimens	Dimensions (mm)		Volume (L)
Beams	b	152.4	21.27
	h	152.4	
	l	916	
Long Prisms	b	75	2.81
	h	75	
	l	500	
Short Prisms	b	75	1.58
	h	75	
	l	280	
Compression cylinders	\emptyset	75	0.6
	h	150	
Splitting cylinders	\emptyset	150	5.3
	h	300	

Both companies conducted the same flow test procedure based on (ASTM-C230, 2010) for testing of hydraulic cement while the in-house design mixture followed (ASTM C1856, 2017) used for fabricating and testing specimens of UHPC. The main difference between both tests is that the former measures two values. The first value is the average of the two diameters, two minutes after lifting the mold known as the “static” flow. The second value accounts for 20 drops and is considered as the “dynamic” flow. However, (ASTM C1856, 2017) only measures the “static” flow.

4.3.1 Commercial K

4.3.1.1 Material, design mix proportions and batching

The company K provided all the necessary materials on February 14, 2018. They also provided the technical support to perform the mixing. They delivered 25 kg ready-mix bags of dry mix materials without providing any information about what they contained. However, since the design mixture is based on UHPC, it was thought to contain fine aggregates and cementitious materials. In terms of the wet materials, water was used in liquid and solid (ice) state along with two types of admixtures (Additive A and Additive B). The ice was used to slow down the cementitious hydration reaction, permitting more time to mix and measure the fresh properties. No details were provided concerning the admixtures. Moreover, short steel fibers ($\ell_f = 13 \text{ mm}$; $\varnothing_f = 0.2 \text{ mm}$) were used. These materials were batched according to a total volume of 200 L based on the proportions provided by the company presented in Table 4-7. Prior to mixing, the first half of the water is added to the Admixture A and stirred to obtain a homogenous fusion while the second half is poured on top of the ice. No pictures were provided for this concrete since they were all labeled.

Table 4-7 Design mix proportions for 200 L (company K)

Constituents	Kg/m ³	Kg
Pre-mix Dry Material	1912.66	382.53
Liquid Material	Water	29.464
	Ice	9.822
	Admixture A	9.592
	Admixture B	5.03
Steel Fibers	156	31.2

4.3.1.2 Mixing procedure

Firstly, the mixed bag of dry material is added inside the pan of the mixer presented in Figure 4-16 and mixed for about 2 minutes. Afterwards, the combined water with admixture A is gradually added in during 20 seconds. Subsequently, for an additional 20 seconds, the blend of water and ice are incorporated progressively and stirred. As can be seen in Figure 4-16, all the constituents mentioned previously were mixed for about 3 minutes.



Figure 4-16 Addition of the wet additives on top of the pre-mixed dry materials

In the following step, admixture B is added while the mixing carries on for about 1 minute. Figure 4-17 depicts the proceeding phase where steel fibers are gradually added into the mix. Once all the steel fibers are incorporated, the mixing continues for 2 additional minutes.



Figure 4-17 Addition of steel fibers

A workability test was conducted to verify the fresh properties of the mixture, reaching 210 mm shown in Figure 4-18 (a) . After the verification of the flow test and before casting, the concrete is mixed for the last time between 2 to 3 minutes as presented in Figure 4-18 (b). The company advised covering the concrete with a plastic sheet while casting to prevent the formation of a thick hardened layer on the surface as depicted in Figure 4-18 (c).

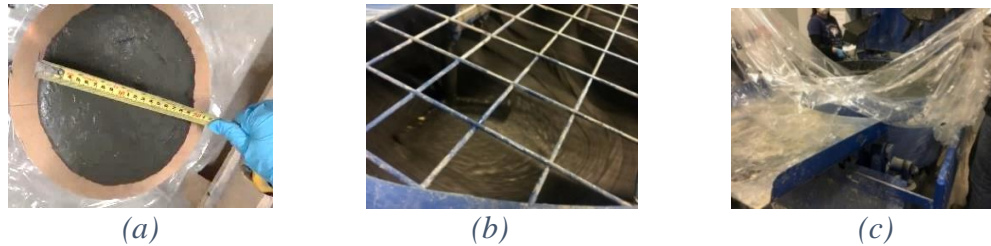


Figure 4-18 (a) Flow test, (b) final mixing after reaching the wanted workability and before casting (c) Covering of the concrete surface during the flowability test and casting

4.3.1.3 Casting and curing

This phase was conducted for all the design mixes once the flowability of the design mixture proposed was reached. The pan was lifted as can be seen in Figure 4-19 (a), and concrete was poured into plastic buckets as can be seen in Figure 4-19 (b) and (c).

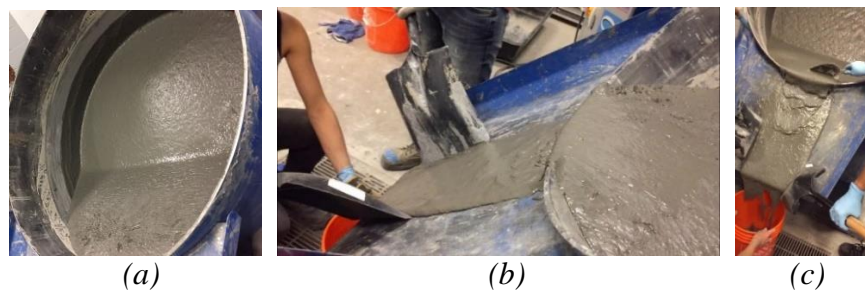


Figure 4-19 Emptying the concrete from the mixing pan (In-house C2 mix)

The buckets were then carried and directly poured inside the formworks following a layered motion as described in Table 4-8 (a). The casting procedure followed (ASTM C1856, 2017) where all the specimens (cylinders, prisms) were filled in one layer. However, the beams were filled according to the available buckets. For the “stiff” UHP-SFRC batches, an additional external vibration was provided using a rubber hammer. The number of hits based on the standards varied around 30 times, yet it stopped once the concrete filled all the corners and around the reinforcement. Another reason for the manual external vibration is to eliminate entrapped air. Once the formworks were filled, they were covered by a plastic sheet as seen in Table 4-8 (b) to prevent any loss of the necessary water for the hydration of the concrete. Table 4-8 (c) presents the demolded specimens two days after casting. They were then covered with wet burlap sheets and a vapour barrier (ref Table C-1). Finally, the beams were stored in the basement of the High-Bay lab considering an ambient temperature for curing until the testing day as presented in Table 4-8 (d). Every week, the beams were hosed with regular

water. The design mixture corresponding to Commercial K resulted in six beams as described in Table 4-3: 2 KE1C1, 2 KE1C2, 1 KE4C1, and 1 KE4C2.

Table 4-8 Casting, curing, demolding and storing of the concrete specimens

Phase	Description
Casting	 <p style="text-align: center;">(a)</p>
Curing	 <p style="text-align: center;">(b)</p>
Demolding	 <p style="text-align: center;">(c)</p>
Storing	 <p style="text-align: center;">(d)</p>

4.3.2 Commercial F

4.3.2.1 Material, design mix proportions and batching

On February 28th 2018, a representative from Company F delivered all the necessary materials to batch and mix their proper UHP-SFRC following a defined mixing procedure and additional supplies differing from the company K. The company had its own ready Drymix material shipped in bulk bags containing sand and cementitious materials (ref: Table 4-9 (a)). In addition, Table 4-9 (b) shows the wet mix material containing the ready mixed water and admixtures. Two types of fiber were used having the same length and diameter ($\ell_f = 13 \text{ mm}$; $\varnothing_f = 0.2 \text{ mm}$). The first type, referred to as Type 1, is short and curved as seen in Table 4-9 (c) while the second, known as Type 2, presents hooked ends (ref Table 4-9 (d)). The company had additional small samples of dry and wet ready mix materials as presented in Table 4-9 (e) and (f) added to the mix to adjust the desired flowability.

Table 4-9 Materials used for the design mixture of company F

Material	Description			
Drymix (a) Wet mix (b)	 (a)		 (b)	
Steel fibers Type 1 - (c) Type 2 - (d)	 (c)		 (d)	
Additives: Drymix (e) Wetmix (f)	 (e)		 (f)	

The company itself prepared all the needed quantities ahead of time for a volume of 80 L as described in Table 4-10. Therefore, the only required procedure was to empty the dry material placed in the bulk bag in pails to be able to carry them and pour them in the mixing pan.

Table 4-10 Design mix proportions for 80 L (company F)

Constituents	Quantity	Measuring unit
Drymix	1	Bulk bag
Wet mix	5	Gallon Pail
Steel Fibre – Type 1	5	Gallon Pail
Steel Fibre – Type 2	5	Gallon Pail
Wet mix additive	3	Liter bottle
Drymix additive	1	4" cylinder molds

4.3.2.2 Mixing procedure

Firstly, all the dry mix materials were emptied in the mixing pan and mixed for 1 minute and 30 seconds as demonstrated in Figure 4-20 (a). Afterwards, five-gallon pails of the wet mix were added and blended for 16 minutes as presented in Figure 4-20 (b). The mixture is shown in Figure 4-20 (c) and considered in a “plastic state”.

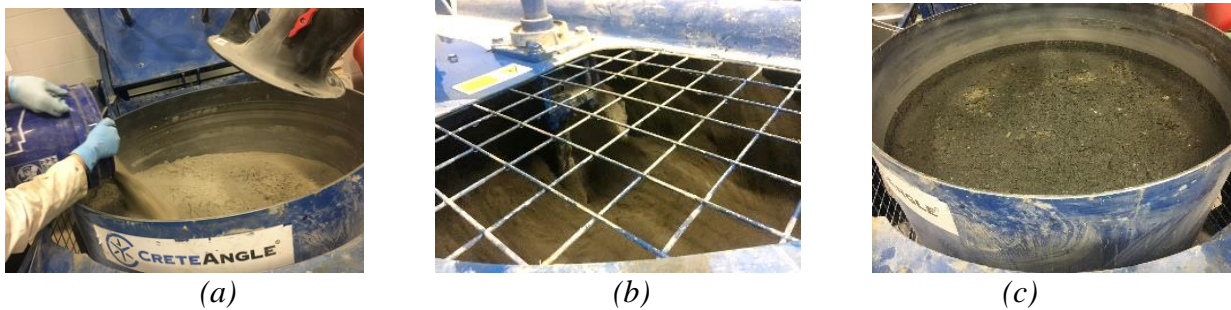


Figure 4-20 (a) Addition of the drymix and wet mix, (b) mixing and (c) plastic state

A flow test was then done for this state of the material using the flow table presented in Table C-1. The surface of the table was cleaned as seen in Figure 4-21 (a), where a small sample of the concrete was poured onto the mold (ref Figure 4-21 (b)). Different flow tests were conducted on the UHPC to achieve an acceptable flowability test result. In case the flow diameter was less than the 220 ± 20 mm target, the mixture was considered too stiff. Thus, a bottle of wet mix additive was needed.

However, if the flow diameter was greater than the target flow, a cylinder of dry mix additive was then added. Once the aimed value was reached, steel fibers were added, and a final flow test was realized.



Figure 4-21 Preparation of (a) the table surface and (b) pouring the sample in the mold

The first flowability test resulted in an average static flow diameter of 122 mm, as seen in Table 4-11 (a). The table was then dropped 20 times, and the dynamic diameter increased to 145 mm as presented in Table 4-11 (b). It was evident that the result obtained was below the optimal value. Therefore, two bottles of wet mix additives were poured into the mix as shown in Figure 4-22. They were mixed afterwards for two additional minutes.



Figure 4-22 Addition of two wet mix additives to increase the flowability of the mixture

The second flow test was then conducted. The average flow diameter increased, and reached 177 mm prior to the drop of the table as seen in Table 4-11 (c), and was around 193 mm after the 20 manual drops as depicted in Table 4-11 (d). Even though these values increased, they were still less than the required threshold. Therefore, one more bottle of wet mix additives was added to the mixture and then mixed for two minutes. Table 4-11 (e) and (f) present the results of the third flow test with 210 mm flow diameter pre-impact and 253 mm post-impact. This value exceeded the necessary flow value by 20 mm. Dry mix additives were added to the entire mixture and then mixed for two additional

minutes. At this stage, the representative advised, based on his experience, not to conduct an additional flow test to prevent any heating of the material for this long period of setting time. The steel fibers were gradually added as shown in Figure 4-23 (a) and then mixed for about three minutes as demonstrated in Figure 4-23 (b).



Figure 4-23 (a) Addition of steel fibers Type 1 and Type 2 and (b) mixing

The last flow test was conducted when all the steel fibers were merged properly inside the mixture. The results are shown in Table 4-11 (g) and (h) with a final dynamic flow test about 210 mm which fits the requirements perfectly. Thus, the mix is ready to be cast. For this design mixtures, four beams were cast in total as described in Table 4-3; 2 FE1C1, 2 FE1C2, and 1FE4C1.

Table 4-11 Measured diameters of different flow test to obtain the optimal value

Flow test attempts	Static flow (mm)	Dynamic flow (mm)
1	 (a) (D ₁ D ₂ D ₃) = (120 125 120)	 (b) (D ₁ D ₂ D ₃) = (145 145 145)
2	 (c) (D ₁ D ₂ D ₃) = (175 180 175)	 (d) (D ₁ D ₂ D ₃) = (200 190 190)

3		
	(e)	(f)
	$(D_1 D_2 D_3) = (205 205 220)$	$(D_1 D_2 D_3) = (250 260 250)$
4		
	(g)	(h)
	$(D_1 D_2 D_3) = (185 195 210)$	$(D_1 D_2 D_3) = (210 220 210)$

4.3.3 In-house mix

4.3.3.1 Material, design mix proportions and batching

Five different batches were developed for the in-house mix design to cast 12 different beams along with prisms and cylinders and companion specimens of a parallel experimental study using DTP specimens. Thus, each batch required a specific concrete volume as can be seen in Table 4-12. All the batches use the same materials and the same design mix proportions presented in Table B-21 apart from the superplasticizer SP3. The amount of SP3 is explained in Step 3 of the mixing procedure discussed in Section 4.3.3.2.

Moreover, the size effect is another parameter that influences the amount of superplasticizers added to obtain the same flow test value. By comparing the casting of C2 and C3 shown in Table 4-12, it can be seen that C2 consumed all the superplasticizers to reach a flowability of 230 mm while casting C3 required 11.814 kg/m³ of SP3.

Table 4-12 Design mixture proportions for all the in-house design mixes

Material	(kg/m ³)	06/11/2018		06/22/2018	07/11/2018	07/12/2018
		C2, V= 50L (kg)	C3,V=100L (kg)	C4,V=75L (kg)	C5, V= 90L (kg)	C6, V=90L (kg)
C2	724.13	36.207	72.413	54.31	65.17	65.17
S3	668.60	33.43	66.86	50.145	60.17	60.17
Slg2	362.06	18.103	36.206	27.154	32.585	32.585
SF2	120.69	6.03	12.07	9.052	10.86	10.86
SP3	12	0.6	1.2 - 0.186	0.9 - 0.07	1.08-0.0989	1.08-0.1
W	241.13	12.06	24.11	18.01	21.7	21.7
SSF	195.75	9.79	19.58	14.68	17.62	17.62

All the materials are weighed in pails depending on the amount needed. Cold water was used in all mixes, where it was weighed and placed in the refrigerator one day before each casting. In addition, the superplasticizer is weighed in two portions, the first to be added on top of the cold water while the second is retained by itself corresponding, respectively, to the left and right pail in Figure 4-24.



Figure 4-24 Bucket containing water and half of SP3 (left) half of SP3 (right)

4.3.3.2 Mixing procedure

The mixing procedure is identical to all the batches and the trial batch B9 (ref Table B-21). Initially, all the dry materials are added in the mixing pan in the following order: SF2, Slg2, C2 and S3 corresponding to Table 4-13 (a), (b), (c) and (d). They are then mixed for 5 minutes until a completely dry and blend state is obtained as seen in Table 4-13 (e). In the second step, the mixture of both the cold water and half of the superplasticizer is added gradually while the pan is rotating as depicted in Table 4-13 (f). During the 5 minutes of mixing, solid balls presenting a wet yet solid surface were

forming as shown in Table 4-13 (g) and (h). Table 4-13 (i) presents the resting 10 minutes phase of the mix in its “wet state” providing time for the materials to react together. Table 4-13 (j) is the first part of Step 3 starting with the gradual addition of the second half of SP3 determining the margin of the flowability of the mixture. After a couple of minutes of mixing, the amount of small balls multiplies where their surface becomes saturated and wet shown in Table 4-13 (k) and (l). While adding small portions of SP3 and mixing, these small balls merge together forming bigger plastic balls as can be seen in Table 4-13 (m). Lastly, Table 4-13 (n) and (o) shows their fusion into one plastic paste. The liquid state in Table 4-13 (p) is the point where the mixing is stopped, and the first flowability test is conducted. The addition of SP3 must reach a flow test of 220-230 mm for the matrix without fibers depicting the last phase of step 3 presented in Table 4-13 (q). At this state, step 4 starts with the addition of steel fibers as can be seen in Table 4-13 (r) for 5 minutes. Afterwards, the second series of flowability test is conducted on the mixture to verify the flowability is approximately 210 mm. If not, superplasticizers are added, and the concrete is mixed for 2 minutes until a second flow test is conducted. Once the targeted workability is obtained, casting can begin.

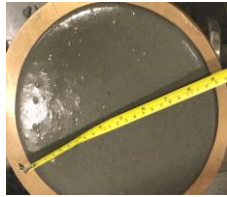
Table 4-13 Mixing procedure for the in-house design mixture divided into different steps

Steps	Description			
Step 1 (Dry state)	 <p data-bbox="508 1409 553 1444">(a)</p>	 <p data-bbox="776 1409 821 1444">(b)</p>	 <p data-bbox="1016 1409 1062 1444">(c)</p>	 <p data-bbox="1292 1409 1338 1444">(d)</p>
	 <p data-bbox="914 1759 959 1795">(e)</p>			

Steps	Description				
Step 2 (Wet state)	 <i>(f)</i>	 <i>(g)</i>	 <i>(h)</i>		
	 <i>(i)</i>				
	Step 3 (Liquid state)	 <i>(j)</i>	 <i>(k)</i>	 <i>(l)</i>	 <i>(m)</i>
		 <i>(n)</i>	 <i>(o)</i>	 <i>(p)</i>	 <i>(q)</i>
Step 4 (Addition of steel fibers)		 <i>(r)</i>			
		 <i>(s)</i>			

During step 3 of mixing batch C2, several flow tests were conducted where each time a small amount of SP3 was added until the flow value was 220-230 mm. The increase in the diameter is evident through the progression seen in Table 4-14 (a-d). At the end of step 4, it is evident from Table 4-14 (e) that the flow value decreases. In this phase, SP3 is added as well until the flow value reaches 210 mm as seen in Table 4-14 (f). The same procedure was followed for all the in-house batches C3, C4, C5, and C6 as shown in Table B-22, Table B-23, Table B-24 and Table B-25, respectively. Each batch covered one series of 3 beams where C2 was cast in the specimens IE1C2, C4 for the beams IE1C1, C5 for IE3C2 and C6 for IE2C2.

Table 4-14 Flow tests for batch C2 of the in-house design mix

Casting	Flow test 1	Flow test 2	Flow test 3	Flow test 4
				
	(a)	(b)	(c)	(d)
	(D ₁ D ₂) = (160 155)	(D ₁ D ₂) = (175 185)	(D ₁ D ₂) = (210 195)	(D ₁ D ₂) = (220 225)
C2				
				
	(e)	(f)		
	(D ₁ D ₂) = (180 185)	(D ₁ D ₂) = (210 207)		

It is evident that even if the commercial and in-house design mixtures followed two different flow tests, the flow value before dropping the table in Table 4-11 (g) is close to the values of the in-house design mixes which fluctuates between 200 and 210 mm. Moreover, from the different volumes cast, it is evident that the amount of superplasticizer used is inversely proportional to the concrete volume. Figure 4-25 shows that the amount of superplasticizer decreases with an increase of the batch volume.

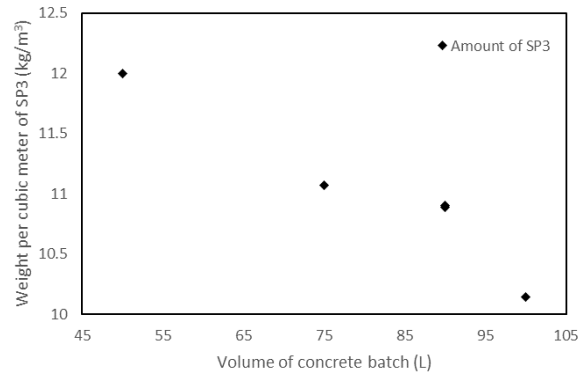


Figure 4-25 Size effect on the amount of superplasticizer used

4.3.3.3 Error during casting

The concrete obtained from casting C2 did not fill all the specimens entirely. Figure 4-26 presents the beam IE1C2 -C- that was left unfilled with 20 mm remaining at the top. Thus, another mixture C3 needed to be realized to fill in the gap. Meanwhile, the top of the beam was roughened then covered with plastic sheets and wet burlap in order to prevent the solidification of the concrete and the formation of a cold joint between the concrete of mix C2 and mix C3. However, this beam was tested to verify the effect of a cold joint on the behavior of the beam.



Figure 4-26 Roughening of the surface of beam IE1C2

C3 was cast in all the IE1C1 beams. However, after demolding the specimens, it became obvious that the specimens were poorly consolidated as shown in Figure 4-27. This can be explained by the fact

that these beams were cast last where the concrete could have reached a hardened state. This beam was as well tested later to determine the capacity of a damaged UHP-SFRC beam.



Figure 4-27 Poorly consolidated beam from batch C3

4.4 Adjustments of the specimens for testing

Prior to testing, the specimens were removed from the curing area of the basement of the High-Bay lab. The foam notch was then removed as can be seen in Figure 4-28.



Figure 4-28 (a) Removal of the foam board and (b) extension of the auxiliary bars

Based on the designs, the notch was considered as a cover chair for the auxiliary bars. Therefore, the auxiliary bars were blocking sight of the primary reinforcing bars as seen in Figure 4-29 (a). To avoid any complication during the DIC of the principle reinforcing bar, the extended parts of the auxiliary bars were removed using a cut metal saw presented in Table C-5 to clear the optical path as shown in Figure 4-29 (b). The reinforcing bar was cleaned from all the playdough used previously to close any openings in the formwork.



(a)



(b)

Figure 4-29: Cutting of the auxiliary bars

Another problem encountered was the upper poured surfaces of the beams that were not level and needed to be smoothed to be subjected to a proper symmetrical loading. In addition, the steel frames placed to measure the deflection during testing required a flat and even surface. To solve the problem, one option was proposed: place a high strength gypsum plaster on top surface. The location of the plaster on the top surface are presented in Figure 3-14.

USG Industrial & Specialty Solutions reported a manual for gypsum cement where the general consistency of 15kg water/ 45kg product resulted in a compressive strength around 68.9 MPa (Solutions, 2016b). In addition, since each beam required small batches (less than 2kg), hand mixing was considered a reasonable choice. Initially, both the plaster and the water were weighed in separate pans as shown in Figure 4-30.



Figure 4-30: Plaster powder and water used to mix the plaster

Afterwards, small portions of the plaster were added to the water as shown in Figure 4-31 (a) to thoroughly soak them and then mix them presented in Figure 4-31 (b). This motion is repeated until the full amount of plaster was wholly incorporated in the water and result in a state as shown in Figure 4-32 (b) (Solutions, 2016a).

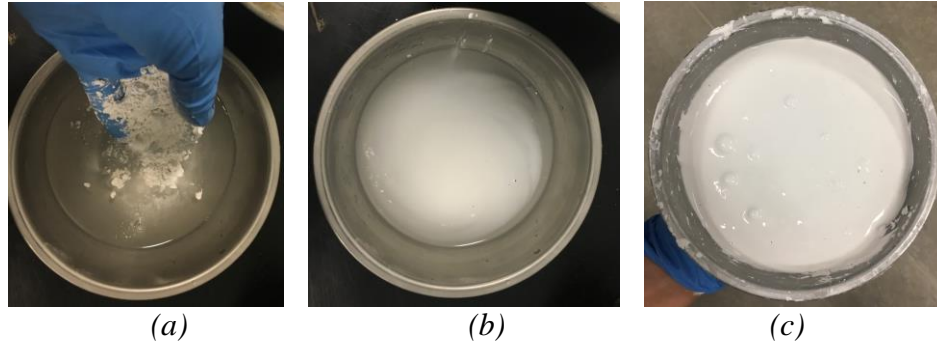


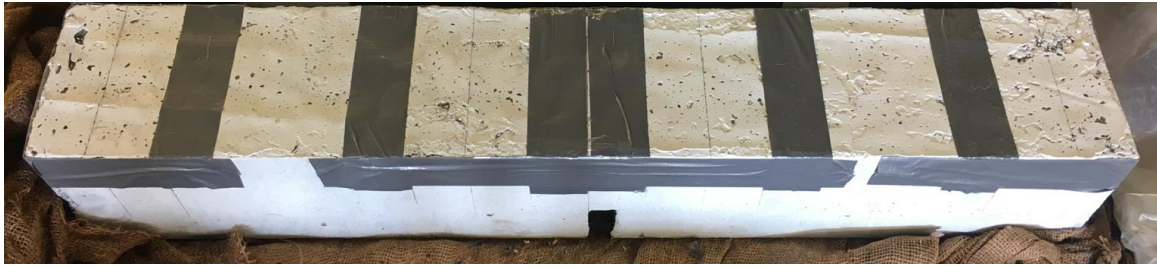
Figure 4-31(a) Addition of plaster to the water, (b) soaking and (c) final state of the plaster

After several trials, Table 4-15 presents the final proportion used to obtain a more or less stiff mix yet still self-consolidating without flow deficiencies.

Table 4-15 Quantity used to smoothen the surface of one beam

Materials	Weight (g)
USG Plaster	200
Water	55

The location where the roller and the frame legs would be placed was marked on each beam. This was realized with the use of a ruler. Duct tape was used to delimit the adjusted areas as shown in Figure 4-32 (a). The surface was chosen large enough (100 mm x 152 mm) to prevent slippage of the rollers during testing. The beams were placed on a leveled surface. Once the plaster was prepared, it was placed on pre-specified spots, as can be seen in Figure 4-32 (b). The steel beams presented in Figure 3-6 (a) were placed on top to exert a pressure owing to their self-weight to flatten the surface. After a couple of minutes, once the plaster hardened, the steel beams were removed. Moreover, Figure 4-32 (c) presents the removal of the duct tape resulting in a smooth rectangular surface.



(a)



(b)



(c)

Figure 4-32 (a) Marking the location of the rollers and the legs of the rods of the frame, (b) placing duct tape and the plaster in the concerned surface, and (c) removal of the beam and the duct tape to obtain a smooth surface

To be able to perform image correlation on the specimens for the tensile, compression and bond tests, a white inelastic primer as shown in Figure 4-33 was used as a base coat that was later speckled with black, white and pink dots. Figure 4-34 presents examples of two different specimens that were speckled using a brush at the mid-span of the beam to capture the deflection by DIC. The bottom face of the specimen was painted in white to detect the onset of cracking at that surface.



(a)



(b)

Figure 4-33 (a) Primer used as finishing, and (b) acrylic paint used to speckle the beams

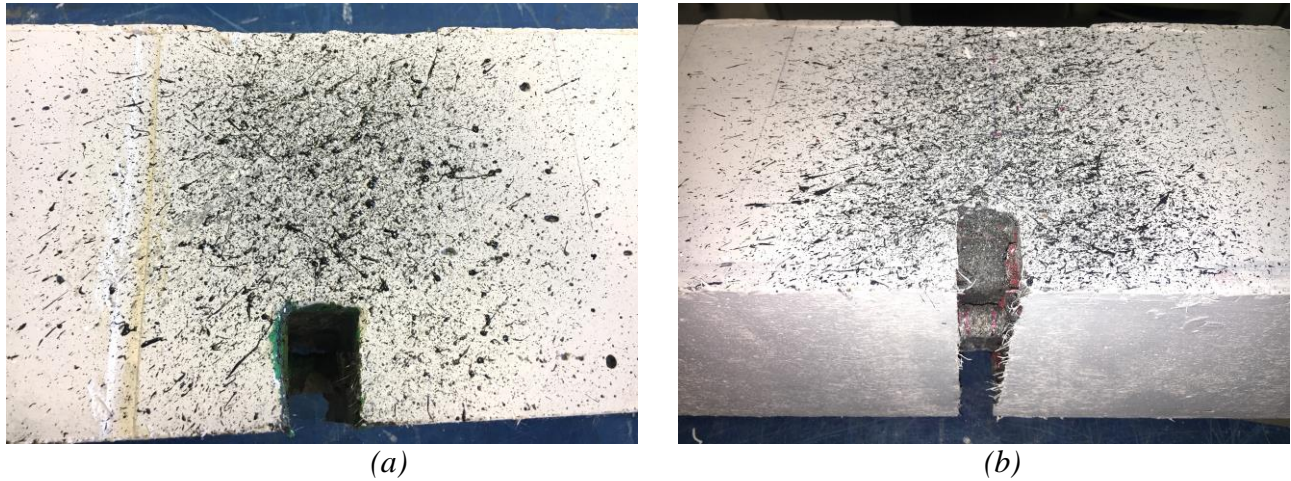


Figure 4-34 (a) Examples of the speckled front face of the beams, and (b) painting of the bottom of the beam

Moreover, the end of the 15M extended bar was smoothed in order to be able to place the linear potentiometer. Figure 4-35 (a) and (b) presents the before and after of the surface area of the reinforcing bar, respectively.

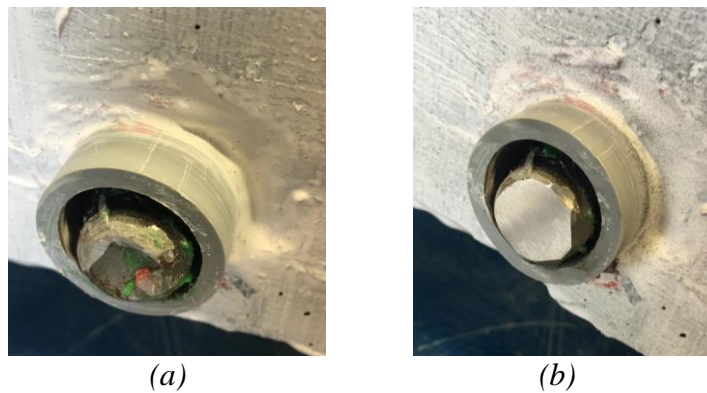
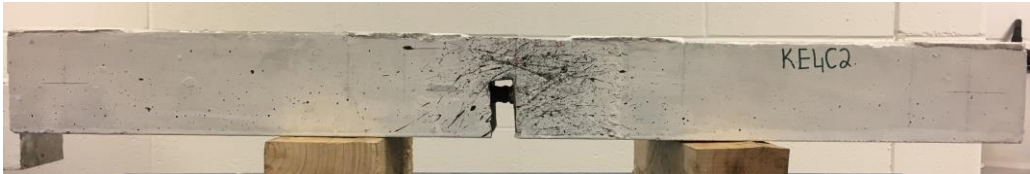


Figure 4-35 (a) Before adjusting the end of the 15M bar, and (b) smoothing of the area

Finally, an example of the four different specimens presented in Section 3.1.4.4 regarding an embedment length of $5d_b$, $10d_b$, $15d_b$ and fully bonded for a concrete cover of $2d_b$ is presented in Table 4-16 (a), (b), (c) and (d), respectively. The same will imply for a concrete cover of $1d_b$. Moreover, all the specimens were marked at the supports and at mid-height by a cross to pin the frame on all sides.

Table 4-16 Prepared beams for different embedment lengths for a concrete cover $2d_b$

l_b	Final specimens
$l_b = 5 d_b$	 <p>(a)</p>
$l_b = 10 d_b$	 <p>(b)</p>
$l_b = 15 d_b$	 <p>(c)</p>
Fully bonded	 <p>(d)</p>

4.5 Experimental testing

4.5.1 Test setup

The steel beam was placed on top of the MTS platform. The supports were fixed on top of the steel beam by clamps ensuring a clear distance of 800 mm. The specimen was then placed on top of the support aligning the crossed mark with the middle-axes of the support as shown in Figure 4-36.



Figure 4-36 Placement of the steel beam, the supports, and the specimen

The linear potentiometer B was attached to the aluminum frame as depicted in Figure 4-37 (a). The latter was hot glued to the side surface of the beam as presented in Figure 4-37 (b) and (c).



(a)



(b)



(c)

Figure 4-37 (a) Aluminum frame and linear pot B, (b) and (c) attachment of the steel frame

Moreover, the aluminum bar was assembled as shown in Figure 4-38 (a) along with the linear potentiometer A. The angle A and B presented in Figure 4-38 (b) were hot glued to the surface of the

beam. Lastly, the aluminum bar with the linear potentiometer A was pinned on the steel frame as shown in Figure 4-38 (c).

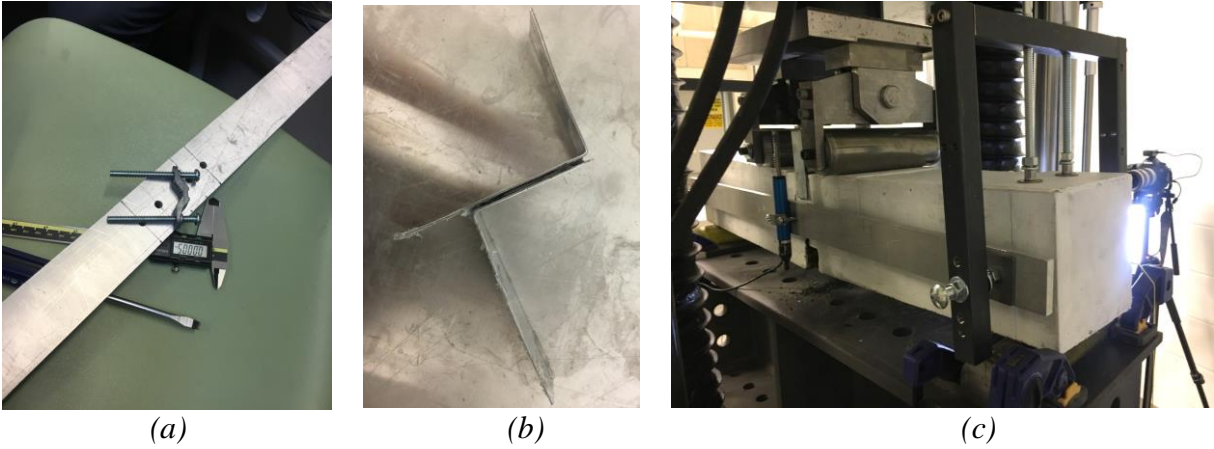


Figure 4-38 (a) Aluminum bar, (b) angle for linear pot and (c) placing bar on the steel frame

Figure 4-39 presents the test setup followed by two sets of cameras, lighting and a video camera. The first camera was used to capture the mid-span of the beam for the measurement of the mid-span deflection. The second camera captured the reinforcing bar placed inside the notch as a backup for the strain measurement of the 15M bar.



Figure 4-39 Test setup followed with the presence of cameras, lighting, and clocks

The camera was focused on the extended part of the reinforcing bar as a backup for the slip measurements. A clock was used in the test setup to link the MTS universal testing machine with the DIC as shown in Figure 4-10.

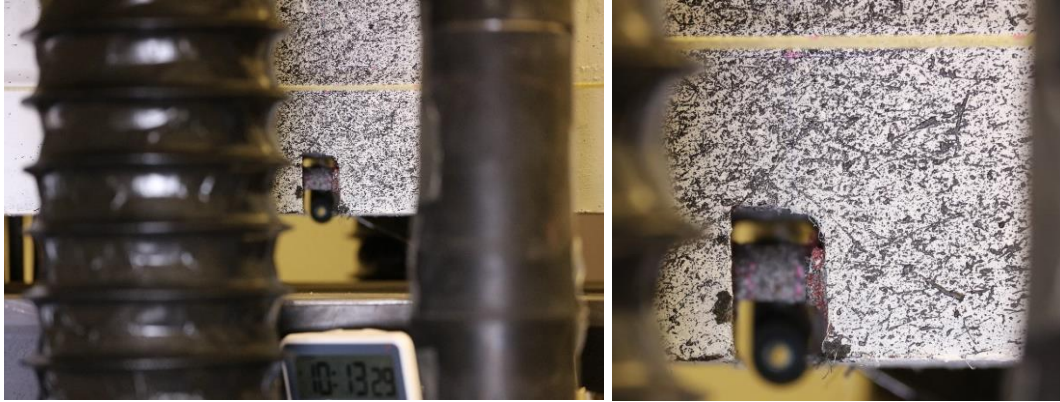


Figure 4-40 Setup to capture the face of the beam at the mid-span with the clock

4.5.2 Modification of the test setup

The specimen KE4C2 was poured halfway due to the limited amount of concrete cast. Thus, the steel frame was adjusted to be attached to the beam at mid-height as shown in Figure 4-41.



Figure 4-41 Modification of the steel frame to accommodate beam KE4C2

The capacity of the jig presented in Figure 3-11 was reached for specimens FE1C2 and IE2C2. Thus, for the beams FE4C1 and IE3C2, another jig was used as shown in Figure 4-42 (a) and (b).

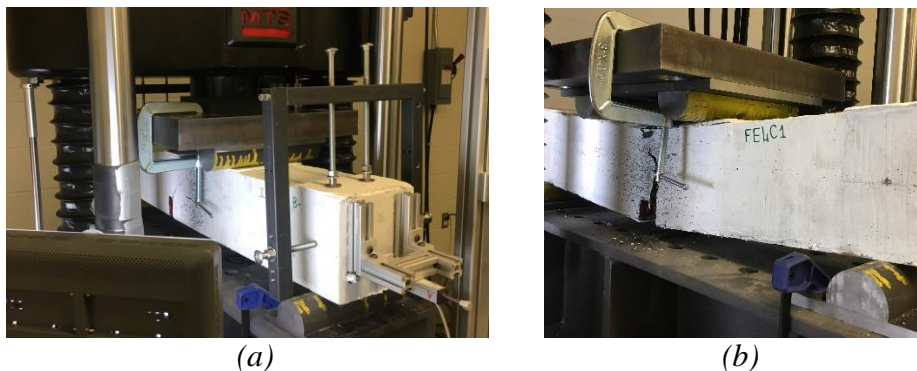


Figure 4-42 (a) Modified test setup and (b) jig used to test beams FE1C2 and IE2C2

The minimal distance between the two loads of this jig was 300 mm. Therefore, an adjustment of the test setup was followed where the shear span was reduced to 250 mm as seen in Figure 4-43.

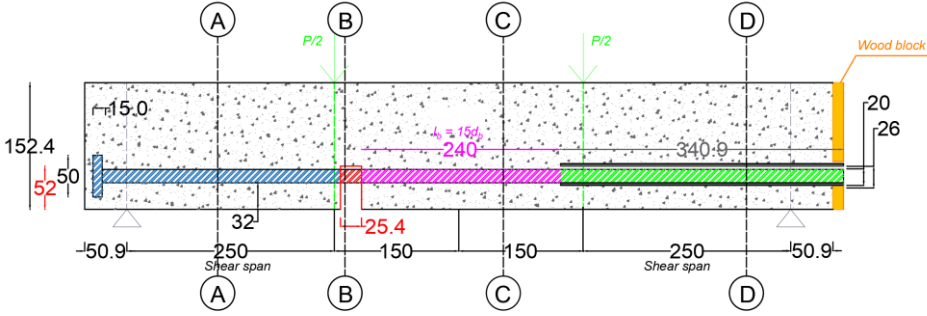


Figure 4-43 Test setup for the specimens FE4C2 and IE3C2

Chapter 5. Experimental Results

The material testing of the commercial design mixes K and F were conducted by another researcher. Thus, the mechanical properties of these materials were provided to the author in terms of compressive strength, flexural strength, and load versus mid-deflection response. However, this chapter will cover the experimental results of the in-house design mixture.

5.1 Cylinder compression strength

5.1.1 The gain in strength values with maturity

Several cylinders were filled from batch C2 (IE1C2), cured, and ready for testing at 7, 28 and 165 days to observe the increase of the compressive strength. For each day, three cylinders were tested and their average was calculated. Figure 5-1 illustrates a sudden increase in the compressive strength during the first 7 days. This rapid gain in strength is due to the presence of silica fume. It is evident that after 28 days, the strength gain reduces and is more gradual. This can be explained by the presence of the slag in the design mixture that tends to influence the compressive strength in the long term due to its pozzolanic activity.

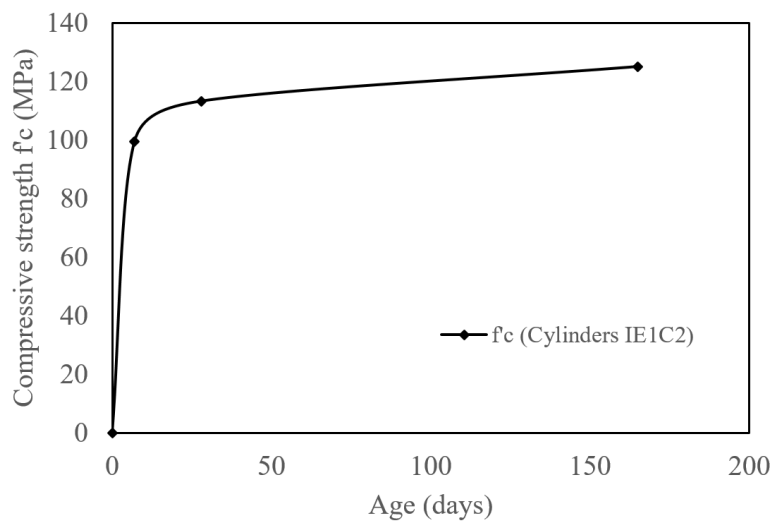


Figure 5-1 Average compressive strength gain as function of days (average of 3 cylinders for each experimental point)

5.1.2 Compressive strength values

The in-house cylinders were tested two weeks after the bond test due to the equipment and laboratory conditions. Both ends of the cylinders were grinded to obtain a smooth and parallel surface to apply the load. Three cylinders per batch were tested; Table 5-1 presents the obtained average compressive strength (three samples each).

Table 5-1 Compression strength of the design mixtures

Specimen	Specimen Age (days)	Compressive strength f'_c (MPa)
IE1C1 (Batch C4)	152	153.5
IE1C2 (Batch C2)	163	125.0
IE2C2 (Batch C6)	132	152.8
IE3C2 (Batch C5)	133	142.2
Commercial K	141	122.6
Commercial F	121	128.4

5.1.3 Pre-peak compressive stress-strain behavior and Young's modulus

Based on the digital image correlation system, the strains experienced by a typical cylinder corresponding to the specimen IE1C1 (Batch C4) under compression were calculated and interrelated to the load. Figure 5-2 presents the pre-peak compression stress versus strain response.

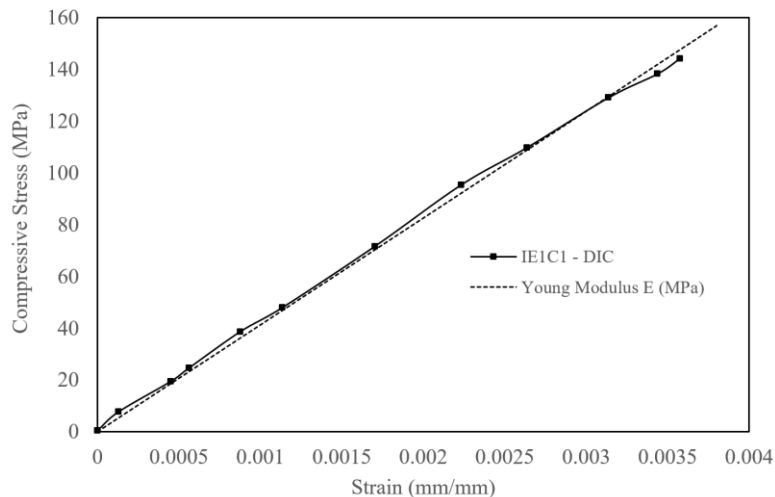


Figure 5-2 Pre-peak stress-strain behavior for a typical cylinder IE1C1

The slope of the curve, corresponding to the Modulus of Elasticity of the material, is equal to 41301 MPa. Nevertheless, the Young's Modulus calculated based on using Equation (2.7) gave a similar result whereas the value obtained from Equation (2.6) was higher and equal to 46000 MPa. The mechanical properties of the in-house design mixture are presented in Table 5-2.

Table 5-2 Mechanical properties of the cylinder IE1C1

Mechanical Properties (IE1C1)	
f'_c (MPa)	153.5
ϵ_c	0.00357
E_c (MPa)	41301

5.1.4 Failure crack pattern

The specimens remained intact after failure owing to the presence of the steel fibers acting as a means of intrinsic confinement. Most of the cylinders developed columnar vertical cracks as depicted in Figure 5-3 from ASTM C39. In fact, this is an adequate behavior where the cracking occurs in the perpendicular direction of the principal tensile hoop stresses.



Type 3
Columnar vertical cracking
through both ends, no well-
formed cones

Figure 5-3 Failure crack patterns extracted from (ASTM C39, 2015)

As can be seen from the failed samples presented in Figure 5-4, longitudinal cracks initiated from both ends and connected to each other by circumferential and diagonal cracks. The failure modes of the other tested cylinders of the in-house design mix are presented in Table D-1. In some cases, the concrete appears to have no damage due to the narrow crack widths developed.

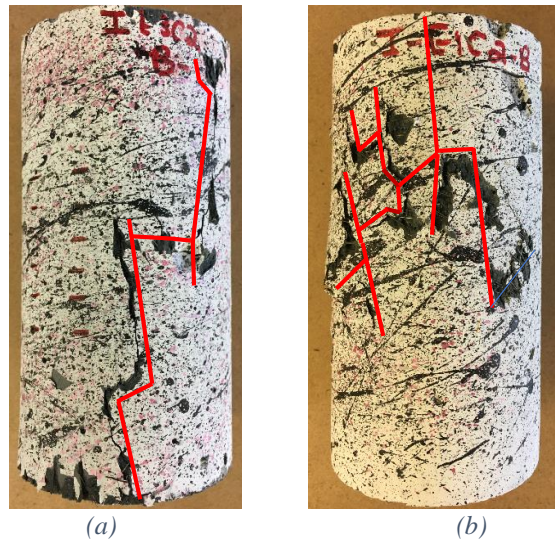


Figure 5-4 Crack pattern of two failed cylinder samples (a) IE3C2 -B- and (b) IE1C2 -B-

5.2 Flexural strength

This paragraph discusses in detail the flexural behavior of the tested prisms. There is a prism sample for each casted batch: Prism G from set S3 for the beams IE1C2, Prism I and J from set S4 corresponding to IE1C1, and Prism K representing IE2C2. Nevertheless, the flexural behavior of the prisms concerning the commercial mixture K and F are presented in section 6.3 since the results were obtained in the framework of a parallel research project.

5.2.1 Load-deformation response from the four-point loading test

In terms of the casting methodology, Figure 5-5 and Figure 5-6 present the load versus mid-deflection of the 280 mm prisms cast in a layered fashion and from a one side flow method, respectively. The layered method of casting resulted in higher loads, varying between 45 to 60 kN, than from the one side flow where loads ranged between 40 to 50 kN. The increase in the flexural strength is due to the higher amount of steel fibers present parallel to the direction of the tensile stresses acting on the cross-section. The response curves of these samples are considered ductile. Still, some of the prisms from series S1 were more ductile than the prisms from series S2 and vice versa. An example is Prism A presenting a deflection of 0.57 mm for a peak load of 62.59 kN while Prism D deflected 0.44 mm when subject to the maximum load of 51.53 kN. Conversely, at a peak load of 45 kN, Prism E

deflected 0.56 mm in comparison to Prism B presenting a deflection of 0.47 mm. In addition, both series presented a post-peak softening behavior. However, the descending branch was steeper for the prisms from set S1 owing to the higher loads they were able to carry. In fact, at a drop of 20% from the peak load, Prism A had deflected 4 mm compared to Prism D with a 5 mm deflection.

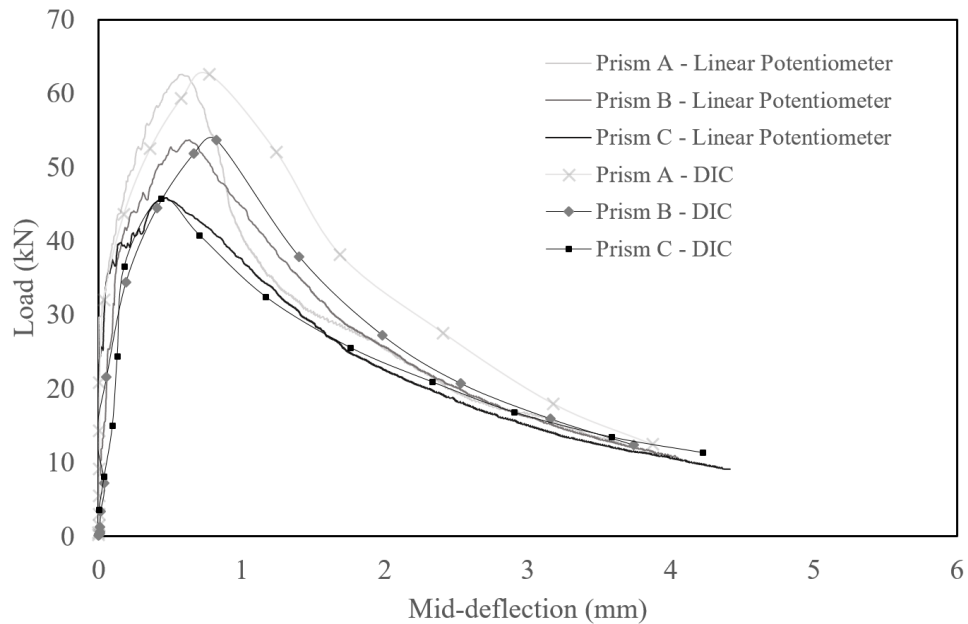


Figure 5-5 Load-deformation response for the 280 mm prism cast in a layered method (92 days)

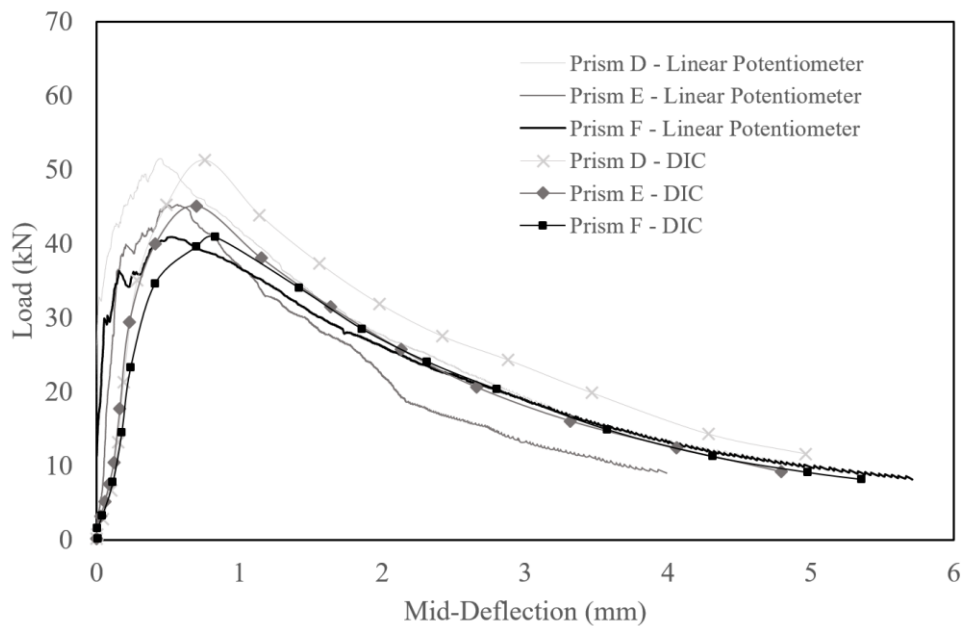


Figure 5-6 Load-deformation response of 280 mm span prisms cast from one-side (92 days)

Figure 5-7 presents the load versus central deflection of the prisms from set S3. The flexural behavior of Prism H and G shows that the presence of steel fibers increased the load capacity from 22 kN to 50 kN respectively. Moreover, Prism H experienced a brittle mode of failure once the tensile capacity of the mixture was attained which is presented by the sudden drop in the response curve. Whereas, Prism G presented a very ductile behavior where the test was intentionally stopped in the post-peak range, when the resistance load dropped by 80% of the peak load; at that point, the specimen was still able to carry the load. It is noteworthy that Prism G was cast in a layered manner and its response curve falls directly between the range obtained in Figure 5-5. In fact, the peak load was 50 kN with a mid-deflection of 0.4 mm. Moreover, for an applied load of 20% of the peak load, the deflection was about 4 mm. This confirms a consistency in terms of the material and casting methodology.

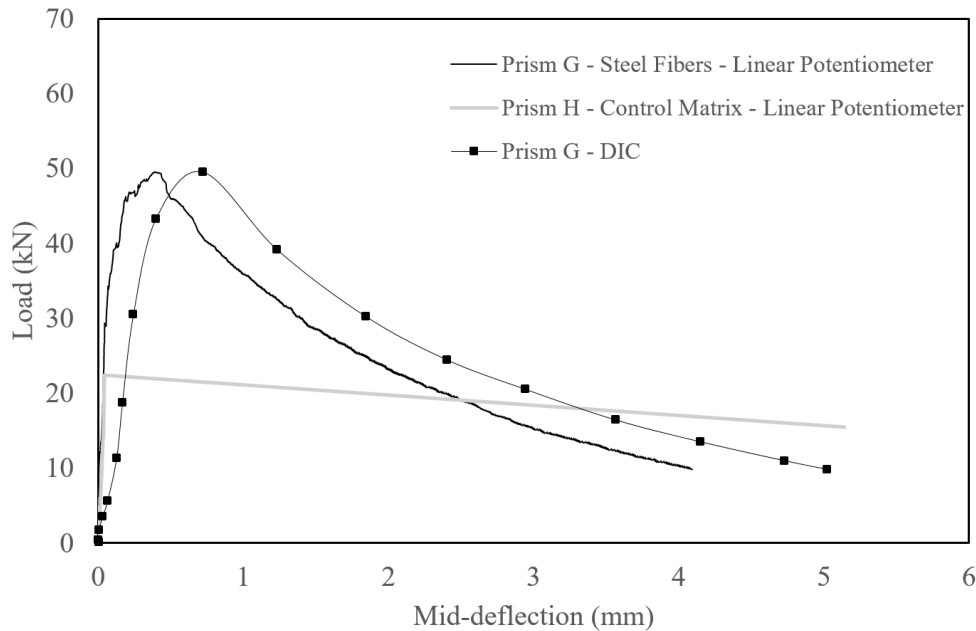


Figure 5-7 Load-deformation response of 280 mm span prisms cast in a layered manner with and without steel fibers (72 days)

Figure 5-8 presents the response curve of the 500 mm long prisms (S4) cast in a layered method. The results of Prism K were disregarded since the crack was developed outside of the maximum constant moment region indicating a defect in the tested prism. Prisms I and J experienced a lower load capacity than the ones obtained from series S1, equal to 24.48 and 28.21 kN, correspondingly. However, they deflected twice as much as the short 280 mm prisms did with a mid-deflection of 1.01 mm for prism I and 1.45 mm for Prism J. Set S1 and S3 resulted in the same modulus of rupture of

28 MPa, stating no effect of the shear span to depth ratio on the flexural strength. The response curve presents a very defined strain-hardening behavior with multiple cracks and a gradual post-peak behavior where the deflection reached almost 6.5 mm at a drop of 70% from the peak load.

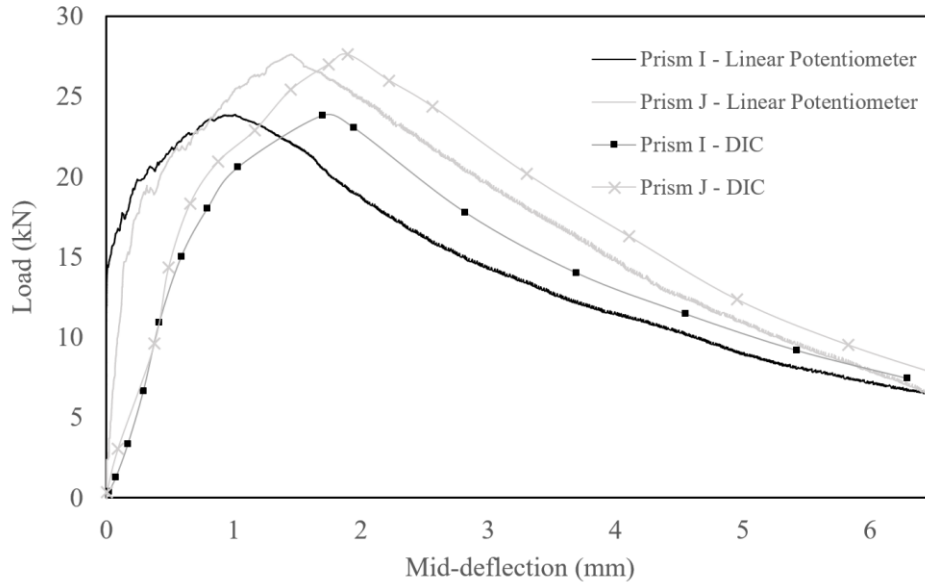


Figure 5-8 Load-deformation response for the 500 mm prisms in a layered casting method (92 days)

5.2.2 Peak load and flexural strength calculations

Table 5-3 presents the dimensions of the prism, the method of casting, the presence of steel fibers, the peak load (F_{peak}), the deflection at the peak load (Δ_{peak}) from the linear potentiometer and the calculated flexural strength (f_{max}).

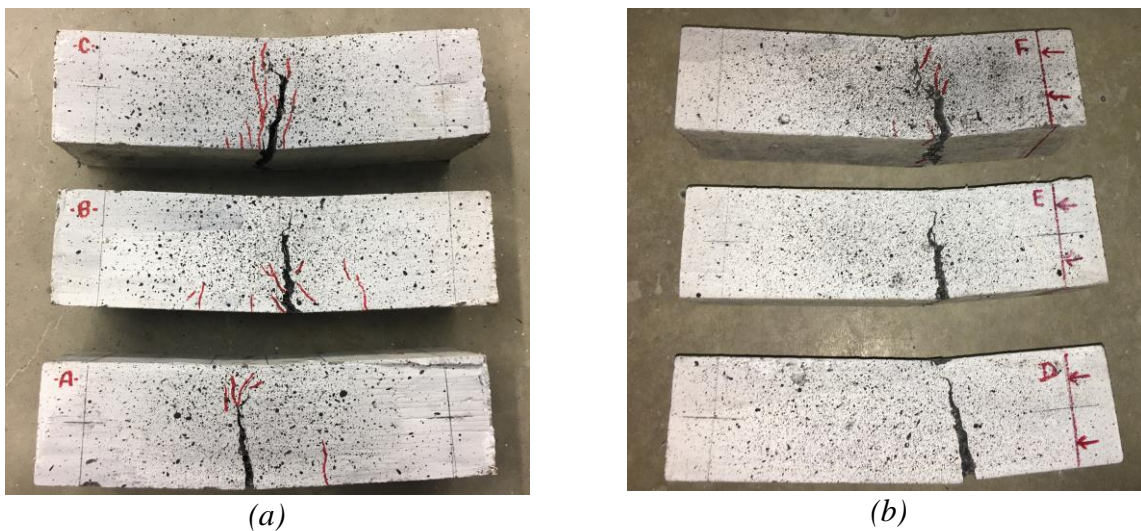
Table 5-3 Summary of the results obtained from flexural tests for the in-house mix

Sets	Annotation	Dimensions (mm)	Casting Method	Steel fibers	F_{peak} (kN)	Δ_{peak} (mm)	f_{max} (MPa)
S1	Prism A	75 x 75 x 280	Layered	Present	62.6	0.57	33.4
	Prism B				53.7	0.63	28.6
	Prism C				45.9	0.47	24.5
S2	Prism D	75 x 75 x 280	Side flow	Present	51.5	0.44	27.5
	Prism E				45.3	0.56	24.1
	Prism F				40.9	0.52	21.8

Sets	Annotation	Dimensions (mm)	Casting Method	Steel fibers	F_{peak} (kN)	Δ_{peak} (mm)	f_{max} (MPa)
S3	Prism G	75 x 75 x 280	Layered	Present	49.5	0.4	26.4
	Prism H			Absent	21.6	-	11.5
S4	Prism I	75 x 75 x 500	Layered	Present	23.9	1.01	25.5
	Prism J				27.6	1.45	29.5
	Prism K				N/A		

5.2.3 Mode of failures observed

Figure 5-9 (a) presents the three prisms cast with the layered method of set S1 with a significant vertical crack in the constant moment region, at the same location. However, set S2 cast with the flow method applied from one side of the mould resulted in the formation of the crack at the end limits of the constant moment region, below the roller. In fact, the developed crack was on the side of the casted side as can be seen in Figure 5-9 (b). This result shows that the flow method creates a weak region on the poured side owing to the type of flow it generates. Moreover, Figure 5-9 (c) highlights the effect of adding steel fibers to the concrete matrix where Prism H with no fibers was split into two pieces whereas the fibers in Prism G were able to bridge through the crack preventing it from opening more. Both sets S1 in Figure 5-9 (a) and S4 in Figure 5-9 (d) developed the localized crack in the middle of the constant region. The cracking pattern of the back and bottom side of the prisms are presented in Appendix D.



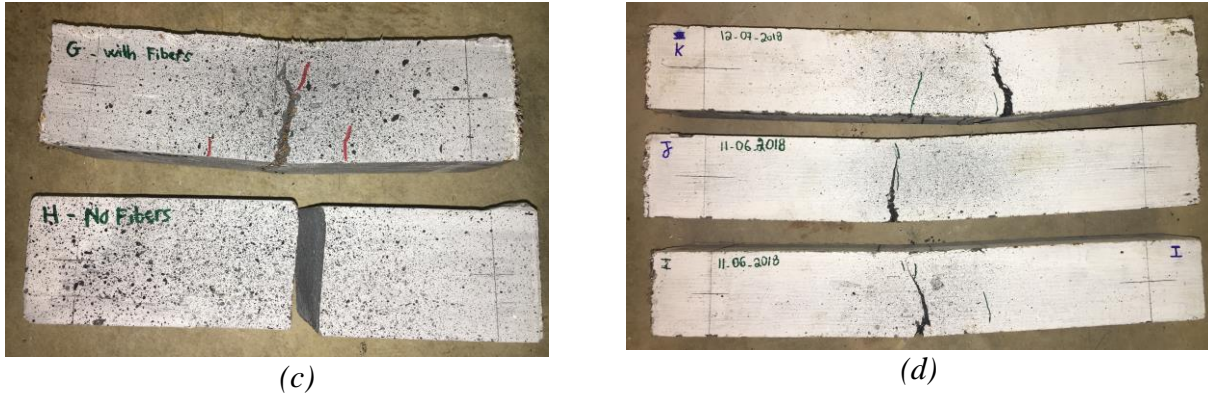


Figure 5-9 Cracking pattern of the speckled front face for prisms (a) Set 1, (b) Set 2, (c) Set 3 and (d) Set 4

Table 5-4 presents the results of the average flexural strength of the design mixes studied. The results of the Commercial K and F were obtained outside the present study.

Table 5-4 Average flexural strength of the design mixes under study

Design mix	Prism	f_{max} (MPa)
Com K	280 mm	23
	500 mm	24.9
Com F	280 mm	31.9
	500 mm	36.2
In-house	280 mm	28.8
	500 mm	27.5

5.3 Splitting tensile strength

5.3.1 Splitting tensile strength

Table 5-5 presents the results obtained from the splitting test with lower values than the flexural test.

Table 5-5 Results for the splitting tensile test

Cylinder	Peak Load (kN)	Splitting Tensile Strength (MPa)
SC 1	523.7	16.7
SC 2	555.5	17.7
SC 3	698.8	22.2

5.3.2 Failure pattern

Multiple longitudinal cracks were developed in the middle of the cross-section perpendicular to the direction of the tensile stresses. This testing terminated without the through splitting of the cylinder in comparison to normal concrete that tends to open with a single crack. The specimen failed with the development of a bunch of coalescent cracks in the diagonal accompanied with several microcracks as depicted in Figure 5-10, but the cylinder maintained its integrity after being removed from the testing frame.



Figure 5-10 Cracking pattern for the splitting tensile test

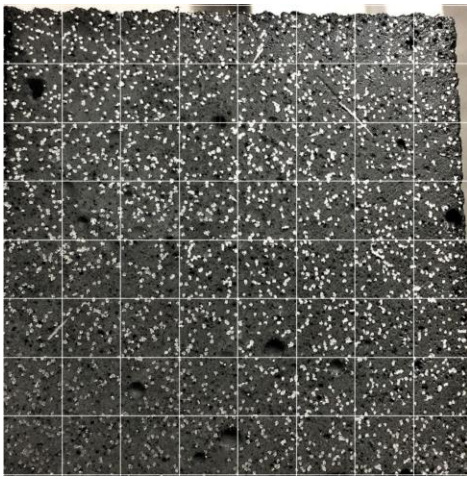
Figure 5-11 (a) presents the longitudinal cracks formed along the lateral surface of the cylinder with discoloration of the concrete that disappeared once the cylinders dried out (ref Figure 5-11 (b)). In fact, the opening of a crack dehydrates the local concrete changing its tone from dark grey (wet state) to light grey (dry state). Thus, testing these cylinders in their wet state can detect all the micro-cracks.



Figure 5-11 Longitudinal cracks developed along the height of the cylinder (a) in a wet state and (b) in a dry state

5.4 Fiber distribution

Two samples of the flexural prisms presented in Table 3-12 were cut at the section near their developed failure crack. A capture of the concerned cross-section was taken and was divided into 64 squares of 9.375 mm. Figure 5-12 (a) and Figure 5-13 (a) represents a cross-section near failure for the layered method of pouring (Prism I from series S4) and the one-sided method of pouring (Prism D from series S2), respectively. The number of fibers for each 9.375 mm x 9.375 mm section was visually computed and reported as shown in Figure 5-12 (b) and Figure 5-13 (b).

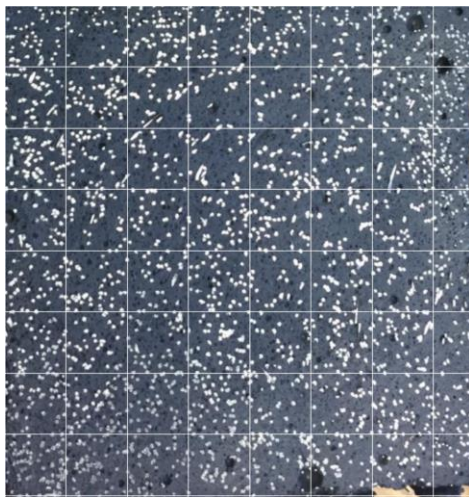


(a)

47	51	52	55	66	57	57	64
55	57	54	38	40	59	58	61
55	47	47	54	48	68	50	37
48	45	59	45	55	44	60	38
50	32	30	48	54	46	65	60
29	40	48	41	40	37	55	53
38	39	39	40	43	46	48	50
49	31	38	31	38	49	57	53

(b)

Figure 5-12 (a) Cross section of Prism I (b) and number of fibers per section



(a)

46	30	52	51	40	32	43	31
39	46	23	22	19	25	41	44
53	38	26	21	31	32	46	33
35	30	32	39	40	26	31	22
40	35	31	42	21	35	35	24
31	41	46	41	30	40	37	13
43	28	23	41	25	35	41	41
37	27	32	25	36	45	44	42

(b)

Figure 5-13 (a) Cross section of Prism D and (b) number of fibers per section

The number of fibers per cross-section near failure for a layered casting method is higher than the value obtained from the flow method applied from one side of the mould. For the flow method from the side, the number of fibers per unit area does not meet the minimum amount of fibers previously calculated in section 3.3.4 ($n_f = 39$) where the steel fibers are more concentrated in the outer regions than the center. By approximation, the layered method of pouring resulted in a total amount of 3088 steel fibers present in the 75 mm x 75 mm studied cross-section. The considered quantity is reasonably higher than the 2545 steel fibers calculated in section 3.3.4. The higher amount can be explained by the layered casting method placing most of the steel fibers in the longitudinal direction perpendicular to the cross-section. This increases the fiber orientation factor α_2 that was assumed 0.5 for a random orientation of fibers. For the sample presented in Figure 5-13, the total number of fibers calculated was 2226 for the cross-section of 75 mm x 75 mm. This number is lower than the total minimum required number of fibers depicting the main difference between the two casting methodologies.

5.5 Experimental observations of the beam specimens

For each specimen, the applied load versus the mid-deflection were plotted to establish a comparison between the measurements of the linear potentiometer and the digital image correlation. Also, for certain beams, the variation of the average bond strength versus the slip of the reinforcing bars was plotted. The front and the bottom face of each specimen are presented as well stating the type of cracking observed at the notch and the bottom concrete cover respectively. All the other sides of the specimens were captured as well and are presented in Appendix D.

5.5.1 Beams KE1C1

Figure 5-14 presents the load versus mid-deflection of the beam specimens KE1C1 A and B experienced similar peak loads of 75.1 and 69.65 kN with a mid-deflection of 1.62 and 1.54 mm, respectively. The specimens presented a post-peak softening behavior. The test terminated at a load of 20 kN with an average of 20 mm mid-deflection. The first crack appeared near the notch at a load equal to 70 % of the peak load and an average mid-deflection of 0.5 mm. The increase of the applied load propagated these cracks upwards in a diagonal direction towards the right roller and entering the

compression zone of the beam section as shown in Figure 5-15. Simultaneously, testing was producing loud noises indicating the pullout of the steel fibers. This can be explained by the strong bond between the concrete matrix and the steel fibers.

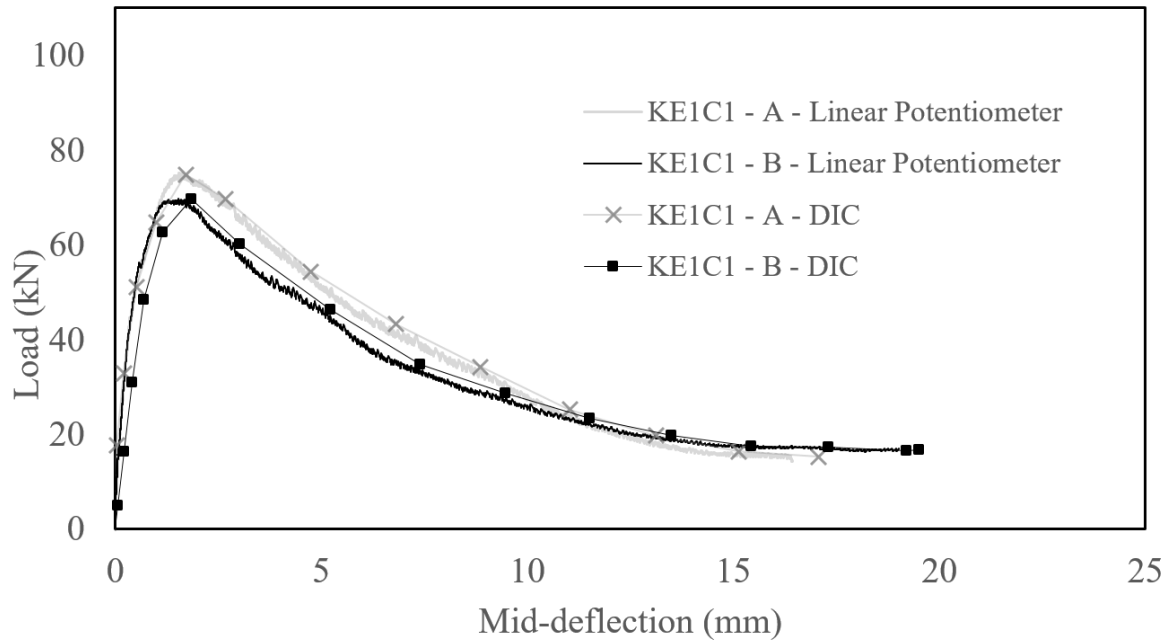


Figure 5-14 Load versus mid-deflection – Beam KE1C1

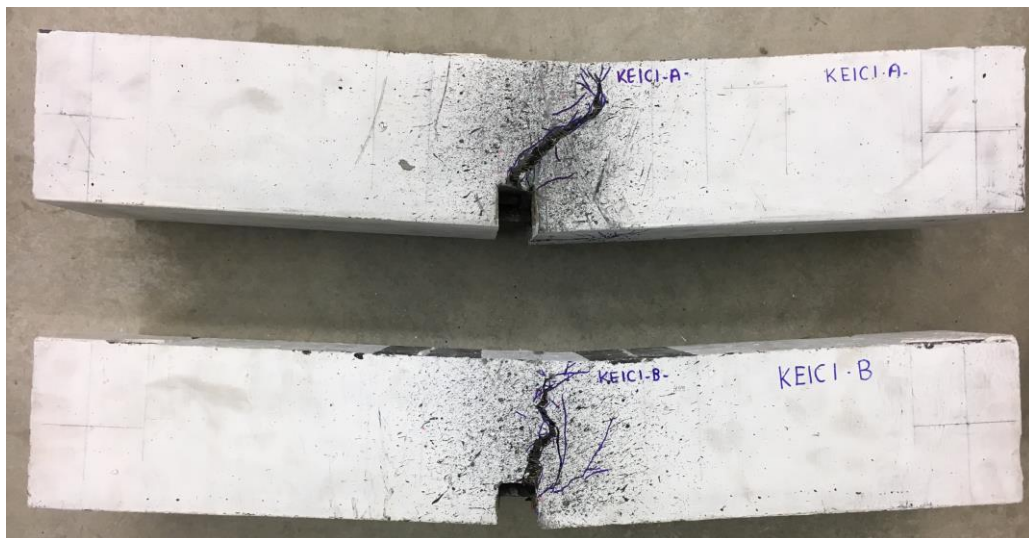


Figure 5-15 Crack pattern after the failure of the beams front face

The specimens failed by a pullout-splitting failure mode. The splitting crack initiated at the bottom face of the beam, in the concrete cover below the 15M reinforcing bar and near the notch. It spread

longitudinally with increased load reaching the end of the $5d_b$ embedment length where it generated a transversal crack as shown in Figure 5-16 (a). Owing to the high confinement provided by the steel fibers, the width of the opening did not enlarge. However, several fine cracks propagated from the single splitting crack and dispersed along the bottom face of the beam. Figure 5-16 (b) and (c) depict the pullout of the main bar and its slippage inside the PVC pipe.

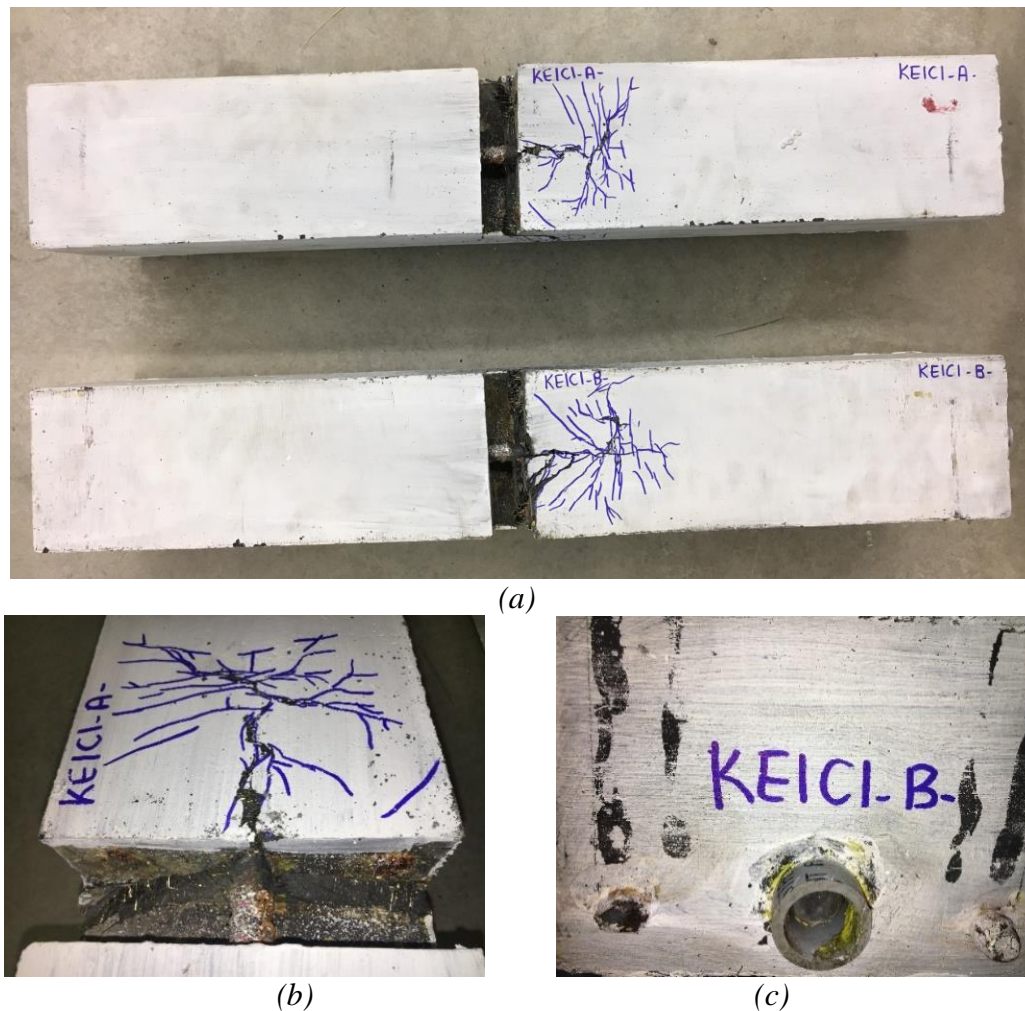


Figure 5-16 (a) Crack pattern after the failure of the bottom cover, (b) pull out of the bar and (c) slip of the bar

Based on Equation (3.13) and assuming a constant bond stress distribution, the average bond stress was calculated for each applied load and plotted as a function of the corresponding measured slip as shown in Figure 5-17. The bond-stress slip relationship presents a steep ascending pre-peak curve reaching maximum bond stress of 23 kN where the reinforcing bar slipped for about 0.5 mm. The slippage of the reinforcing is mobilized in the post-peak phase where it reached around 12.5 mm.

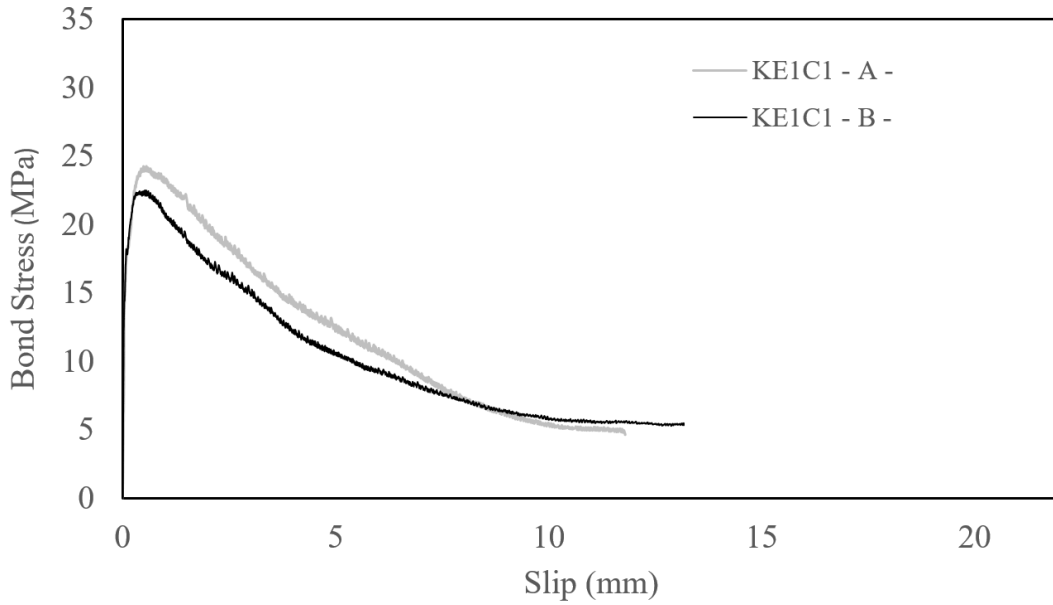


Figure 5-17 Average bond-stress vs. slip (loaded end)– Beam KE1C1

5.5.2 Beams KE1C2

The response curve of the specimens described in Figure 5-18 presented a steep initial stiffness with a linear descending post peak curve. The peak load of KE1C2A was around 56.36 kN compared to 68.74 kN for KE1C2B with a mid-deflection of 1.5 mm and 1.86 mm, respectively.

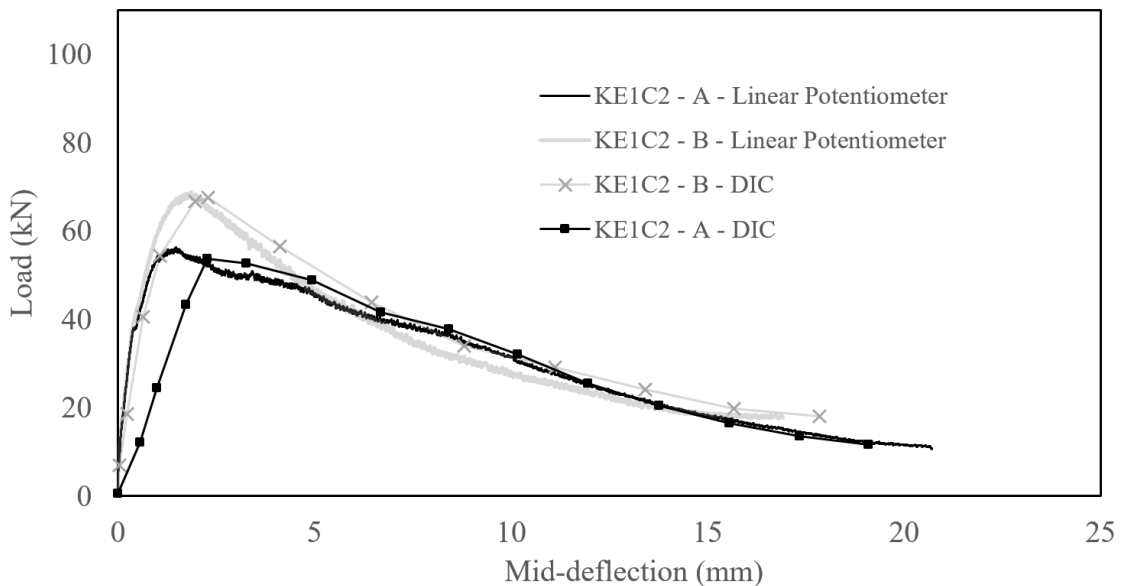


Figure 5-18 Load versus mid-deflection – Beam KE1C2

The initial cracks were generated at 75% of the peak load with a deflection of 0.56 mm for KE1C2A and 0.75 mm for KE1C2B. The first cracks propagated in the same direction as KE1C1 as shown in Figure 5-19 (a). Both specimens failed by pullout-splitting as shown in Figure 5-19 (b-c) with a final slip of 12mm for the 15M bar depicted in Figure 5-19 (d). The bar of KE1C2A yielded while the bar stress reached almost 443.9 MPa.

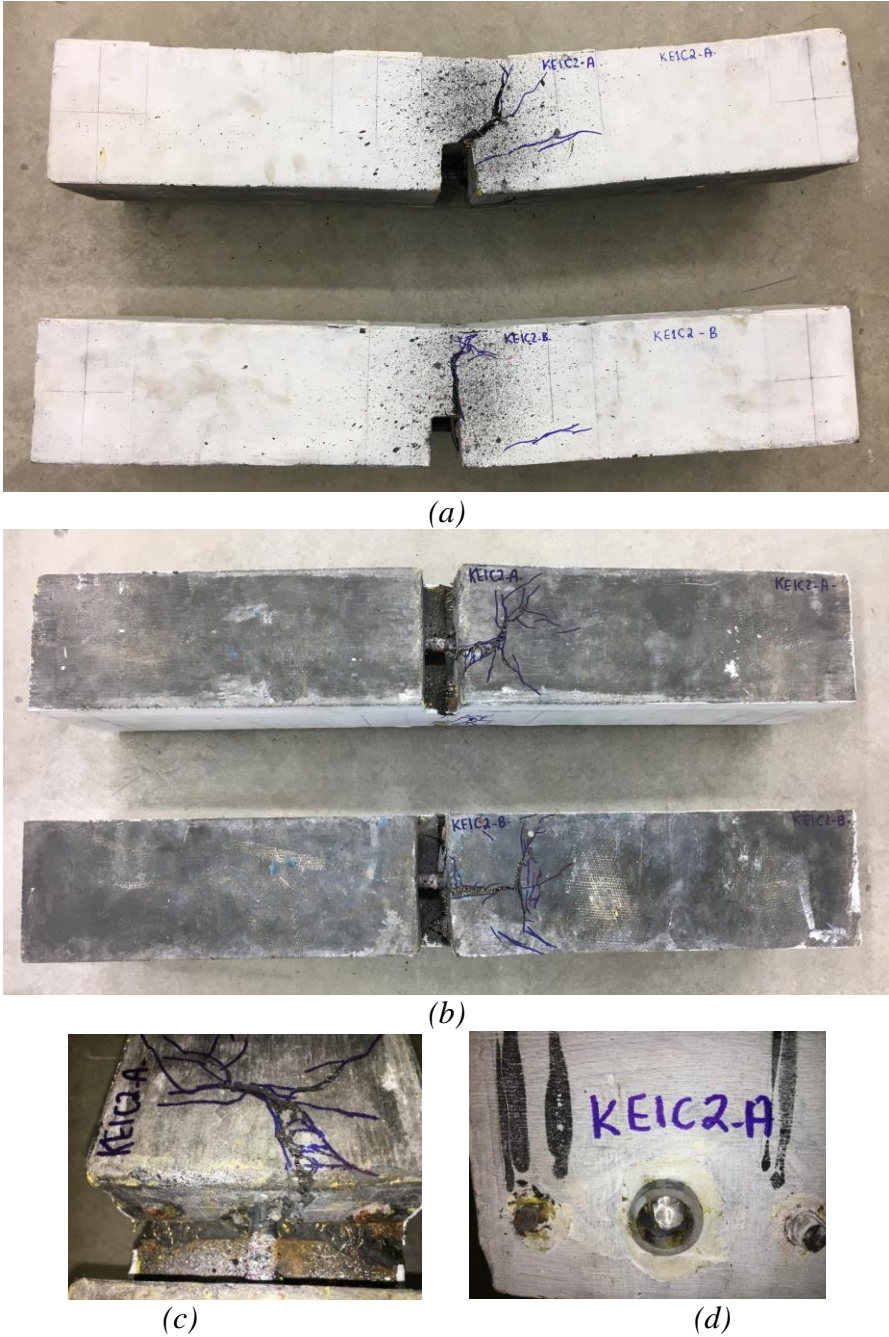


Figure 5-19 (a) Crack pattern of the front face, (b) cover after failure, (b) pullout of the bar and (c) slip of the bar

The bond-stress slip relationship was plotted in Figure 5-20 where the average bond strength was 23 MPa with a slip of 0.52 mm on average. Afterwards, the bond strength reduced to approximately 5 kN at a slippage of 12 mm of the 15M bar.

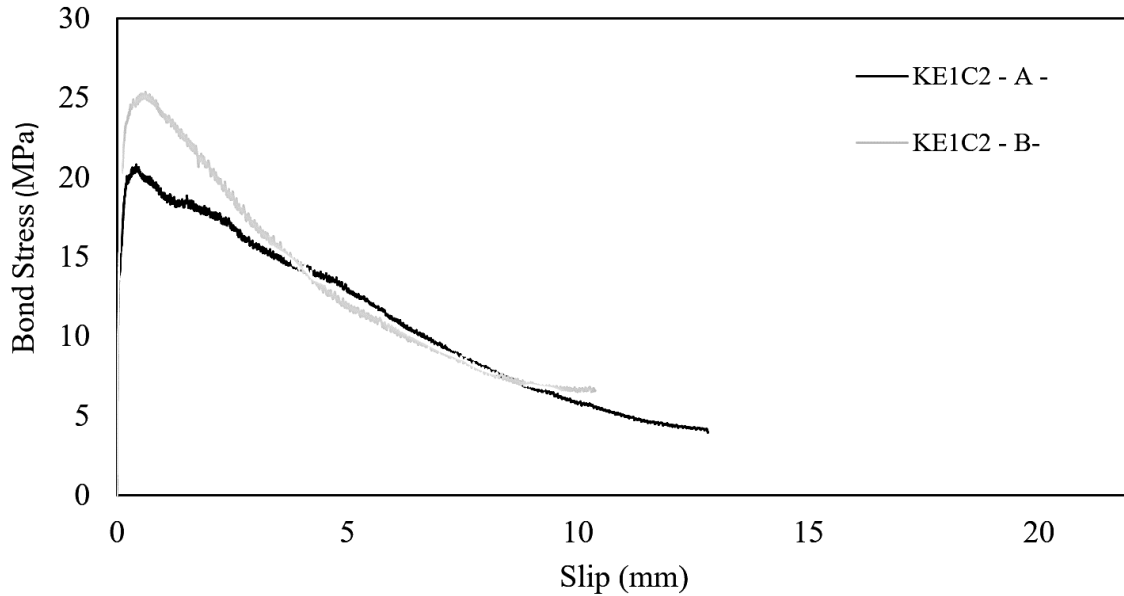


Figure 5-20 Average bond-stress vs. slip (loaded end) – Beam KE1C2

5.5.3 Beams KE4C1

KE4C1 is not considered as a sample for the bond test studies but for the calibration of the beam tests that will be discussed in detail in Chapter 6. The beam experienced two sets of loading: The first was stopped and unloaded during the strain-hardening phase of the beam. During the second phase of loading, the reinforcing bar reached its ultimate strength and suddenly ruptured. Figure 5-21 presents a ductile behavior of the beam reaching a deflection of 24.78 mm at failure with a negligible relative slip of 0.13 mm as presented in Figure 5-22 (d). Initially, the concrete beam was maintained together with the ruptured 15M bar. However, during several displacements of the beam, the beam was split into two separate pieces as evident in Figure 5-22 (a). Lastly, the embedment length of each side of the beam is about 450 mm generating a non-linear distribution of bar stresses leading to the development of longitudinal cracks on both sides of the bottom of the specimen observed in Figure 5-22 (c).

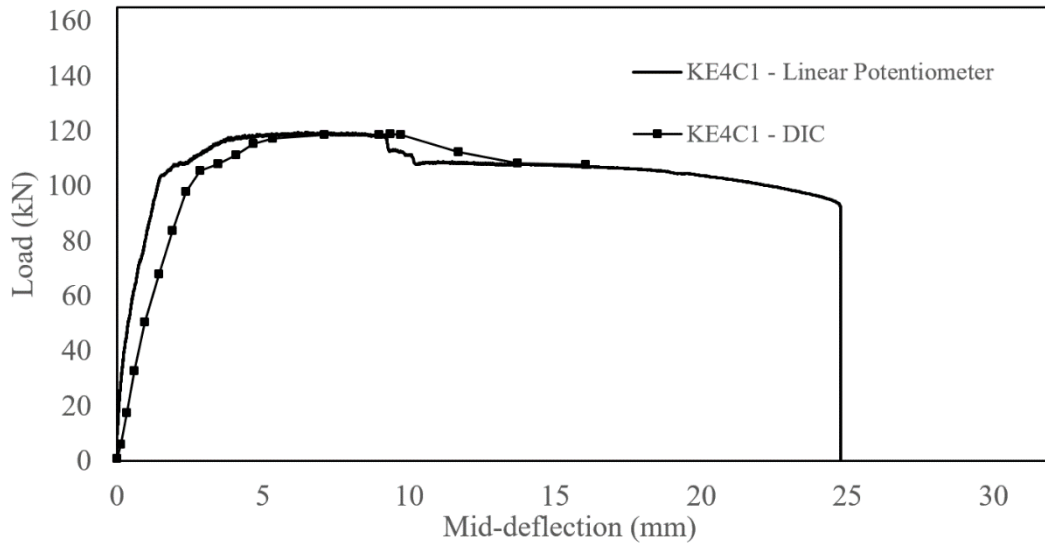
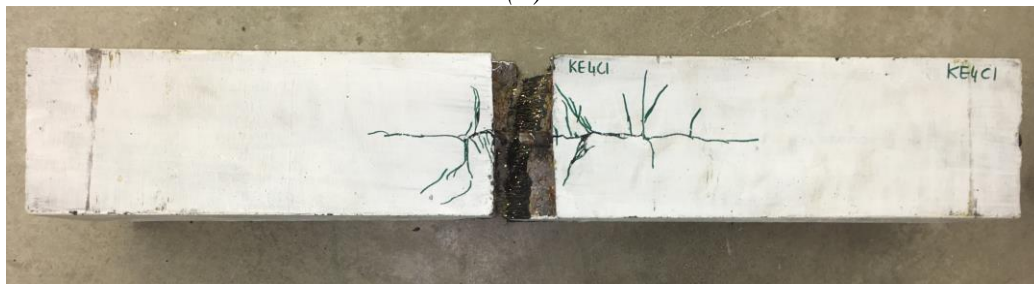


Figure 5-21 Load versus mid-deflection – Beam KE4C1



(a)



(b)



(c)



(d)

Figure 5-22 (a) Front face of the beam, (b) crack pattern of the bottom face, (c) rupture of the bar and (d) no slippage

5.5.4 Beams KE4C2

Owing to the shortage of materials, the height of the specimen was around 80 mm. Figure 5-23 presents the load versus deflection with a maximum deflection of 29.86 mm for a 22.42 kN load. No slippage of the 15M bar was observed around 0.008 mm as shown in Figure 5-24 (c). The beam failed in flexure (ref: Figure 5-24 (a-b)) where the bar exceeded its yielding strength.

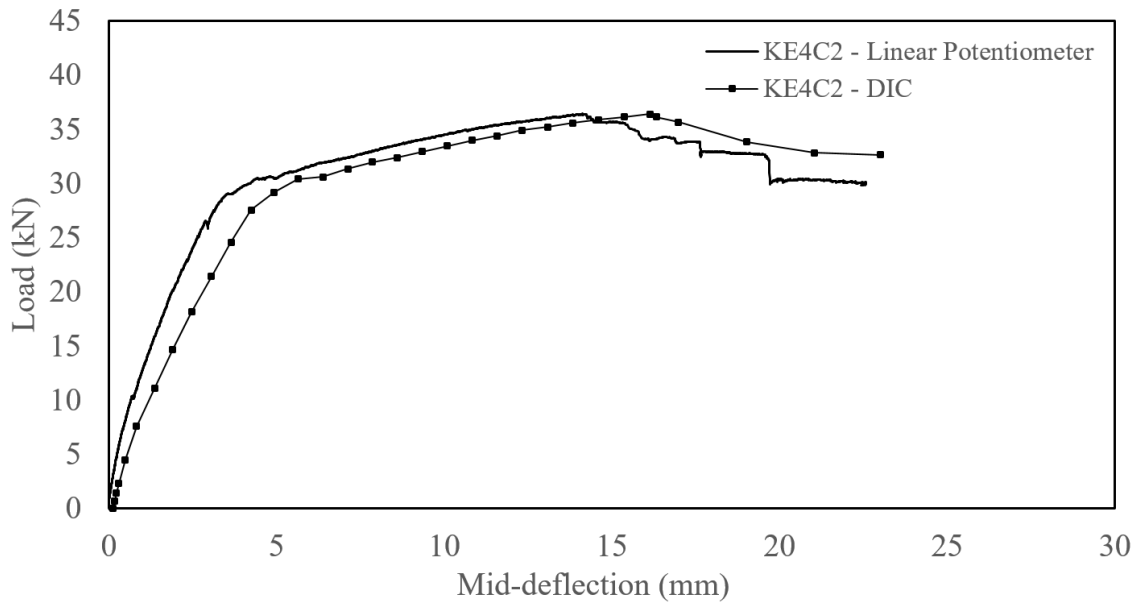


Figure 5-23 Load versus mid-deflection – Beam KE4C2



(a)



(b)



(c)

Figure 5-24 (a-b) Crack pattern at failure at the front and bottom face and (c) no slip of the bar

5.5.5 Beams FE1C1

Figure 5-25 presents the load versus deflection of the beams FE1C1 with a very ductile behavior reaching a peak load of 92.05 kN for FE1C1A and 100.9 kN for FE1C1B with a deflection of 2.96 and 3.24 mm, respectively. The softening curve is almost parabolic. At 25kN applied load, FE1C1A deflected about 23.35 mm and FE1C1B 27.21 mm. Figure 5-26 shows the crack in the front face of the beam starting at the top middle of the notch and propagating almost vertically to the top of the beam.

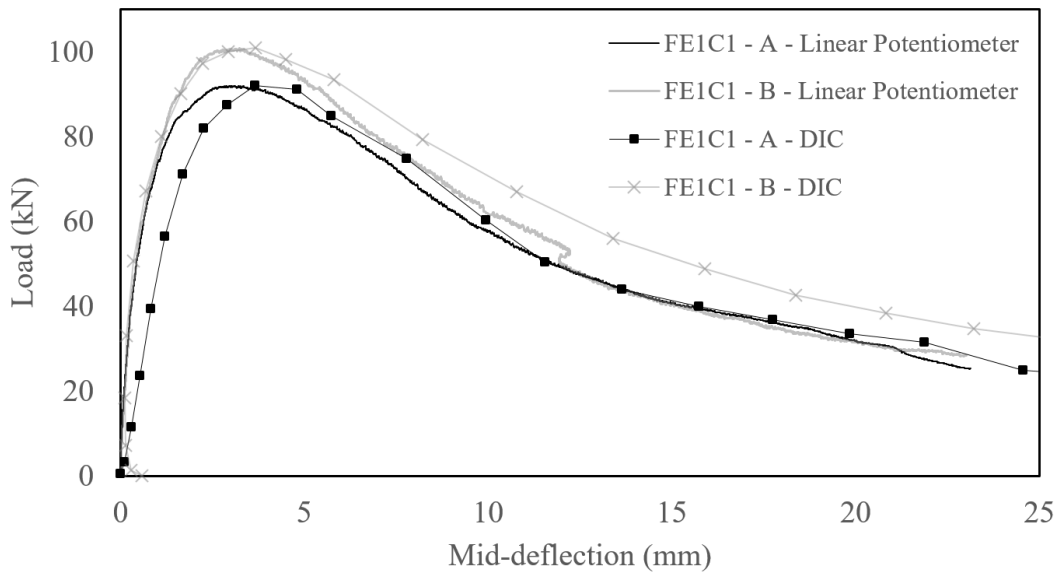


Figure 5-25 Load versus mid-deflection – Beam FE1C1



Figure 5-26 Crack pattern after failure - Beam FE1C1

FE1C1A failed by a splitting crack as shown in Figure 5-27(a) with the pullout of the reinforcing bar presented in Figure 5-27 (b) considered to be significant. FE1C1B failed by the half-V splitting crack. When the load dropped to 25 kN, the bar had already slipped about 12.04 mm for FE1C1A and 19 mm for FE1C1B as presented in Figure 5-27 (c).

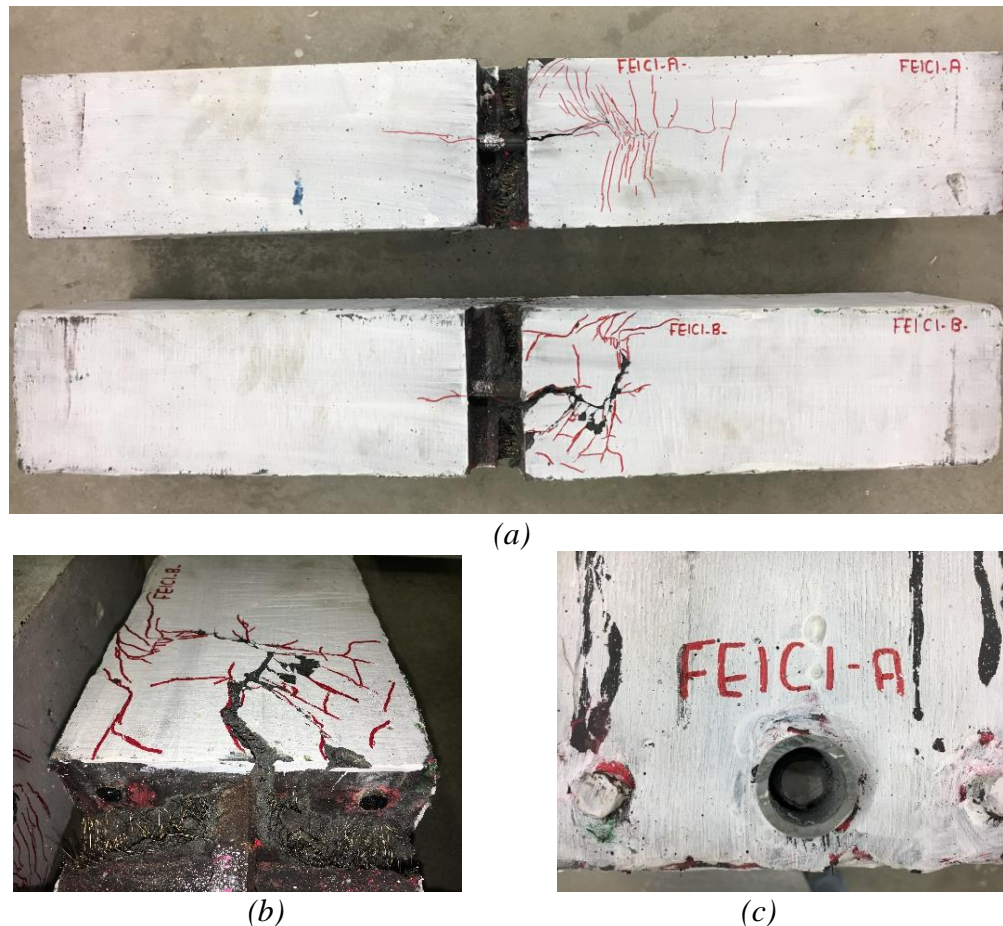


Figure 5-27 (a) Crack pattern of cover after failure, (b) pullout of the bar and (c) slip of the bar

Figure 5-28 presents the plot of the bond stress-slip response, where FE1C1A and B experienced a maximum average bond strength of 29.72 and 32.59 MPa with a slippage that is considered high of 1.39 and 1.58 mm, respectively. For a bond strength of about 5 kN, FE1C1 B slipped more than 20 mm. This high bond capacity can be directly related to the presence of a hybrid set of short hooked and straight steel fibers where the characteristic of each one is highly used in terms of mechanical bond and group effect.

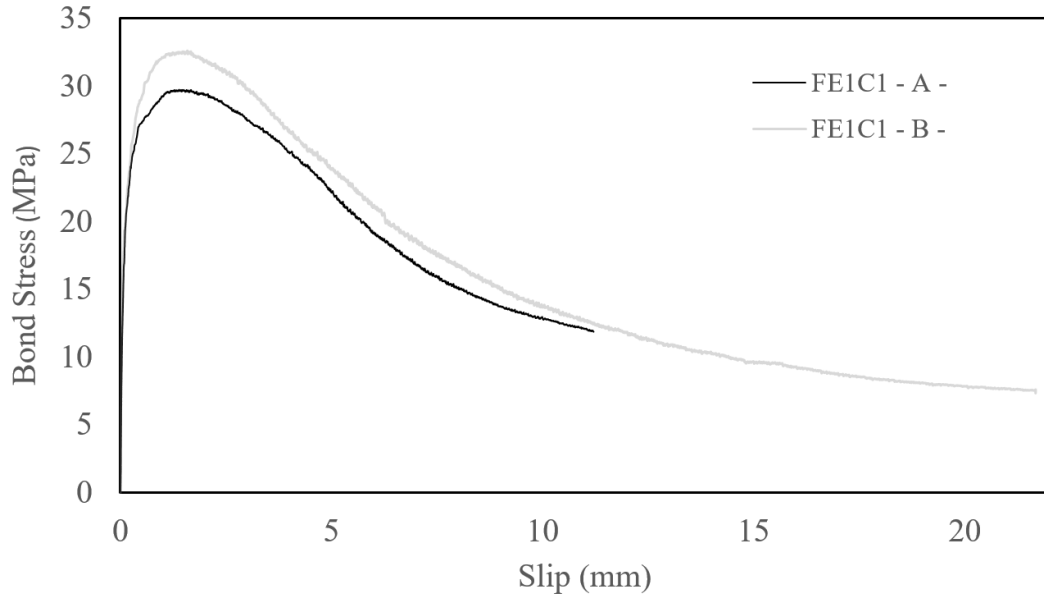


Figure 5-28 Average bond-stress vs. slip (loaded end) – Beam FE1C1

5.5.6 Beams FE1C2

The response curve of FE1C2 presents an almost parabolic shape, where the peak load reached 83.66 kN with a deflection of 3.13 mm as presented in Figure 5-29. At a load of 25 kN, the beam was able to deflect about 26.99 mm.

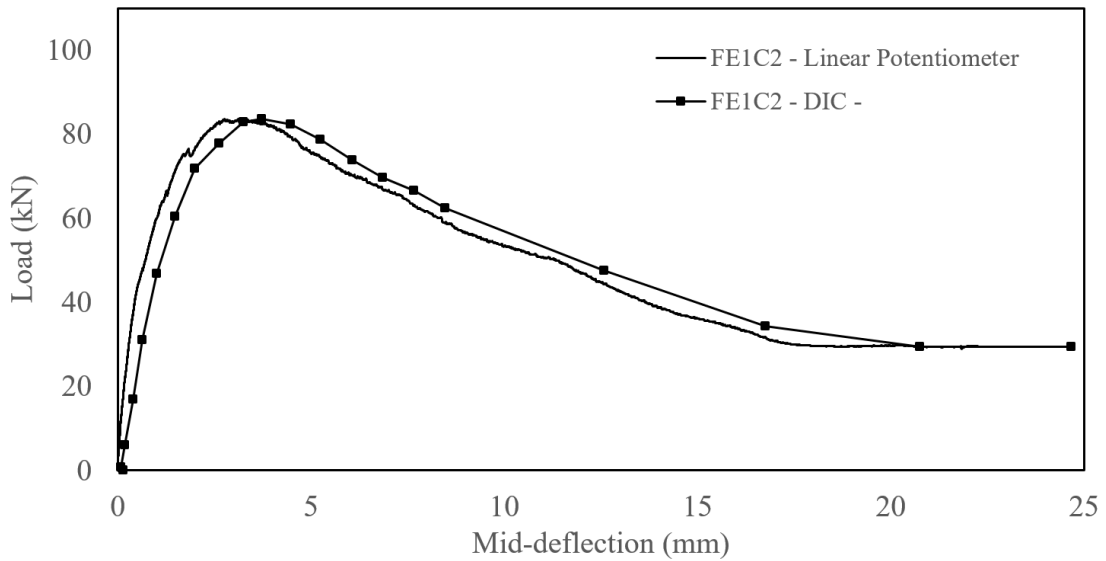


Figure 5-29 Load versus mid-deflection – Beam FE1C2

The crack in the front was developed in the same manner described for FE1C1 presented in Figure 5-30. The bond-stress slip relationship in Figure 5-31 has a steep ascending branch reaching a bond strength of 30.86 MPa with a bar slippage of 1.04 mm. The area under the descending branch is significant with the slip reaching 20 mm when the bond stress is reduced to 5 MPa. Figure 5-32 (a, b and c) shows the pullout-splitting crack failure of the beam presenting a slip value of around 20 mm.



Figure 5-30 Crack pattern after failure - Beam FE1C2

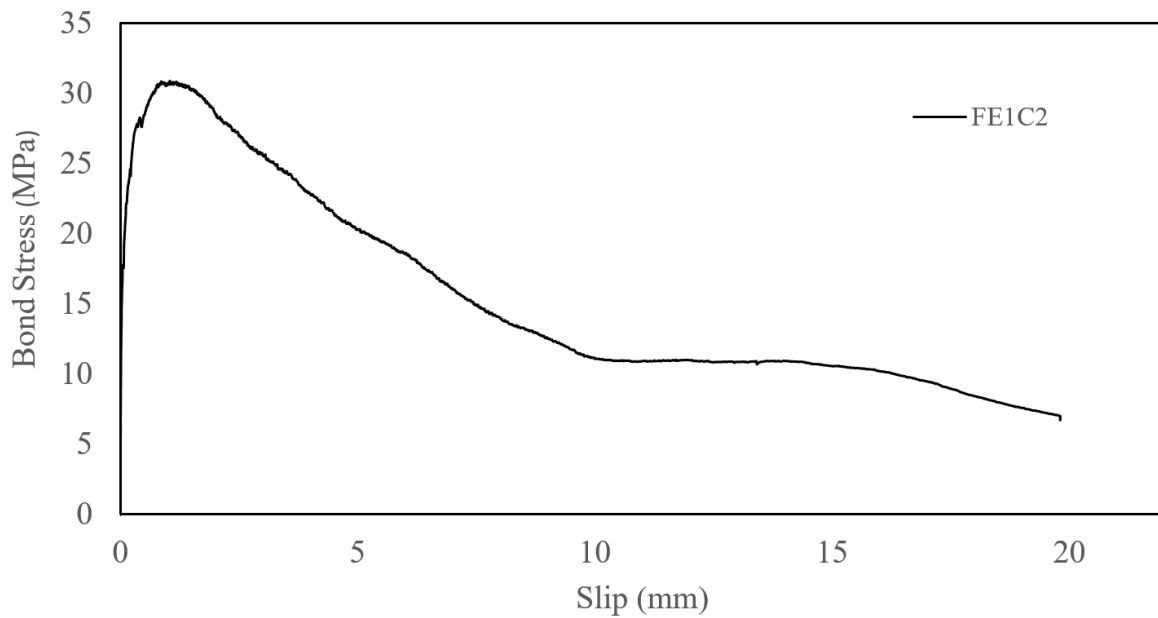


Figure 5-31 Average bond-stress vs. slip (loaded end)– Beam FE1C2



(a)



Figure 5-32(a) Crack pattern of cover after failure, (b) pullout of the bar and (c) slip of the bar

5.5.7 Beams FE4C1

FE4C1 is used for modeling purposes. From Figure 5-33, the beam yielded at a load of 120 kN and a mid-deflection of about 2.5 mm. During the increase of the load, the response showed strain hardening curve attaining a peak load of 144.1 kN and a mid-deflection of 7.24 mm. The testing was halted at a mid-deflection of 27.78 mm without slippage of the 15M reinforcing bar (0.075 mm). A crack developed at the right end of the notch leading to the crushing of the concrete in compression zone as shown in Figure 5-34 (a). The bottom of the beam experienced some splitting cracks owing to the long embedment length of 450 mm that was able to yield the bar as shown in Figure 5-34 (b).

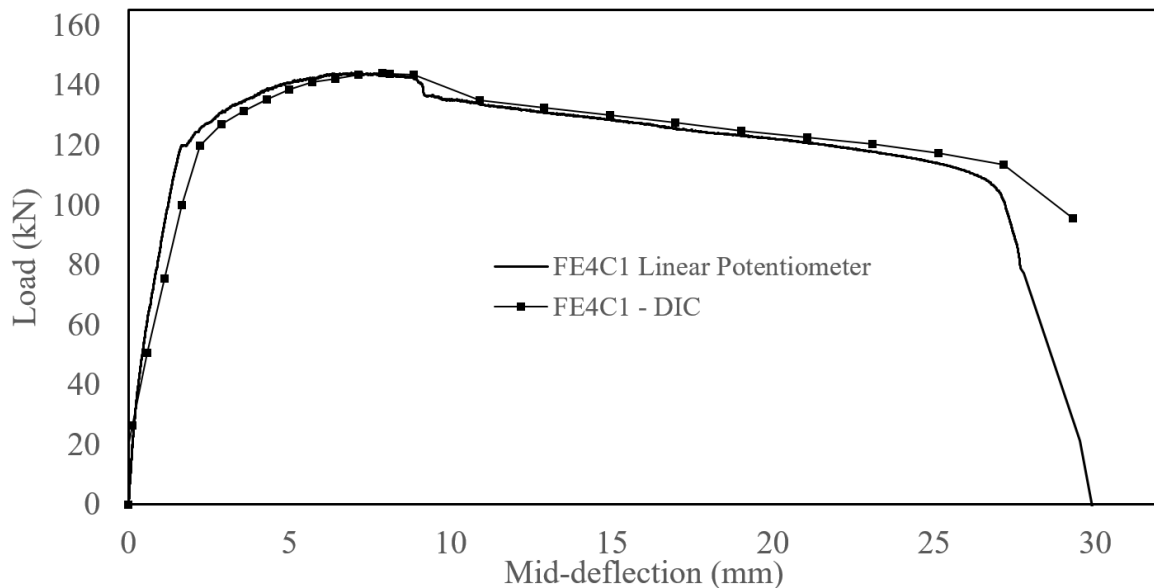


Figure 5-33 Load versus mid-deflection – Beam FE4C1

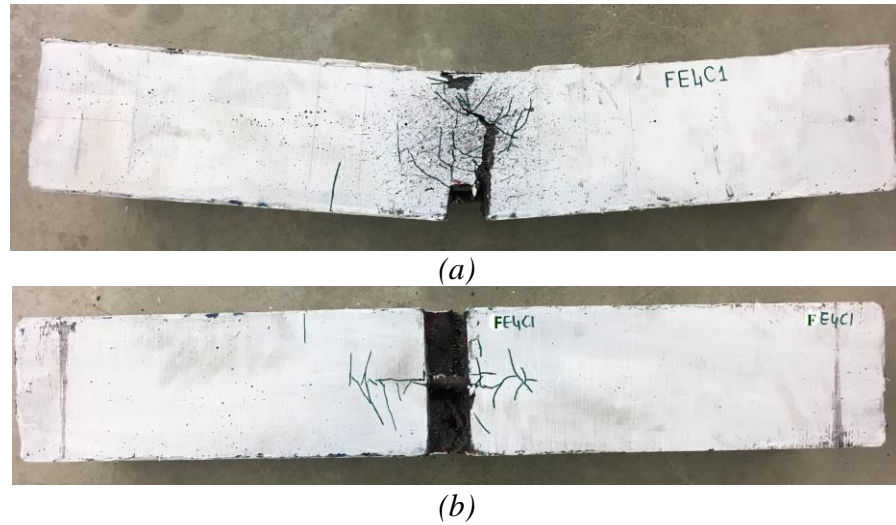


Figure 5-34 Crack pattern after failure - Beam FE4C1

5.5.8 Beams IE1C1

The three beams presented a ductile response with a peak load of 72.57, 91.45 and 79.48 kN for IE1C1 A, B and C, respectively, developing a deflection between 1.78 and 2.04 mm as can be seen in Figure 5-35. The front face of the beam showed the formation of a crack on the right end of the notch that propagated in an inclined direction to reach the left side of the mid-span and entering the compression zone as presented in Figure 5-36.

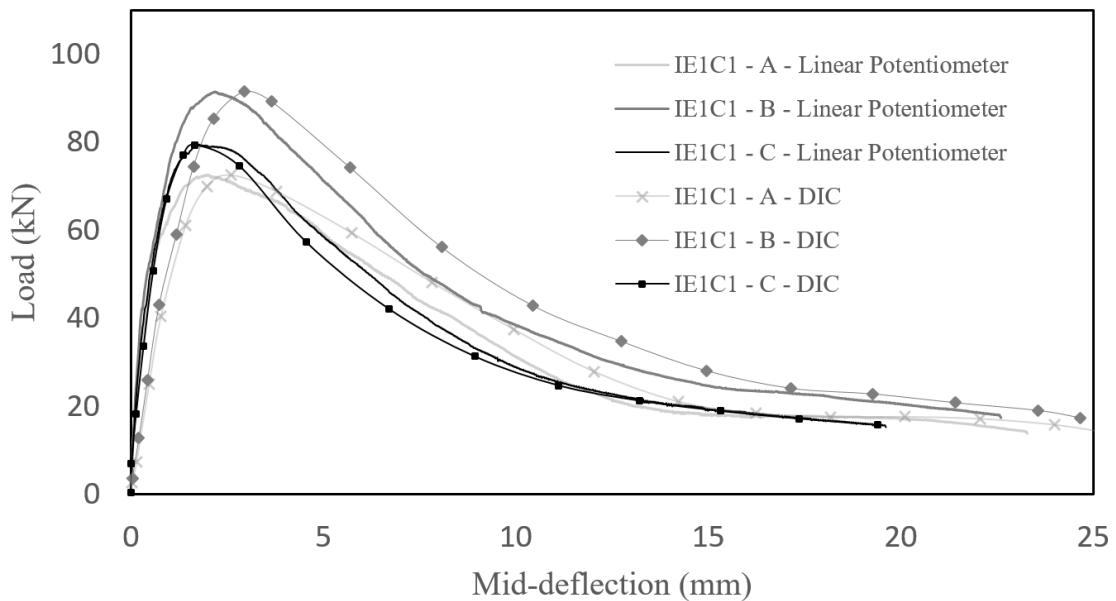


Figure 5-35 Load versus mid-deflection – Beam IE1C1



Figure 5-36 Crack pattern after failure - Beam IE1C1

Each beam experienced different modes of failure: IE1C1A failed by regular pullout-splitting (ref: Figure 5-37 (c)), Beam IE1C1 B experienced a V-type splitting mode of failure (ref: Figure 5-37 (b)), and beam IE1C1 C developed a cone failure (ref: Figure 5-37 (c)).

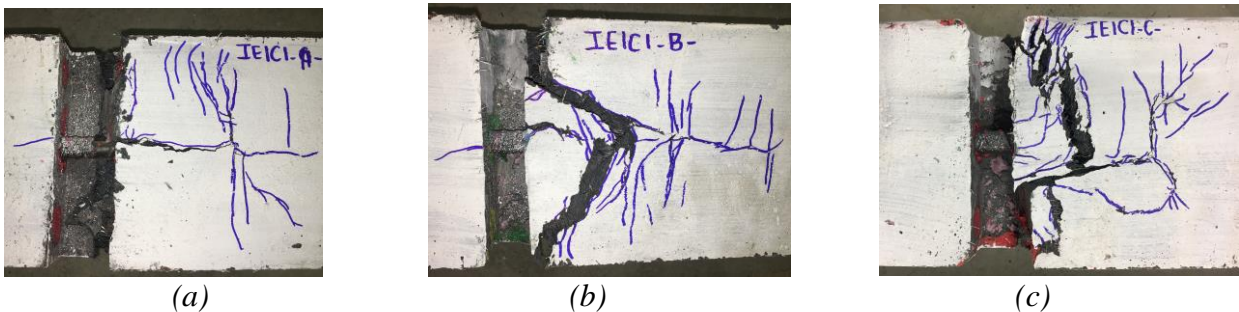


Figure 5-37 (a) Crack pattern of cover for IE1C1 -A-, (b) IE1C1-B- and (c) IE1C1 -C-

The response curves of these specimens is reflected in the bond-stress slip behaviour in Figure 5-38 presenting an average bond strength of 28.3 MPa with a slip around 0.8 mm. The bond stress then decreases gradually to reach at a value of 10 MPa with a slip 12.5 mm.

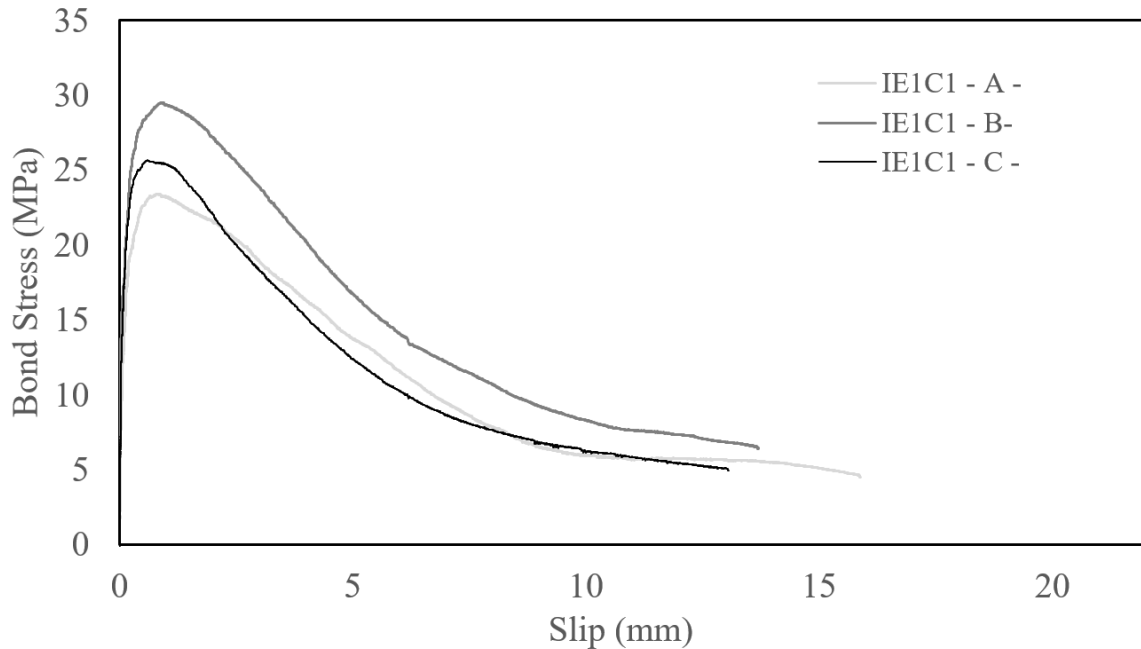


Figure 5-38 Bond-stress vs. slip – Beam IE1C1

5.5.9 Beams IE1C2

Similar shapes of the response curve were observed in Figure 5-39 where the peak loads of IE1C1A and B are 80.32 and 83.31 kN with a mid-deflection of 2.04 and 2.61 mm. The cracking pattern of IE1C2A and B started on the right end of the notch as described in beams IE1C1, yet, they propagated vertically to reach the top of the beam as can be seen in Figure 5-40. This was different for beam IE1C2C presenting a cold joint (marked in blue) formed during casting as discussed in Section 4.3.3.3. The crack at the front face started at the left end of the notch and propagated in an inclined direction to reach the line of the cold joint. Afterwards, the crack became horizontal spreading along the line. However, the formation of a cold joint did not affect the load capacity of the beam, and IE1C2C was able to carry the highest load of 86.03 kN with a mid-deflection of 2.2 mm. The other difference that is observed between these beams is that IE1C2C had a sharper slope of the softening curve than IE1C2 A and B. An example is the applied load of 25 kN, where the mid-deflection was 21.27 mm for IE1C2 A, 14.71 mm for IE1C2B and 12.67 mm for IE1C2C.

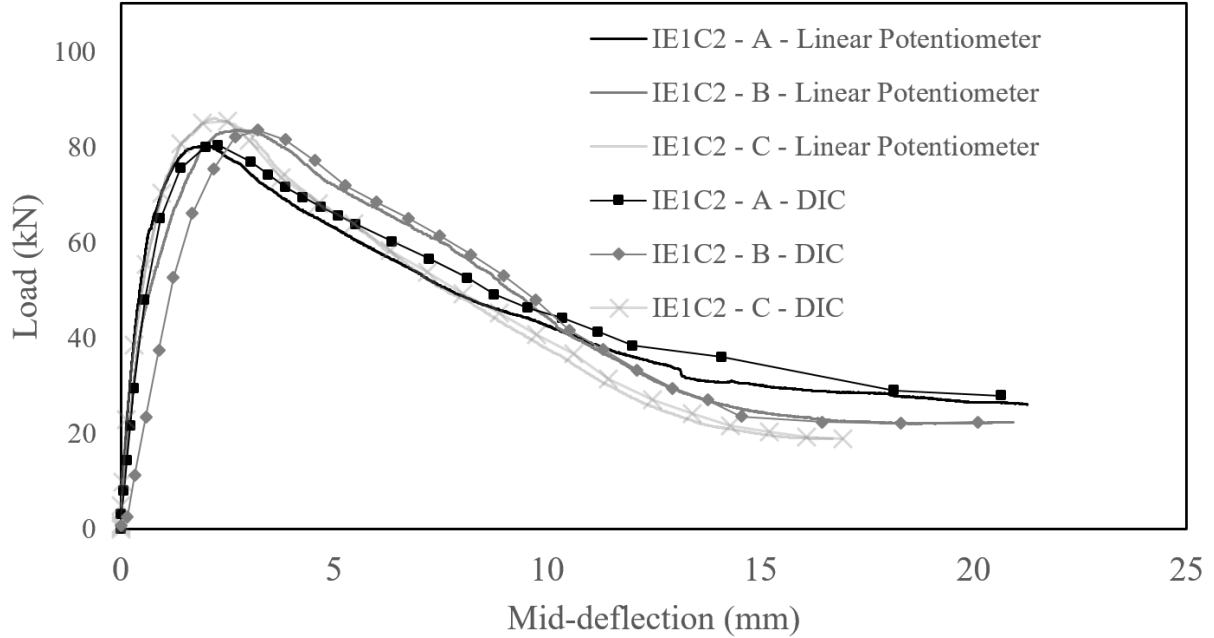


Figure 5-39 Load versus mid-deflection – Beam IE1C2

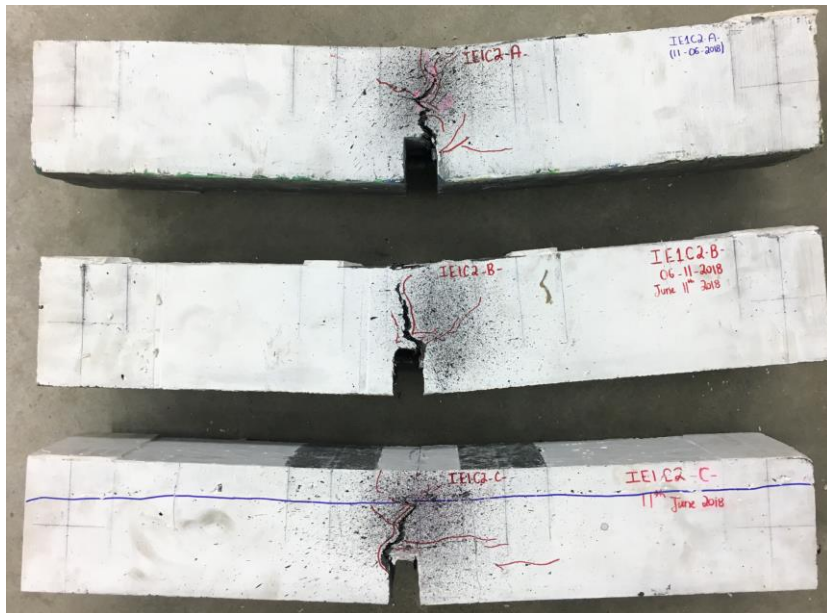


Figure 5-40 Crack pattern after failure - Beam IE1C2

The bond-stress slip relationship is presented in Figure 5-41 where the average bond strength obtained is 30 MPa accompanied by a slip of 0.9 mm. The curve presented a steeper descending branch to reach bond stress of 10 MPa with a slip of 10 mm.

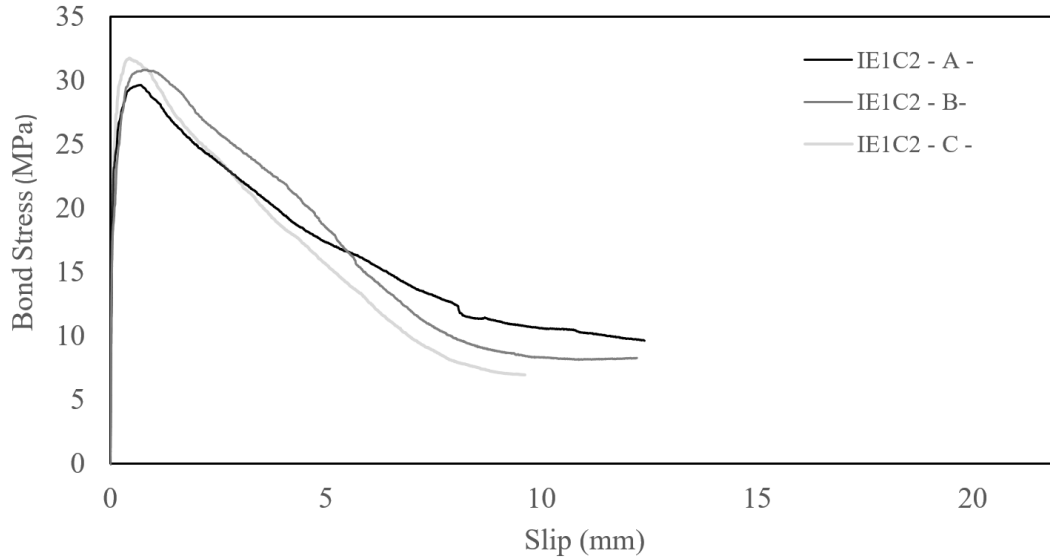
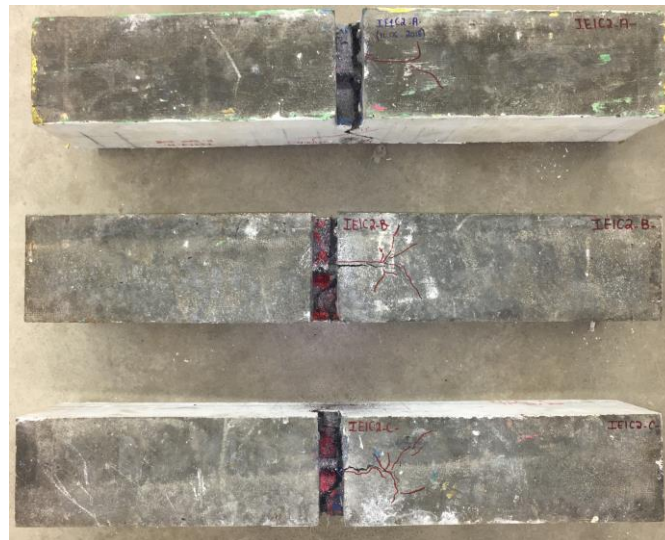


Figure 5-41 Local bond-stress vs. slip (loaded end)– Beam IE1C2

All three beams failed by pullout-splitting failure mode where a very narrow crack was observed in the bottom of the beams along the embedment length of $5d_b$, as depicted in Figure 5-42 (a, b and c).



(a)



(b)



(c)

Figure 5-42(a) Crack pattern of cover after failure, (b) pullout of the bar and (c) slip of the bar

5.5.10 Beams IE2C2

IE2C2 are characterized by a long embedment length of $10d_b$ with a concrete cover of $2d_b$. Figure 5-43 illustrates a very ductile behavior where the beams failed by the splitting-pullout of the 15M bar and its yielding. All the beams mainly reached 103 kN of peak load with a mid-deflection of 6.8 mm. Figure 5-44 shows the initiation of the crack from the left corner of the notch, propagating diagonally to the top surface of the beam.

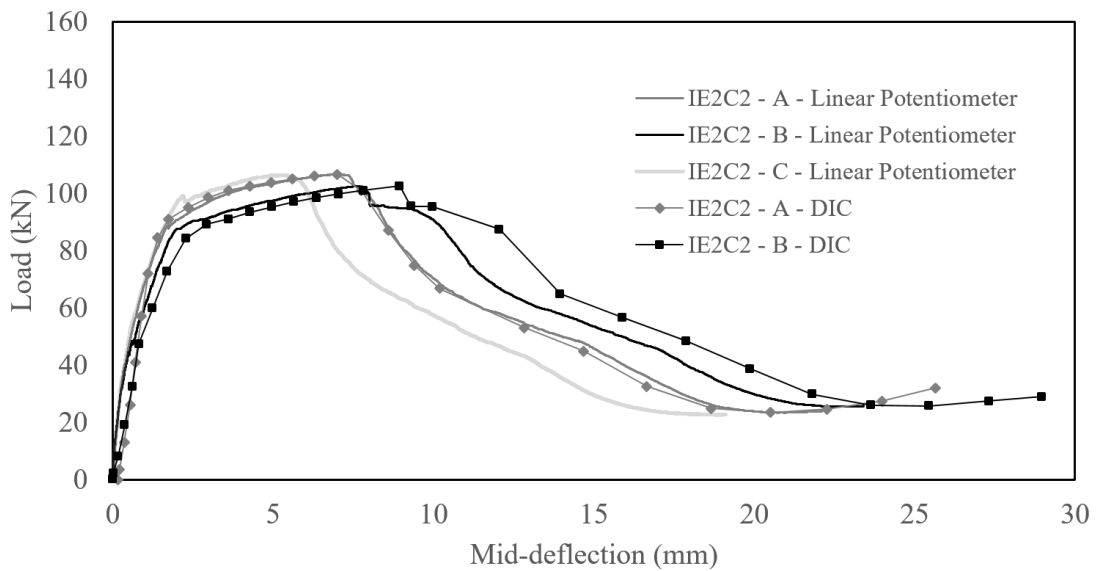


Figure 5-43 Load versus mid-deflection – Beam IE2C2



Figure 5-44 Crack pattern after failure - Beam IE2C2

The beams presented one major splitting failure at their bottom side that extended up until $10d_b$ as can be seen in Figure 5-45 (a). Figure 5-45 (b) presents the pullout of the 15M rebar where the maximum bar slip was around 8.7 mm at a load of 25 kN as can be seen in Figure 5-45 (c).

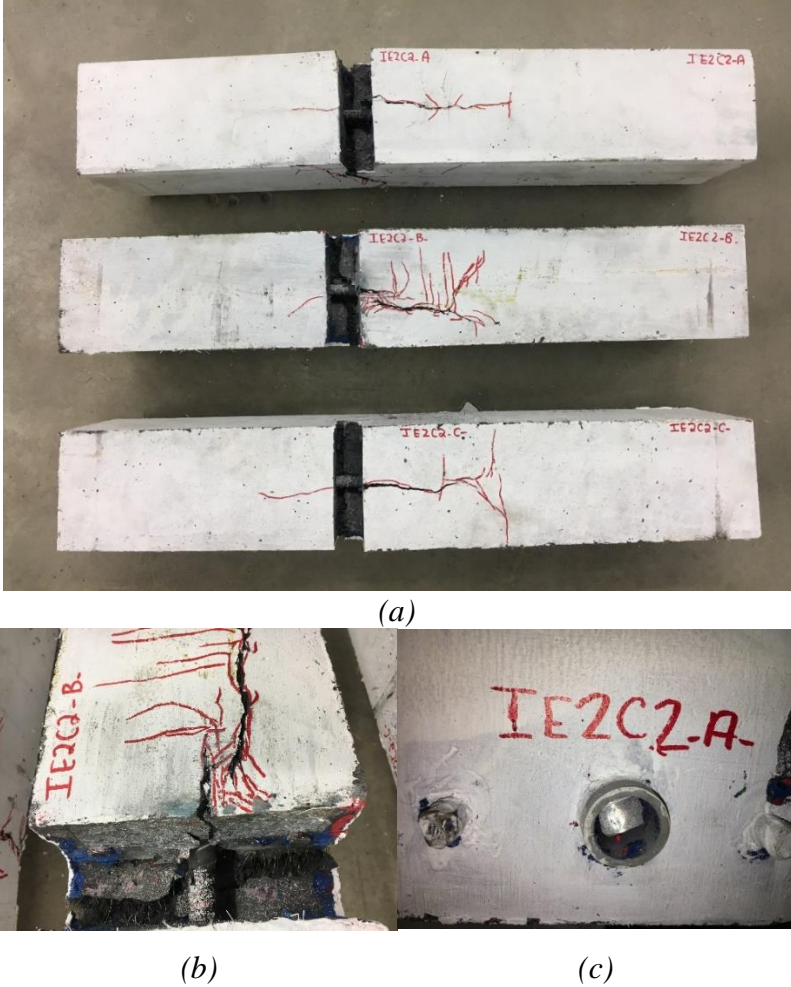


Figure 5-45 Crack pattern of cover after failure, (b) pullout of the bar and (c) slip of the bar

The bond stress is evidently no longer uniform for these higher embedment lengths. However, Figure 5-46 presents the empirical bar stress-slip response, where it can be seen that the bar stress increases to reach a maximum load capacity of the reinforcing bar for a minimal slip of 0.6 mm. Afterwards, the bar stress decreases with increasing slip values.

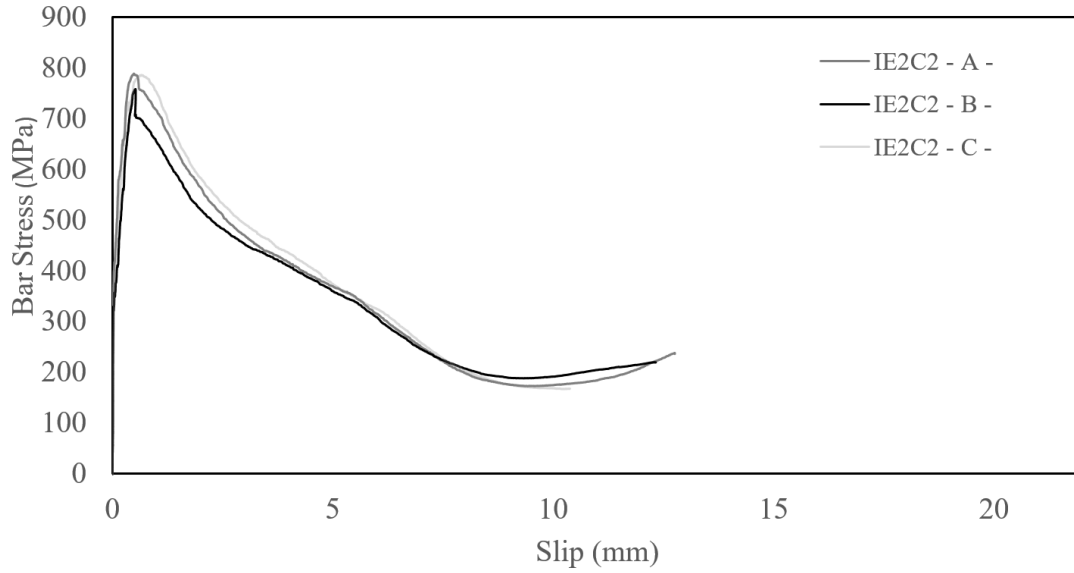


Figure 5-46 Loaded end bar-stress vs. slip – Beam IE2C2

5.5.11 Beams IE3C2

Specimens IE3C2 A, B, and C experienced a maximum deflection of 27.18 mm, 30.18 mm and 27 mm with a slip of 0.7 mm, 0.61 mm and 0.73 mm, respectively, as shown in Figure 5-47. The response curve is very ductile. The long embedment length of $15d_b$ changed the mode of failure from bond to flexural/shear.

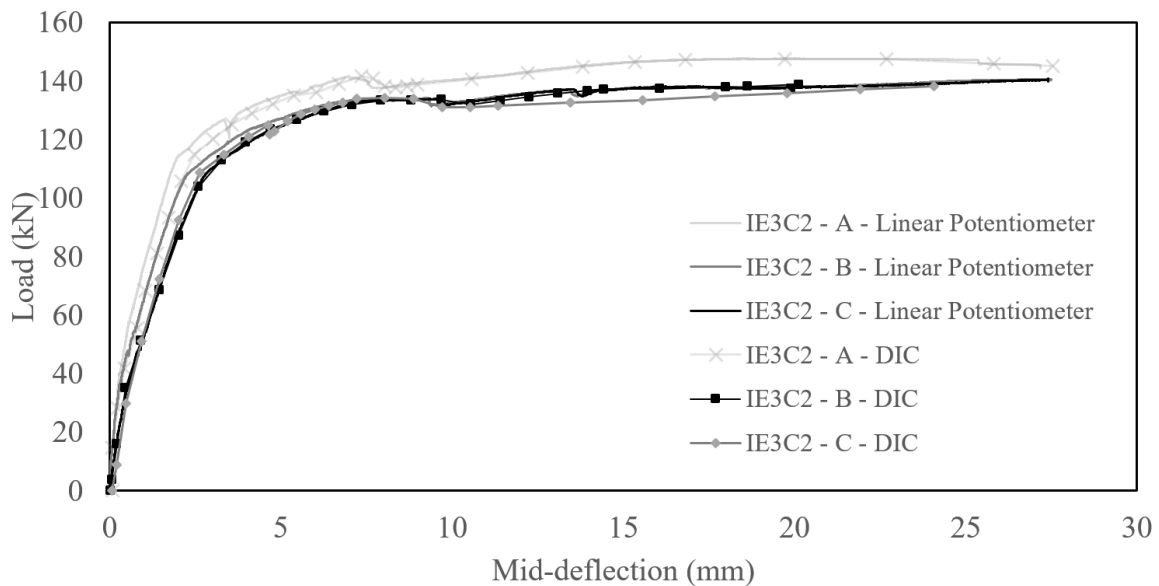


Figure 5-47 Load versus mid-deflection – Beam IE3C2

As can be seen from Figure 5-48 (a), the crack starts at the notch and propagates in an inclined direction to reach the top of the beam. It can be seen that beam IE3C2 A and C presented flexural cracks along the shear span while IE3C2 B developed a shear crack. The shear crack is mainly due to the subtle change in the jig with a longer distance between the rollers changing the designed shear span from 270 mm to 250 mm and increasing the chance of shear failure. It can be seen that no pullout nor slippage of the reinforcing bar was observed in Figure 5-48 (b) and (c).

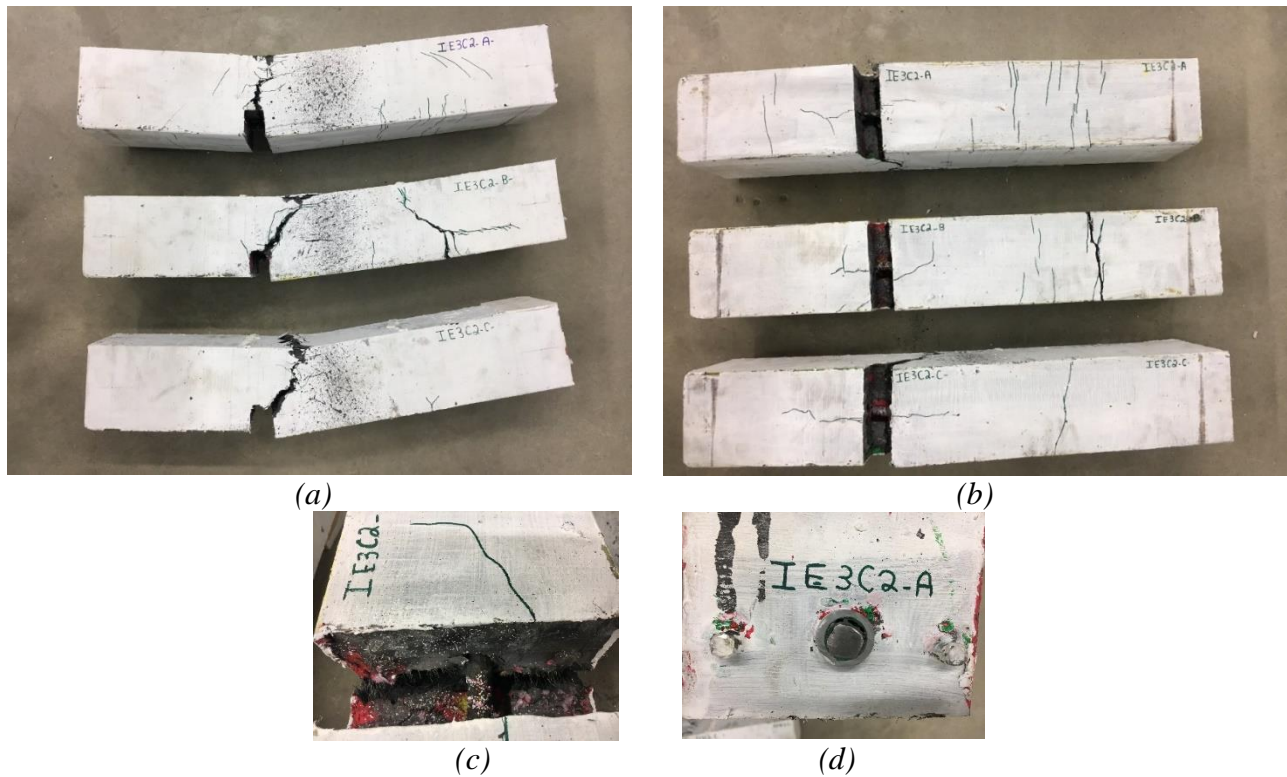


Figure 5-48 (a) Crack pattern on the front, (b) crack pattern of cover after failure, (c) pullout of the bar and (d) no slip

5.5.12 Summary of results

The concrete cover of the beam IE1C1 A presenting a pullout-splitting failure was removed to verify any crushing of the concrete in between the ribs identifying a pure pullout failure. As shown in Figure 5-49, the concrete in between the ribs remained the same. This can be explained by the exceptionally higher compressive strength of this concrete, leading to preferential cover cracking before the crushing of the concrete present between the ribs preventing the possibility of obtaining a pure pullout.



Figure 5-49 Shape of the concrete in between the ribs (Beam IE1C1 – A)

Table 5-6 presents a summary of the mid-span deflection ($\Delta_{\text{first crack}}$) generated by the load at first crack ($F_{\text{first crack}}$), the maximum peak load (F_{peak}) and the corresponding mid-deflection (Δ_{peak}), the maximum bar stress (f_s), the average bond strength (f_b), the slip, the deflection of the beam ($\Delta_{P=25\text{kN}}$) and the slip of the reinforcing bar ($\text{slip}_{P=25\text{kN}}$) when the load drops to 25 kN and finally the type of failure experienced. The values of the applied load and the mid-deflection regarding the appearance of the first crack of the front face of the beam were obtained by relating the time observed in the captured picture with the recorded data as shown in Figure 5-50.

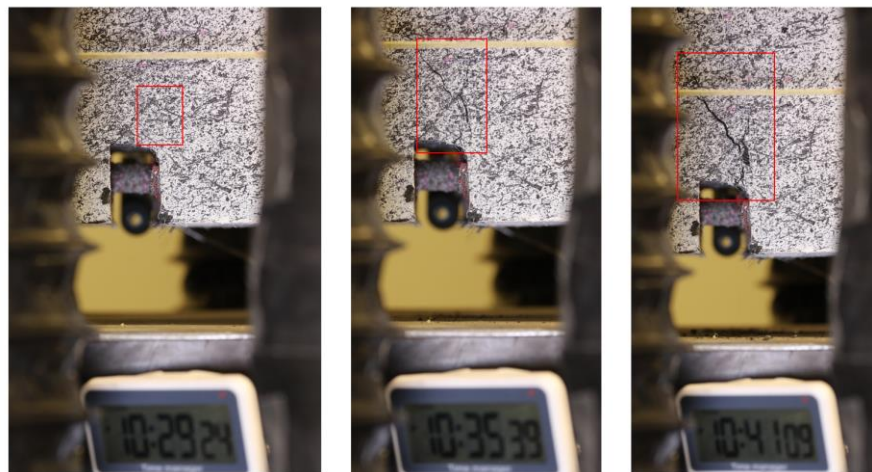


Figure 5-50 Evolution of the development of the crack

Based on the cracking pattern and the reinforcing bar state, several modes of failure were detected. In other words, each mode is characterized by a letter where; C, V, P-S, P-Y, P-R, P-S/V, Y-S depicts respectively cone, v-type split, pullout-split, pullout yield, pullout-rupture, V-Type split with pullout, and yielding with splitting, respectively.

Table 5-6 Summary of salient parameters from beam tests

Beam	F_{1st crack} (kN)	Δ_{1st crack} (mm)	F_{peak} (kN)	Δ_{peak} (mm)	f_s (MPa)	f_b (MPa)	Slip (mm)	Δ_{25kN} (mm)	Slip_{25kN} (mm)	Failure mode
KE1C1A	53.51	0.55	75.1	1.62	484.98	24.25	0.56	10.54	7.41	P-S
KE1C1B	48.76	0.45	69.65	1.54	449.77	22.5	0.52	10.32	7.11	P-S
KE1C2A	42.27	0.56	56.36	1.5	415.82	20.79	0.42	12.11	7.15	P-S
KE1C2B	52.12	0.75	68.74	1.86	443.9	25.35	0.62	11.3	6.98	P-S
KE4C1	74.86	0.86	119	5.49	> fu	-	0.01	-	-	P-R
KE4C2	23.26	2.39	36.4	14	> fu	-	0.01	-	-	S-Y
FE1C1A	66.43	0.78	92.05	2.96	> fu	29.72	1.39	23.35	12.04	P-S
FE1C1B	75.71	1.03	100.95	3.24	> fu	32.59	1.58	27.21	19.00	P-S/V
FE1C2	58.53	0.95	83.67	3.13	540.3	30.86	1.04	26.99	17.25	P-S
FE4C1	86.52	1.00	144.19	7.24	> fu	-	0.06	-	-	Y-S
IE1C1A	54.4	0.64	72.58	2	468.06	23.36	0.81	11.37	7.8	P-S
IE1C1B	68.59	0.85	91.45	2.17	590.6	29.52	0.89	14.8	10.25	V
IE1C1C	58.02	0.68	79.48	1.78	513.25	25.66	0.58	11.36	7.52	C
IE1C2A	57.65	0.57	80.32	2.04	592.5	29.62	0.71	21.27	12.38	P-S
IE1C2B	59.98	0.13	83.31	2.61	> fu	30.72	0.73	14.71	8.51	P-S
IE1C2C	60.22	0.71	86.03	2.2	> fu	31.73	0.44	12.67	7.28	P-S
IE2C2A	74.77	1.17	106.81	7.1	> fu	-	0.49	19.15	8.44	P-S
IE2C2B	72.89	1.37	102.67	7.71	> fu	-	0.52	22.15	8.99	P-S
IE2C2C	72.43	1.11	106.43	5.28	> fu	-	0.66	16.29	8.56	P-S
IE3C2A	93.84	1.41	144.38	18.47	> fu	-	0.68	-	-	Y
IE3C2B	87.04	1.55	139.82	28.92	> fu	-	0.6	-	-	Shear
IE3C2C	84.63	1.26	134.34	22.03	> fu	-	0.73	-	-	Y

5.6 Comparison and discussion

5.6.1 Effect of the properties of UHP-SFRC

The auxiliary bars are located far away from the main bar, therefore not interfering in the bond strength. The latter becomes mainly dependent on the concrete's mechanical properties. Figure 5-51 presents the load versus mid-deflection of the three design mixes for comparison with the same concrete cover $c = 1d_b$ and embedment length $5d_b$. The main difference in the properties of these three design mixes is their flexural strength previously presented in section 5.2.2 where the flexural strength is 24 MPa, 28 MPa, and 31 MPa for Commercial K, In-house design mixture and Commercial F, respectively. It is noted that the flexural strength and the peak load with the corresponding mid-deflection are proportional. These values are introduced starting from the weakest material with a peak load and mid-deflection of 72.4 kN and 1.6 mm for Commercial K, to 81.2 kN and 2 mm for the in-house design mixture to finally 96.5 kN and 3.1 mm for commercial F. All the materials have the same pre-peak ascending slope, yet widely vary in the post-peak descending phase. It is evident that the high flexural strength leads to wider response curves stating a higher ductile capacity and energy dissipation to carry greater loads for the same mid-deflection. For the same applied load of 25 kN, the mid-deflection was 10.4 mm for KE1C1, 12.5 mm for IE1C1 and 25.3 mm for FE1C1.

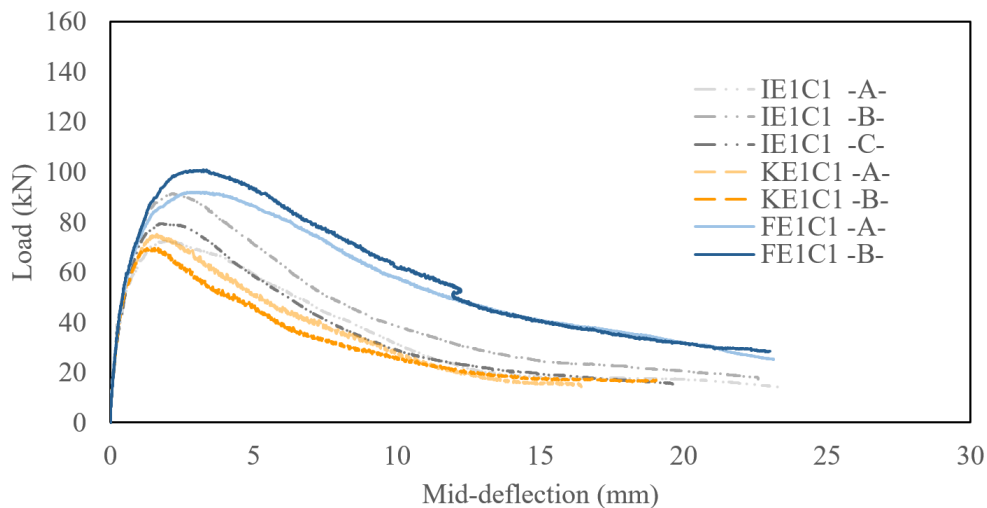


Figure 5-51 Load vs. mid-deflection for different mixes (I, K and F) for a concrete cover equal to the bar diameter and an embedment length equal to 5 times the bar diameter (E1C1)

This affects as well the bond strength where the higher the flexural strength, the more significant the bond strength as shown in Figure 5-52. Simultaneously, this will result in a higher relative displacement between the reinforcing bar and the concrete where for a 25 kN of load at the end of the testing, the 15M reinforcing bar slipped 7.3 mm when embedded in Commercial K's concrete, 8.5 mm for the in-house design mixture and lastly 15.5 mm for the Commercial F mix.

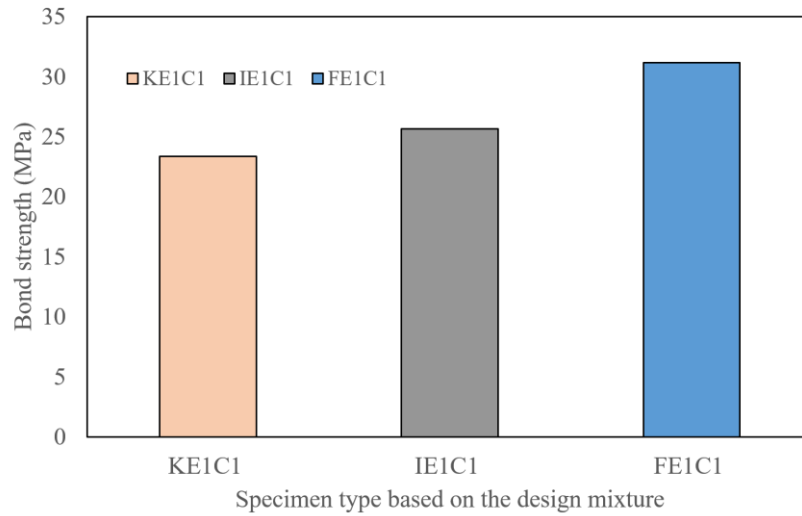


Figure 5-52 Comparison of the bond strength for different mixes with a concrete cover equal to the bar diameter

It can be seen that the beams from Commercial K's specimens failed by pullout-splitting mode of failure. One of the specimens from commercial F failed by pullout-splitting (FE1C1A) while the second specimen (FE1C1B) developed a splitting crack with half of a V-type split. However, in the case of the in-house design mixtures: IE1C1A developed a splitting crack, IE1C1B presented a cone failure, and IE1C2C failed by a V-type split. Thus, it can be seen that the high properties of the concrete can change the mode of failure from splitting to the cone and V-type splitting failure.

Almost the same behavior was observed for the beams with a concrete cover of $2d_b$ presented in Figure 5-53 except for the in-house design mixture IE1C2 with an increase in the sustained load to 83.2 kN and a mid-deflection of 2.3 mm. Thus, the comparison of the commercial K and F was only conducted. In fact, the beams of commercial K were able to sustain a load of 62.6 kN for a mid-deflection of 1.7 mm. The peak load sustained by Commercial F's beam was 83.66 kN with a deflection of 3.13mm. Thus, owing to the high tensile properties of commercial F, the beam always presented a higher deformation capacity and strength.

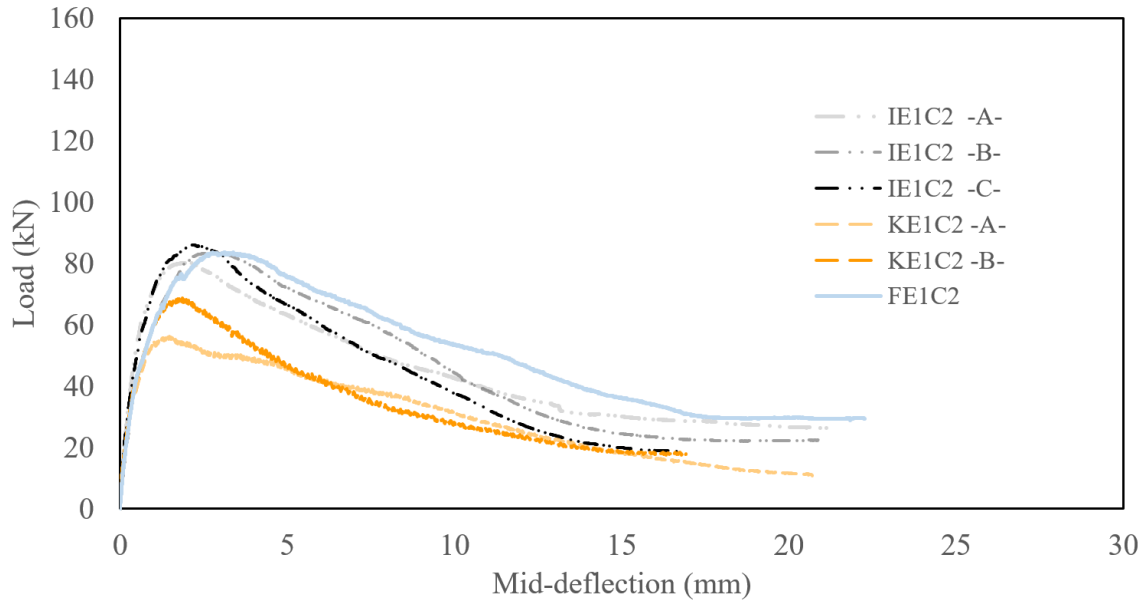


Figure 5-53 Load vs. mid-deflection for different mixes (I, K and F) for a concrete cover equal to twice the bar diameter and an embedment length equal to 5 times the bar diameter (E1C2)

The effect of the concrete matrix properties is presented in Figure 5-54 where the bond strength for the commercial F remained the highest, and the Commercial K was the lowest where the 15M slipped about 1.04 mm at the peak point.

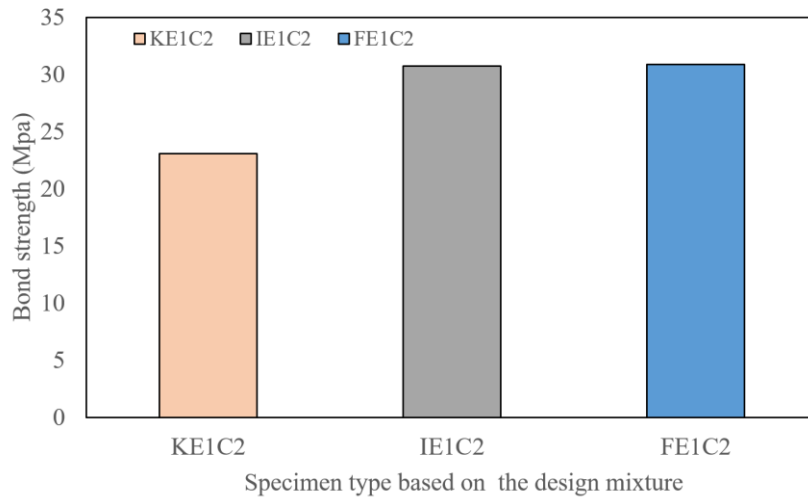


Figure 5-54 Comparison of the bond strength for different mixes with a concrete cover equal to twice the bar diameter

The same behavior was observed in Figure 5-55 presenting the response curves of beams FE4C1 and KE4C1 where the higher tensile properties lead to a more ductile behavior with a higher strength capacity.

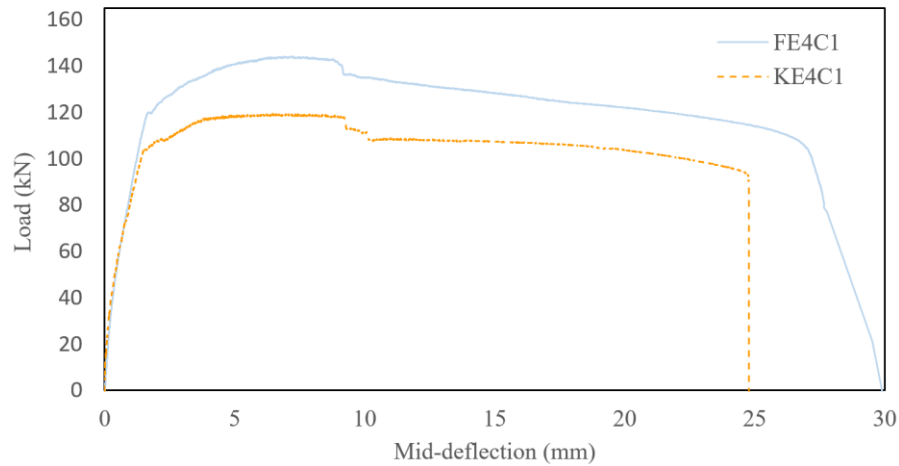


Figure 5-55 Load vs. mid-deflection for mixes (K and F) for a concrete cover equal to the bar diameter (E4C1)

5.6.2 Effect of the concrete cover

Figure 5-56 presents the load versus deflection response of IE1C1 and IE1C2, which differ mainly in their concrete cover. Both specimens present similar response curves with an identical initial stiffness and a strain-softening post-peak behavior. The average peak load was 81.2 kN with a mid-deflection of 2 mm for IE1C1 and 83.2 kN with a mid-deflection of 2.3 mm for IE1C2. Moreover, for a load of 25 kN in the descending branch, beam IE1C1 deflected 26.2 mm in comparison to 30.7 mm for IE1C2. Thus, it is observed that for the in-house design mixture, the increase of the concrete cover from $1d_b$ to $2d_b$ slightly increased the peak load behavior.

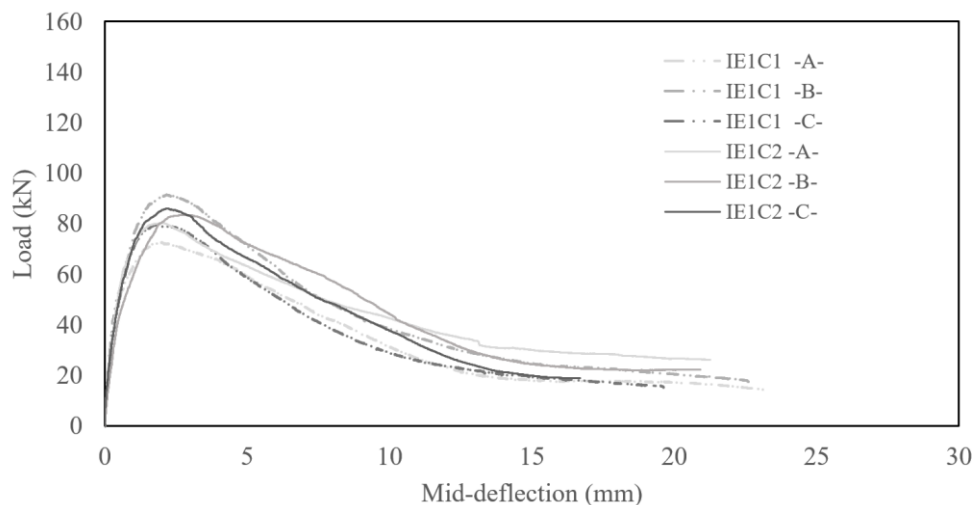


Figure 5-56 Load vs. mid-deflection for the in-house mix (I) for two different concrete covers (C1 - C2) and (E1)

Owing to the similarity in the response curve and the difference in the concrete covers, an enhancement of the bond strength was observed when increasing the concrete cover from $1d_b$ to $2d_b$. Figure 5-57 shows that the bond strength increased from 26.2 MPa for the beams IE1C1 to 30.7 MPa for the beams IE1C2.

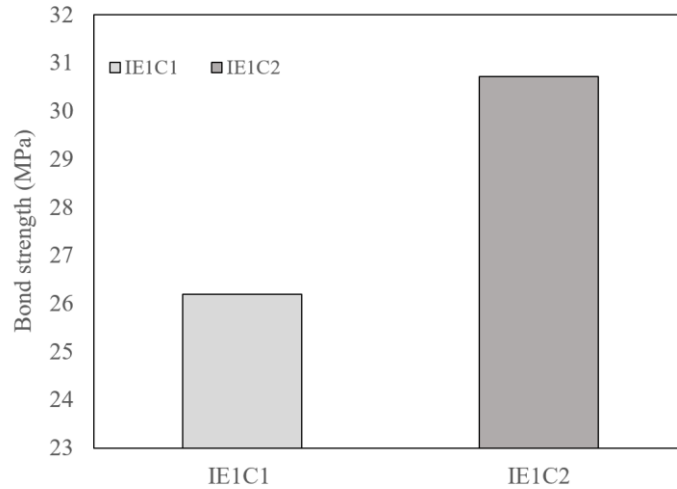


Figure 5-57 Comparison of the bond strength for the different mixes with a concrete cover equal the bar diameter

The increase of the concrete cover from $1d_b$ to $2d_b$ lead to the change of the mode of failure from cone failure and V-type split failure for the small concrete to a pullout-splitting failure for higher concrete covers values. Moreover, it is apparent that beams with a higher concrete cover value present a reduction of the slip of the reinforcing bar. In fact, IE1C1 developed a bar slippage of 0.8 mm while IE1C2 experienced a slip of 0.6 mm at peak load.

In terms of the commercial K design mixture, the increase of the concrete covers up to two times the bar diameter led to the reduction of the response curve of the specimens shown in Figure 5-58. In fact, beams KE1C1 experienced a peak load of 72.4 kN with a mid-deflection of 1.6 mm while beams KE1C2 are able to sustain a load of 62.6 kN for a mid-deflection of 1.7 mm. However, when calculating the bond strength, both beams resulted in the same average bond strength of 23.4 MPa.

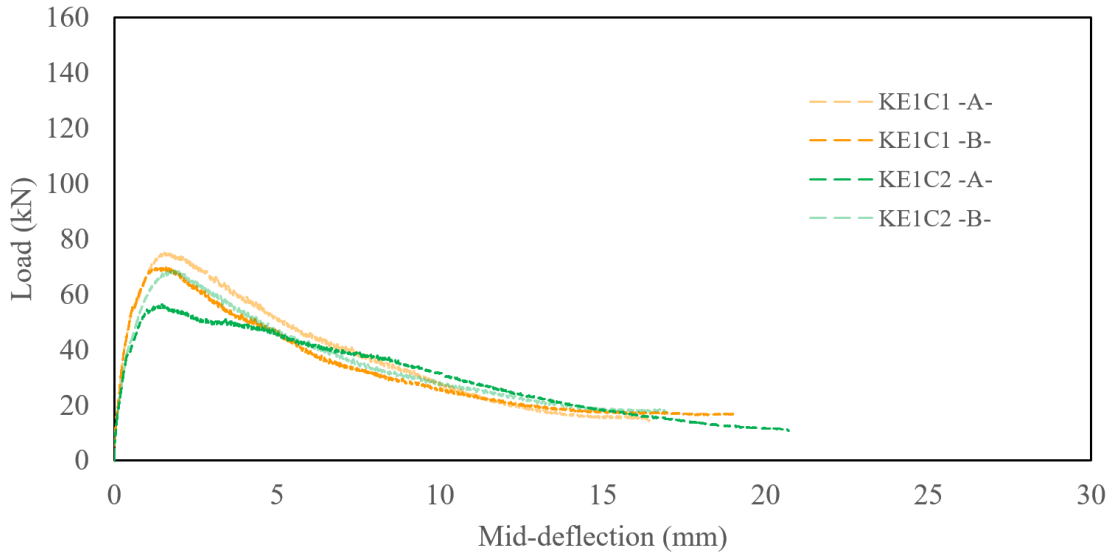


Figure 5-58 Load vs. mid-deflection for the company (K) for two different concrete covers (C1 - C2) and the same embedment length equal to 5 times the bar diameter (E1)

The same was observed for the beams of the Commercial Mix F, where though the response curve was enhanced as shown in Figure 5-59 when the concrete cover was increased, the bond strength was calculated to be the same in both cases.

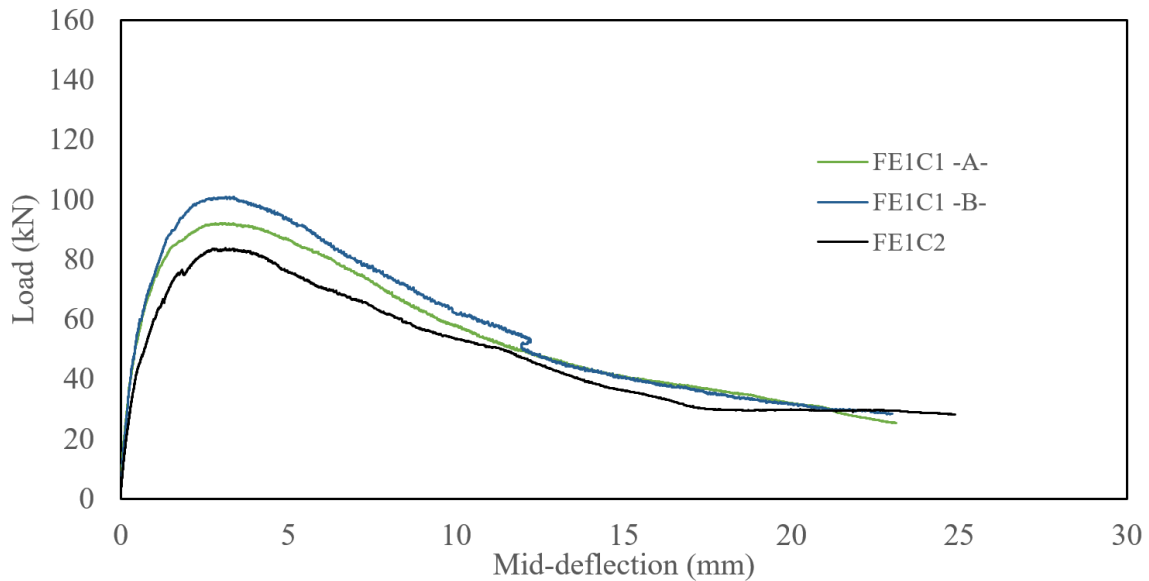


Figure 5-59 Load vs Mid-deflection for company F for two different concrete covers (C1 – C2) and the same embedment length equal to 5 times the bar diameter (E1)

Therefore, in terms of the commercial mixes, a concrete cover of $1d_b$ was enough to provide the necessary confinement to reach the ultimate bond strength of this novel concrete. By comparing the splitting cracks for the three design mixes, it can be seen that the specimens with a concrete cover of $1d_b$ present a higher number of microcracks along the main splitting crack than the ones with a concrete cover of $2d_b$. This can be explained by the fact that higher confinement is provided when the concrete cover is increased, which contributes more to resisting tensile stresses. Moreover, the crack width developed near the notch is reduced for the concrete cover of $2d_b$. In terms of modes of failure, all the specimens with a concrete cover of $2d_b$ failed by pullout-splitting failure. Moreover, the larger the concrete cover, the more closed is the longitudinal crack due to the confinement.

5.6.3 Effect of the embedment length

Figure 5-60 presents the load versus mid-deflection of the beams cast with the in-house design mix (IE1C2, IE2C2, and IE1C3). The average strength capacity increases for longer embedment lengths starting with a load of 83.2 kN and a deflection of 2.3mm for an embedment length of $5d_b$. The applied load then increased to 105.27 kN with a deflection of 6.7 mm for an embedment length of $10d_b$, and for an anchored length of $15d_b$ a load carried was 142.25 kN for a mid-deflection of 23.1 mm. This is due to the fact that more ribs are engaged in resisting the applied load. Moreover, the post-peak response changes for the longer embedment length. It follows a softening behavior for specimen IE1C2 and a short plateau prior to the strain-softening for IE2C2. IE3C2 exhibited a continuous plateau before the test was stopped due to a load drop.

All specimens experienced the same manner of the propagation of the crack at the front face of the beam in an upward and inclined direction reaching the right side of the beam. However, when comparing the location of the initiation of the crack, for the beams IE2C2 it initiated from the left end of the notch, while it surfaced from the right end of the notch for IE3C2.

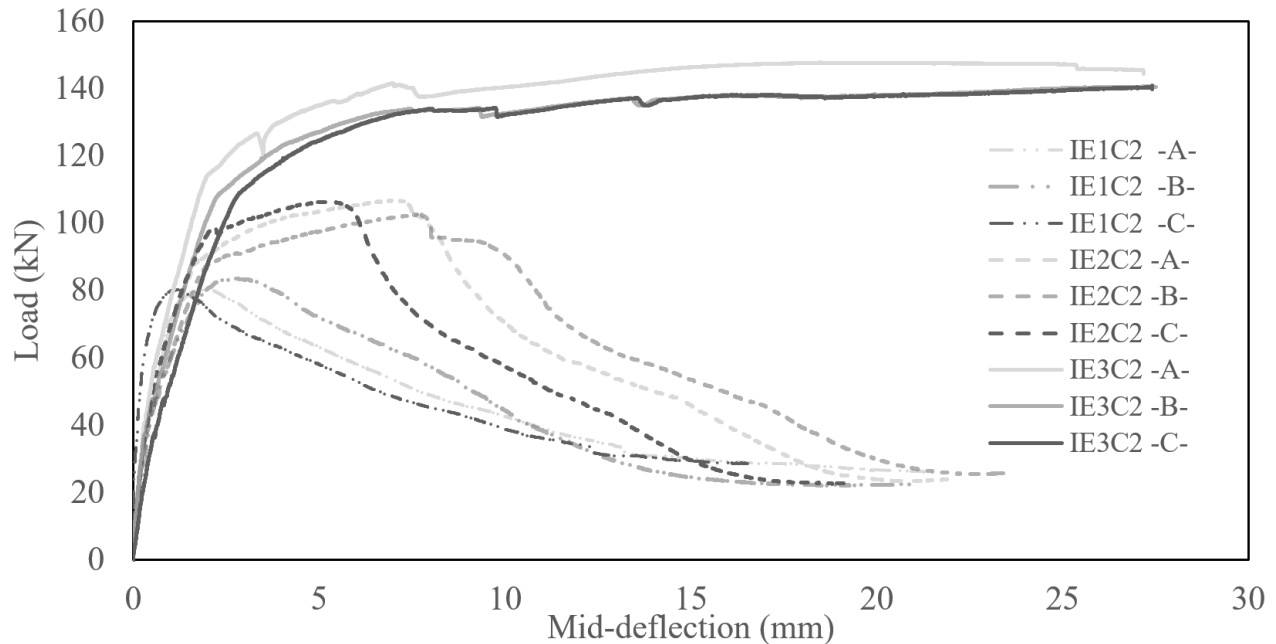


Figure 5-60 Load vs. mid-deflection for the in-house mix (I) for the same concrete cover equal to twice the bar diameter (C2) and different embedment length (E1-E2-E3)

It was shown that for an embedment length of $10d_b$, specimen IE2C2 failed by bond. The bar was able to pull-out, yet with small slip values. However, no slippage of the 15M bar was observed for the specimens IE3C2. Thus, the mode of failure of the specimen changed from pullout-splitting of the reinforcing bar to yielding. Moreover, specimens IE3C2 experienced a flexural and shear failure rather than a bond failure, owing to the increase of the distance between the rollers and the reduction of the shear span. Thus, the increase of the embedment length to $10d_b$ delays the splitting mode of failure whereas in the case of higher embedment length, such as $15d_b$ this mode of failure will be completely eliminated.

Assuming a uniform distribution of the bond strength, which may only be a valid approximation for very short anchorage lengths, the average bond value was calculated. As provided in Figure 5-61, the average bond strength decreases for longer embedment length. This means that the bond stress is not distributed uniformly along the embedment length.

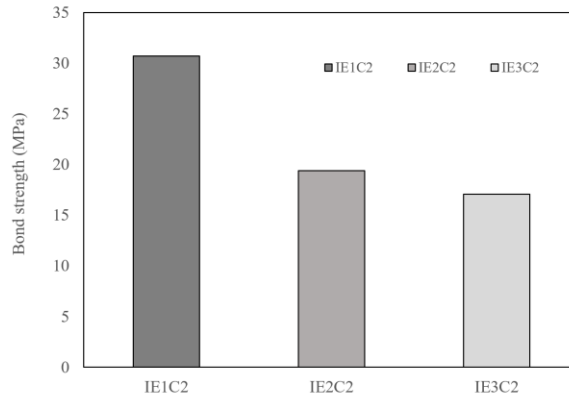


Figure 5-61 Variation of the average bond strength in terms of the embedment length

5.7 Comparison between deflection obtained from the linear potentiometer and DIC

In general, a minimal difference was observed between the mid-deflection when measured with the linear potentiometer and the Digital image correlation. In fact, all the prisms presented the same pattern of the response curve with a minimal translational difference of about 0.5 mm. Nevertheless, the response behavior defined by a linear potentiometer was stiffer than the DIC method; the deflection of prism G in Figure 5-7 at a peak load of 49.55 kN was 0.4 mm when measured with the linear potentiometer in comparison to 0.72 mm obtained from the DIC. The same occurred in the beam specimens, where the mid-deflection was greater when measured with the DIC method than with the linear potentiometer. This can be due to the incapability of the linear potentiometer to measure insignificant vertical translations of the beam when small loads are applied. Another possibility could be the deficiencies presented in the DIC methodology such as the equipment used, the position of the camera, the quality and clarity of the captured images, the efficiency of the calibration, the time intervals and the expertise of the user. Another detail that the linear potentiometer was able to capture unlike the DIC was the indication of a crack development presented by small discontinuities along the curve representing the strain-hardening plateau. This can be explained by the fact that the linear potentiometer is a continuous measuring tool while the DIC considers intervals of measurements depending on the number of pictures chosen. Another criterion regarding the DIC is its inability to capture the deflection of a brittle material such as the prism H since the failure could occur in a short period of time. Therefore, DIC is recommended with greater confidence for materials and structural members exhibiting a ductile behavior.

Chapter 6. Numerical Study

6.1 Introduction

Over the past few decades, reinforced concrete structures have been analyzed through finite element formulations due to their precision of the method and its relatively easy implementation into computational software. Nonlinear Finite Element Stress Analysis (NLFEA) is a numerical method that can be used to solve the differential equations that govern physico-chemo-mechanical phenomena that occur inside reinforced concrete structures when subject to any type of loading, i.e., flexural behavior of beams, and flexural-compression behavior in columns. Consistent linearization of these methods depend on a particular manner of discretization (mesh), dividing the domain in a number of elements (finite elements) connected by nodes, and then solving each one of the elements to obtain an overall response. Figure 6-1 represents a finite element model of a directly supported beam subjected to a point load in the middle of its span.

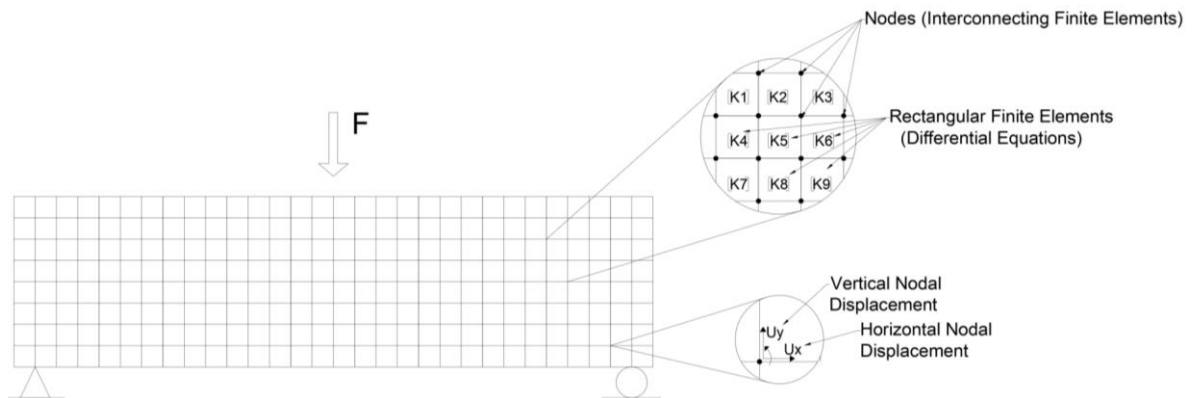


Figure 6-1 Finite element model representation of a simply supported beam subjected to a point load

The higher number of elements are utilized to discretize the structure; the more exact is the solution. Therefore, the selection of the elements' size with a fine mesh that will be utilized in the analysis, becomes crucial. Each element has geometrical and physico-mechanical properties of their own. These properties can be grouped in elemental stiffness matrices $[K_n]$ that are obtained with approximations of the differential equation together with weak formulations and the constitutive laws of the material (Yamaguchi, 2014). All the elements interact between each other throughout nodes that unite them, and therefore, assemble the totality of the structure to be analyzed. The global

stiffness matrix $[K_{global}]$ is then generated by the sum of all the local stiffness matrices formed by each element. This matrix is then multiplied by the vector of nodal displacements $\{U\}$, giving as a result the value of the external applied loads (F). The process explained extends to a more complex analytical approach that generates a broad system of equations that is generally too extensive to be solved by hand calculations. Moreover, there are different computational tools that implement this method used in this thesis.

6.2 Non-linear modeling tool (VecTor2)

VecTor2, a two-dimensional nonlinear finite element program is used for the numerical analyses. The program uses the Modified Compression Field Theory (MCFT) (Vecchio and Collins 1986) and the Disturbed Stress Field Model (DSFM) (F. J. Vecchio, 2000). In addition, it is based on an incremental, total load approach with a smeared, rotating crack model for reinforced concrete, in which cracked concrete is represented as an orthotropic material. Furthermore, an iterative procedure based on a secant stiffness formulation is utilized to verify the convergence of the results (Vecchio, Wong and Trommels, 2013). To understand the formulation behind the software, the Compression Field Theory (CFT) does not consider any tensile stresses in the concrete once it cracks (Collins and Mitchell, 1980).

This theory was modified by Vecchio and Collins (1986) and is known as Modified Compression Field Theory (MCFT), where the tensile stresses of the concrete in the cracked regions were taken into consideration. Figure 6-2 represents a membrane element subject to in-plane loading, formed by concrete and reinforcement, both in the longitudinal and vertical direction superposing the orthogonal system axes. In addition, the element is assumed in its cracked condition with the purpose to relate the average normal and shear stresses to their appropriate strains (Vecchio and Collins, 1986).

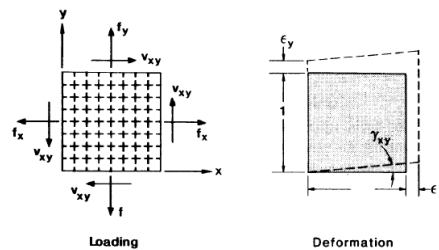


Figure 6-2 Reinforced concrete membrane element (Vecchio and Collins, 1986)

Figure 6-3 shows the transfer of stresses across cracks for the reinforced concrete membrane element.

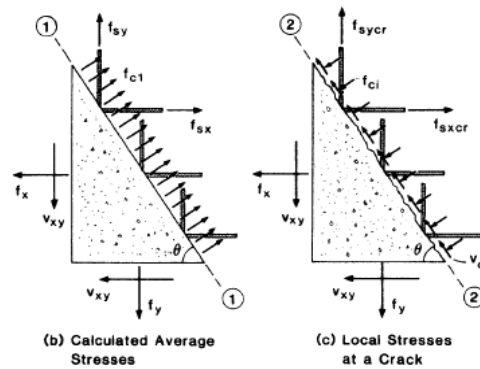


Figure 6-3 Transfer of stresses across cracks (Vecchio and Collins, 1986)

This is achieved by using firstly the compatibility conditions indicating that the strains are the same between the concrete and the reinforcement ($\epsilon_x = \epsilon_{sx} = \epsilon_{cx}$ and $\epsilon_y = \epsilon_{sy} = \epsilon_{cy}$), where the transition between the principal plane and the x-y direction can be easily obtained. Secondly, this methodology is achieved by the equilibrium conditions along the crack plane in the principal direction, taking into account the tensile stresses in the concrete in between cracks and the shear and compression stresses of the concrete along the cracks. Moreover, the average principle stresses are calculated from the average principle strains using conventional stress strain models obtained from compression and tension tests on cracked concrete. The tensile stress of the cracked concrete f_{c1} or in other terms the residual tensile strength, by which is characterized this model, is called tension-stiffening and can be seen as the post-peak branch of the curve shown in Figure 6-4.

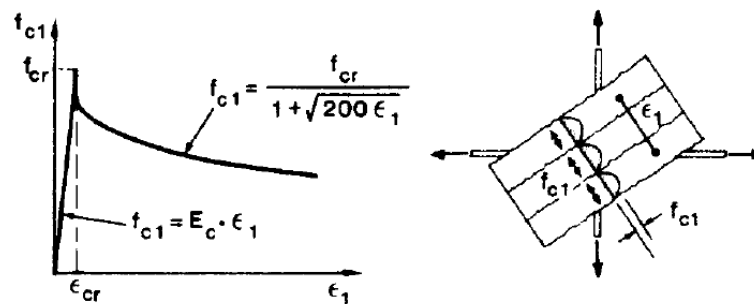


Figure 6-4 Uniaxial tension stress-strain curve representing the post-peak branch known as tension-stiffening (Vecchio and Collins, 1986)

Even though the MCFT has proven to function properly by providing accurate simulations of behavior, the addition of the Disturbed Stress Field Model (DSFM) as an extension of its formulation improved the overall response of structures by allowing slip along the crack in the element (neglected in MCFT) and removing the restriction that the principal stress and strains directions had to remain coincident (Vecchio, 2000).

The software utilizes different element types to represent the structures being studied: a 3-node constant strain triangular element, a 4-node plane stress rectangular element, and a 4-node quadrilateral element are typically used depending on the complexity of the structure to model concrete elements with smeared reinforcement. For discrete reinforcement, a two-node truss bar element is used. Finally, to represent the interaction (bond-slip) between concrete elements and discrete reinforcement, a two-node bond-link and a 4-node contact element can be generated. It is known that prior to loading, there is perfect compatibility between the concrete and the reinforcement; both elements share the same nodes as shown in Figure 6-5. VecTor2 assumes the radial stiffness to be 100 times the tangential stiffness suppressing the radial displacement of the bar.

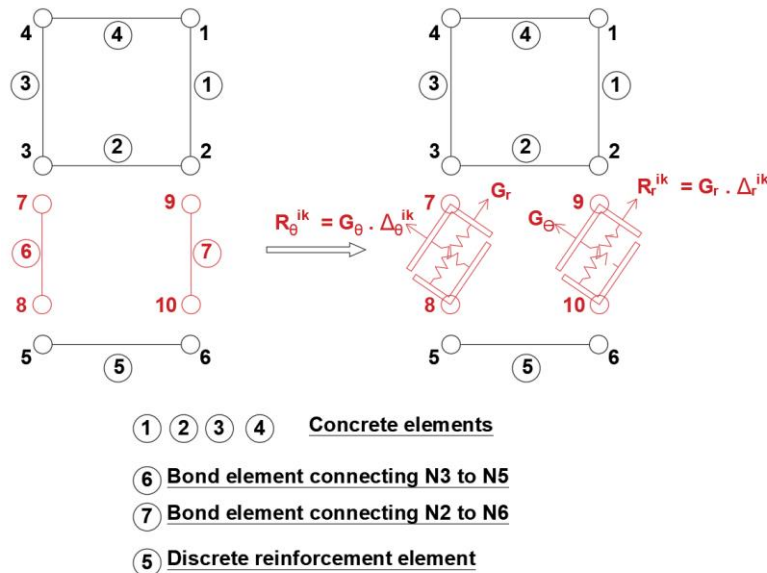


Figure 6-5 Description of the link elements in VecTor2

(Martin-Perez and Pantazopoulou, 2001) noted that the bond strength between the reinforcement and the concrete constitute a part of the tension-stiffening. The intervention of concrete is shown in Figure 6-6 where along the cracks the tensile stresses of the bar reach their maximum f_{scr} while once anchored in the concrete in between known as the smeared values the stress in the reinforcing bar reduces since it is shared with the surrounding concrete through bond in terms of residual tensile strength.

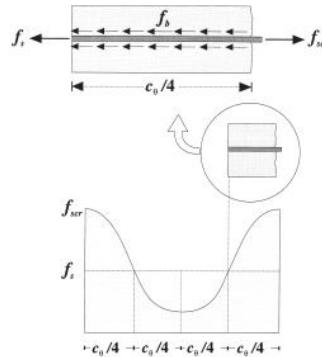


Figure 6-6 The change of stress in the reinforcing bars due to the presence of a bond (Martin-Perez and Pantazopoulou, 2001)

However, even though tension stiffening is somehow capable of modeling bond it cannot represent the bond-slip relationship, therefore reinforcing bars cannot be taken as smeared elements fully bonded to the concrete. Thus, the reinforcing bars will be modeled as discrete elements. In addition, as this model assumes smeared cracking, and considering that the auxiliary bars are not distributed uniformly in the beam, then the smeared cracking hypothesis cannot be adopted. Since concrete and the steel reinforcement will be modeled separately, then the tension-softening law shown in Figure 6-7 considers the case of cracked concrete elements with their residual tensile strength in principle direction, thereby eliminating the intervention of reinforcement in the equations that will be used to model the concrete properties.

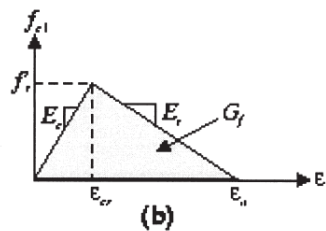


Figure 6-7 Tension stress-strain curve of concrete

VecTor2 contains a library of constitutive models for smeared reinforced concrete, discrete reinforcement and bond materials. In addition, it has the capability to represent second-order mechanisms for reinforced concrete structures including tension stiffening, softening and splitting effects, compression softening, dilation, confinement, crack width and slip and bond-slip behavior. Furthermore, additional models can be selected to simulate: reinforcement buckling, dowel action, concrete hysteresis and simulation of the chronology of construction and loading of structures for retrofitting and forensic engineering purposes through the theory of engaging and disengaging of the elements (Vecchio and Bucci, 1999). FormWorks and Augustus function as the preprocessor and postprocessor for VecTor2, respectively. (Wong, 2002) created FormWorks as the graphical interface - pre-analysis with a user-friendly approach that comprises the necessary tools to develop the Finite Element (FE) model, including manual and auto-meshing, the definition of concrete and reinforcement materials, selection of constitutive models, loading protocols, etc. A complete description of the software can be found elsewhere (Vecchio *et al.*, 2013). On the other hand, once the VecTor2 analyses is complete, Augustus, designed by (Bentz, 1996), provides graphical content regarding stresses, strains, combined load-deformation responses, failure modes and other structural responses obtained with VecTor2.

6.3 Modeling methodology

UHP-SFRC is globally recognized as a novel and smart material that can be used for specific cases where high properties of ductility and stiffness are required. However, due to the complexity of its composition, different types of fiber and the great variety of mixtures in the market, it is still a material under development. Therefore, the majority of nonlinear analysis software platform do not possess a specific constitutive model that describes the behavior of this type of concrete. The approach taken in VecTor2 to recreate the response of this material involved preliminary analyses where the prisms tested were modeled and analyzed under similar loading conditions with the objective of matching the analytical response with the one obtained experimentally. This facilitated on understanding of the required input data (concrete properties) for VecTor2 that served as the basis of the FE models to represent the beams studied.

6.4 UHP-FRC concrete modeling in VecTor2

6.4.1 Concrete model

Commonly, the pre-established default models present in VecTor2 are appropriate to perform the nonlinear analysis. However, given the complexity of the structure and the fact that currently there are no specific models for UHP-SFRC, special considerations were made in the constitutive models for the tensile behavior of the concrete. Table 6-1 summarizes the constitutive models selected

Table 6-1 Constitutive models for the concrete behavior utilized in VecTor2

Material Behavior	Constitutive Model
Concrete Compression Pre-Peak	Popovics (HSC) *
Concrete Compression Post-Peak	Modified Park-Kent
Concrete Compression Softening	Vecchio 1992-A (e1/e2-Form)
Concrete Tension Stiffening	Not Considered*
Concrete Tension Softening	Custom Input (Strain Based)*
Concrete FRC Tension	Not Considered*
Concrete Confined Strength	Kupfer/Richart
Concrete Dilation	Variable – Isotropic (Kupfer-with cut-off)
Concrete Cracking Criterion	Mohr-Coulomb (Stress)
Concrete Crack Width Check	Agg/2.5 Max Crack Width
Slip Distortion	Walraven
Concrete Creep and Relaxation	Not Considered
Concrete Bond	Eligehausen
Concrete Hysteretic Response	Nonlinear w/ Plastic Offsets

“*” represents a non-default model

Popovics-HSC was selected as the compression pre-peak response of the concrete; this model is a variation of the original Popovics curve that was modified to better reflect the response in high strength concrete ($f_c > 50$ MPa). The default model Modified Park-Kent was selected as the compression post-peak response. The compression softening effect takes into consideration the reduction of compression strength and stiffness, due to coexisting transverse cracking and tensile straining. The Vecchio 1992-A (e1/e2-Form) model was selected. When the concrete is subjected to high compressive stresses, the rate of concrete lateral expansion increases as the compressive stresses

increase, this dilation phenomenon is modeled by the Kupfer - with the cut-off constitutive model. Additionally, the Kupfer/Richart model selected accounts for the enhancement in the confinement strength in a triaxially compressed concrete. For the cracking criterion, the Mohr-Coulomb stress model is used. The crack slip which is only evaluated with the MCFT was represented by the Walraven model. The concrete crack width check serves to reduce average compressive stresses in the element when the crack width at that point exceeds a specified limit, a limit of 25% of the aggregate size was used. The loading protocol followed, did not involve hysteresis response of the concrete nor the reinforcement. Nevertheless, the default models were selected (Nonlinear w/ Plastic Offsets and Bauschinger Effect, respectively). As discussed previously, FRC composites are divided between strain-hardening and strain-softening composites. The tensile concrete model for FRC implemented in VecTor2 corresponds to the response present in Figure 6-8 (b) representing a strain-softening response. However, for UHP-SFRC the strain-hardening response as implemented in Figure 6-8 (a). Nevertheless, in the case of UHP-FRC, the full tensile stress-strain behavior is depicted in Figure 6-8 (c) and should be considered to model this novel concrete. Thus, the type of tensile behavior for the FRC shown in the model cannot be considered.

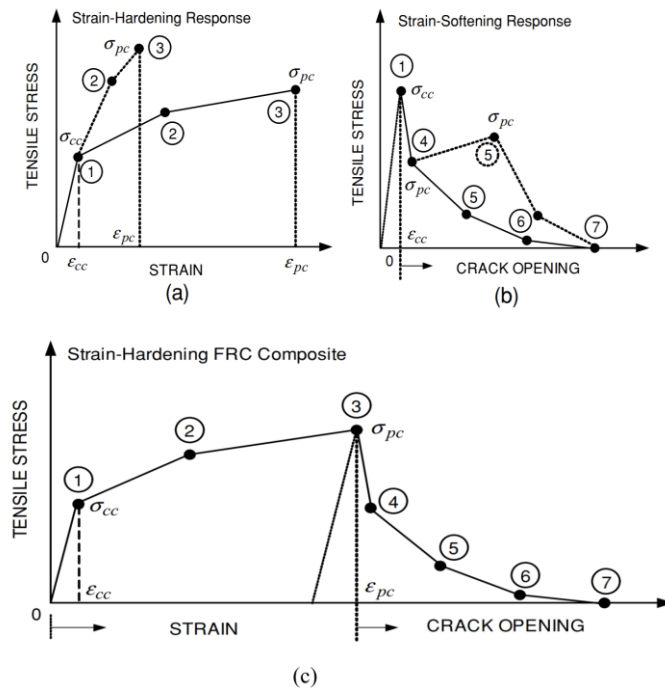


Figure 6-8 (a) Strain-hardening response of HPFRC composites (b) strain-softening response of FRC composite and (c) HPFRC tensile stress-strain response (Naaman and Reinhardt, 2006)

Therefore, to consider the strain hardening effect from Figure 6-9, the $(f_c, \epsilon_c)_1$ at point 3 is sufficient. Then, $(f_c, \epsilon_c)_2$, $(f_c, \epsilon_c)_3$ and $(f_c, \epsilon_c)_4$ can be represented by points 5-6-7 from Figure 6-8 (c) to depict the post-softening phase.

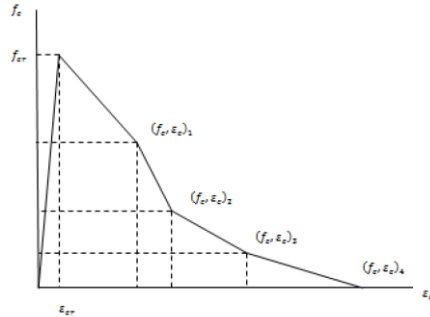


Figure 6-9 Custom input-strain based tension softening in VecTor2

No reinforcing bars exist in the studied prisms; therefore the tension stiffening is not considered. The envelope of this type of concrete through the effects of tension softening is manually inputted by using stress-strain values. The detailed formulation of each one of the constitutive models selected can be found in the VecTor2 manual (Vecchio *et al.*, 2013). This is the methodology followed to model each of the design mixes under study. In fact, the tensile strength along with the input points presented in Figure 6-9 of the concrete was determined by calibrating the models created in the platform VecTor2 along with the experimental response curve of the four-point bending prism 280 mm. They are then verified by modeling the 500 mm long prisms.

6.4.2 Models of the prisms in VecTor2

Figure 6-10 presents the FE models developed for: (a) prisms with 275 mm and (b) 500 mm lengths, respectively. Both models measure 75 mm in depth and were simulated as simply supported beams at the base. Regarding the loading protocol, to simulate the four-point bending test that the actual prisms were subjected, two-point loads were applied to the models following a quasi-static type of loading with 0.1 mm increments per load step. A total of 825 plane stress rectangular elements were utilized for Figure 6-10 (a) and 1500 for (b) as UHP-SFRC elements, measuring 5 mm x 5 mm on each side.

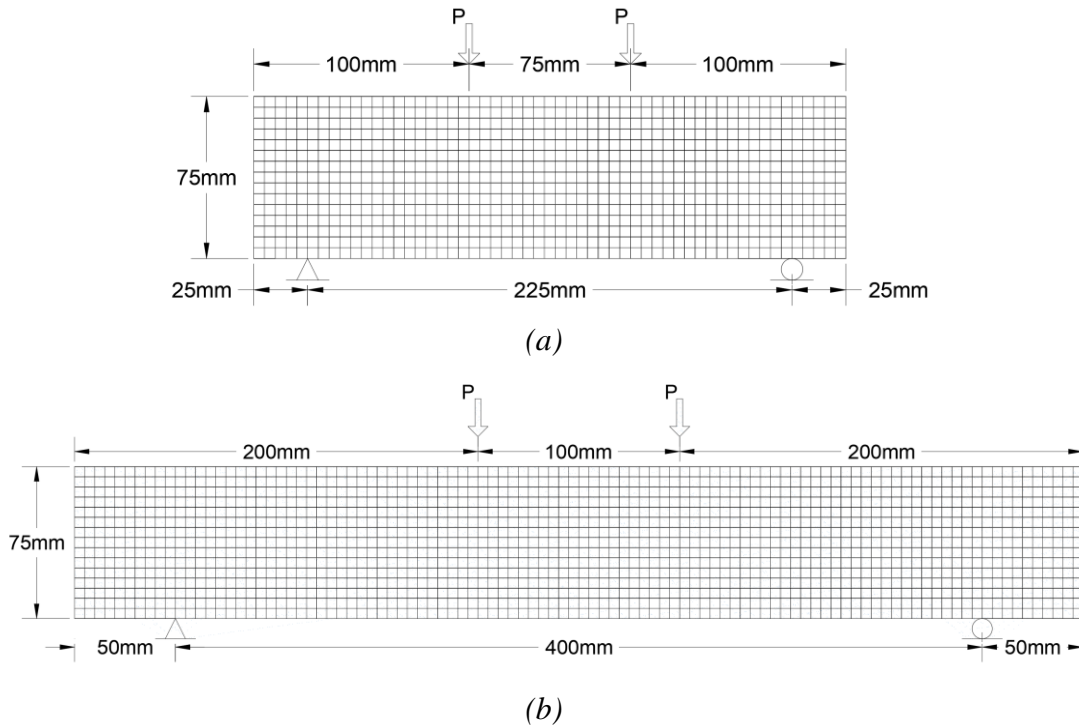


Figure 6-10 FE model for the prisms (a) 280 mm and (b) 500 mm in VecTor2

The geometry of the structures and their discretization remained the same during the analyses; the properties of the concrete on the other hand, differed depending on the type of mix selected. For all the prisms, an iterative procedure was adopted in order to generate a similar response to the one obtained experimentally with the 500 mm long prisms, where the tensile curve of the concrete was regularly modified until the results matched. These developed concrete properties were then verified with the response of the 280 mm long prisms. In section 6.4.3 the final mechanical properties are presented.

6.4.3 Mechanical properties for each design mixture:

6.4.3.1 In-house design mixture

The flexural behavior was provided for the short and long prisms in Figure 3-24. Two prisms from Set S4, cast on 11 June 2018, were chosen as reference. Thus, through an iterative procedure, the tensile strength and the tension softening curve were modified until a similar response curve for both prisms is obtained. As can be seen from Table 6-2, the average compression strength was around

126.13 MPa. The strain for this compressive strength was taken as 0.00357 with a Young's modulus of 41301 MPa calculated previously in section 5.1.

Table 6-2 Compression test results

Cylinder	D _{top} (mm)	D _{bottom} (mm)	Height(mm)	P _{peak} (kN)	f' _c (MPa)
C1	76	76	148	589.6	130.04
	75	77			
C2	77	76	145	571.7	125.26
	76	76			
C3	76	75	146	554.4	123.08
	75	77			

Sieve analysis was conducted on the fine aggregate to obtain the maximum aggregate size as can be seen in Table B-1. The last two maximum aggregate size had a very low percentage of volume. Thus, the maximum aggregate size a_{max} used in the modeling is considered as 0.542 mm. The final manual input of the concrete's properties to represent the in-house design mixture is presented in Figure 6-11. The tensile strength of the in-house design mixture was approximately 10 MPa.

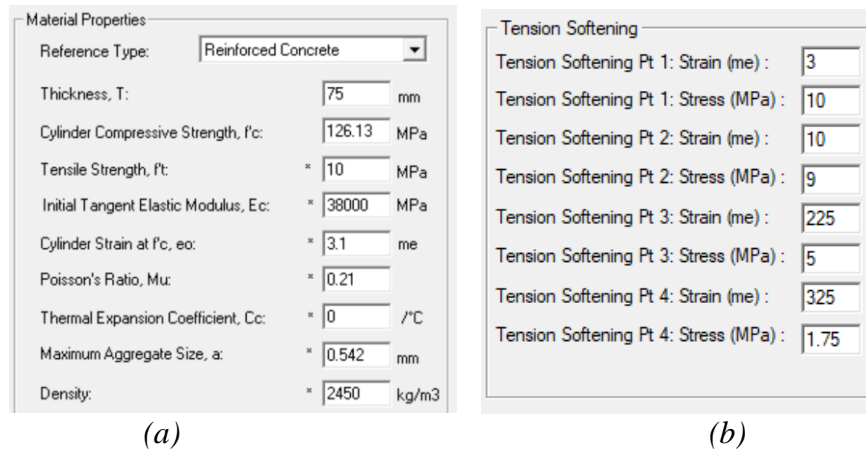


Figure 6-11 (a) Material properties and (b) tension softening behavior of In-house design mixture

After several iterations, the properties presented above were able to present a similar response curve as the experimental flexural testing of the 500 mm long prisms previously obtained in Section 5.2 and presented in Figure 6-12. These properties were verified by modeling the short 280 mm prisms as can be seen in Figure 6-13.

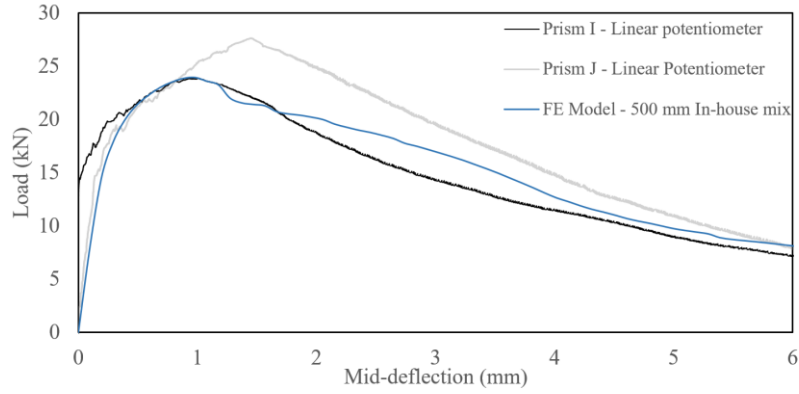


Figure 6-12 Experimental and analytical response curve of the 500 mm long prisms

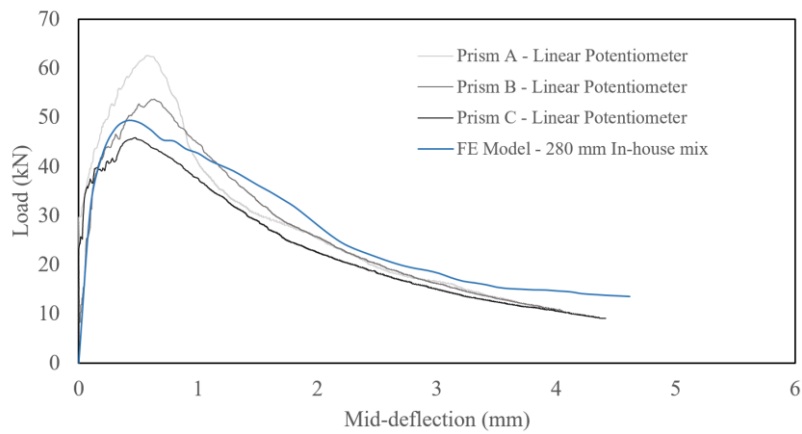


Figure 6-13 Experimental and analytical response curve of the 280 mm long prisms

6.4.3.2 Mechanical properties for Commercial K

It was reported that the compressive strength was $f'_c = 122.6$ MPa. The final mechanical properties of the Commercial K design mixture are presented in Figure 6-14. The tensile strength of the material was approximately 8 MPa.

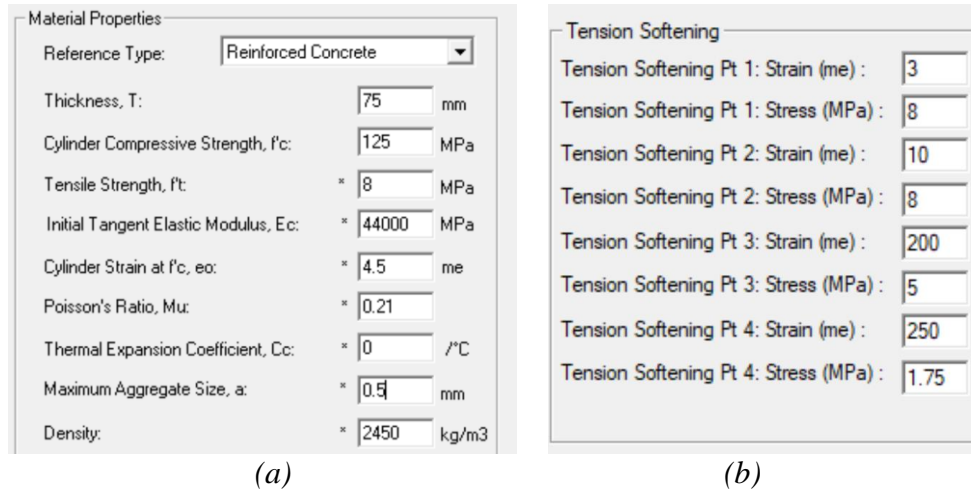


Figure 6-14 (a) Material properties and (b) tension softening behavior

These properties were developed with the response curve of the 500 mm long prisms as shown in Figure 6-15. Afterwards, these properties were verified with the flexural behavior of the 280 mm long prisms under four-point bending as presented in Figure 6-16.

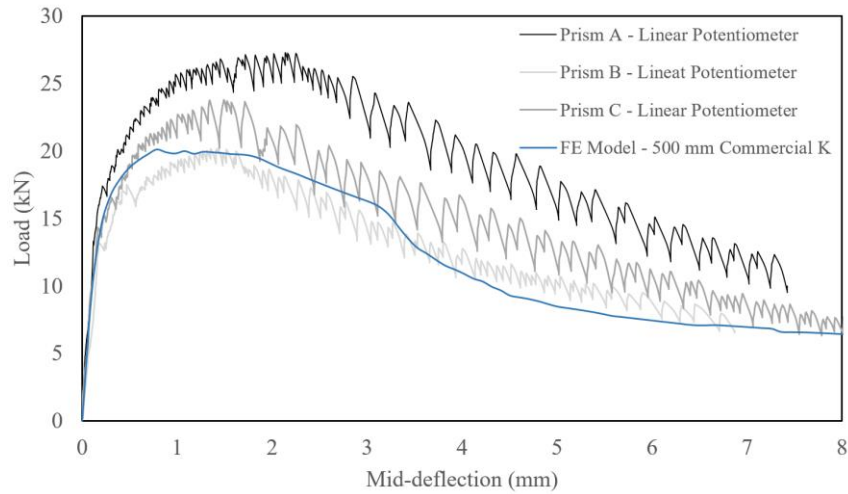


Figure 6-15 Experimental and analytical response curve of the 500 mm long prisms

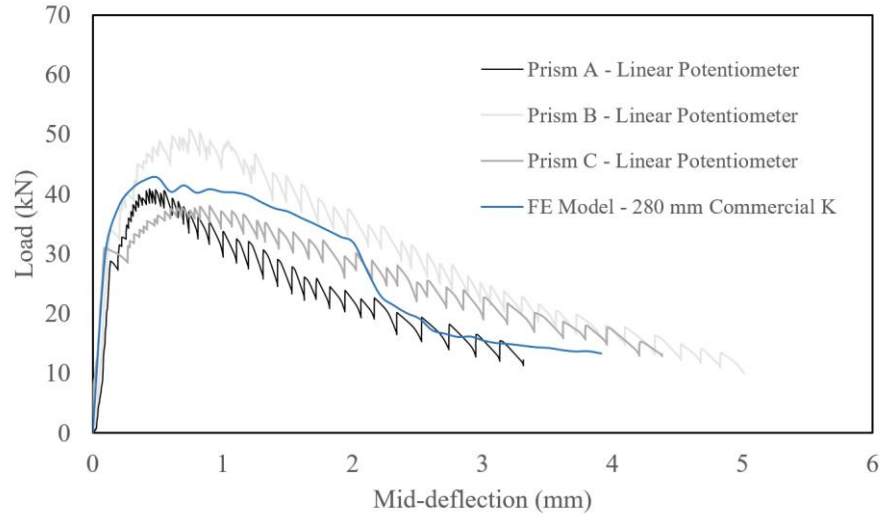


Figure 6-16 Experimental and analytical response curve of the 280 mm long prisms

6.4.3.3 Mechanical properties for Commercial F

The compressive strength of the Commercial F was $f'_c = 128.36$ MPa. The final mechanical properties of the Commercial K design mixture are presented in Figure 6-17. The tensile strength of the material was approximately 11 MPa.

Material Properties	
Reference Type:	Reinforced Concrete
Thickness, T:	75 mm
Cylinder Compressive Strength, f'_c :	128.36 MPa
Tensile Strength, f_t :	* 11 MPa
Initial Tangent Elastic Modulus, E_c :	* 35000 MPa
Cylinder Strain at f'_c , ϵ_o :	* 3.3 me
Poisson's Ratio, μ_c :	* 0.21
Thermal Expansion Coefficient, C_c :	* 0 /°C
Maximum Aggregate Size, a :	* 0.5 mm
Density:	* 2450 kg/m ³

Tension Softening	
Tension Softening Pt 1: Strain (me):	2
Tension Softening Pt 1: Stress (MPa):	11
Tension Softening Pt 2: Strain (me):	20
Tension Softening Pt 2: Stress (MPa):	11
Tension Softening Pt 3: Strain (me):	265
Tension Softening Pt 3: Stress (MPa):	6
Tension Softening Pt 4: Strain (me):	375
Tension Softening Pt 4: Stress (MPa):	3.5

Figure 6-17 Concrete properties and tension softening input

These properties were obtained based on the flexural behaviour of the 500 mm long prisms presented in Figure 6-18 and then verified with the flexural behavior of the 280 mm long prisms under four-point bending as shown in Figure 6-19.

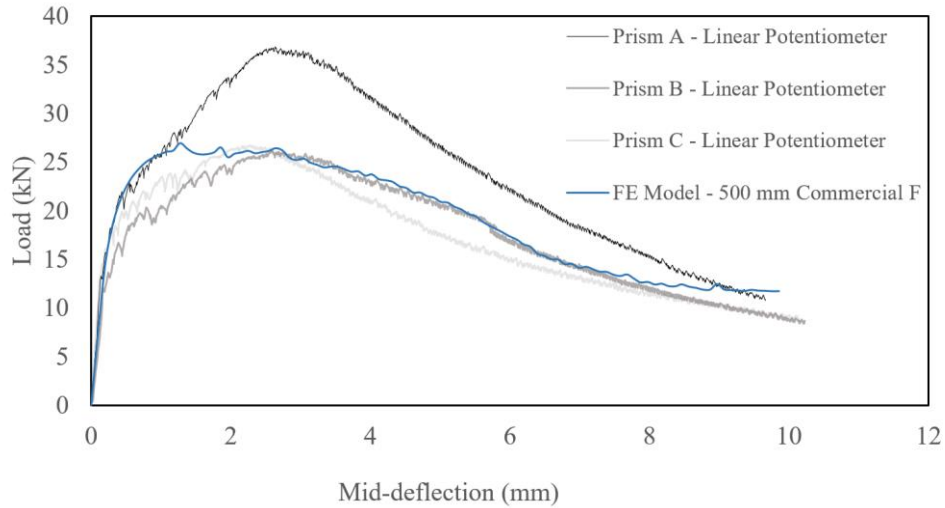


Figure 6-18 Experimental and analytical response curve of the 500 mm long prisms

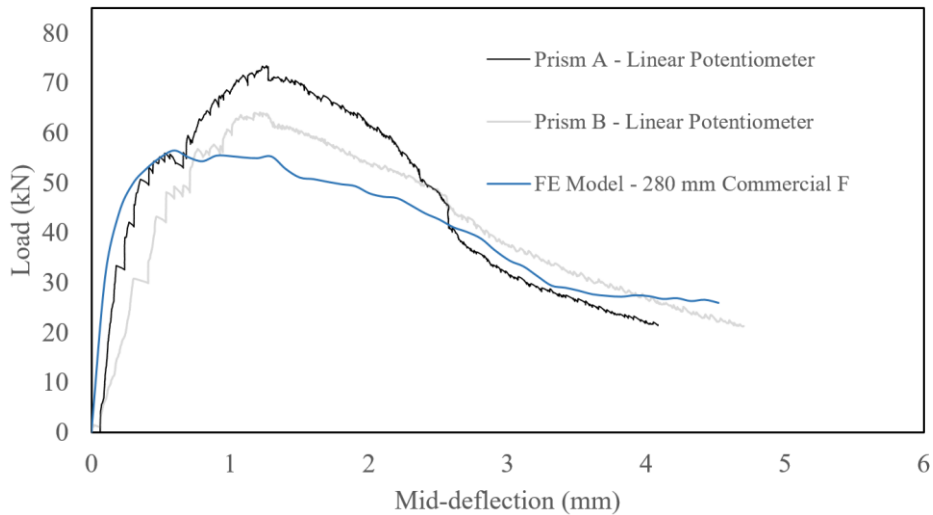


Figure 6-19 Experimental and analytical response curve of the 280 mm long prisms

6.5 Finite element models developed for beam specimens

A total of 5400, 4-noded plane stress rectangular elements were used to represent the concrete material, together with 192 truss bar elements recreating the longitudinal reinforcement and 195 elements for bonding. The rectangular elements were generated with the smallest dimensions possible, 5 mm in the horizontal direction and 5 mm in the vertical direction, maintaining an optimal aspect ratio of 1:1, without exceeding the number of elements available. The specimens were expected to fail by de-bonding, this is a localized type of failure, and therefore it becomes necessary

to develop a sufficiently fine mesh to capture this type of behavior. Figure 6-20 to Figure 6-25 depict the FE models constructed.

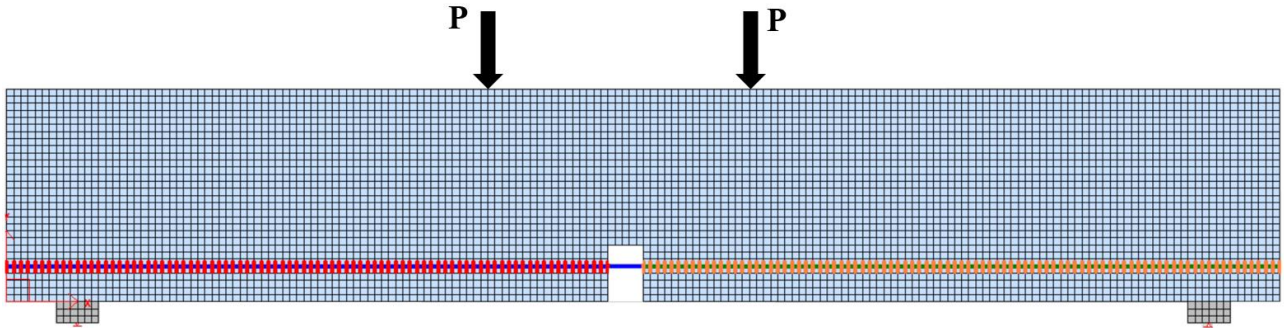


Figure 6-20 Finite element model developed for beam specimens K-F E4C1

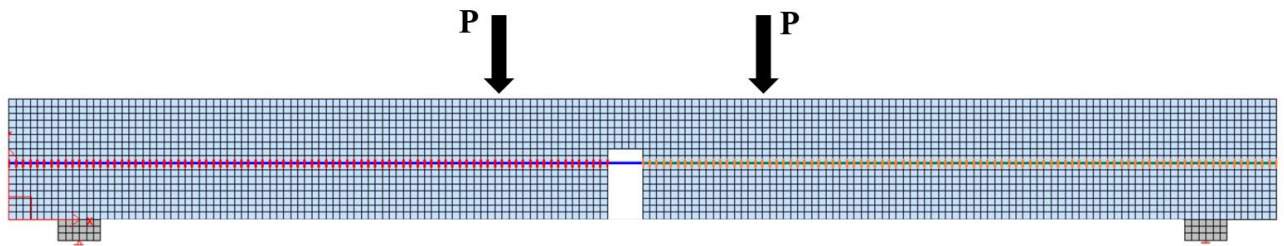


Figure 6-21 Finite element model developed for beam specimen K-E4C2

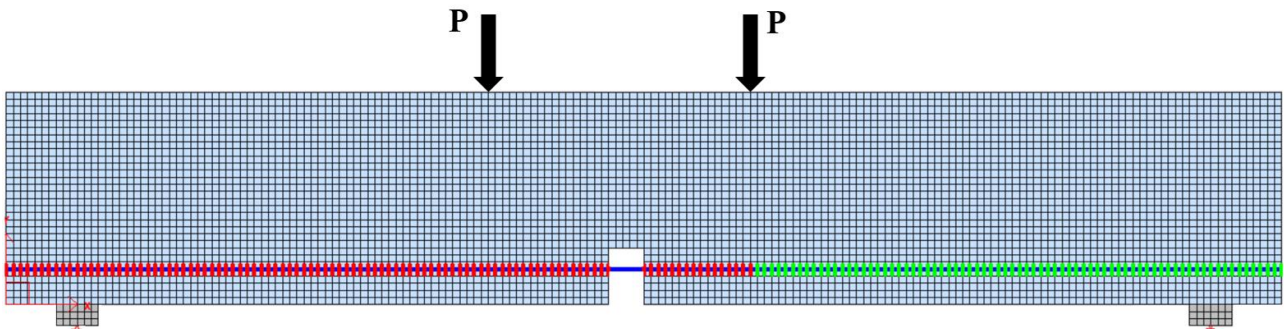


Figure 6-22 Finite element model developed for beam specimens I-K-F E1C1

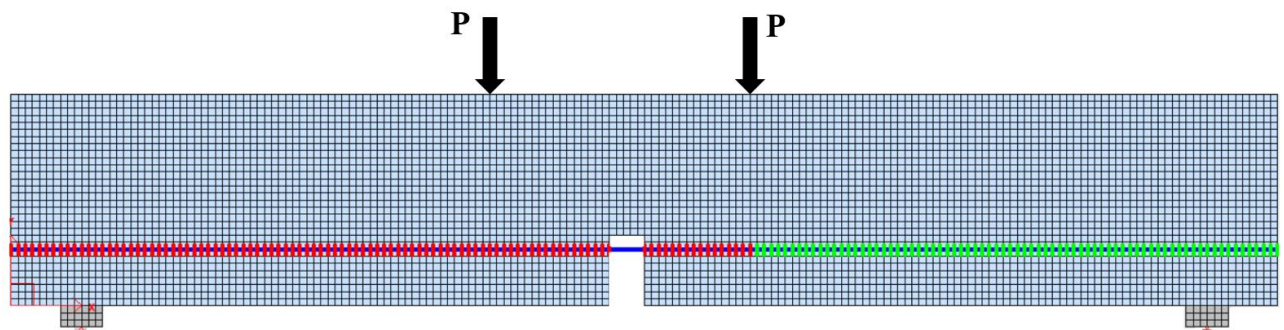


Figure 6-23 Finite element model developed for beam specimens I-F-K E1C2

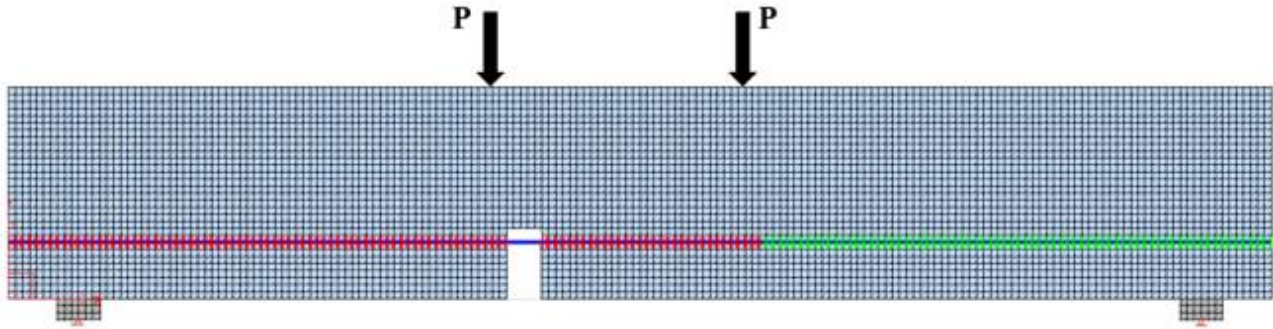


Figure 6-24 Finite element model developed for beam specimens IE2C2

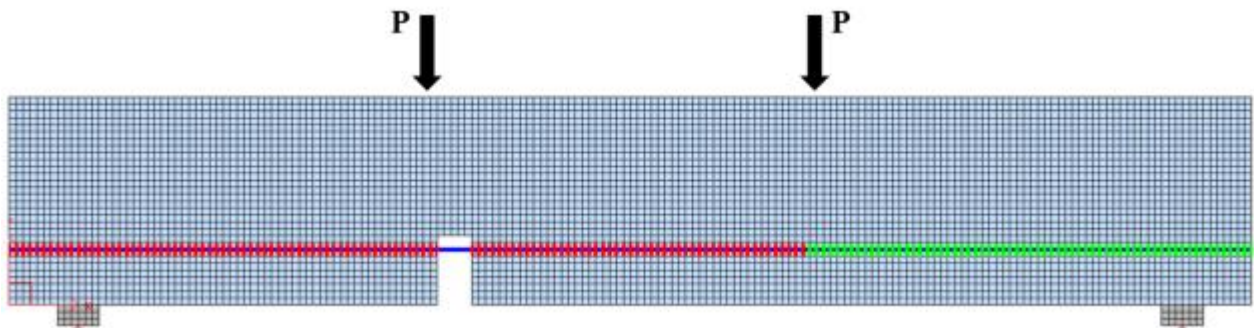


Figure 6-25 Finite element model developed for beam specimens IE3C2

6.5.1.1 Constitutive model for reinforcing steel

The constitutive models utilized for the reinforcing bars are presented in Table 6-3. The monotonic stress-strain curve for ductile steel reinforcement describes the backbone curve of the Seckin model, including initial linear-elastic response, a yield plateau and a nonlinear strain hardening phase until rupture. When necessary, partial bonding between the concrete and the reinforcement is assumed by the well-known Eligehausen model. For the reinforcement buckling behavior, the Akkaya 2012 constitutive model was employed. Finally, the dowel action of the reinforcement takes into consideration the shear resistance of the reinforcing bars crossing a crack. The constitutive model for this effect was the one proposed by Tassios.

Table 6-3 Constitutive models for the steel reinforcement utilized in VecTor2

Material Behavior	Constitutive Model
Reinforcement Hysteretic Response	Bauschinger Effect (Seckin)
Reinforcement Dowel Action	Tassios (Crack Slip)
Reinforcement Buckling	Akkaya 2012

6.5.1.2 Discrete reinforcement elements

2-noded truss-bar elements were used to model the reinforcement located at the bottom of the beam. The developed models vary according to the development length for each of the specimens. As explained previously, the bar that travels through the PVC sleeve was simulated by assuming the truss-bar fully de-bonded to the concrete.

6.5.1.3 Bond link element properties

All FE models used bond-link elements to simulate the interaction between concrete and reinforcing steel materials with the ability to detect bond failure. Different types of bonding conditions were recreated, including the bonding of embedded deformed bars with truss elements that were in direct contact with the concrete, and the debonded bars to the concrete with truss bar elements that were modeled as the elements passing through the PVC's.

6.5.1.4 Support conditions

Steel plates were generated as stiff materials to model the supports and avoid local crushing at the bearing zones; the beams were simple supported allowing translational movement at one end.

6.5.1.5 Loading protocol

The loading conditions were replicated by inputting two nodal loads on the surface of the beams spanning 200 mm between each other with the exception for the specimen FE4C1 and all the in-house IE3C2 specimens that spanned 300 mm. The loading followed a displacement control approach with increments of 0.1 mm per load stage.

6.6 Results

The properties for the concrete elements were based on those presented in Section 6.4.3 using an input model for the tension softening. Meanwhile, the properties for the reinforcing bars were a result of the tensile test performed in Section 3.3.5. Below are the experimental and numerical load vs. mid-deflection responses for all the specimens.

6.6.1 Beam KE1C1

The blue line in Figure 6-26 represents the analytical response of the KE1C1 FE model. Overall, a similar behavior was captured. The initial secant stiffness of the response was compatible with the experimental data. Furthermore, the peak load recorded by the FE analysis was 63.44 kN with a mid-span deflection of 2.00 mm. As a comparison, the deflection measured with the linear potentiometer for the specimen KE1C1-A- was 1.62 mm at a load of 75.10 kN. The post-peak branch of the curve of the analytical model overestimated the softening effect when compared to the experimental data. Nevertheless, the response proved to be sufficiently accurate.

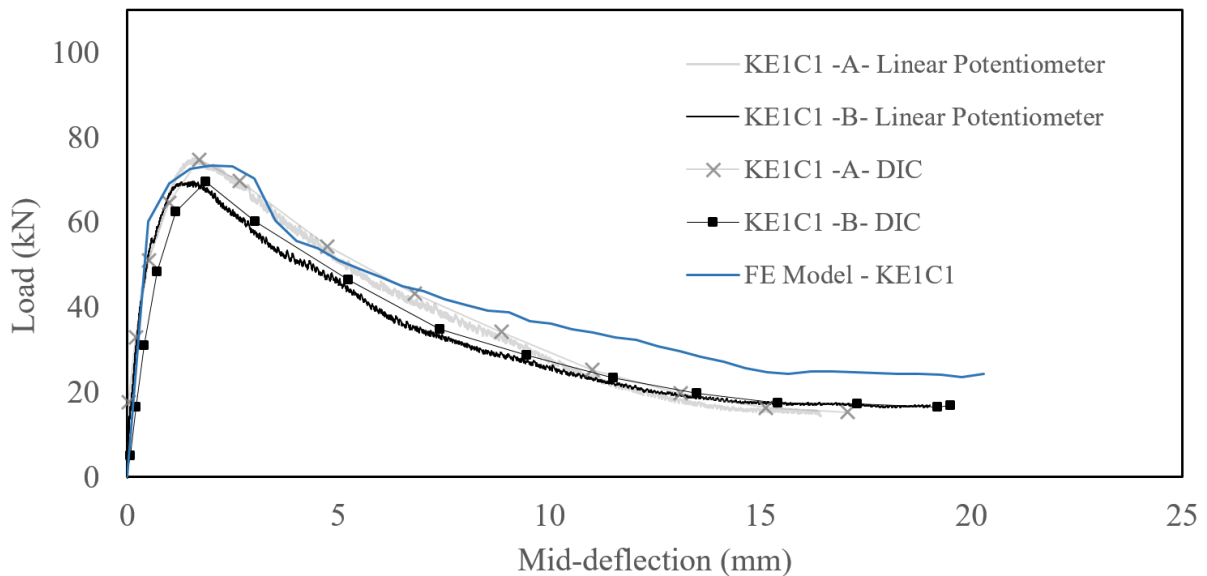


Figure 6-26 FE model – Load vs. mid-deflection response for KE1C1 specimens

6.6.2 Beam KE1C2

The results for this model depicted in Figure 6-27 illustrate a slight increase in the initial stiffness of the structure compared to the DIC results. The FE beam sustained a higher peak load (72.96 kN) and peak deflection (2.47 mm) when compared to the original beams. Nevertheless, the general behavior followed the same response, including cracking pattern and mode of failure (vertical crack at the notch and pullout-splitting of the reinforcing bar).

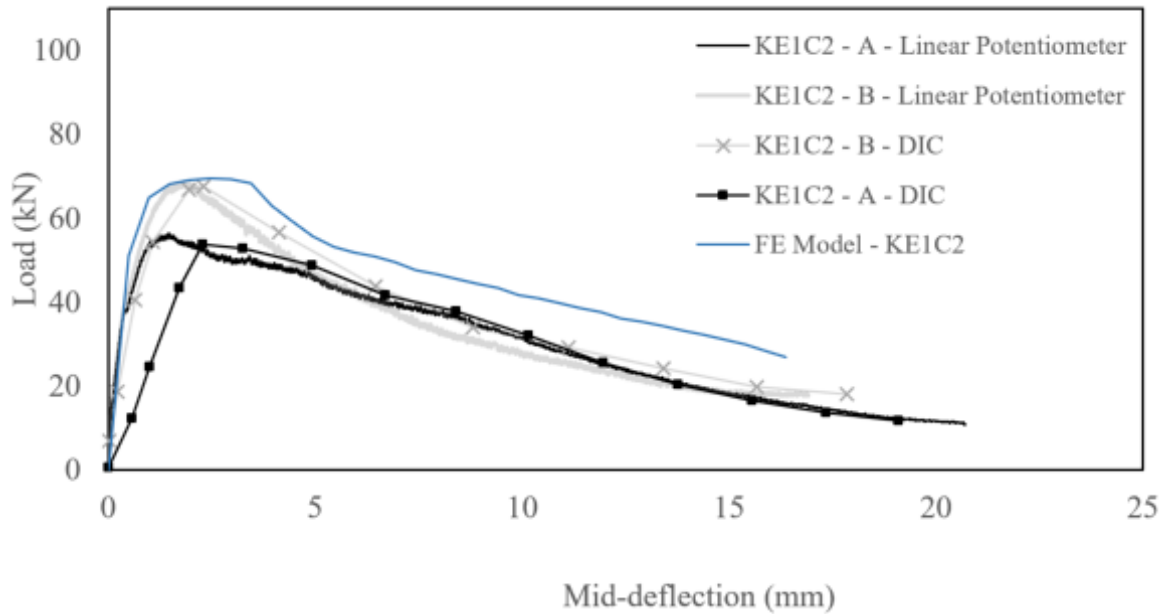


Figure 6-27 FE model – Load vs. mid-deflection response for KE1C2 specimens

6.6.3 Beam KE4C1

The response of the K4EC1 FE model presented a substantial decrease in the ductility capacity as shown in Figure 6-28 when compared to the experimental results. The analytical model retained a load of 106 kN when suddenly at a displacement of 13.5 mm the structure experienced an abrupt degradation, failing by the rupture of the 15M rebar. The actual specimens sustained approximately the same loading but at a much higher deflection (24 mm).

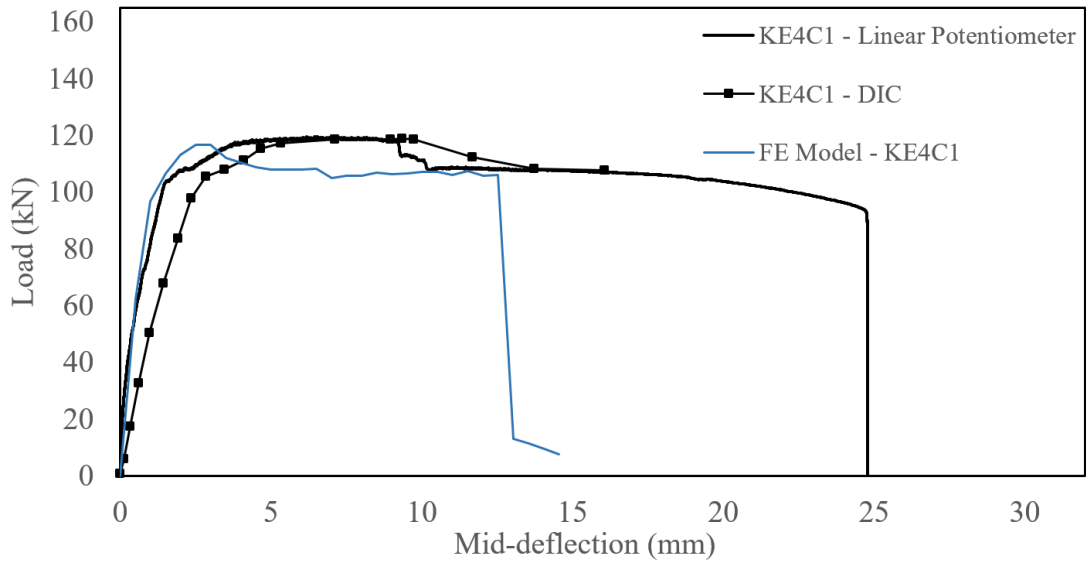


Figure 6-28 FE model – Load vs mid-deflection response for KE4C1 specimens

6.6.4 Beam KE4C2

The FE model developed for KE4C2 possessed an initial higher secant stiffness with a lower peak load (33.98 kN) as shown in Figure 6-29. However, the response followed the behavior of the experimental data captured with the linear potentiometer and the DIC. It was able to properly capture the relatively large deflection of this set of beams when compared to the rest, appropriately simulating what was captured in the experimental tests.

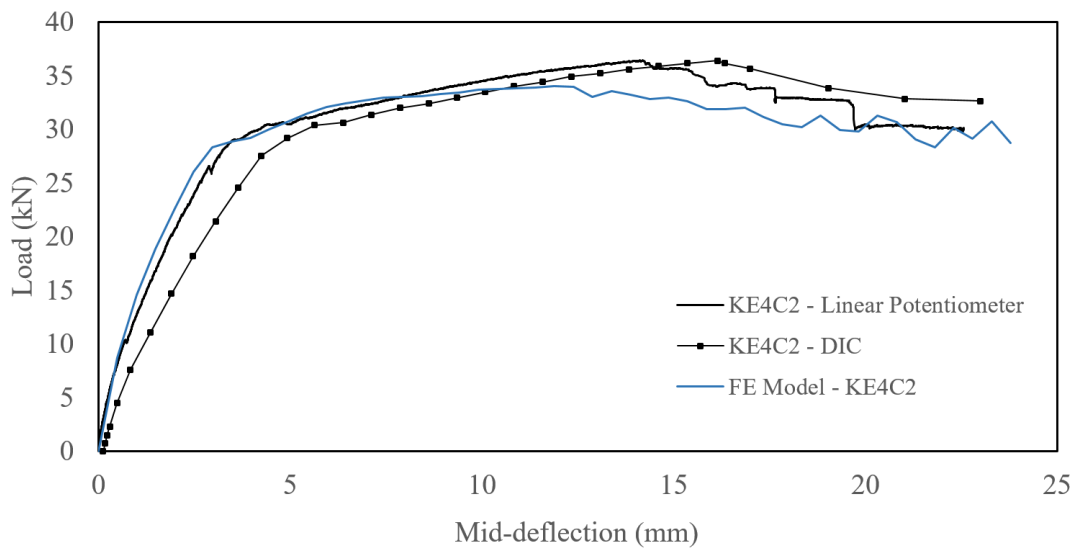


Figure 6-29 FE model – Load vs. mid-deflection response for KE4C2 specimens

6.6.5 Beam FE1C1

Figure 6-30 shows how the FE model of the FE1C1 specimens successfully simulated the pre-peak of the response while the initial stiffness ranges between the responses of the experimental tests for the beams FE1C1 -A- and FE1C1 -B-. The peak load was 90 kN with a mid-span deflection of 3.05 mm, values that as well remained within the acceptable range. Nevertheless, the post-peak descending curve predicted a much faster decay when compared to the experimental beams, creating a sudden drop of stiffness and ductility.

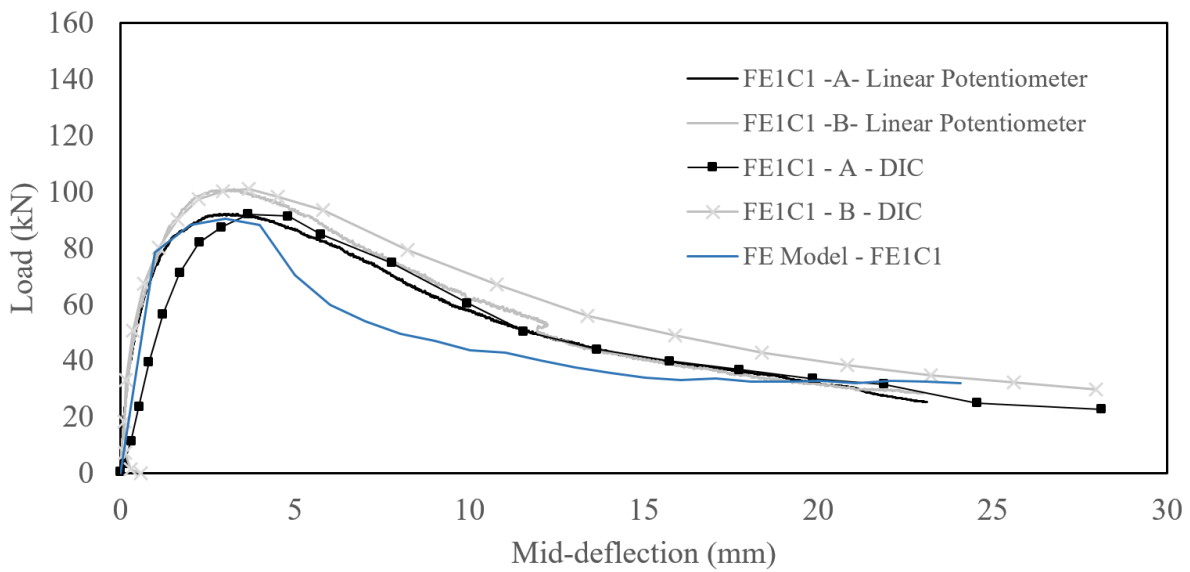


Figure 6-30 FE model – Load vs mid-deflection response for FE1C1 specimens

6.6.6 Beam FE1C2

The response of the FE model for FE1C2 is depicted in Figure 6-31. Compared to the experimental responses of the specimens, the model overestimated the initial tangent stiffness, with a higher peak load but a similar deflection. The post-peak branch presented a similar softening curve. Additionally, the failure mode was in close agreement with the experimental data, by failing due to pull-out of the bar.

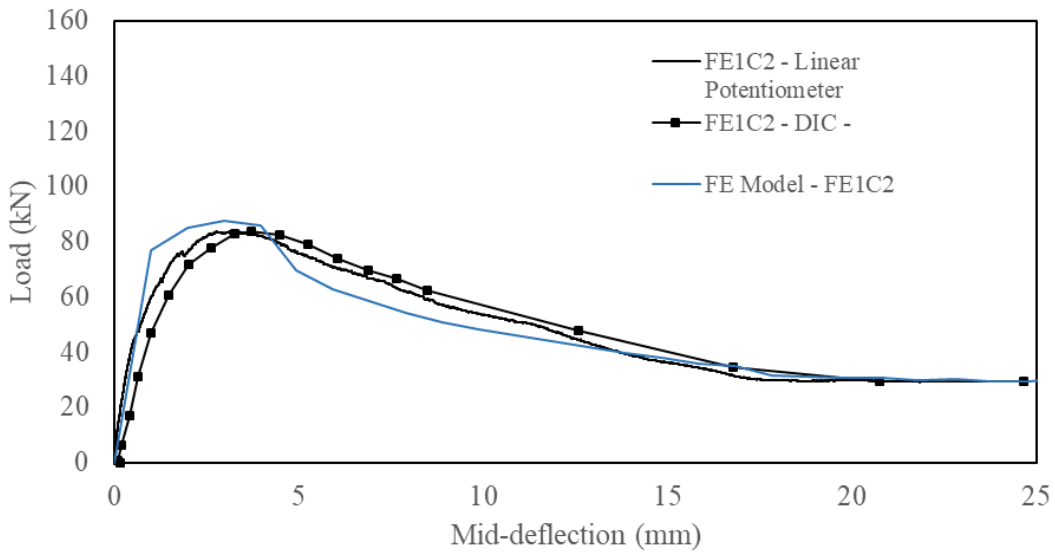


Figure 6-31 FE model – Load vs mid-deflection response for FE1C2 specimens

6.6.7 Beam FE4C1

A comparison between the responses of the FE model and the experimental beams for the set FE4C1 is shown in Figure 6-32. In this specific case, the analytical results did not reflect reality; an increased pre-peak slope was seen in the analytical estimation, with a slightly higher peak load but with a significant reduction in peak mid-span deflection and overall ductility. Failure arrived for the FE model at a displacement of 17.86 mm, whereas with the experimental beams failure occurred at approximately 30.00 mm. In this specific case, the response did not reflect accurately the behavior of the beam studied.

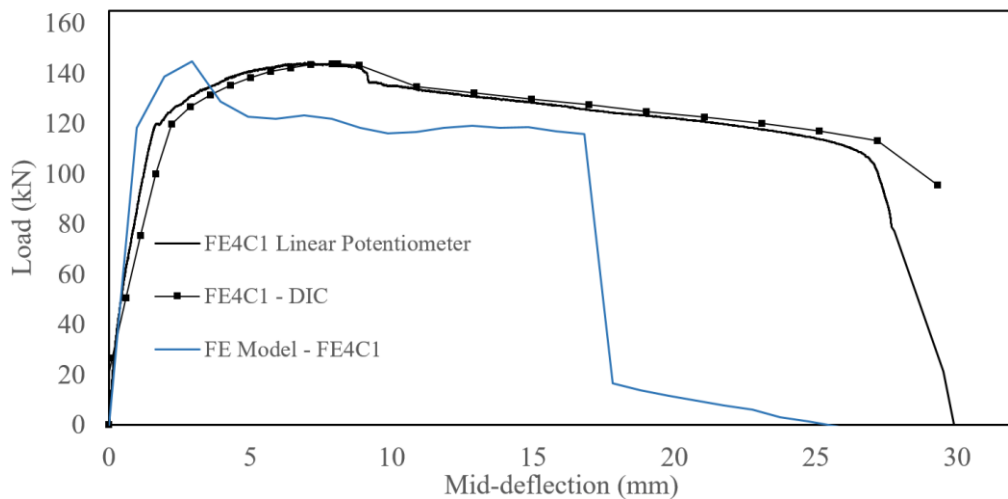


Figure 6-32 FE model – Load vs mid-deflection response for FE4C1 specimens

6.6.8 Beam IE1C1

The response of the FE model for the IE1C1 specimen represented in Figure 6-33 is located in between the range of the different experimental tests that were performed. Overall, the FE model was able to capture correctly the initial stiffness and the softening effect of the curve after the peak. Furthermore, there is a small difference in the peak load experienced.

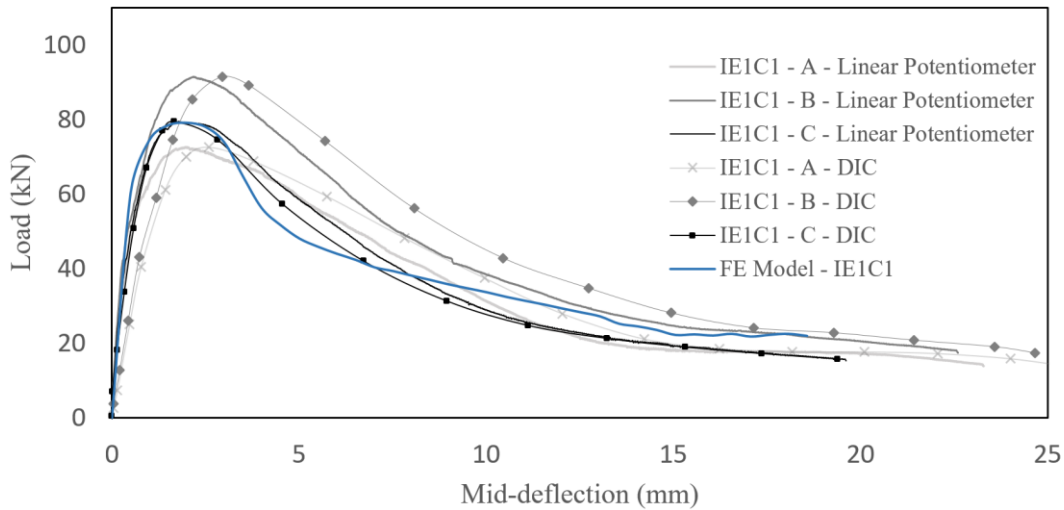


Figure 6-33 FE model – Load vs. mid-deflection response for in-house IE1C1 specimens

6.6.9 Beam IE1C2

The analytical model captured a reasonably appropriate response with an underestimation of the main characteristics of the curve, including the peak load and deflection, the softening of the post-peak branch, and initial tangent stiffness as shown in Figure 6-34. The model was able to capture a similar failure mode as IE1C1A including pull-out of the rebar and the cracking near the notch.

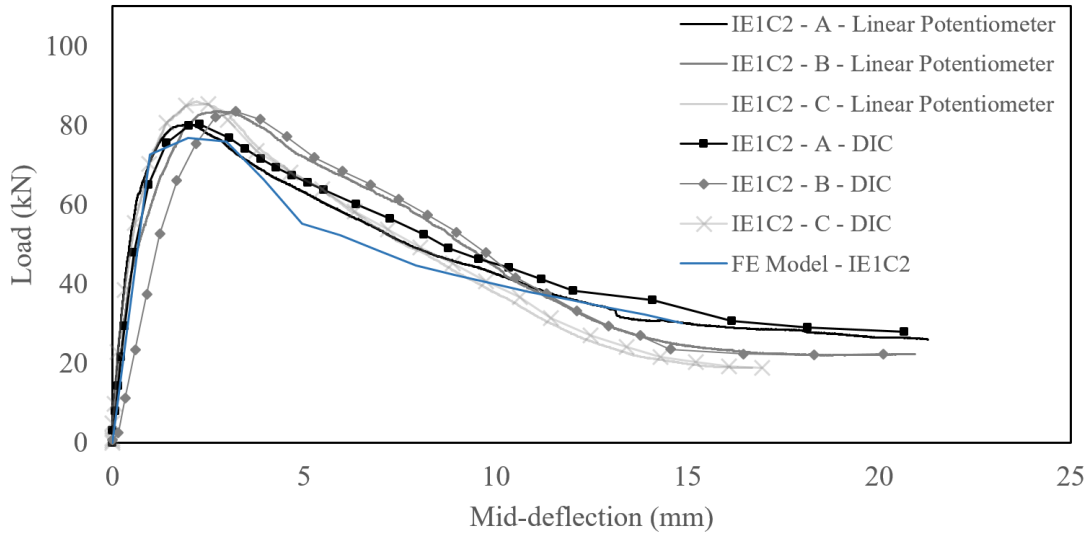


Figure 6-34 FE model – Load vs. mid-deflection response for in-house IE1C2 specimens

6.6.10 Beam IE2C2

The response to the FE model of the IEC2 specimen shown in Figure 6-35 did not reflect the proper behavior of the experimental data. Even though it experienced a similar peak load, the calculated reduced plateau did not match the response of the actual beams. Furthermore, it is clear that in terms of mid-span deflection, the model was not able to reach the experimental values. Beyond the peak point, the response developed a substantial reduction of strength and stiffness that did not reflect the observed behaviour.

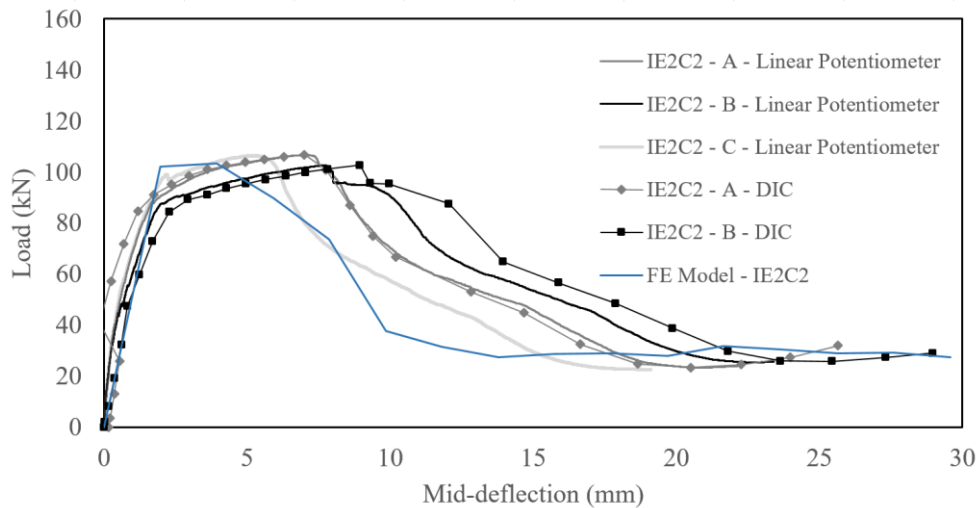


Figure 6-35 FE model – Load vs. mid-deflection response for in-house IE2C2 specimens

6.6.11 Beam IE3C2

Figure 6-36 illustrates the response for the FE model of the IE3C2 specimens compared to the experimental responses. The peak load and peak deflections were 149.47 kN and 4.00 mm, respectively. Meanwhile, for the experimental beams, the average peak load and deflection recorded from the linear potentiometer and the DIC were 143.32 kN and a much higher displacement of 30.00 mm. The FE model experienced a premature failure that did not develop sufficient ductility to match the recorded experimental data. Additionally, the descending branch of the curve was not able to capture the plateau effect that was characteristic for these specimens in the experimental test.

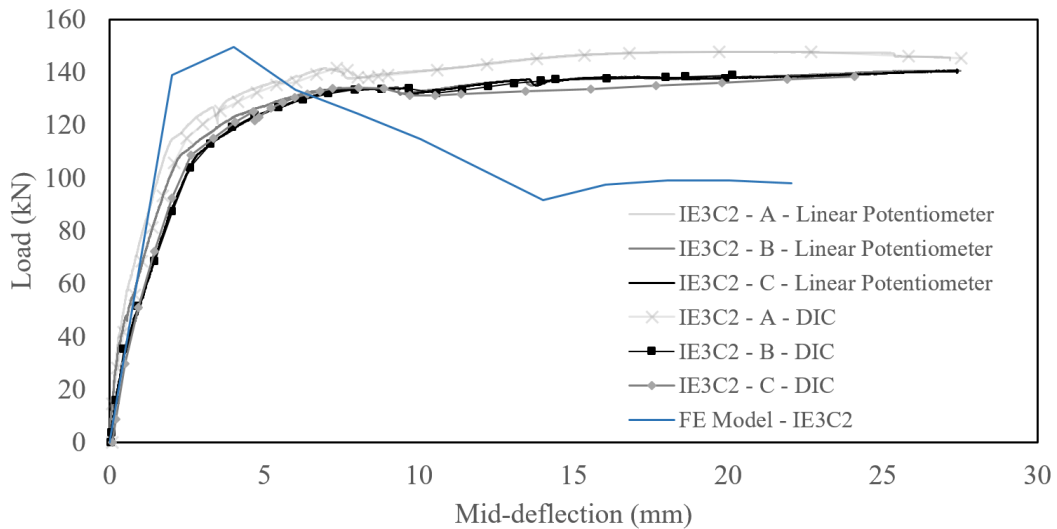


Figure 6-36 FE model - Load vs mid-deflection response for in-house IE3C2 specimens

Figure 6-37 and Figure 6-38 show the displaced shape and cracking patterns for the FE model and the actual specimen KE1C1, respectively. For both cases, vertical cracking initiated at a high load at the center of the span and shear cracks were evident at the side of the notch as the load was increasing. Gradually, the 15M bar started to pull-out, and the vertical crack at the notch started to rotate until it reached approximately 45° at the top surface, causing the splitting of the beam. The FE model was able to capture this behavior successfully. In Figure 6-37, it is evident that the 15M bar represented by the truss element pulled out, and the progression of the major crack over the notch was captured. The FE model was in the post-peak loading phase where the reinforcing bar was mobilized, and the crack in the front face reached the compression zone of the beam section.

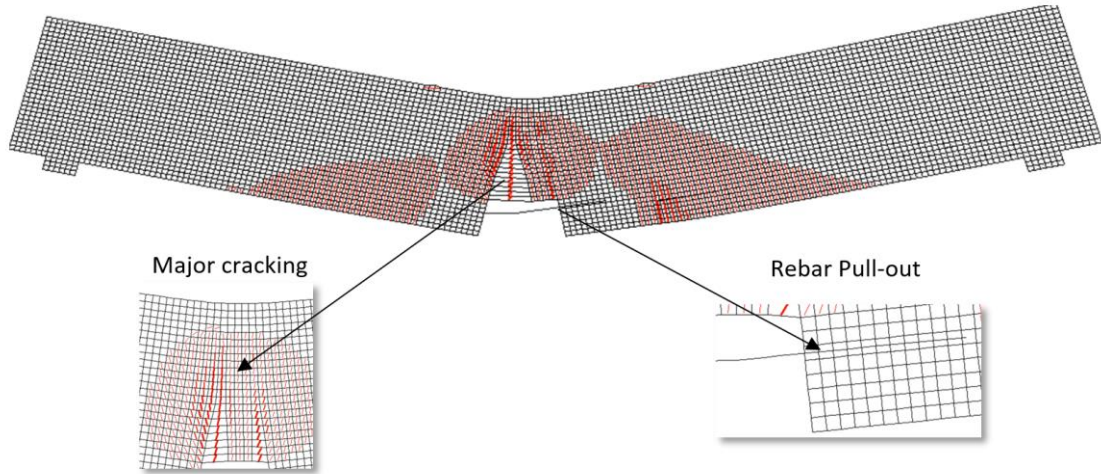


Figure 6-37 Cracking pattern and the slippage of the reinforcing bar for the FE beam KE1C1

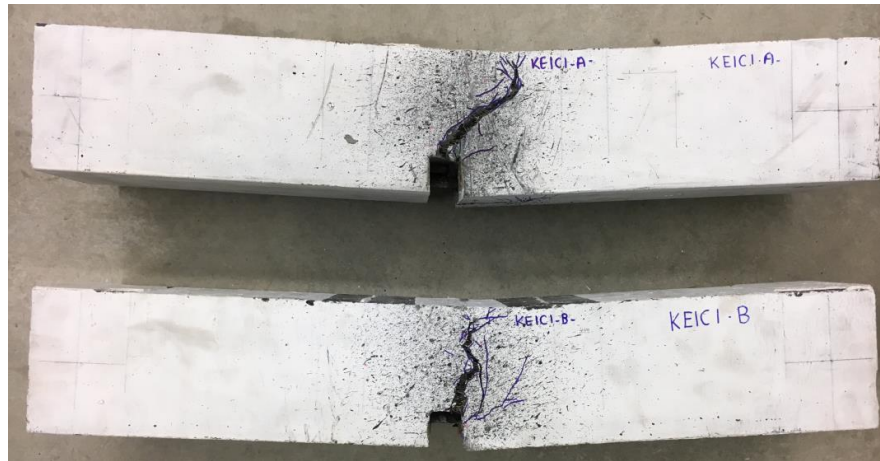


Figure 6-38 Experimental cracks on the front face of the beam KE1C1

Another failure mode is the one experienced by beam KE1C4 failing by the rupture of the reinforcing 15M bar similarly to the results observed in the model. Figure 6-39 presents the cracking state of the FE KE1C4 at the peak load.

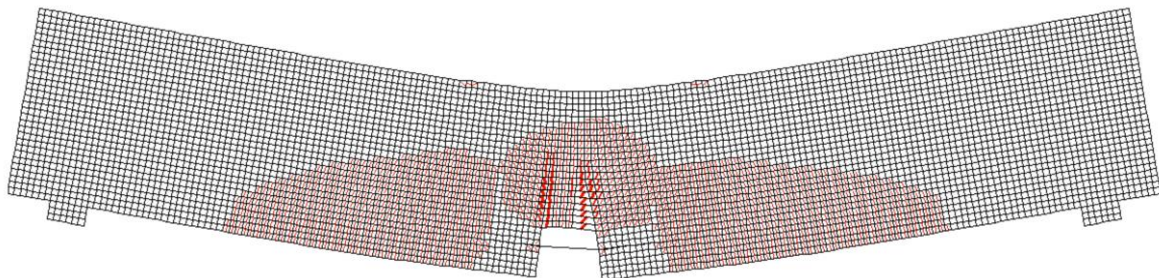


Figure 6-39 Cracking along the notch and rupture of the reinforcing bar for beam KE4C1

Chapter 7. Conclusions

The work presented in this thesis concerned the bond behavior of reinforcing bars embedded in the emerging class of Ultra-High-Performance Steel Fiber Reinforced Concrete's which are characterized by resilience and ductility when subjected to tension. This resilience and high tensile strength of concrete is effectively engaged in hoop stresses that develop in the concrete cover of reinforcing bars when, under the action of axial tensile stress the ribs of the bars' lateral surface attempt to slip relative to the surrounding concrete. The hoop action thus sustained in turn enhances the bond strength and development capacity of the bar, thereby leading to enhanced performance, delayed splitting and reduced anchorage lengths. In the present work this behavior was experimentally and numerically confirmed and quantified. A detailed study was conducted in order to determine the mechanical behavior of bond, the local bond-slip law that corresponds to the bar - matrix interaction, and the role of important design variables on the problem. The following sections summarize the main findings of the study and conclusions drawn from the experiment.

7.1 Mechanical properties of UHP-FRC

Around 21 trials and 6 casting batches were directed to profoundly understand the properties and characteristic of fresh properties of UHP-FRC. This was followed by conducting flow tests, compressive strength tests, flexural strength tests, splitting tensile tests and the analysis of fiber distribution. The observations are discussed below:

1. An important parameter in order to obtain an appropriate UHP-FRC with proper fresh and hardened properties is the gradual insertion of superplasticizer in small portions followed by a continuous flow test to verify the workability of the mixture.
2. The behavior of UHPC prisms without steel fibers was marked by brittle, abrupt failure. Addition of steel fibers increased the flexural strength of the concrete by 127% from 11.6 MPa for plain UHPC to 26.4 MPa for UHP-FRC, fluctuating to a more ductile failure.

3. The compressive strength increases sharply in the first days when the mix contains silica fume reaching almost 80% of its maximum strength in 7 days. However, if the mix contains slag, the compressive strength continues to increase gradually to reach 150 MPa after 167 days from casting. The failure mode of the concrete cylinders is ductile with the formation of longitudinal cracks.
4. The splitting tensile test provides lower values than the flexural strength in terms of indirect methodologies to measure the tensile strength. Nevertheless, it still over-estimates the concrete's tensile strength obtained from direct tension tests. For the in-house design mixture, the flexural strength was about 28 MPa, the splitting tensile strength 18.86 MPa, and the tensile strength 10 MPa.
5. The casting flow method had an influence on the fiber distribution which is directly related to the flexural strength. Thus, the layered casting method increases the flexural strength by 16% from the flow method applied from one side of the mould from 24 MPa to 28 MPa, respectively. The location of the localization of the crack is shifted near the side that it was casted from.
6. The change of the shear span to depth ratio from $a/d = 1$ to $a/d = 2$ did not affect the flexural strength for the In-house mix.

7.2 Beam bond test

A four-point bending test was conducted to obtain experimental bond-stress slip responses. The test setup was proposed to mainly investigate the contribution of this innovative concrete for embedded reinforcing bars for different concrete covers and embedment lengths.

7.2.1 Resistance curve

1. The initial crack initiated near the notch around 70-75% of the peak load indicating the high tensile strength of this novel design mix. These high values of applied load generated minimal mid-deflections stating a high ductile material and a very steep initial stiffness.

2. Before reaching the peak, one narrow micro-splitting crack was detected in the bottom cover starting from the loaded end of the bar and entering throughout the end of the embedment length $5d_b$ and $10d_b$. Due to the presence of the steel fibers, they were able to bridge through the crack prohibiting it from opening and preventing uncontrolled bar slip.
3. Once the localization of the crack took place, additional perpendicular cracks developed due to the pullout of the reinforcing bar. This was accompanied by a gradual reduction of the load emphasizing the role of the steel fibers to bridge through the cracks eliminating any brittle mode of failure. The beams with an embedment length of $5-10 d_b$ failed by pullout/splitting failure mode.
4. The peak load and the mid-deflection are directly proportional to the flexural/tensile strength of the material: Commercial K with a tensile strength of 8 MPa was able to sustain 72.4 kN with a mid-deflection of 1.6 mm, the In-house design mixture with a direct tensile strength of 10 MPa carried 81.2 kN for a mid-deflection of 2 mm, and the Commercial F presenting the highest tensile strength of about 11 MPa reached loads up to 96.5 kN with a mid-deflection of 3.1 mm.
5. The comparison of the load-deformation responses of the different mixes showed that higher tensile strength leads to a more ductile behavior presenting a higher area below the response curve with greater ductile capacity and energy absorption.
6. The 15M reinforcing bar yielded for all the commercial K specimens and for the specimens of the in-house design mixture with the shortest embedment length $5d_b$ with the smallest concrete cover of $1d_b$. However, the reinforcing bar for the specimens of commercial F ($l_b = 5d_b$ and $c_b = 1-2 d_b$) and the rest of the in-house design mixture ($l_b = 5-10-15d_b$ and $c_b = 1-2d_b$) exceeded their ultimate tensile strength.
7. When the concrete cover is $2d_b$, the applied load decreased; an example is Commercial K with a capacity load of 72.4 kN for a concrete cover of $1d_b$ which reduced to 62.6 kN for a concrete

cover of $2d_b$. This however does not imply a reduction in bond strength – instead, it was a result of the reduced internal lever arm for the bar force in the case of the thicker cover.

8. The width of the crack and the development of several additional cracks can be reduced by increasing the concrete cover from $1d_b$ to $2d_b$ generating higher confinement.
9. Longer embedment lengths engage a more considerable amount of ribs increasing the applied load. The applied peak load for $5d_b$ was 56 kN and 144.38 kN for a fully bonded length. This is accompanied by changing the pullout-splitting bond failure to either flexural or shear.

7.2.2 Bond strength

1. The experimental bond response follows the same behaviour for all the specimens starting with a high initial stiffness reaching a high bond strength with minimal slippage. In fact, the slippage of the reinforcing bar is mobilized, once the crack is localized in the post-peak phase.
2. The average bond strength and the slippage of the reinforcing bar are linearly proportional to the concrete's tensile properties. By assuming a uniform distribution of bond stress along the embedment length, the bond strength calculated was 20 MPa for a tensile strength of 8 MPa with a slip of 0.42 mm, and 32.56 MPa with a slip of 1.58 mm for concrete with 11 MPa of tensile strength.
3. The use of concrete incorporating high tensile materials can change the mode of failure from pullout-splitting to cone and V-type splitting failure.
4. The increase of the concrete cover from $1d_b$ to $2d_b$ had no effect on the average bond strength developed along an embedment length of $5d_b$ for the Commercial design mixes. This can be explained by the fact that higher confinement is provided when the concrete cover is increased which contributed to resisting tensile stresses. This was not the case for the in-house design mix with a different compressive strength of the materials where the bond strength increased.

5. Embedment length reaching $15d_b$ changes the mode of failure from splitting pullout to flexural with no slippage of the reinforcing bar.
6. The average bond strength is reduced with the increase of the embedment length meaning a non-uniform bond stress distribution along the embedment length.
7. The digital image correlation tool was proven to give very similar results to the experimental and numerical deflections, yet it estimated a slight decrease of the initial stiffness and an increase of the deflection values.

7.2.3 UHP-FRC numerical modeling

1. The proposed methodology to represent the different UHP-FRC design mixes consisting of modeling the flexural prisms and calibrating the concrete properties and tension softening was capable of predicting the tensile strength of the mix design without going through the inverse calculations.
2. The proposed model was able to provide a strain-hardening and strain softening behavior of the different specimens tested.
3. The numerical response curves matched the experimental load-deflection responses of most beams by obtaining the same initial stiffness, peak load, mid-deflection at peak load and the strain-softening curve.
4. The study of concrete cover was satisfactory captured by the analysis, where it was shown that the peak load was reduced for larger concrete covers in a manner proportional to the reduction of the internal lever arm.
5. A discrepancy between the numerical model and the experimental response was evident for the cases with longer embedment lengths where the model was not able to capture the

deformation response curve correctly. However, it was able to reproduce the increase in the load capacity for higher embedment lengths.

6. The model obtained the same mode of failures as the experimental beams, presenting a pullout failure of the reinforcing bar. The same crack patterns were developed as well.

7.3 Discussion for further development of the research

The results illustrate that the basic length of $5d_b$ which was considered short enough to yield an average bond stress that would be a good approximation of the local bond strength (in a local bond - slip law) may still be too large for the UHPC matrix. Admittedly this length, which is considered an established norm for conventional concrete was overly sufficient in most cases to fully develop bar yielding. Therefore, the bond stress distribution cannot be considered constant along this development length; shorter anchorage lengths should be considered to obtain an adequate measurement of local bond strength.

The beam end test setup was generally found to provide favorably high values of bond strength, probably owing to the dowel effect of the bar from the bending rotation of the reinforcing bar. This is an effect that likely is not observed in direct pullout tests. However the increased bond strength values is commensurate to the tensile strength estimates obtained from prism flexural testing, which is also significantly higher from the dog bone test results.

A future improvement of the experimental procedure could be the addition of strain measurements along the embedment length so as to understand the pointwise distribution of the bond stress and the effect of the embedment length increase. If beam tests are repeated, possibly use of optical fiber along the bar length would further clarify the behavior of the strain distribution along the entire embedded length.

References

1. A3001, C. (2013) 'Cementitious materials used in concrete', *Canadian Standards Association, Mississauga, Ontario*.
2. Aaleti, S. and Sritharan, S. (2014) 'Design of Ultrahigh-Performance Concrete Waffle Deck for Accelerated Bridge Construction', *Transportation Research Record: Journal of the Transportation Research Board*. doi: 10.3141/2406-02.
3. Abu-Lebdeh, T., Hamoush S., Heard W. and Zornig B (2011) 'Effect of matrix strength on pullout behavior of steel fiber reinforced very-high strength concrete composites', *Construction and Building Materials*. doi: 10.1016/j.conbuildmat.2010.06.059.
4. ACI Committee 408 (2003) *ACI 408R-03 Bond and Development of Straight Reinforcing Bars in Tension*, American Concrete Institute.
5. Akca, A. H. and Zihnioğlu, N. Ö. (2013) 'High performance concrete under elevated temperatures', *Construction and Building Materials*, 44, pp. 317–328. doi: 10.1016/j.conbuildmat.2013.03.005.
6. AL-Ameeri, A. (2013) 'The Effect of Steel Fiber on Some Mechanical Properties of Self Compacting Concrete', *American Journal of Civil Engineering*. doi: 10.11648/j.ajce.20130103.14.
7. Alford, N. M. and Birchall, J. D. (1985) 'Fibre toughening of MDF cement', *Journal of Materials Science*. doi: 10.1007/BF00555896.
8. Alford, N. M., Groves, G. W. and Double, D. D. (1982) 'Physical properties of high strength cement pastes', *Cement and Concrete Research*, 12(3), pp. 349–358. doi: 10.1016/0008-8846(82)90083-7.
9. Alkaysi, M. and El-tawil, S. (2016) 'Bond between Ultra-High Performance Concrete and Steel Bars', c, pp. 1–10.
10. Alsadey, S. (2013) 'Effects of Super Plasticizing and Retarding Admixtures on Properties of Concrete', in *International Conference on Innovations in Engineering and Technology (ICIET'2013)*, December 25-26, Bangkok (Th. doi: 10.15242/IIIE.E1213607.
11. American Society of Testing Materials (2015) *ASTM C39: Standard Test Method for Compressive Strength of Cylindrical Concrete Specimens*, ASTM International. doi: 10.1520/C0039.
12. Andreasen, A. H. M. and Andersen, J. (1930) 'Ueber die Beziehungen zwischen Kornabstufungen und Zwischenraum in Produkten aus losen Körnern (mit einigen Experimenten)', *Kolloid-Zeitschrift*, 50, pp. 217–228.

13. Aspdin, J. (1824) ‘An improvement in the modes of producing an artificial stone’.
14. ASTM-C230 (2010) ‘Standard Specification for Flow Table for Use in Tests of Hydraulic Cement 1’, *Annual Book of ASTM Standards*. doi: 10.1520/C0230.
15. ASTM C1856 (2017) ‘Standard Practice for Fabricating and Testing Specimens of Ultra-High Performance Concrete’, *ASTM International*. doi: 10.1520/C1856.
16. ASTM C496/C496M – 17 (2011) ‘Standard Test Method for Splitting Tensile Strength of Cylindrical Concrete Specimens ASTM C-496’, *ASTM International*. doi: 10.1111/j.1547-5069.2008.00253.x.
17. Bache, H. H. (1981) ‘Densified Cement / Ultra-Fine Particle-Based Materials’, *the Second International Conference on Superplasticizers in Concrete*, (0 6), pp. 1–34.
18. Bache, H. H. (1987) ‘Introduction to Compact Reinforced Composite’, *Nordic concrete research*, No. 6, pp. 19–33.
19. Baqersad, M., Amir, E. and Mortazavi, H. (2017) ‘State of the Art : Mechanical Properties of Ultra-High Performance Concrete’, *Civil Engineering Journal*, 3(3), pp. 190–198.
20. Basheerudeen, A. and Anandan, S. (2015) ‘Simplified mix design procedures for steel fibre reinforced self compacting concrete’, *Engineering Journal*. doi: 10.4186/ej.2015.19.1.21.
21. Best, J. F. and Lane, R. O. (1980) *Testing for Optimum Pumpability of Concrete*, *Concrete International*.
22. Bilodeau, A. and Mohan Malhotra, V. (2000) ‘High-volume fly ash system: Concrete solution for sustainable development’, *ACI Structural Journal*. doi: 10.14359/804.
23. Breitenbucher, R. (1999) ‘High performance fibre concrete SIFCON for repairing environmental structures’, in *HIGH PERFORMANCE FIBER REINFORCED CEMENT COMPOSITES (HPFRCC3)*.
24. Bye, G. C. (1983) *Portland Cement: Composition, Production and Properties*.
25. C1856/C1856M (no date) ‘Standard Practice for Fabricating and Testing Specimens of Ultra-High Performance Concrete’.
26. Cairns, J. and Plizzari, G. A. (2003) ‘Towards a harmonised European bond test’, *Materials and Structures/Materiaux et Constructions*. doi: 10.1617/13887.
27. Chan, Y. W. and Chu, S. H. (2004) ‘Effect of silica fume on steel fiber bond characteristics in reactive powder concrete’, *Cement and Concrete Research*. doi: 10.1016/j.cemconres.2003.12.023.

28. Chan, Y. W. and Li, V. C. (1997) 'Effects of transition zone densification on fiber/cement paste bond strength improvement', *Advanced Cement Based Materials*. doi: 10.1016/S1065-7355(97)90010-9.
29. Chao, S. H., Naaman, A. E. and Parra-Montesinos, G. J. (2009) 'Bond behavior of reinforcing bars in tensile strain-hardening fiber-reinforced cement composites', *ACI Structural Journal*, 106(6), pp. 897–906. doi: 10.14359/51663191.
30. Cheyrezy, M., Maret, V. and Frouin, L. (1995) 'Microstructural analysis of RPC (Reactive Powder Concrete)', *Cement and Concrete Research*. doi: 10.1016/0008-8846(95)00143-Z.
31. CSA (Canadian Standards Association) (2014) 'Design of Concrete Structures', *CAN/CSA S23.3-14*. doi: 10.1007/BF02479623.
32. Csa, S. (1995) 'S478-95: Guideline on Durability in Buildings', *Canadian Standards Association, Rexdale, Canada*.
33. Czoboly, O. *et al.* (2017) 'Fibers and fiber cocktails to improve fire resistance of concrete', *Journal of Thermal Analysis and Calorimetry*, 128(3), pp. 1453–1461. doi: 10.1007/s10973-016-6038-x.
34. Dagenais, M. A. and Massicotte, B. (2012) 'Tension lap slices strengthened with ultra high performance fibre reinforced concrete', *8th RILEM International Symposium on Fibre Reinforced Concrete: challenges and opportunities (BEFIB 2012)*, pp. 198–208. Available at: http://www.rilem.org/gene/main.php?base=500218&id_publication=419&id_papier=8627.
35. Dean, S. and Graybeal, B. (2006) 'Practical Means for Determination of the Tensile Behavior of Ultra-High Performance Concrete', *Journal of ASTM International*. doi: 10.1520/JAI100387.
36. Doiron, G. (2017) 'Uhpc Pier Repair / Retrofit Examples of Completed Projects in North America', *AFGC-ACI-fib-RILEM Int. Symposium on Ultra-High Performance Fibre-Reinforced Concrete*.
37. Eleftheriou, T. E., Tastani, S. P. and Pantazopoulou, S. J. (2017) 'Development of Reinforcing Bars in SRCC Matrix: Modeling and Interpretation', *Journal of Structural Engineering (United States)*. doi: 10.1061/(ASCE)ST.1943-541X.0001845.
38. European Committee for Standardization (2004) 'Design of concrete structures - Part 1-2: General rules - Structural fire design', *Eurocode 2, BS EN 1992*, p. 97.
39. European Union, T. (2004) *Eurocode 2, Design of concrete structures - Part 1-2: General rules- Structural fire design*. Available at: <papers2://publication/uuid/1B0960C1-28E7-4B6A-ADFE-19C0455EDFD3>.
40. Fehling, E. (2004) *Ultra high performance concrete (UHPC), Proceedings of the International Symposium on Ultra High Performance Concrete*. doi: ISBN: 3-89958-086-9.

41. Fehling, E., Lorenz, P. and Leutbecher, T. (2012) 'Experimental Investigations on Anchorage of Rebars in UHPC', *Proceeding of Hipermat 2012. Third International Symposium on UHPC and Nanotechnology of High Performance Constructions Materials*, pp. 1–8.
42. Gales, J. A., Bisby, L. A. and Stratford, T. (2012) 'New parameters to describe high-temperature deformation of prestressing steel determined using digital image correlation', *Structural Engineering International: Journal of the International Association for Bridge and Structural Engineering (IABSE)*. doi: 10.2749/101686612X13363929517730.
43. Garlock, M. *et al.* (2012) 'Fire hazard in bridges: Review, assessment and repair strategies', *Engineering Structures*, 35, pp. 89–98. doi: 10.1016/j.engstruct.2011.11.002.
44. Georgiou, A. V. and Pantazopoulou, S. J. (2016) 'Effect of fiber length and surface characteristics on the mechanical properties of cementitious composites', *Construction and Building Materials*. doi: 10.1016/j.conbuildmat.2016.09.009.
45. Graybeal, B. (2006) 'Material Property Characterization of Ultra-High Performance Concrete', *Fhwa*. doi: 10.1063/1.456828.
46. Graybeal, B. A. (2007) 'Compressive behavior of ultra-high-performance fiber-reinforced concrete', *ACI Materials Journal*. doi: 10.14359/18577.
47. Graybeal, B. A. (2013) 'Ultra-High Performance Concrete : A State-of-the-Art Report for the Bridge Community', (June).
48. Graybeal, B. A. and Baby, F. (2013) 'Development of direct tension test method for ultra-high-performance fiber-reinforced concrete', *ACI Materials Journal*. doi: 10.14359/51685532.
49. Graybeal, B. and Davis, M. (2008) 'Cylinder or cube: Strength testing of 80 to 200 MPa (11.6 to 29 ksi) ultra-high-performance fiber-reinforced concrete', *ACI Materials Journal*. doi: 10.14359/20202.
50. Gürkan, Yıldırım; Mustafa, Şahmaran; Özgür, A. (2018) '15 - Engineered cementitious composites-based concrete', in *Eco-Efficient Repair and Rehabilitation of Concrete Infrastructures*. Elsevier, pp. 387–427.
51. György L. Balázs; Éva Lublós; Olivér A. Czoboly (2017) 'Effectiveness of fibres for structural elements in case of fire.', *American Concrete Institute*, 310, pp. 269–278.
52. Habel, K. *et al.* (2006) 'Development of the mechanical properties of an Ultra-High Performance Fiber Reinforced Concrete (UHPFRC)', *Cement and Concrete Research*, 36(7), pp. 1362–1370. doi: 10.1016/j.cemconres.2006.03.009.
53. Habel, K. *et al.* (2008) 'Ultra-high performance fibre reinforced concrete mix design in central Canada', *Canadian Journal of Civil Engineering*. doi: 10.1139/L07-114.

54. HABEL, K. (2004) 'Structural Behaviour Of Elements Combining Ultra-High Performance Fibre Reinforced Concretes (UHPFRC) And Reinforced Concrete', *Fifth RILEM Symposium on Fibre-Reinforced Concretes (FRC) - BEFIB' 2000*. doi: 10.1146/annurev-environ-030117-020220.
55. Haber, Z. B., De la Varga, I. and Graybeal, B. A. (2018) 'Properties and Behavior of UHPC-Class Materials', (February).
56. Harajli, M., Hamad, B. and Karam, K. (2002) 'Bond-slip Response of Reinforcing Bars Embedded in Plain and Fiber Concrete', *Journal of Materials in Civil Engineering*, 14(6), pp. 503–511. doi: 10.1061/(ASCE)0899-1561(2002)14:6(503).
57. Hassan, A. M. T., Jones, S. W. and Mahmud, G. H. (2012) 'Experimental test methods to determine the uniaxial tensile and compressive behaviour of Ultra High Performance Fibre Reinforced Concrete(UHPFRC)', *Construction and Building Materials*. doi: 10.1016/j.conbuildmat.2012.04.030.
58. Hertz, K. D. (2003) 'Limits of spalling of fire-exposed concrete', *Fire Safety Journal*, 38(2), pp. 103–116. doi: 10.1016/S0379-7112(02)00051-6.
59. Holschemacher, K., Klotz, S. and Weiße, D. (2004) 'Bond of Reinforcement in Ultra High-Strength Concrete', in *Ultra High Performance Concrete (UHPC) Proceedings of the International Symposium on Ultra High Performance Concrete*. doi: 10.14359/14489.
60. Hooton, R. D., Nokken, M. and Thomas, M. D. A. (2007) *Portland-Limestone Cement : State-of-the-Art Report and Gap Analysis for CSA A 3000*, Cement Association of doi: 10.1016/j.fss.2012.08.014.
61. Ibrahim, M. A. *et al.* (2017) 'Effect of material constituents on mechanical & fracture mechanics properties of ultra-high-performance concrete', *ACI Structural Journal*. doi: 10.14359/51689717.
62. Kabir, R. and Islam, M. (2014) 'Bond stress behavior between concrete and steel rebar : Critical investigation of pull-out test via Finite Element Modeling', *International Journal of Civil and Structural Engineering*, 5(1), pp. 80–90. doi: 10.6088/ijcser.2014050008.
63. Kodur, V. K. R. *et al.* (2003) 'Effect of Strength and Fiber Reinforcement on Fire Resistance of High-Strength Concrete Columns', *Journal of Structural Engineering*, 129(2), pp. 253–259. doi: 10.1061/(ASCE)0733-9445(2003)129:2(253).
64. Krstulovic-Opara, N. *et al.* (1997) 'Flexural behavior of composite R.C.-Slurry Infiltrated Mat Concrete (SIMCON) members', *ACI Structural Journal*.
65. Kumar Mehta, P. and Burrows, R. W. (2001) 'Building durable structures in the 21st century', *Indian Concrete Journal*.
66. Lagier, F., Massicotte, B. and Charron, J. P. (2015) 'Bond strength of tension lap splice specimens in UHPFRC', *Construction and Building Materials*. doi: 10.1016/j.conbuildmat.2015.05.009.

67. Lagier, F., Massicotte, B. and Charron, J. P. (2016) 'Experimental investigation of bond stress distribution and bond strength in unconfined UHPFRC lap splices under direct tension', *Cement and Concrete Composites*. doi: 10.1016/j.cemconcomp.2016.08.004.
68. Lankard, D. R. (1985) 'Slurry Infiltrated Fiber Concrete (Sifcon): Properties and Applications', *Mat. Res. Soc. Symp. Proc.* doi: 10.1557/PROC-42-277.
69. Leboeuf, S. V. (2016) 'DÉVELOPPEMENT DE JOINTS DE CONNEXION EN BFUP POUR DES', (Génie Civil).
70. Lee, N. K. *et al.* (2018) 'Uncovering the role of micro silica in hydration of ultra-high performance concrete (UHPC)', *Cement and Concrete Research*. doi: 10.1016/j.cemconres.2017.11.002.
71. Lemnitzer, M. J. and Curbach, M. (2012) 'Bond in reinforced concrete under transverse tension', *Bond in Concrete 2012*.
72. Lepech, M. D. and Li, V. C. (2009) 'Water permeability of engineered cementitious composites', *Cement and Concrete Composites*. doi: 10.1016/j.cemconcomp.2009.07.002.
73. LeRoy, A. L. and Peter, G. (1967) 'Mechanics of Bond and Slip of Deformed Bars in Concrete', *Journal Proceedings*. doi: 10.14359/7600.
74. Li, V. C. and Leung, C. K. Y. (1992) 'Steady-State and Multiple Cracking of Short Random Fiber Composites', *Journal of Engineering Mechanics*. doi: 10.1061/(ASCE)0733-9399(1992)118:11(2246).
75. Maca, P., Zatloukal, J. and Konvalinka, P. (2012a) 'Development of Ultra High Performance Fiber Reinforced Concrete mixture', in *ISBEIA 2012 - IEEE Symposium on Business, Engineering and Industrial Applications*. doi: 10.1109/ISBEIA.2012.6423015.
76. Maca, P., Zatloukal, J. and Konvalinka, P. (2012b) 'Development of Ultra High Performance Fiber Reinforced Concrete Mixture', *2012 IEEE Symposium on Business, Engineering and Industrial Applications*. doi: 10.1109/ISBEIA.2012.6423015.
77. Markovic, I. (2006) *High-Performance Hybrid-Fibre Concrete*. doi: 10.1038/ncb1298.
78. Martin-Perez, B. and Pantazopoulou, S. J. (2001) 'Effect of bond, aggregate interlock and dowel action on the shear strength degradation of reinforced concrete', *Engineering Structures*. doi: 10.1016/S0141-0296(00)00004-3.
79. Massazza, F. (1993) 'Pozzolanic cements', *Cement and Concrete Composites*, 15(4), pp. 185–214. doi: 10.1016/0958-9465(93)90023-3.
80. Mindess, Sidney; Young, J. Francis; Darwin, D. (2003) *Concrete. second edition*. Prentice Hall,

Pearson Education, Inc. Upper Saddle River, NJ 07458, U.S.A.

81. De Morais, M. V. G. *et al.* (2010) 'Contribution to the explanation of the spalling of small specimen without any mechanical restraint exposed to high temperature', in *Nuclear Engineering and Design*, pp. 2655–2663. doi: 10.1016/j.nucengdes.2010.04.041.
82. Naaman, a. E. and Reinhardt, H. W. (2003) 'High Performance Fiber Reinforced Cement Composites HPFRCC-4: International RILEM Workshop', *Materials and Structures*. doi: 10.1007/BF02479507.
83. Naaman, A. E. and Reinhardt, H. W. (2006) 'Proposed classification of HPFRC composites based on their tensile response', *Materials and Structures/Materiaux et Constructions*. doi: 10.1617/s11527-006-9103-2.
84. Okamura, H. (1988) 'Self-Compacting High-Performance Concrete', *Concrete International*, 19(7), pp. 3–5.
85. Orange, G., Dugat, J. and Acker, P. (2000) 'Ductal®: new ultra high performance concretes - Damage resistance and micromechanical analysis', in *Fifth RILEM Symposium on Fibre-Reinforced Concretes (FRC) BEFIB' 2000 Lyon, France (2000)*.
86. Phan, L. T. and Carino, N. J. (2000) 'Fire Performance of High Strength Concrete: Research Needs', *Nist*. doi: doi:10.1061/40492(2000)181.
87. Phan, T. S. (2012) *Modélisation numérique de l'interface acier-béton: application au comportement des structures en béton renforcées par des aciers plats crantés*. Université Paris-Est.
88. Plank, J. *et al.* (2009) 'Effectiveness of Polycarboxylate Superplasticizers in Ultra-High Strength Concrete: The Importance of PCE Compatibility with Silica Fume', *Journal of Advanced Concrete Technology*. doi: 10.3151/jact.7.5.
89. Ramirez, D. N. (2005) *Etude de la liaison acier-béton: de la modélisation du phénomène à la formulation d'un élément fini enrichi "béton armé"*. École normale supérieure de Cachan - ENS Cachan.
90. Richard, P. and Cheyrezy, M. (1995) 'Composition of reactive powder concretes', *Cement and Concrete Research*, 25(7), pp. 1501–1511. doi: 10.1016/0008-8846(95)00144-2.
91. Ronanki, V. S., Valentim, D. B. and Aaleti, S. (2016) 'Development length of reinforcing bars in UHPC: An experimental and analytical investigation', *First International Interactive Symposium on UHPC*, 4, pp. 1–9. doi: 10.21838/uhpc.2016.85.
92. Rossi, P. (1997) 'High performance multimodal fiber reinforced cement composites

- (HPMFRCC): The LCPC experience’, *ACI Materials Journal*, 94(6), pp. 478–483. doi: 10.14359/331.
93. Rossi, P. *et al.* (2005) ‘Bending and compressive behaviours of a new cement composite’, *Cement and Concrete Research*, 35(1), pp. 27–33. doi: 10.1016/j.cemconres.2004.05.043.
 94. Rossi, P. (2013) ‘Influence of fibre geometry and matrix maturity on the mechanical performance of ultra high-performance cement-based composites’, *Cement and Concrete Composites*. doi: 10.1016/j.cemconcomp.2012.08.005.
 95. Rossi, P., Acker, P. and Malier, Y. (1987) ‘Effect of steel fibres at two different stages: The material and the structure’, *Materials and Structures*, 20(6), pp. 436–439. doi: 10.1007/BF02472494.
 96. Roy, D. M., Gouda, G. R. and Bobrowsky, A. (1972) ‘Very high strength cement pastes prepared by hot pressing and other high pressure techniques’, *Cement and Concrete Research*. doi: 10.1016/0008-8846(72)90075-0.
 97. Sahmaran, M., Li, M. and Li, V. C. (2007) ‘Transport properties of engineered cementitious composites under chloride exposure’, *ACI Materials Journal*. doi: 10.14359/18964.
 98. Schoening, J. and Hegger, J. (2012) ‘Lapped splices in UHPC joints’, (2003), pp. 687–694.
 99. Serrano, R. *et al.* (2016) ‘Analysis of fire resistance of concrete with polypropylene or steel fibers’, *Construction and Building Materials*, 122, pp. 302–309. doi: 10.1016/j.conbuildmat.2016.06.055.
 100. Shao, B. (2016) ‘Mix Development of PLC-based Ultra-high Performance Fibre Reinforced Concrete and Characterization of Key Mechanical Properties and Time-Dependent Behaviour’, pp. 1–130. Available at: <https://tspace.library.utoronto.ca/handle/1807/76013>.
 101. Solutions, U. I. & S. (2016a) *Plaster Mixing Procedures*. Available at: https://www.usg.com/content/dam/USG_Marketing_Communications/united_states/product_promotional_materials/finished_assets/plaster-mixing-procedures-application-en-IG503.pdf.
 102. Solutions, U. I. & S. (2016b) *USG HYDRO-STONE BRAND Gypsum Cement*. Available at: https://www.usg.com/content/dam/USG_Marketing_Communications/united_states/product_promotional_materials/finished_assets/hydro-stone-gypsum-cement-data-en-IG1379.pdf.
 103. Spasojević, A. (2008) *Structural Implications of ultra-high performance fibre-reinforced concrete in bridge design*. doi: 10.1093/infdis/jir317.
 104. Sritharan, S. *et al.* (2018) ‘First Application of UHPC Bridge Deck Overlay in North America’, *Transportation Research Record*. doi: 10.1177/0361198118755665.
 105. Tastani, S. P. *et al.* (2016) ‘The effect of carbon nanotubes and polypropylene fibers on bond of

- reinforcing bars in strain resilient cementitious composites’, *Frontiers of Structural and Civil Engineering*, 10(2), pp. 214–223. doi: 10.1007/s11709-016-0332-3.
106. Tastani, S. P. and Pantazopoulou, S. J. (2010) ‘Direct Tension Pullout Bond Test: Experimental Results’, *Journal of Structural Engineering*, 136(6), pp. 731–743. doi: 10.1061/(ASCE)ST.1943-541X.0000159.
107. Tastani, S. P. and Pantazopoulou, S. J. (2013) ‘Reinforcement and Concrete Bond: State Determination along the Development Length’, *Journal of Structural Engineering*. doi: 10.1061/(ASCE)ST.1943-541X.0000725.
108. Tastani, S. and Pantazopoulou, S. (2002) ‘Experimental evaluation of the direct tension-pullout bond test’, in *Bond in concrete from research to standards*.
109. Thomas, M. (2007) *Optimizing the Use of Fly Ash in Concrete*, Skokie, Ill. : Portland Cement Association. doi: 10.15680/IJRSET.2015.0409047.
110. Ulm, F.-J., Acker, P. and Lévy, M. (1999) ‘The “Chunnel” Fire. II: Analysis of Concrete Damage’, *Journal of Engineering Mechanics*, 125(3), pp. 283–289. doi: 10.1061/(ASCE)0733-9399(1999)125:3(283).
111. University of Illinois (1979) ‘The History of Concrete’, <http://matse1.matse.illinois.edu/concrete/hist.html>, pp. 9–11. doi: 10.1016/B978-0-7506-7523-9.50022-2.
112. Vecchio, F. and Bucci, F. (1999) ‘Analysis of repaired reinforced concrete structures’, *Journal of Structural Engineering*. doi: 10.1061/(ASCE)0733-9445(1999)125:6(644).
113. Vecchio, F. J. (2000) ‘Disturbed Stress Field Model for Reinforced Concrete: Formulation’, *Journal of Structural Engineering*. doi: 10.1061/(ASCE)0733-9445(2000)126:9(1070).
114. Vecchio, F. J. and Collins, M. P. (1986) ‘The Modified Compression Field Theory for reinforced concrete elements subjected to shear’, *ACI Structural Journal*.
115. Vecchio, F. J., Wong, P. and Trommels, H. (2013) ‘Vector2 & Formworks User’s Manual.’, *Second Edition*. doi: 10.1007/s007690000247.
116. Vitek, J. L., Coufal, R. and Čítek, D. (2013) ‘UHPC - Development and testing on structural elements’, in *Procedia Engineering*. doi: 10.1016/j.proeng.2013.09.033.
117. Weisse, D. and Holschemacher, K. (2012) ‘Behaviour of lap splices in ultra high strength concrete’, (Figure 1), pp. 695–702.
118. Weng, J. K., Langan, B. W. and Ward, M. a. (1997) ‘Pozzolanic reaction in portland cement,

- silica fume, and fly ash mixtures’, *Canadian Journal of Civil Engineering*. doi: 10.1139/cjce-24-5-754.
119. White, D. J., Take, W. A. and Bolton, M. D. (2003) ‘Soil deformation measurement using particle image velocimetry (PIV) and photogrammetry’, *Géotechnique*. doi: 10.1680/geot.53.7.619.37383.
120. Wight, J. K. and MacGregor, J. . (2012) *Reinforced concrete: mechanics and design*. 6th ed. Pearson, Toronto.
121. Wille, K. *et al.* (2012) ‘Ultra-high performance concrete and fiber reinforced concrete: Achieving strength and ductility without heat curing’, *Materials and Structures/Materiaux et Constructions*. doi: 10.1617/s11527-011-9767-0.
122. Wille, K., El-Tawil, S. and Naaman, A. E. (2014) ‘Properties of strain hardening ultra high performance fiber reinforced concrete (UHP-FRC) under direct tensile loading’, *Cement and Concrete Composites*. doi: 10.1016/j.cemconcomp.2013.12.015.
123. Wille, K., Kim, D. J. and Naaman, A. E. (2011) ‘Strain-hardening UHP-FRC with low fiber contents’, *Materials and Structures/Materiaux et Constructions*. doi: 10.1617/s11527-010-9650-4.
124. Wille, K. and Naaman, A. E. (2010) ‘Bond stress-slip behavior of steel fibers embedded in ultra high performance concrete’, in *Proceedings of 18th European Conference on Fracture and Damage of Advanced Fiber-Reinforced Cement-Based Materials*.
125. Wille, K. and Naaman, A. E. (2012) ‘Pullout behavior of high-strength steel fibers embedded in ultra-high-performance concrete’, *ACI Materials Journal*. doi: 10.14359/51683923.
126. Wille, K. and Naaman, A. E. (2013) ‘Effect of ultra-high-performance concrete on pullout behavior of high-strength brass-coated straight steel fibers’, *ACI Materials Journal*. doi: 10.5194/npg-12-661-2005.
127. Wille, K., Naaman, A. E. and Parra-Montesinos, G. J. (2011) ‘Ultra-high performance Concrete with compressive strength exceeding 150 MPa (22 ksi): A simpler way’, *ACI Materials Journal*. doi: 10.14359/51664215.
128. Wu, Z. *et al.* (2016) ‘Effects of steel fiber content and shape on mechanical properties of ultra high performance concrete’, *Construction and Building Materials*. doi: 10.1016/j.conbuildmat.2015.11.028.
129. Yamaguchi, E. (2014) ‘Finite element method’, in *Bridge Engineering Handbook: Fundamentals, Second Edition*. doi: 10.1201/b15616.
130. Yermak, N. *et al.* (2017) ‘Influence of steel and/or polypropylene fibres on the behaviour of

- concrete at high temperature: Spalling, transfer and mechanical properties’, *Construction and Building Materials*, 132, pp. 240–250. doi: 10.1016/j.conbuildmat.2016.11.120.
131. Yoo, D. Y. and Banthia, N. (2016) ‘Mechanical properties of ultra-high-performance fiber-reinforced concrete: A review’, *Cement and Concrete Composites*. doi: 10.1016/j.cemconcomp.2016.08.001.
132. Yoo, D. Y., Kang, S. T. and Yoon, Y. S. (2016) ‘Enhancing the flexural performance of ultra-high-performance concrete using long steel fibers’, *Composite Structures*. doi: 10.1016/j.compstruct.2016.03.032.
133. Yu, R., Spiesz, P. and Brouwers, H. J. H. (2014) ‘Mix design and properties assessment of Ultra-High Performance Fibre Reinforced Concrete (UHPFRC)’, *Cement and Concrete Research*, 56, pp. 29–39. doi: 10.1016/j.cemconres.2013.11.002.
134. Yu, R., Spiesz, P. and Brouwers, H. J. H. (2014) ‘Mix design and properties assessment of Ultra-High Performance Fibre Reinforced Concrete (UHPFRC)’, *Cement and Concrete Research*. doi: 10.1016/j.cemconres.2013.11.002.
135. Yu, R., Spiesz, P. and Brouwers, H. J. H. (2015) ‘Development of Ultra-High Performance Fibre Reinforced Concrete (UHPFRC): Towards an efficient utilization of binders and fibres’, *Construction and Building Materials*. doi: 10.1016/j.conbuildmat.2015.01.050.
136. Yuan, J. and Graybeal, B. A. (2014) ‘Bond Behavior of Reinforcing Steel in Ultra-High Performance Concrete’, *Engineering Structures*, 1(6), pp. 228–235. doi: 10.1159/000331754.
137. Yudenfreund, M., Odler, I. and Brunauer, S. (1972) ‘Hardened portland cement pastes of low porosity I. Materials and experimental methods’, *Cement and Concrete Research*. doi: 10.1016/0008-8846(72)90073-7.
138. Zdeb, T. and Śliwiński, J. (2009) ‘The influence of steel fibre content and curing conditions on mechanical properties and deformability of reactive powder concrete at bending’, in *Brittle Matrix Composites 9*. doi: 10.1533/9781845697754.
139. Zhou, B. and Chida, Y. (2013) ‘Fiber Orientation in Ultra High Performance Fiber Reinforced Concrete and Its Visualization’, *VIII International Conference on Fracture Mechanics of Concrete and Concrete Structures FraMCoS-8*.
140. Zollo, R. F. (1997) ‘Fiber-reinforced concrete: an overview after 30 years of development’, *Cement and Concrete Composites*. doi: 10.1016/S0958-9465(96)00046-7.
- 1.

Appendices

Appendix A Instrumentation drawings and detailing

A.1 Four-point bending jig drawings

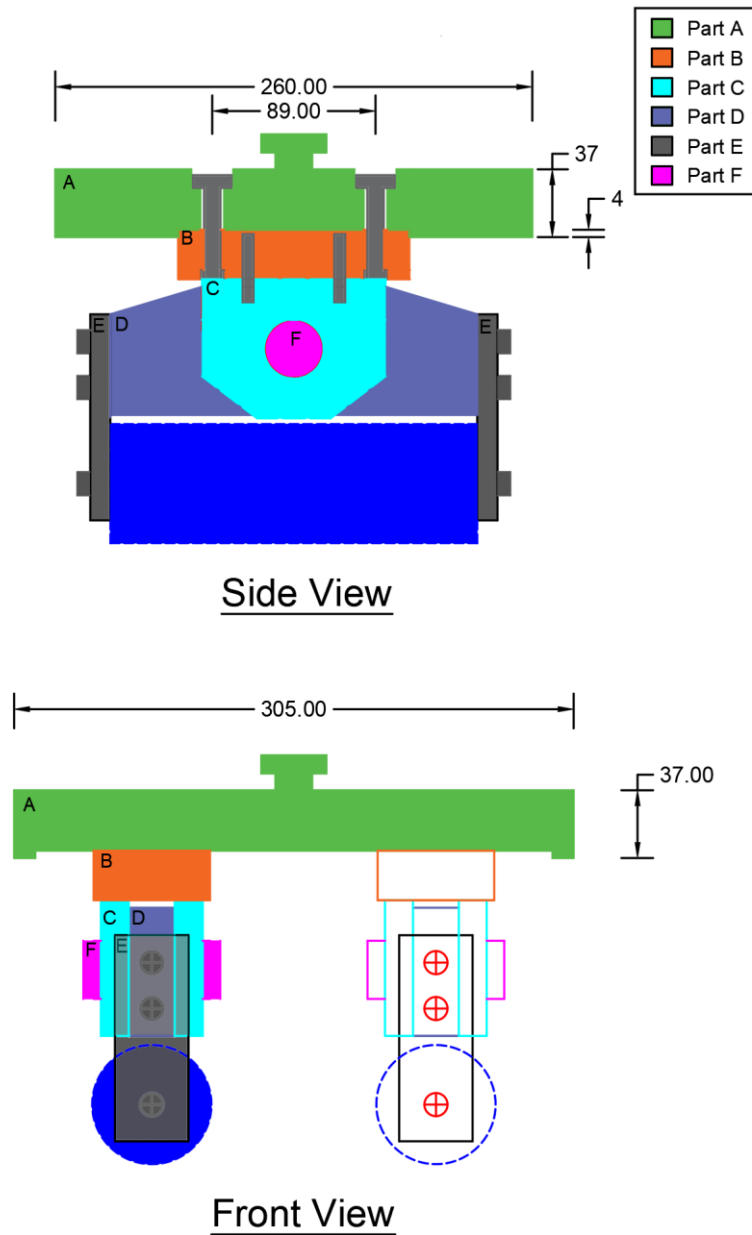


Figure A-1 Side and Front view of the jig

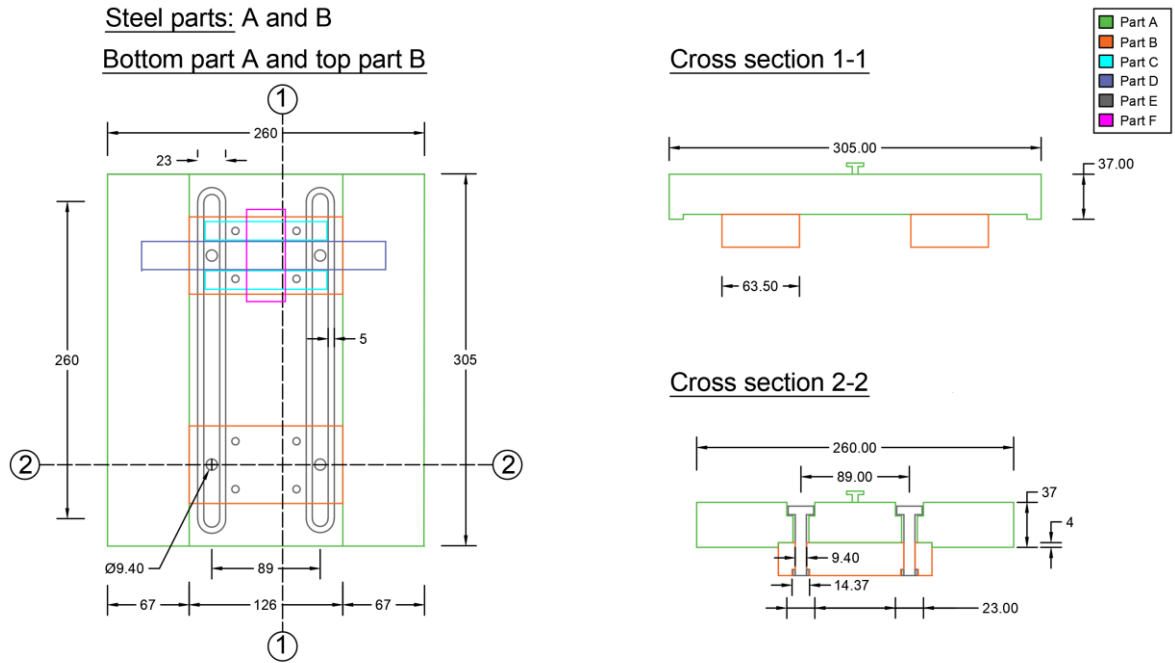


Figure A-2 Detailing of part A and B

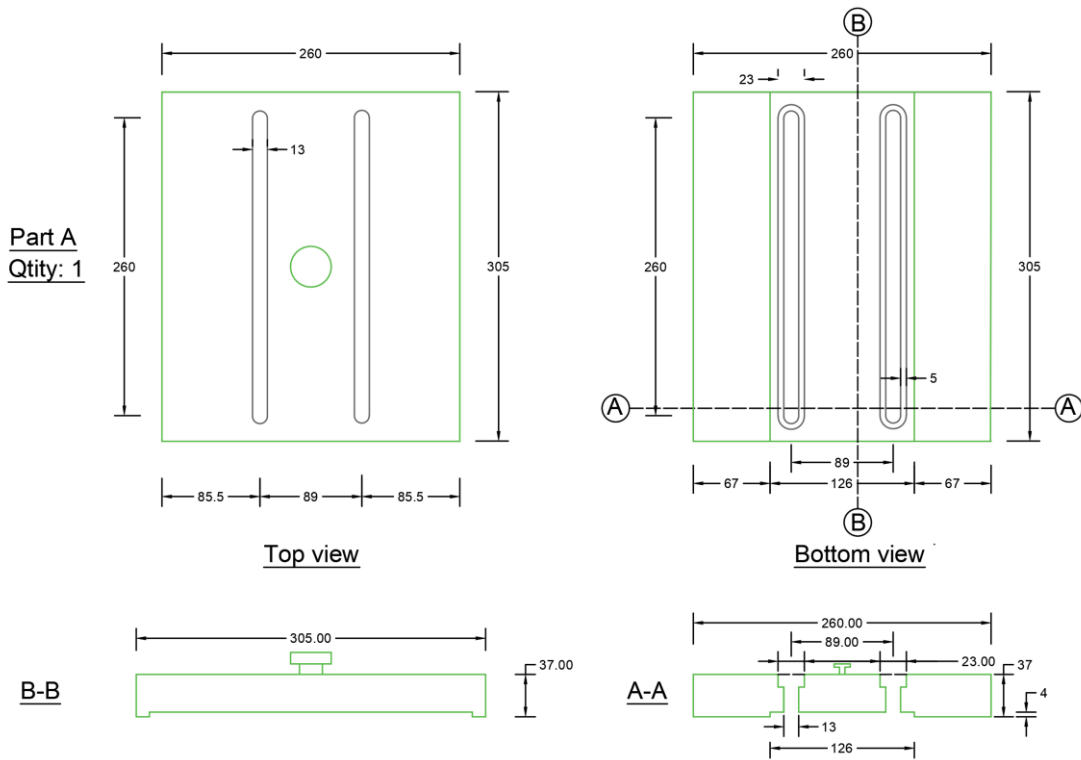


Figure A-3 Detailing of part A

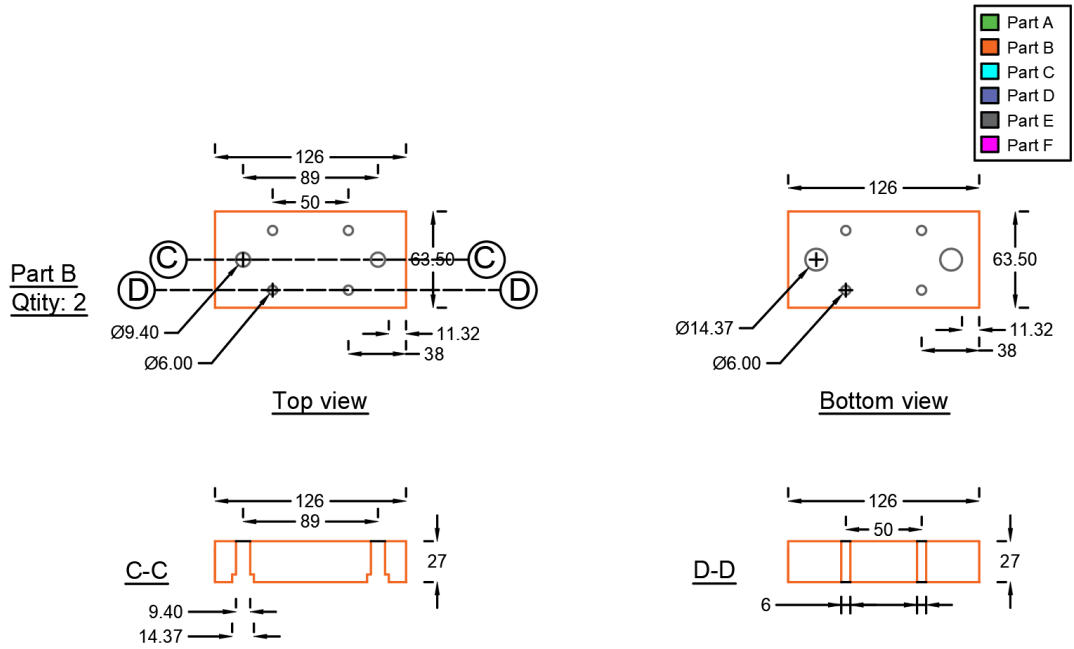


Figure A-4 Detailing of part B

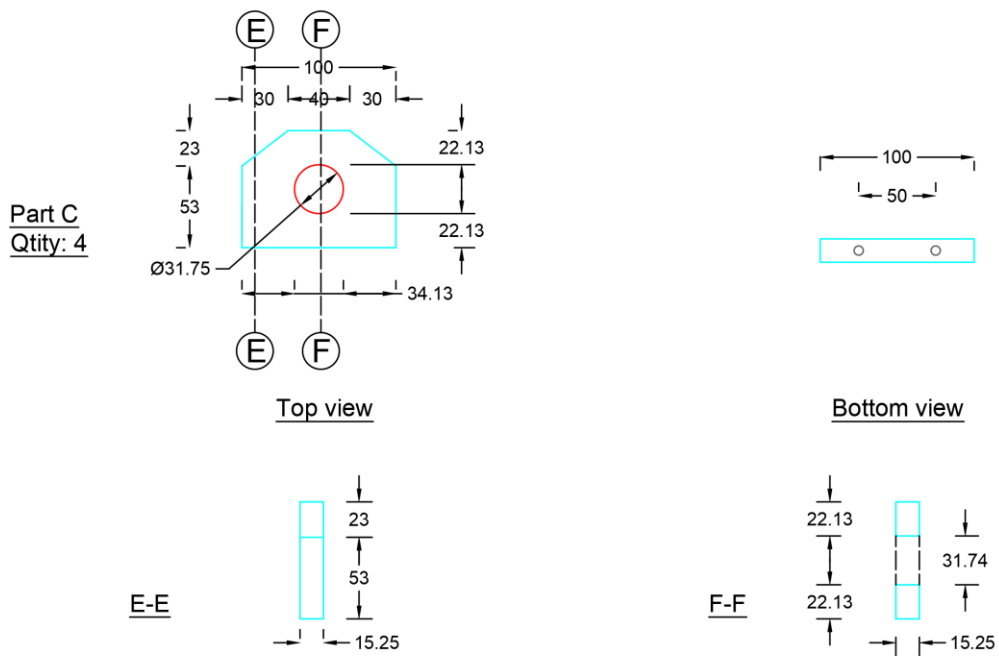


Figure A-5 Detailing of part C

A.4 Slip frame compartments drawings

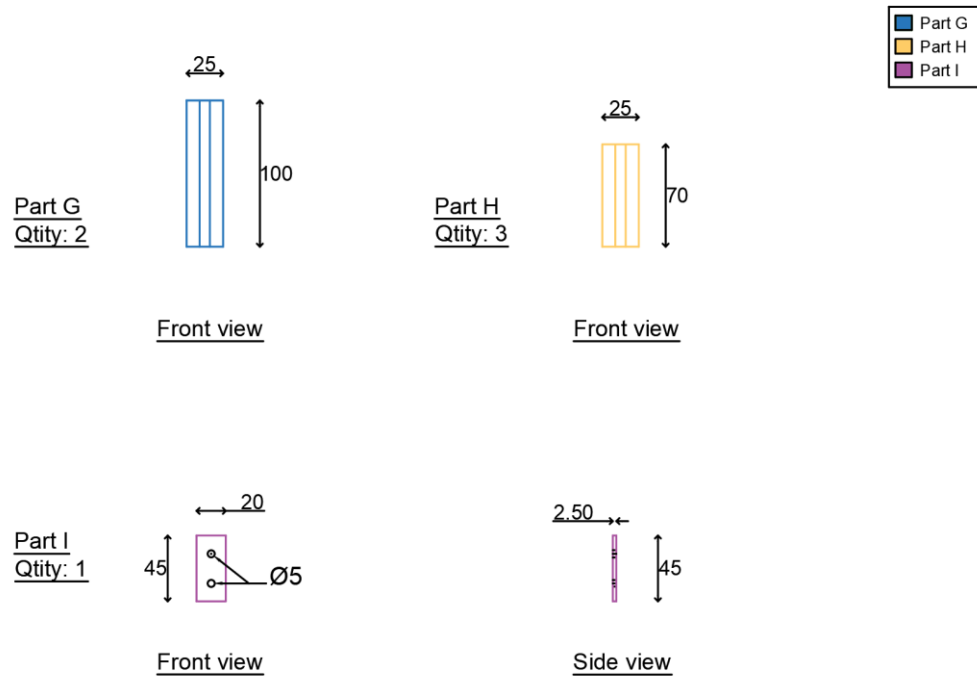
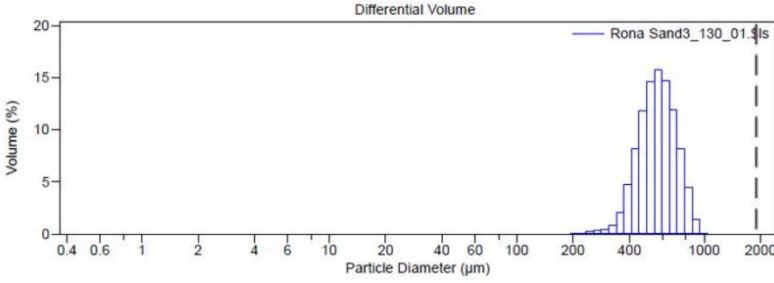
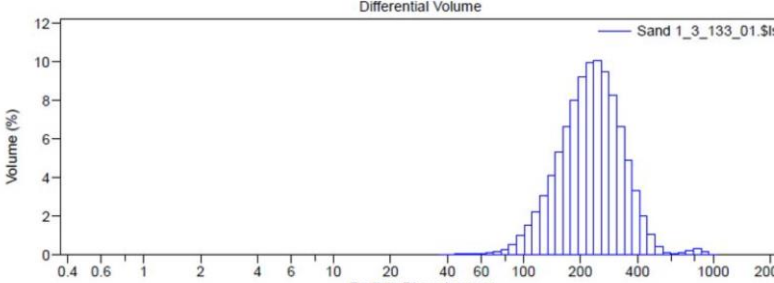
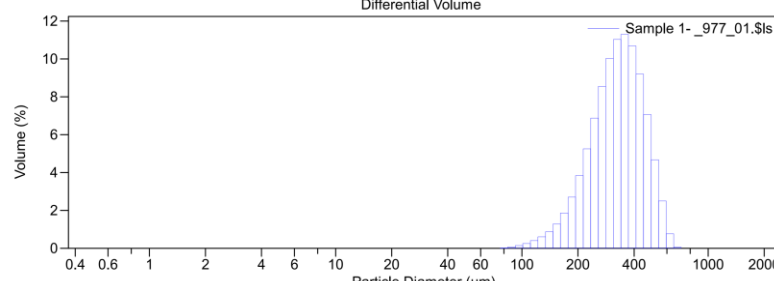


Figure A-10 Dimensions of the parts forming the frame

Appendix B In-house design mix trials

B.1 Sieve analysis to obtain the maximum grain size for each sand type S1, S2, and S3

Table B-1 Sieve analysis for the sand used

Sand Type	Sieve Analysis	a_{max} (mm)
S1		0.772
S2		0.370
S3		0.542

B.2 Trial mixes for (Yu et al., 2014)

Table B-2 Design mix for the 2nd trial to compare the flowability caused by SP1 and SP2

M2 (V = 0.275 L, 12/07/2017)			Flowability	
Material	kg/m ³	(g)		
C1	859.5	236.36		
LP	0	0		
S2	221.1	60.8		
S1	1061.2	291.83		
SF1	24.8	6.82		
SP2	44.2	12.1		
W	176.9	48		
CSF	156	42.9		

Table B-3 Design mix for the 3rd trial where the LP was replaced by FA instead of C

M3 (V = 0.275 L, 12/07/2017)		
Material	kg/m ³	(g)
C1	594.2	163.4
LP	0	0
FA	265.3	73
S2	221.1	61
S1	1061.2	291.83
SF1	24.8	6.82
SP2	44.2	12.1
W	176.9	48
CSF	156	42.9

Table B-4 Design mix for the fourth trial with type of sand S1(w/b = 0.2)

M4 (V = 0.275 L, 12/07/2017)		
Material	kg/m ³	(g)
C1	594.2	163.4
LP	0	0
FA	265.3	73
S1	1282.3	352.63
SF1	24.8	6.82
SP2	44.2	12.1
W	176.9	48
CSF	156	42.9

Table B-5 Design mix for the fifth trial where the volume is doubled ($w/b = 0.37$)

M5 (V = 0.5 L, 12/07/2017)				
Material	kg/m ³	(g)	Flowability	f'_{cc} (MPa)
C1	594.2	297.1		07 days: 21/07/2017 44
LP	0	0		14 days: 28/07/2017 45
FA	265.3	132.65		
S1	1282.3	641.15		
SF1	24.8	12.4		
SP2	44.2	22.1		
W	176.9	96 + 89		
CSF	156	42.9		

Table B-6 Design mix for the 6th trial, addition of water and superplasticizer ($w/b = 0.28$)

M6 (V = 0.275 L, 14/07/2017)				
Material	kg/m ³	(g)	Flowability	
C1	594.2	163.405		
LP	0	0		
FA	265.3	72.96		
S1	1282.3	352.63		
SF1	24.8	6.82		
SP2	44.2	12 + 4		
W	176.9	48 + 20		
CSF	156	42.9		

Table B-7 Design mix for the 7th trial, addition of water and superplasticizer ($w/b = 0.22$)

M7 (V = 0.275 L, 14/07/2017)				
Material	kg/m ³	(g)	Flowability	f'_{cc} (MPa)
C1	594.2	163.4		07 days: 1/07/2017 79
LP	58.8	16.2		14days: 28/07/2017 80
FA	206.5	56.8		
S2	221.1	61		
S1	1061.2	291.83		
SF1	24.8	6.82		
SP2	44.2	12.1 + 8		
W	176.9	48 + 7		
CSF	156	42.9		

Table B-8 Design mix for the 8th and 9th trial with 30% FA and 70% Slg1, cubes at 7 days

M8 / M9 (V = 1.2 L, 26/07/2017)				
--	--	--	--	--

Material	kg/m ³	(g)	f'_{cc} (MPa)	
C1	594.2	713.04	07 days: 02/08/2017	88.98
LP	58.8	70.58	14 days: 09/08/2017	89.21
FA	61.95	74.34		
Slg1	144.55	173.46		
S2	221.1	265.32		
S1	1061.2	1273.44		
SF1	24.8	29.76		
SP2	44.2	53.04		
W	176.9	212.28		
CSF	156	187.2		

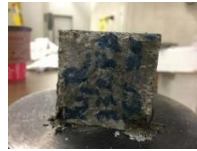
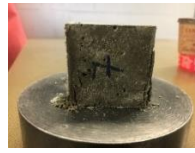


Table B-9 Design mix for the 10th trial with 50% FA and 50% Slg1, cube at 28 days

M10 (V = 1.2 L, 27/07/2017)				
Material	kg/m ³	(g)	f'_{cc} (MPa)	
C1	594.2	713.04	07 days: 03/08/2017	81
LP	58.8	70.58	28 days: 24/08/2017	96.6
FA	103.3	123.9		
Slg1	103.3	123.9		
S2	221.1	265.32		
S1	1061.2	1273.44		
SF1	24.8	29.76		
SP2	44.2	53.04		
W	176.9	212.28		
CSF	156	187.2		

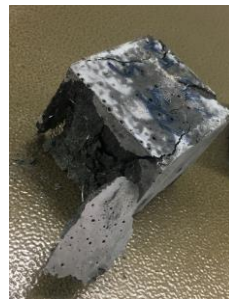


Table B-10 Design mix for the 11th trial with 70% FA and 30% Slg1, cube at 28 days

M11 (V = 1.2 L, 27/07/2017)				
Material	kg/m ³	(g)	f'_{cc} (MPa)	
C1	594.2	713.04	07 days: 03/08/2017	79
LP	58.8	70.58	28 days: 24/08/2017	99.6
FA	144.55	173.46		
Slg1	61.95	74.34		
S2	221.1	265.32		
S1	1061.2	1273.44		
SF1	24.8	29.76		
SP2	44.2	53.04		
W	176.9	212.28		
CSF	156	187.2		



Table B-11 Design mix for the trial 12 with 70% of Slg1 and 30% of SF1, cube at 28 days

M12 (V = 3.5 L, 28/08/2017)				
Material	kg/m ³	(g)	<i>f'</i> _{cc} (MPa)	
C1	594.2	2079.7	28 days	
LP	58.8	204.75	C1	105.63
Slg1	144.55	505.925	C2	104.14
S2	221.1	773.85	C3	109.27
S1	1061.2	3714.2		
SF1	24.8+ 61.95	303.6		
SP2	44.2	154.7		
W	176.9	619.15		
CSF	156	546		

Table B-12 Design mix of trial 13 with the new materials; 15% FA, 25% SF2, 60%Slg2

M13 (V = 2L, 30/01/2018)				
Material	kg/m ³	(g)	Flowability	<i>f'</i> _{cc} (MPa)
C2	594.2	1188.4		07 days: 05/02/2018 65.65
LP	58.8	117.6		14 days: 12/02/2018 89.07
FA	30.975	61.95		21 days: 19/02/2018 106
Slg2	123.9	247.8		28 days: 28/02/2018 116
S2	221.1	442.2		
S3	1061.2	2122.4		
SF2	24.8 + 51.62	152.85		
SP3	44.2	88.4		
W	176.9	353.8		
SSF	156	312		

Table B-13 Design mix for the 14th trial identical to M13 with different mixing procedure

M14 (V = 2L, 31/01/2018)				
Material	kg/m ³	(g)	<i>f'</i> _{cc} (MPa)	
C2	594.2	1188.4	07 days: 06/02/2018	77.4
LP	58.8	117.6	14 days: 13/02/2018	101.2
FA	30.975	61.95	21 days: 20/02/2018	109
Slg2	123.9	247.8	28 days: 27/02/2018	120
S2	221.1	442.2		
S3	1061.2	2122.4		
SF2	24.8 + 51.63	152.85		
SP3	44.2	88.4		
W	176.9	353.8		
SSF	156	312		

B.3 Mixing trials for (Shao, 2016)

Table B-14 Design mixture for the first trial with S1 and S2 divided equally (Shao, 2016)

B1 (V = 1.1 L, 11/07/2017)				
Material	kg/m ³	(g)	Flowability	f'_{cc} (MPa)
C1	757.81	833.6		07 days: 07/18/2017
S2	349.85	384.8		14 days: 07/25/2017
S1	349.85	384.8		78
Slg1	378.90	416.8		84
SF1	126.30	138.9		
SP1	25.83	28.4 + 49		
W	227.34	250.1 + 10		
CSF	197.75	217.5		

Table B-15 Design mix for the 2nd trial with 20% S2 and 80% S1, SP2 (w/b = 0.18)

B2 (V = 0.275 L, 12/07/2017)			
Material	kg/m ³	(g)	Flowability
C1	757.81	208.4	
S2	139.94	38.48	
S1	559.76	153.934	
Slg1	378.90	104.2	
SF1	126.30	34.73	
SP2	25.83	7.1 + 9	
W	227.34	62.52 + 12	
CSF	197.75	54.381	

Table B-16 Design mix for the third trial (w/b = 0.2)

B3 (V = 0.3 L, 27/07/2017)		
Material	kg/m ³	(g)
C1	724.13	217.2
S2	139.94	42
S1	534.88	160.5
Slg1	362.06	108.6
SF1	120.69	36.2
SP2	17.01	5.103 + 20
W	241.13	72.3
CSF	197.75	59.3

Table B-17 Design mix for the fourth trial using the same reference materials ($w/b = 0.2$)

B4 (V = 2L, 13/02/2018)				
Material	kg/m ³	(g)		f'_{cc} (MPa)
C2	724.13	1448.26	7 days: 20/02/2018	102.9
Slg2	362.06	724.12	14 days: 27/02/2018	122.8
S3	668.6	1337.2	28 days: 16/03/2018	139.7
SF2	120.69	241.38		
SP3	17.01	34.02		
W	241.13	482.26		
SSF	195.75	391.5		

Table B-18 Design mix for batch 6 with same liquid additives but longer mixing time

B6 (V = 2L, 30/05/2018)				
Material	kg/m ³	(g)	Flow test	
C2	724.13	1448.26	 $D_{\text{matrix}} > 230 \text{ mm}$	 $D_{\text{matrix/fibers}} > 230 \text{ mm}$
Slg2	362.06	724.12		
S3	668.6	1337.2		
SF2	120.69	241.38		
SP3	17.01	34.02		
W	241.13	482.26		
SSF	195.75	391.5		

Table B-19 Design mix for the seventh batch with less superplasticizer and same extended mixing time ($w/b = 0.2$)

B7 (V = 2L, 31/05/2018)				
Material	kg/m ³	(g)	Flow test	
C2	724.13	1448.26	 $D_{\text{matrix}} > 230 \text{ mm}$	 $D_{\text{matrix/fibers}} < 230 \text{ mm}$
Slg2	362.06	724.12		
S3	668.6	1337.2		
SF2	120.69	241.38		
SP3	15	30		
W	241.13	482.26		
SSF	195.75	391.5		

Table B-20 Design mix of batch 8 with same proportions as B7 to study the size effect

B8 (V = 6L, 05/06/2018)			
Material	kg/m ³	(g)	Flow test
C2	724.13	4344.78	
Slg2	362.06	2172.36	
S3	668.6	4011.6	
SF2	120.69	724.14	
SP3	15	90 – 12.5	
W	241.13	1446.78	
SSF	195.75	1174.5	

Table B-21 Design mixture for the final batch for casting (w/b = 0.2)

B9 (V = 6L, 06/06/2018)			
Material	kg/m ³	(g)	Flow test
C2	724.13	4344.78	
Slg2	362.06	2172.36	
S3	668.6	4011.6	
SF2	120.69	724.14	
SP3	12.5	75 – 2	
W	241.13	1446.78	
SSF	195.75	1174.5	

B.4 Flow test procedure for the in-house design mixture for the different casting batches

Table B-22 Flowability tests for batch C3 (in-house design mix)

Casting	Flow test 1	Flow test/fibers 1
C3	 <p>(a)</p> <p>(D₁ D₂) = (220 225)</p>	 <p>(b)</p> <p>(D₁ D₂) = (210 205)</p>

Table B-23 Flowability tests for batch C4 of the (in-house design mix)

Casting	Flow test 1	Flow test 2	Flow test 3	Flow test/fibers 4									
													
	(a) (D ₁ D ₂) = (210 210)	(b) (D ₁ D ₂) = (210 220)	(c) (D ₁ D ₂) = (220 220)	(d) (D ₁ D ₂) = (140 145)									
C4	<table border="1"> <thead> <tr> <th>Flow test/fibers 5</th> <th>Flow test/fibers 6</th> <th>Flow test/fibers 7</th> </tr> </thead> <tbody> <tr> <td></td> <td></td> <td></td> </tr> <tr> <td>(e) (D₁ D₂) = (160 160)</td> <td>(f) (D₁ D₂) = (170 180)</td> <td>(g) (D₁ D₂) = (210 212)</td> </tr> </tbody> </table>				Flow test/fibers 5	Flow test/fibers 6	Flow test/fibers 7				(e) (D ₁ D ₂) = (160 160)	(f) (D ₁ D ₂) = (170 180)	(g) (D ₁ D ₂) = (210 212)
Flow test/fibers 5	Flow test/fibers 6	Flow test/fibers 7											
													
(e) (D ₁ D ₂) = (160 160)	(f) (D ₁ D ₂) = (170 180)	(g) (D ₁ D ₂) = (210 212)											

Table B-24 Flowability tests for batch C5 of the (in-house design mix)

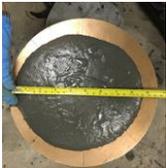
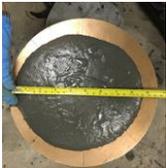
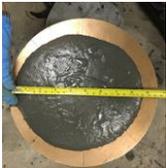
Casting	Flow test 1	Flow test 2	Flow test/fibers 1	Flow test/fibers 2			
							
	(a) (D ₁ D ₂) = (175 180)	(b) (D ₁ D ₂) = (210 220)	(c) (D ₁ D ₂) = (170 175)	(d) (D ₁ D ₂) = (195 200)			
C5	<table border="1"> <thead> <tr> <th>Flow test/fibers 5</th> </tr> </thead> <tbody> <tr> <td></td> </tr> <tr> <td>(e) (D₁ D₂) = (200 220)</td> </tr> </tbody> </table>				Flow test/fibers 5		(e) (D ₁ D ₂) = (200 220)
Flow test/fibers 5							
							
(e) (D ₁ D ₂) = (200 220)							

Table B-25 Flowability tests for batch C6 of the in-house design mix

Casting	Flow test 1	Flow test 2	Flow test 3	Flow test 4
C6				
	(a)	(b)	(c)	(d)
	$(D_1 D_2) = (160 155)$	$(D_1 D_2) = (165 170)$	$(D_1 D_2) = (180 175)$	$(D_1 D_2) = (190 190)$
	Flow test 5	Flow test 6	Flow test/fibers 1	
				
	(e)	(f)		
$(D_1 D_2) = (200 200)$	$(D_1 D_2) = (210 210)$	$(D_1 D_2) = (200 210)$		

Appendix C Material and equipment

C.1 Material and Equipment for batching, casting, curing and testing concrete

Table C-1 Tools used to batch, mix and cast concrete

Equipment	Item picture	Type
Mixer for casting large batches		CRETEANGLE Model "TEC 225" Pan Type Mixer
Mixer for small trial batches		Globe Model SP20
Scale for small weights		Mettler Toledo ME4002TE
Aluminum concrete slump scoop and shovel		N/A
Manual flow table		10" (254mm) cast bronze table supported in a cast iron base
Rigid cylinder molds		75 x 150 mm
Compression testing on cubes and cylinders		Controls PILOT 50-C46C02

Equipment	Item picture	Type
Steel molds for concrete compression cubes		(50 x 50 x 50mm)
Steel molds for concrete flexural prisms		(a x b) = (50 x 50 mm) l = 280 mm
Burlap roll		N/A
CGSB Approved Vapour Barrier		SUPER-SIX 10 t. X 100 ft.

C.2 Material and Equipment for building the formwork and test setup

Table C-2 List of materials used to build the beams (Source: Home Depot)

Item name	Item picture	Dimensions	Price/unit	#
23/32 in (18.3mm) Sanded Fir Plywood (Model # 2332FG1s)	 (a)	Depth (ft): 8 Height (in): 0.72 Width (ft): 4	\$59.97	1
2x2x8 Framing Lumber (Model # 173732)	 (b)	Depth (ft): 8 Height (in): 1.5 Width (in): 1.5	\$2.82	6

Item name	Item picture	Dimensions	Price/ unit	#
Green Deck Screws 500 Pieces (Model # 173732)	 (c)	6x1 ^{5/8}	\$22.68	1
Green Deck Screws 500 Pieces (Model # 214-546)	 (d)	8x1 ^{1/4}	\$26.24	1
1/4- 20 Stainless Steel thread Rod 3.' Model # 5091-314	 (e)	Height (ft) = 3 Width (in) = 0.25	\$7.48	4
20 Steel Wingnut Model # 103-014	 (f)	1/4	\$0.63	24
B.S. Plain Steel Washer Model # 146-114	 (g)	1/4	\$0.12	24

Table C-3 Materials used to build the beam setup

Item name	Item picture	Dimensions	Price/ unit	#
G1S Plywood 1/2 In X 24 In X 24 In (Model # 0621792)	 (a)	Depth (ft): 2 Height (in): 0.5 Width (ft): 2	\$10.63	1
Foam Insulation 2x2 Project Panels (Model # 756889)	 (b)	Depth (ft): 2 Height (in): 1 Width (ft): 2	\$7.50	1

Item name	Item picture	Dimensions	Price/ unit	#
Schedule 40 PVC Conduit 3/4 in (Model # 49007CC-010)	 (c)	$\varnothing_{\text{external}}(\text{in}):$ 1.05 $\varnothing_{\text{internal}}(\text{in}):$ 0.75 $t_{\text{PVC}} = 3 \text{ mm}$ Height (ft): 10	\$6.49	1
Crayola® Modelling Clay, Assorted Colours, 453g (Model # 57-0304)	 (d)	N/A	\$3.62	1
Steel plate	 (e)	$t = 1.25 \text{ cm}$	N/A	N/A

Table C-4 Material used for the frame measuring the slip of the reinforcing bar

Item name	Item picture	Dimensions	Price/ unit	#
Profile group 20 mm, H-slot, P	 (a)	Depth (mm): 20 Height (mm): 6 Width (mm): 20	\$59.9 7	1
T-Nut	 (b)	Depth (ft): 8 Height (in): 1.5 Width (in): 1.5	\$2.82	6

Green Deck Screws 500 Pieces (Model # 173732)		6x1 ^{5/8}	\$22.6 8	1
Angle		25 cm x 25 cm	N/A	4

Table C-5 Tools used for the experimental execution

Item name & number	Item picture
Cutting-Bending reinforcing bar	
20-Volt MAX XR Lithium-Ion Cordless 1/2 in. Compact Brushless Drill/Driver Model # DCD791B	
BESSEY 4 Inch Heavy Duty Bench Vise with Swivel Base Model # BV-HD40	
Bosch Multipurpose Drill Bit Model # MP06 & Bosch Daredevil Standard Spade Bit Model # DSB5010	

Item name & number	Item picture
<p>DEWALT 6-inch Bench Grinder Model # DW756</p>	 <p>(h)</p>
<p>MAKITA 7- Inch Angle Grinder Model # GA7050</p>	 <p>(i)</p>
<p>Diablo 7 x 1/16 in. Metal DC Cut Off Disc Type 27 Model # CDD070063701F</p>	 <p>(j)</p>

Appendix D Additional data of failed specimens

D.1 Cylinders mode of failure

Table D-1 Failure mode of the cylinders for the in-house design mixture

IE1C1	Front face	Back face
IE1C1-A-		
IE1C1-B-		

IE1C2-A-



IE1C2-B-



IE2C2-A-



IE2C2-B-



IE3C2-A-



IE3C2-B-



D.2 Flexural prisms mode of failure

Table D-2 The other failed faces of the prisms from Series S1, S2, S3 and S4

Series	Side supporting the linear potentiometer	Lower face of the prism
S1		

S2



S3

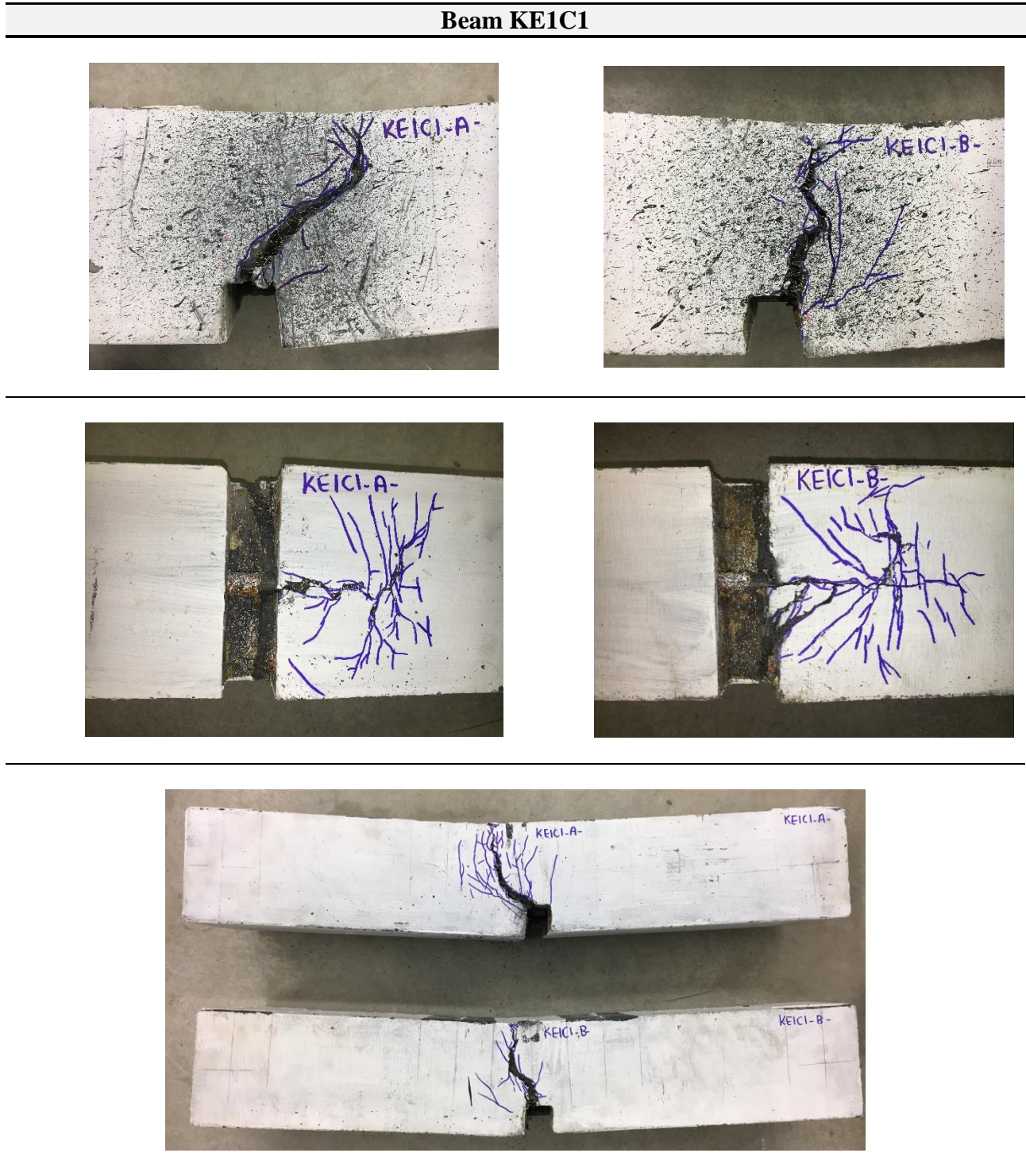


S4



D.3 Bond failure and mode of failure

Table D-3 Cracking pattern for all faces of Beam KE1C1

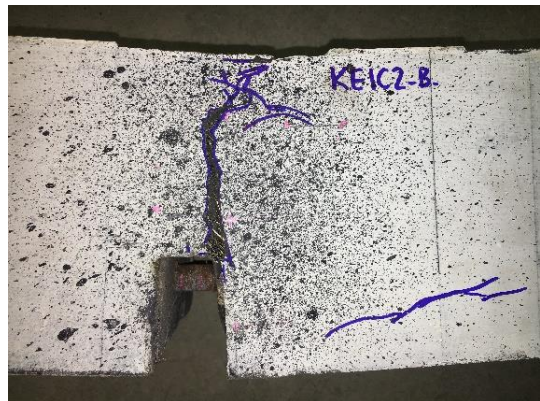


Beam KE1C1



Table D-4 Cracking pattern for all faces of Beam KE1C2

Beam KE1C2



Beam KE1C2



Table D-5 Cracking pattern for all faces of Beam KE4C1

Beam KE4C1



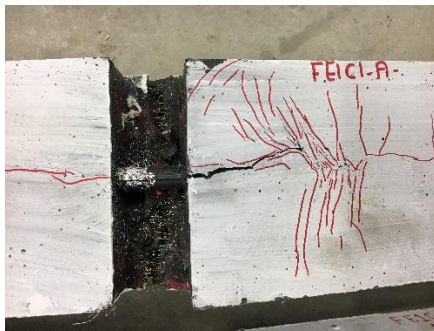
Table D-6 Cracking pattern for all faces of Beam KE4C2

Beam KE4C2



Table D-7 Cracking pattern for all faces of Beam FE1C1

Beam FE1C1



Beam FE1C1



Table D-8 Cracking pattern for all faces of Beam FE1C2

Beam FE1C2



Beam FE1C2



Table D-9 Cracking pattern for all faces of Beam FE4C1

Beam FE4C1

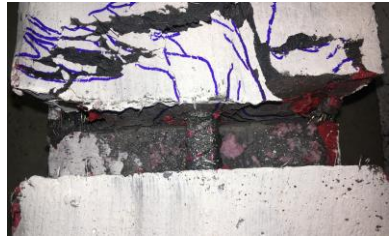
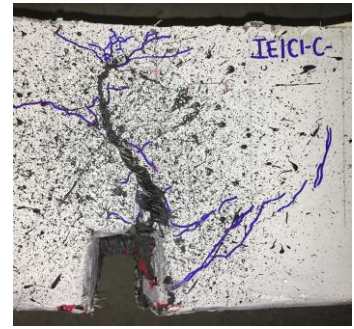
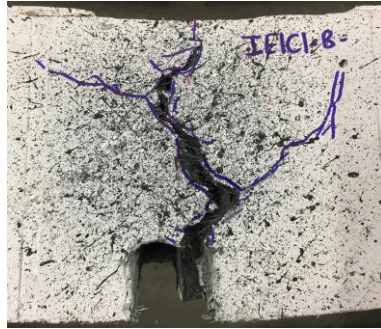
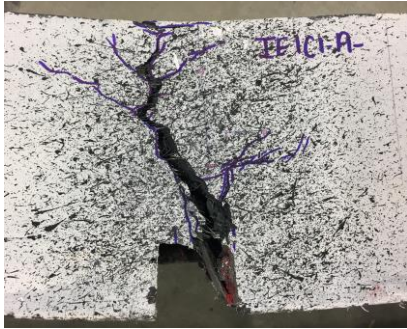


Beam FE4C1



Table D-10 Cracking pattern for all faces of Beam IE1C1

Beam IE1C1



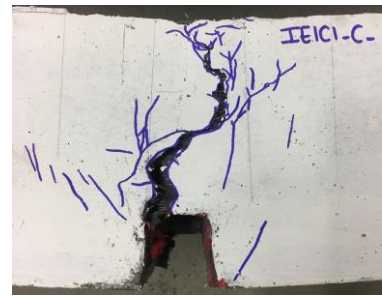
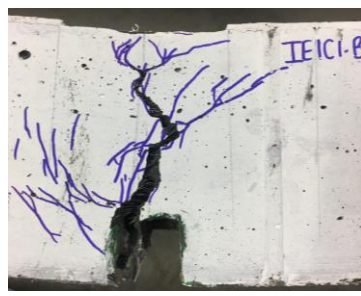
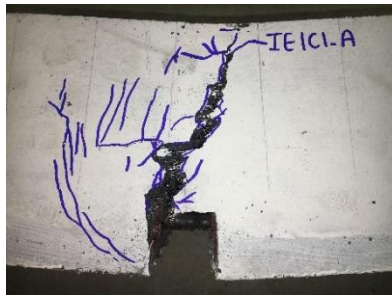


Table D-11 Cracking pattern for all faces of Beam IE1C2

Beam IE1C2



Beam IE1C2

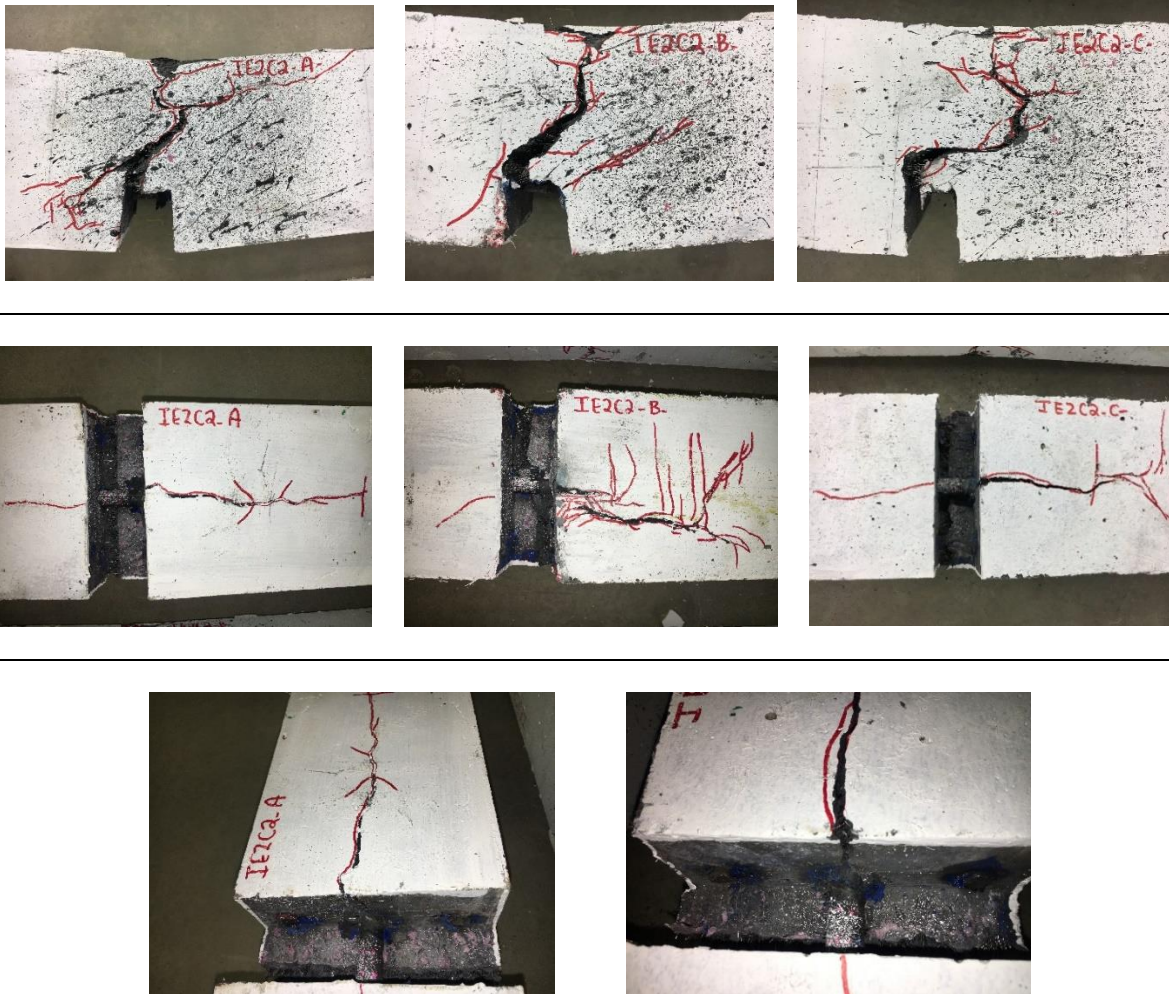


Beam IE1C2



Table D-12 Cracking pattern for all faces of Beam IE2C2

Beam IE2C2



Beam IE2C2

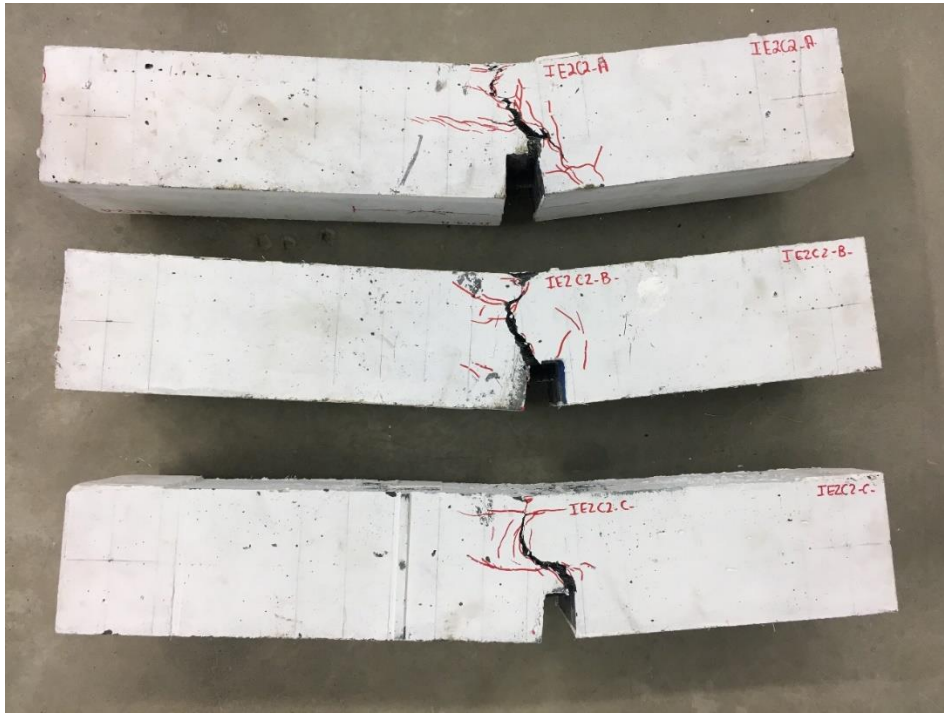
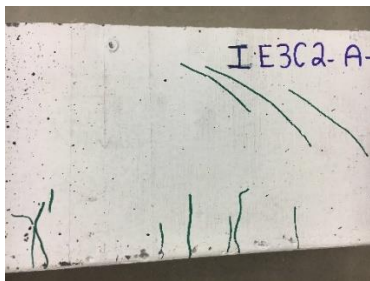
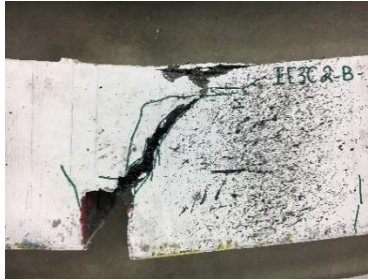


Table D-13 Cracking pattern for all faces of Beam IE3C2

Beam IE3C2



Beam IE3C2



Beam IE3C2



D.3.1 First cracking

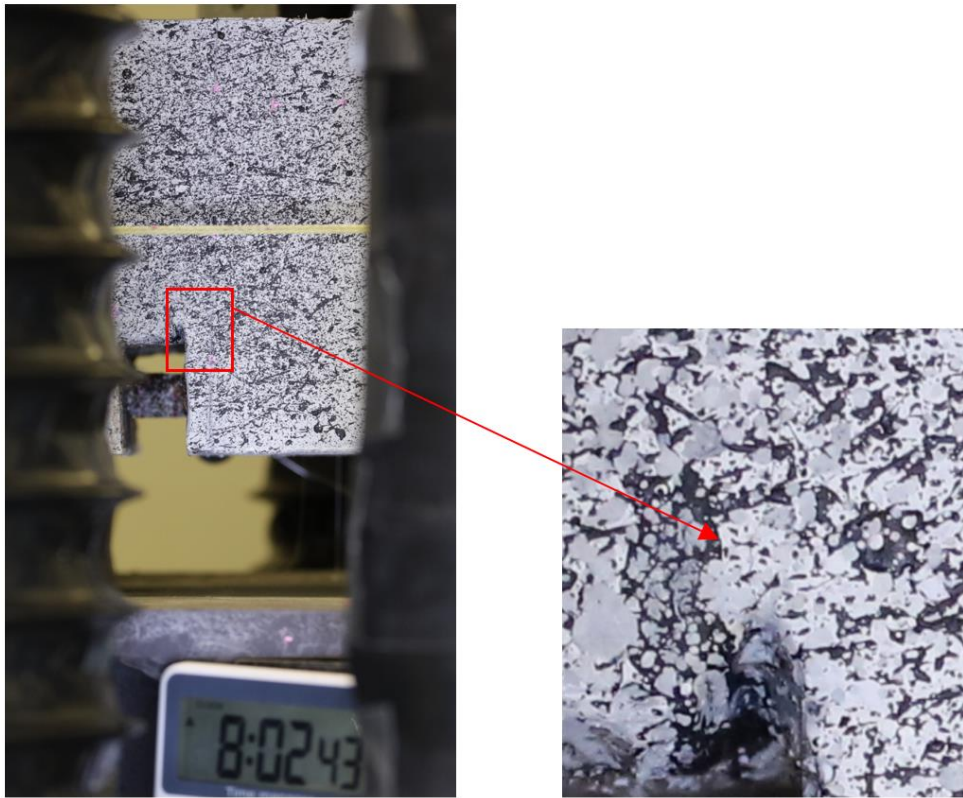


Figure D-1 First crack for beam KE1C1 - A -

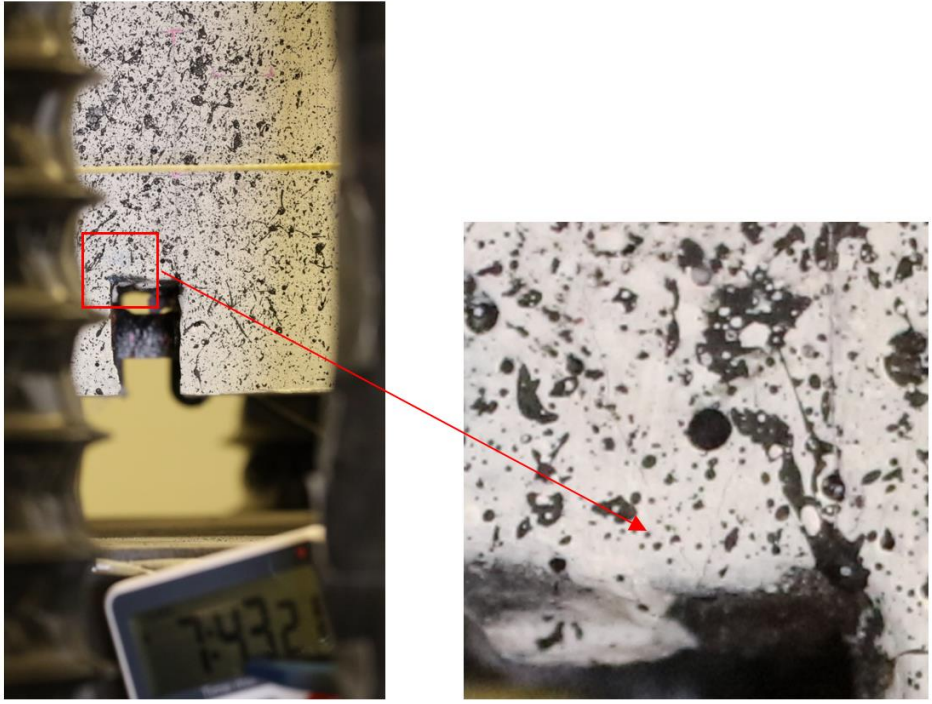


Figure D-2 First crack for beam FE1C1 - A -

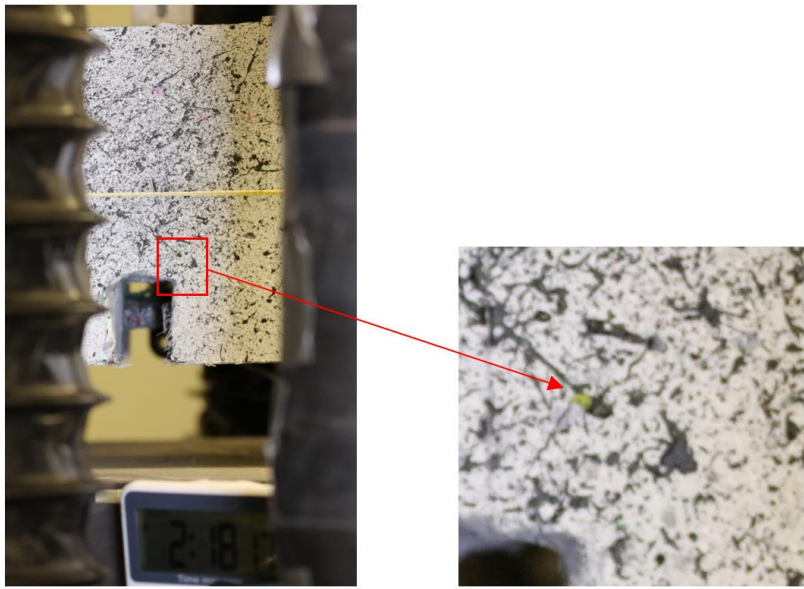


Figure D-3 First crack for beam IE1C1 - B -

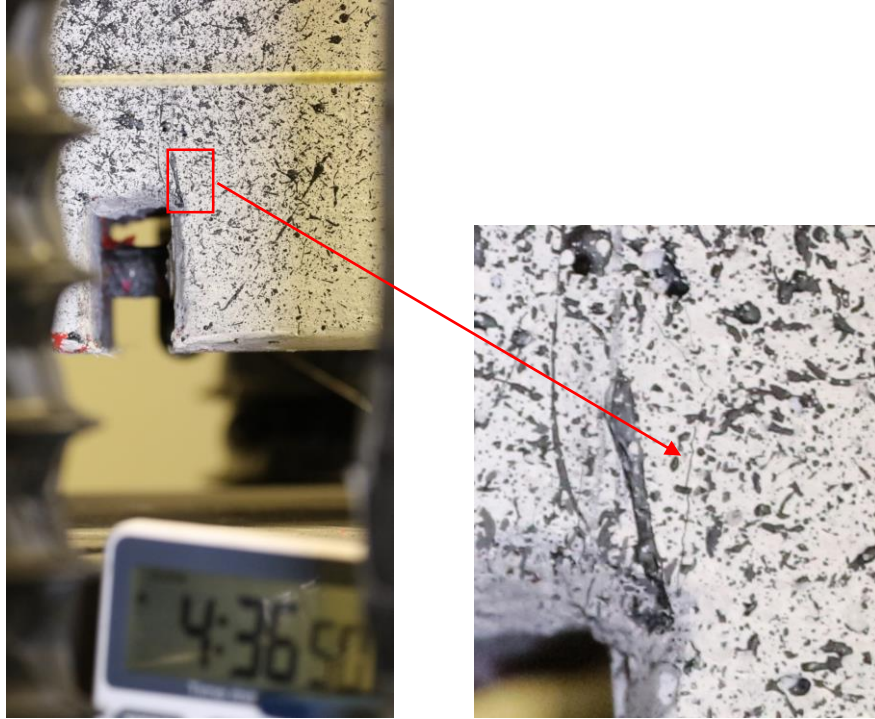


Figure D-4 First crack for beam IE1C1 - C -